Distributed Actuation and Control of Smart Structures

Zhou, Hongzhao

Award date:
2019

Awarding institution:
University of Bath

Distributed Actuation and Control of Smart Structures

Hongzhao Zhou

A thesis submitted for the degree of Doctor of Philosophy

University of Bath

Department of Mechanical Engineering

June 2019

Abstract

The aim of future dynamic machine development is to make them lighter, move faster, use less energy, be more human-friendly, and be more adaptable. A promising solution is distributed actuation integrated with load-bearing structures, which can potentially provide better static and dynamic performance, redundancy and more adaptability than current designs. Such structures can be referred to as smart structures. A morphing aircraft wing is a good example for the application of smart structures, which is deemed to provide better aerodynamic performance and higher wing efficiency than conventional designs. A tensegrity structure is a strong candidate for this integration due to its potentially high stiffness-to-mass ratio and inherent advantage of being a multi-element structure, into which actuators can be embedded. The research presented in this thesis concerns the study of a smart structure, and its integration with a morphing aircraft wing. A structure design method has been developed for an active tensegrity structure. The high external load level and actuator size constraints are the main challenges at the design stage. A case study design for a smart structure integrated in a morphing wing to be tested in the University of Bath wind tunnel is presented. A forward kinematic calculation method has been developed to transform the actuator axial displacements to structure shape changing degree of freedom (DOF) form. Six actuators and four shape-changing DOF are considered in the analysis, and two internal load paths are also under closed loop control. An

antagonistic multi-axial control scheme has been developed for the smart structure, which is capable of motion and internal force control.

An experimental smart structure prototype has been built, along with the morphing wing assembly. Pneumatic cylinders are embedded into the structure; switching valves are selected for the pneumatic control. A simulation model is developed for the prototype, including a dynamic model for the pneumatic system and a multi-body simulation for the structure. The dynamic behaviour of the smart structure has been investigated via a series of simulations and experiments. The wind tunnel test results have demonstrated that the prototype morphing wing is capable of accurate shape-changing control, and offering reasonable aerodynamic performance, while maintaining a desired level of internal load in a stiff structure, with different wind speeds.

Acknowledgements

I would like to express my gratitude to my supervisors Prof. Andrew Plummer and Dr. David Cleaver for their continuous support, guidance and valuable advice. Thanks to technicians Guy Brace, Nicholas Waywell, Steve Thomas and Steve Coombes, for their practical support.

I would like to thank my fellow colleagues and friends in the Department of Mechanical Engineering for all the stimulating discussions and valuable feedback. Thanks to all staff at the Centre for Power Transmission and Motion Control for their daily support.

Finally, a special thanks goes to my wonderful family, especially my parents, and my wife, Luqi, for their vast support and continuous encouragement.

Table of contents

Abstract I

Acknowledgements III

Table of contents IV

List of figures VIII

Notations XVIII

1 Introduction 1

1.1 Motivation 1

1.2 Aims and objectives 3

1.3 Original research contribution 3

1.4 Thesis outline 4

2 Literature review 6

2.1 Introduction to smart structures 6

2.1.1 Smart structure overview 6

2.1.2 Tensegrity structure concept 11

2.1.3 Active tensegrity structure studies 14

2.2 Morphing aircraft wings 18

2.2.1 Morphing wing categories and research 19

2.2.2 Poly-morphing and smart structures 32

2.2.3 Flexible skin for morphing aircraft wings 35

2.3 Conclusions 40

3 Active structure design and kinematics 42
3.1 Introduction 42
3.2 Wing morphing structure concept design 42
3.3 Wing load simulation and actuator selection 46
3.3.1 Aerodynamic load simulation 48
3.3.2 Tensile force estimation under external loads 50
3.3.3 Preload tension on actuators 53
3.3.4 Actuator selection and dimension optimization 54
3.4 Direct kinematics of proposed structure 59
3.4.1 Configuration of the structure 59
3.4.2 Kinematic analysis 59
3.4.3 Structure deformation modes 60
3.5 Conclusions 62
4 Experimental systems 64
4.1 Structural components and node design 64
4.2.1 Actuator and valves 68
4.2.2 Assembly of actuators 70
4.3 Displacement and motion tracking 72
4.4 Force measurement in wind tunnel 75
4.5 Extension wing and skin 76
4.5.1 Wing rib and extension wing 76
4.5.2 Flexible skin 77

4.5.3 Wing design scaling 81
4.6 Signal processing and real-time control environment 89
4.7 Wind tunnel 90
4.8 Conclusions 91
5 Simulation and control scheme 92
5.1 Modeling of Pneumatic Valve and Actuator groups 92
5.1.1 Modeling of SMC V114/124 3 port solenoid valve 92
5.1.2 Modeling of FESTO DSNU25-25 Pneumatic Actuator 95
5.2 Multi-body modeling for active tensegrity structure 97
5.3 Control scheme 100
5.4 Simulation results 105
5.4.1 Motion control with square wave demand 106
5.4.2 Motion control with sine wave demand 109
5.4.3 Comparison between simulation and experimental motion control results 112
5.5 Conclusions 117
6 Motion and internal load control of active structure 118
6.1 Motion control with fixed internal load 119
6.1.1 Motion control with square wave demand 119
6.1.2 Discussion of step response results 122
6.2 The effect of tensile member elasticity on motion control 123
6.3 Motion and internal load control with reinforced tensile members 129

6.3.1 Motion control with square wave demand 130
6.3.2 Motion control with sine wave demand 135
6.3.3 Motion control with ramp demand 139
6.4 Conclusions 141
7 Morphing wing tests in a wind tunnel 143
7.1 Twist motion 144
7.1.1 Twist motion wind tunnel test results 145
7.1.2 XFLR5 simulation results 154
7.1.3 Discussion of twist wind tunnel tests 157
7.2 Bend motion 162
7.2.1 Bend motion wind tunnel test result 162
7.2.2 Discussions on bend wind tunnel tests 167
7.3 Comparison between bench top and wind tunnel test 169
7.4 Conclusions 171
8 Conclusions and future work 173
8.1 Conclusions 173
8.2 Future work 176
Publications: 178
References 179
Appendix 185

List of figures

Figure 2.1 VGT structure modules (Left) (Miura 1984), and VGT manipulator actuated by DC motor (Right)(MIURA, FURUYA et al. 1985) 7

Figure 2.2 Four candidate VGT topologies: (a) stacked octahedral; (b) stacked cubic; irregular tetrahedral; (d) stacked regular tetrahedral. (Hughes, Sincarsin et al. 1991) 8

Figure 2.3 Tendon-actuated compliant truss (Ramrakhyani, Lesieutre et al. 2005) 8

Figure 2.2.4 Clustered actuated tensegrity structures(Moored and Bart-Smith 2009) 9

Figure 2.5 A tetrahedral truss unit actuated by shape memory wire actuators (Sofla, Elzey et al. 2009) 10

Figure 2.6 VGWingbox prototype with hydraulic actuators (Moosavian, Xi et al. 2014) 10

Figure 2.7 A class 2 and a class 3 tensegrity system (Skelton and Oliveira 2009) 12

Figure 2.8 Integration of actuators (Averseng, Dubé et al. 2005) 15

Figure 2.9 A Tensegrity flight simulator (Sultan, Corless et al. 2000) 17

Figure 2.10 SUPERball performing a single punctuated roll or face-change movement (Sabelhaus, Bruce et al. 2015) 18

Figure 2.11 Wright Flyer wing control method (Wright and Kelly 1988) 19

Figure 2.12 Morphing wing categories 20

Figure 2.13 Scissor wing section: un-morphed and morphed configurations 22

Figure 2.14 Boeing 2707-200 variable-geometry supersonic transport (Weisshaar 2013) 23

Figure 2.15 Morphing wing configurations for (left to right) high-lift, climb, cruise, loiter, and maneuver. b is wing span and S is wing area. (Bowman, Sanders et al. 2007) 23

Figure 2.16 Batwing model in the NASA Langley wind tunnel(Bowman, Sanders et al. 2007) 24
Figure 2.17 Active aeroelastic wing F/A-18 airplane on flight test program(Clarke, Allen et al. 2005) 25
Figure 2.18 VSS mechanism (Chen, Sarhaddi et al. 2000).....26
Figure 2.19 Single VVS (left) and VVS/TF design(right) (Chen, Sarhaddi et al. 2000).....26
Figure 2.20 A torque rod embedded within the membrane wing (Stanford, Abdulrahim et al. 2007) 27
Figure 2.21 Shape of morphing wing (Top), position of the SMA wires within the morphing wing section (bottom) (Rodrigue, Cho et al. 2016) 27
Figure 2.22 Construction of shape-changing structures from discrete lattice building-block elements (Jenett, Calisch et al. 2017).....28
Figure 2.23 The North American XB-70A Valkyrie (s/n 62-0207)(U.S. 1966) 29
Figure 2.24 Multiple exposure photograph of Lockheed Martin MAS wind tunnel model during a morphing sequence (Ivanco, Scott et al. 2007).....30
Figure 2.25 Experimental model as mounted in the wind tunnel; left: both winglets planar; right: both winglets upright (Bourdin, Gatto et al. 2008).....30
Figure 2.26 FishBAC wind tunnel model: (a) baseline state (b) deflected 31
Figure 2.27 Wing planform schematic of baseline and MORPHLET 33
Figure 2.28 Rolled out and canted mechanical demonstrator (30 deg dihedral and 5 deg twist) (Ursache, Melin et al. 2008) 33
Figure 2.29 Overview of internal vehicle structure for a 3DOF morphing wing(Neal, Good et

al. 2004) 34

Figure 2.30 Side and front views of the prototype showing poses 0, 1, 2, and 3. (Moosavian, Xi et al. 2013) 34

Figure 2.31 (a) A three-strut, a four-strut and a six-strut tensegrity prism (b) a tensegrity wing structure with a cable actuation cluster (black) (Moored and Bart-Smith 2009) 35

Figure 2.32 Lockheed Martin MAS model with flexible seamless skins (Ivanco, Scott et al. 2007) 37

Figure 2.33 An F-14 “Tomcat” fighter aircraft with black inflated air bag at wing root (O'Connor 2003) 38

Figure 2.34 Simulation of surface segmentation and morphing.(Guo, Qiang et al. 2016) 38

Figure 2.35 FE models for auxetic honeycomb design(Huang, Zhang et al. 2017) 38

Figure 2.36 Schematics of FMC fiber orientation for (a) span morphing and (b) camber or chord morphing.(Murray, Gandhi et al. 2010) 39

Figure 2.37 Proposed morphing skin prototype including PAM actuation system. (Bubert, Woods et al. 2010) 39

Figure 2.38 Schematic (left) and picture (right) of segmented skin bonded to the corrugated laminate (Thill, Etches et al. 2010) 39

Figure 3.1 a) octahedron frame b) unit tensegrity. (Dashed lines are members which are behind the imagined front faces of the structure; blue lines are cables) 43

Figure 3.2 Frame (left) and tensegrity (right) joints 44

Figure 3.3 Tensegrity in morphing modules a) neutral b) twist c) bend d) shear. Black lines are struts, blue lines are cables, and red lines are actuators. 45

Figure 3.4 Pair of unit cells sharing a side strut....46

Figure 3.5 fully integrated cell with additional actuators....46

Figure 3.6 Lift coefficient vs angle of attack: simulation result for different chord lengths....49

Figure 3.7 Drag coefficient vs angle of attack: simulation result for different chord lengths ..49

Figure 3.8 Lift L vs angle of attack: simulation result for different chord lengths 49

Figure 3.9 Drag D vs angle of attack: simulation result for different chord lengths 49

Figure 3.10 Structure and element parameter notations 51

Figure 3.11 Load F_1 on actuators 51

Figure 3.12 Load F_2 on actuators 52

Figure 3.13 Cable preload on actuators 53

Figure 3.14 Illustrated tensegrity embedded....55

Figure 3.15 Active tensegrity structure in its neutral position 58

Figure 3.16 Twist actuation example: a) top view b) front view c) end view 62

Figure 3.17 Bend actuation example (downward)....62

Figure 4.1 A single-unit tensegrity structure with springs instead of actuators....64

Figure 4.2 Unactuated tensegrity structure cell (210×150×94mm outer dimension)....67

Figure 4.3 Node design before (a) and after (b) refinement (c) ball joint 67

Figure 4.4 Node design example....68

Figure 4.5 Circuit diagram for a single actuator 69

Figure 4.6 V124 exhaust valve group on manifold....69

Figure 4.7 V114 supply valve group with pressure transmitters 70

Figure 4.8 Compact cylinder and fittings 71

Figure 4.9 Clevis with spacer 71

Figure 4.10 Structure full assembly 71

Figure 4.11 Repetition accuracy as a function of position measuring range *s* (FESTO 2018) 73

Figure 4.12 Cameras and markers arrangement on test rig 74

Figure 4.13 Cameras and markers arrangement in wind tunnel 74

Figure 4.14 Force measurement balance a) front view b) top view 76

Figure 4.15 Nylon ribs and foam in-fill before skin attached. Ribs held at correct spacing by temporary fixture. 77

Figure 4.16 Test specimen section (dimensions in mm) 79

Figure 4.17 Stress-strain test specimen a) top view b) back view 79

Figure 4.18 Tensile test specimen clamped with V-jaws 79

Figure 4.19 Tensile test result for the specimen 80

Figure 4.20 Wing morphing part with skin attached (trailing edge not trimmed yet) 81

Figure 4.21 Scale using a different span wise factor, top view. 86

Figure 4.22 Wind tunnel test section and wing 90

Figure 4.23 Force balance mounted on the wind tunnel frame 91

Figure 5.1 Circuit diagram for an actuator pulling a mass block 93

Figure 5.2 Actuator diagram defining notation 96

Figure 5.3 Spherical joint for strut-to-node joint 99

Figure 5.4 Simulated structure in neutral position isometric view 99

Figure 5.5 Control scheme for the discussed structure 101

Figure 5.6 Actuator orientation in model.....103

Figure 5.7 Simulated structure top view with neutral (top) and 12° twist (bottom).....106

Figure 5.8 Simulated structure front view with neutral (top) and 8°bend(bottom).....107

Figure 5.9 Simulation results with square wave twist demand of 12° 107

Figure 5.10 Simulation results with square wave bend demand of 8° 108

Figure 5.11 Simulation results with sine wave twist of 6° (around 6° baseline) 110

Figure 5.12 Simulation results with sine wave bend of 4° (around 4° baseline) 111

Figure 5.13 Results with step twist demand and 140N internal load 113

Figure 5.14 Results with step twist demand and 70N internal load.....114

Figure 5.15 Results with step bend demand and 140N internal load 114

Figure 5.16 Simulation and experimental results with sine wave twist demand and 140N internal load.....115

Figure 5.17 Simulation and experimental results with sine wave bend demand and 140N internal load.....115

Figure 5.18 Results with step twist demand and 140N internal load, T_c=10ms 116

Figure 5.19 Results with sine twist demand and 140N internal load, T_c=10ms.....116

Figure 6.1 the prototype structure with neutral (left) twist (mid) and bend (right).....118

Figure 6.2 Twist angle from actuator position measurements and optical tracker, with a square wave twist demand r_t.....120

Figure 6.3 Bend angle from actuator position measurements and optical tracker, with a square wave twist demand r_t.....120

Figure 6.4 Controlled actuator force result during square wave twist demand.....120

Figure 6.5 Bend angle from actuator position measurements and optical tracker, with a square wave demand r_b.....121

Figure 6.6 Twist angle from actuator position measurements and optical tracker, with a zero demand r_t.....121

Figure 6.7 Controlled actuator force result during bending 121

Figure 6.8 Tensile member example used in prototype 124

Figure 6.9 Pin joint model of the prototype 124

Figure 6.10 Tensile test set up.....124

Figure 6.11 Cable tensile test result.....125

Figure 6.12 Twist angle from actuator position measurements and optical tracker, kinematics refined. 127

Figure 6.13 Bend angle from actuator position measurements and optical tracker, with a zero bend demand r_b, kinematics refined.....127

Figure 6.14 Controlled actuator force result during twisting 127

Figure 6.15 Bend angle from actuator position measurements and optical tracker, with a square wave demand r_b, kinematics refined. 128

Figure 6.16 Twist angle from actuator position measurements and optical tracker,, with a zero demand r_t, kinematics refined. 128

Figure 6.17 Controlled actuator force result during bending 128

Figure 6.18 a) Mechanical damage b) Tensile failure 129

Figure 6.19 Cable types a) 7×7strands b) 1×19 strands (TECHNI-CABLE 2019).....130

Figure 6.20 Results with square wave twist demand of 0° to 12°, 140N internal load. 131

Figure 6.21 Results with square wave twist demand of 0° to 12°, 70N internal load. 132

Figure 6.22 Results with square wave bend demand of 0° to 8°, 140N internal load. 133

Figure 6.23 Results with square wave bend demand of 0° to 8°, 70N internal load. 134

Figure 6.24 Results with sine wave twist demand, 140N internal load. 136

Figure 6.25 Results with sine wave twist demand, 70N internal load. 136

Figure 6.26 Results with sine wave bend demand, 140N internal load. 138

Figure 6.27 Results with sine wave bend demand, 70N internal load. 138

Figure 6.28 Results with ramp twist demand, 140N internal load. 140

Figure 6.29 Results with ramp bend demand, 140N internal load. 141

Figure 7.1 Full prototype wing in wind tunnel test section 143

Figure 7.2 Prototype wing with neutral and 12°twist (bottom view through glass floor) 145

Figure 7.3 α_{tip} and α_{bend} optical tracker and actuator sensor angles, and actuation force, at α_{root} =0°, v=12.5m/s.....146

Figure 7.4 α_{tip} and α_{bend} optical tracker and actuator sensor angles, and actuation force, at α_{root} =3°, v=12.5m/s.....147

Figure 7.5 α_{tip} and α_{bend} optical tracker and actuator sensor angles, and actuation force, at α_{root} =6°, v=12.5m/s.....148

Figure 7.6 α_{tip} and α_{bend} optical tracker and actuator sensor angles, and actuation force, at α_{root} =9°, v=12.5m/s.....149

Figure 7.7 α_{tip} and α_{bend} optical tracker and actuator sensor angles, and actuation force, at α_{root} =12°, v=12.5m/s 150

Figure 7.8 α_{tip} and α_{bend} optical tracker and actuator sensor angles, and actuation force, at α_{root}

=12°, v=10m/s.....151

Figure 7.9 α_{tip} and α_{bend} optical tracker and actuator sensor angles, and actuation force, at α_{root} =12°, v=15m/s.....152

Figure 7.10 α_{tip} and α_{bend} optical tracker and actuator sensor angles, and actuation force, at α_{root} =12°, v=17.5m/s 153

Figure 7.11 Expected wing twist distribution along span 153

Figure 7.12 C_l, C_d and C_l/C_d contour for v=12.5m/s.....154

Figure 7.13 Far-field plane method for lift calculating(Deperrois 2019).....156

Figure 7.14 XFLR5 simulation panel with α_{root} = 12°, α_{twist} = 9° 157

Figure 7.15 Prototype wing in neutral and 4°bend (front view from flow direction).....162

Figure 7.16 α_{bend} and α_{tip} optical track and sensor measure result with actuation force, at α_{root} =0°, v=12.5m/s.....163

Figure 7.17 α_{bend} and α_{tip} optical track and sensor measure result with actuation force, at α_{root} =3°, v=12.5m/s.....164

Figure 7.18 α_{bend} and α_{tip} optical track and sensor measure result with actuation force, at α_{root} =6°, v=12.5m/s.....165

Figure 7.19 α_{bend} and α_{tip} optical track and sensor measure result with actuation force, at α_{root} =9°, v=12.5m/s.....166

Figure 7.20 α_{bend} and α_{tip} optical track and sensor measure result with actuation force, at α_{root} =12°, v=12.5m/s 167

Figure 7.21 Optical tracker and actuator sensor angles with increasing twist, and actuation force, at α_{root} =0°, v=12.5m/s, compared with bench top test.....169

Figure 7.22 Optical tracker and actuator sensor angles with decreasing twist, and actuation force, at α_{root} =0°, v=12.5m/s, compared with bench top test.....170

Figure A0.1Wingtip twist /bend optical track and sensor measure result with actuation force, at α_{root} =0°.....185

Figure A0.2 Wingtip twist /bend optical track and sensor measure result with actuation force, at α_{root} =3 °.....186

Figure A0.3 Wingtip twist /bend optical track and sensor measure result with actuation force, at α_{root} =6 °.....187

Figure A0.4 Wingtip twist /bend optical track and sensor measure result with actuation force, at α_{root} =9°.....188

Notations

Variables

A_t	Valve opening orifice area
A_o	Valve maximum orifice area
a	Number of actuators
b	Span length
b_v	Critical pressure ratio
C	Sonic conductance
$\mathbf{C}$	Position transformation matrix to actuator displacement
c	Chord length
C_d	Drag coefficient
C_l	Lift coefficient
C_v	Flow coefficient
D	Drag
$\mathbf{D}$	Force transformation matrix to individual actuator
D_l	Supply air pipe diameter
D_o	Valve orifice diameter
d	Number of individual DOF
$\mathbf{d_a}$	Actuator displacement vector
$\mathbf{d_c}$	Measured structure displacement in DOF
dl_i	Displacement for an actuator from its neutral position

dl_c	Cable length change
E	Modulus of elasticity
F_i	Load on tensegrity structure member
F_{ij}	Resolved force components of F_i
F_{a1}	Pneumatic actuation force on actuator
F_{a2}	Friction on actuator
F_{a3}	Load on actuator
$\mathbf{f_a}$	Measured force vector
$\mathbf{f_d}$	Averaged force vector
I	Moment of inertia
K_p, K_i, K_d, K_{pf}, K_{if}	Controller parameters
k	Heat capacity ratio
k_i	Correction factor for position transformation matrix P
L	Lift
l	Element length of a tensegrity structure member
l_{ac}	Cell actuator overall length at neutral
l_{ac}'	Actuator's built-in length
l_{as}	Actuator's maximum stroke
l_c	Cable length
l_{IA}	Intermediate actuator overall length at neutral
$\dot{m}$	Mass flow rate of air to pneumatic cylinder

N_{ij}	Nodal position
L_{s1}, L_{s2}	Strut length
$\mathbf{P}$	Position transformation matrix to DOF form
P_{atm}	Atmospheric pressure
P_u	Compressed air supply pressure
P_l	Pneumatic actuator chamber pressure
p	Static atmospheric pressure in lab
p_∞	Static pressure in the test section free stream
$\mathbf{Q}$	Force transformation matrix to averaged values
R	Individual gas constant of air
r_{ac}	Diameter of an inscribed sphere
$\mathbf{r_p}$	Motion control demand vector
$\mathbf{r_f}$	Force control demand vector
r_t	Twist motion control demand
r_b	Bend motion control demand
S	Wing area
s	Measurement range for a displacement sensor
T	Temperature in lab
V_2	Cylinder annulus chamber volume
v	Free stream velocity
W	Applied load on a cable

x	Measured axial displacement of an actuator
$\dot{x}$	Actuator piston axial velocity
$\ddot{x}$	Actuator piston axial acceleration
x_i, y_i, z_i *(Chapter 3 only)*	Nodal position coordinates
$\mathbf{y_c}$	Structure displacement vector

Greeks

α	Angle between a strut to ground plane in active unit
α_{bend}	Wingtip bend angle
α_{root}	Wing root AOA
α_{tip}	Wingtip AOA
α_{twist}	Wingtip twist angle
β	Angle between two actuators in active unit
Γ	Calculator for wing tip vortex
γ	Angle between two cables in active unit
γ_{114}	Valve charge parameter
γ_{124}	Valve exhaust parameter
ϕ	Bend, angular deformation about the y-axis
φ	General control variable of motion
θ	Twist, angular deformation about the x-axis
ρ	Air density
ψ	Sweep, angular deformation about the z-axis

Acronyms

ACARE	Advisory Council for Aviation Research and innovation in Europe
AAW	Active Aeroelastic Wing
AOA	Angle of Attack
DAQ	Data Acquisition
DOF	Degree of Freedom
DC	Direct Current
FMC	Flexible Matrix Composite
HECS	Hyper-elliptic Cambered Span
MAS	Morphing Aircraft Structures
ODE	Ordinary Differential Equation
PAM	Pneumatic Artificial Muscle
PDE	Partial Differential Equation
PID	Proportional-Integral-Derivative
PWM	Pulse-Width-Modulation
ReCTeR	Reservoir Compliant Tensegrity Robot
SMA	Shape Memory Alloy
SST	Supersonic Transport
SUPERball	Spherical Underactuated Planetary Exploration Robot ball
TF	Torsion Free
UAV	Unmanned Aerial Vehicle

VGT	Variable Geometry Truss
VSS	Variable Stiffness Spar

1 Introduction

1.1 Motivation

The aim of future dynamic machine development is to make machines lighter, move faster, use less energy, be more human-friendly, and be more adaptable. A solution is distributed actuation integrated with load-bearing structures, which can potentially provide better static and dynamic performance, redundancy and more adaptability than current designs.

One example of future smart structure application is the aviation industry. At present, aircraft manufacturers are subject to increased pressure to improve aircraft performance for economic and environmental legislative reasons. Passenger numbers are estimated to have a growth between 1-3% per year from 2010 to 2050 in the UK according to the Department for Transport (2013). According to ACARE's (2001) view the CO_2 emission of the aviation industry is expected to reduce by 50% in 2020, and by a further 25% in 2050 (Krein and Williams 2012), compared to the emission level in 2000. Innovative technologies are needed for future designs for a more efficient aircraft, including engines, airframes and aerodynamics.

A potential research area is morphing wing design, which refers to the wing's ability to change shape smoothly during flight. In present aircraft, wing configuration is changed via additional fixed surfaces (leading slats, flaps and ailerons), which relies on the deflection around fixed hinges, therefore creating discontinuous control surfaces. The discontinuous surfaces and sharp edges on the airfoil will produce flow separation

regions, which results in low wing efficiency. Replacing part of the conventional wing structure with distributed actuated smart structures that change shapes would be a more efficient approach for continuous aerodynamic control in different flight conditions.

A truss structure can be used as the basis of a morphing wing by replacing some of the truss elements with linear actuators. A tensegrity structure is a truss-like structure, which is composed of strut and cable members. All members are axially loaded, while cable members can only withstand tensile forces, and strut members are intended to take compression forces in static equilibrium conditions, and may take tensile forces in dynamic conditions or with changing external load. Compared with conventional truss members, tensegrity structure members can potentially be designed to be lighter, because they do not have to take bending loads. For cable members, in addition they have the advantage that they do not have to resist buckling. A tensegrity structure can be activated by replacing some members with actuators, and it has a potentially high stiffness-to-mass ratio, which makes it a strong candidate for a smart structure. In this research, an active tensegrity structure will be investigated as the basis of a morphing wingbox.

Based on the motivation, this research is pursued by addressing the following questions. How to design and control a distributed actuation dynamic structure? How to integrate the smart structure into a wing, and can it be made strong and stiff enough to carry the loads while still remain light weight?

1.2 Aims and objectives

The aim of the research is to develop and investigate smart structure, which is capable of changing shape while remaining load-bearing and light weight. The aim is also to integrate the designed structure into to a prototype morphing wing and experimentally determine aerodynamic performance.

The detailed objectives are as follow:

1. Review previous research into smart structures and morphing wings, with a particular focus on active tensegrity structures.
2. Design of smart structure, including structural, actuation and sensing elements, and refinement based on wing morphing requirements.
3. Kinematic analysis and modelling for the morphing structure and motion control method development.
4. Determine airfoil and wing parameters for a morphing wing which can be tested experimentally in the University of Bath wind tunnel.
5. Morphing structure construction and benchtop testing, to justify the proposed kinematic analysis and control method, and to investigate the structure dynamic.
6. Prototype wing construction and wind tunnel testing, to investigate the active structure characteristics with external load, and validate the aerodynamic behavior.

1.3 Original research contribution

The original research contributions in this research are:

1. A detailed design procedure for a tensegrity structure for a morphing application

is developed and presented with a case study of an active tensegrity structure embedded into a prototype wing to be tested in wind tunnel experimental test.

2. A forward kinematic analysis is established to transform the axial length change of tensile members to structure shape changing in degree of freedom form, which is a vital step for active tensegrity structure motion control.
3. A motion and internal load control scheme is developed, based on the multi-axis motion control framework by (Plummer 2010). A study on dynamic behaviour of an active tensegrity structure with different inertias and with different external load levels is presented.
4. Experimental evidence is collected to validate the morphing wing concept based on an active tensegrity structure.

1.4 Thesis outline

Chapter 2 presents a literature review of smart structures, focusing on tensegrity and truss-like structures, which are light in weight and load-bearing. A review is also made of morphing wings, including some feasibility studies of smart structures applied to morphing wings, and review for materials, which could be used for morphing wing skins.

Chapter 3 presents the design of an active tensegrity structure for application in an experimental morphing wing. The design procedure is described, including single cell design, expansion to multi cell and refinement for the specified application. For this research, the morphing structure is designed in a non-redundant manner. The

kinematic analysis of the complete structure and load calculation is also covered in this chapter.

Chapter 4 describes the experimental setup for this research, including the manufacture of the active smart structure and wing. Sensing systems for tests and the wind tunnel test venue are introduced.

Chapter 5 presents the detailed modeling of smart structure. The pneumatic actuation system is mathematically modeled, and the multi-body simulation is done to solve the 3D multi-body motion equations. Simulation results are presented in this chapter and compared with examples of bench-top experimental results.

Chapter 6 presents the methodology and setup of the bench-top experiments. The smart structure is tested with various motion commands at different internal load levels, and results are presented in detail. Motion results are validated with and independent sensing systems.

Chapter 7 presents the prototype wing wind tunnel test results, which includes twist and bend deformation with various baseline wing root angle of attack (AOA). The results are compared with an airfoil simulation to have a quantified study of aerodynamic performance. And they are also compared with the bench-top test results from Chapter 6 to study the dynamic performance of the smart structure under distributed external load and different inertia levels.

Chapter 8 includes conclusions and future research recommendations.

2 Literature review

This chapter provides a review of literature on morphing smart structures, focusing on morphing aircraft wings as its application. Section 2.1 reviews smart structures, with particular emphasis on the concept of tensegrity structures, and how these can be made active by embedding actuators. Section 2.2 presents an overview on morphing aircraft wings; Including recent research on morphing wings as smart structures, as well as the flexible skin for wings, which will be further developed and experimental evaluated in this thesis.

2.1 Introduction to smart structures

Smart structure research is a multidisciplinary area. Structures that change shape as demanded is the main interests of this research, including the structural design, sensing and actuation. Approaches to smart structure design are overviewed in section 2.1.1. A tensegrity structure is a strong candidate due to its unique properties, and the basic concept and design is reviewed, and some active tensegrity structure research studies are introduced in section 2.1.3.

2.1.1 Smart structure overview

Truss structures are good bases for smart structures, by replacing struts with linear actuators. The concept of variable geometry truss (VGT) structures was first proposed by Miura(1984) as shown in Figure 2.1, as a one dimensional deployable structure, consisting of octahedral truss modules, the structure was deployed by contracting the

lateral beams.

A VGT manipulator is developed based on deployable truss concept (MIURA, FURUYA et al. 1985), which may be the first shape changing truss with 3 degrees of freedom (3 DOF). The configuration of VGT manipulator is shown in Figure 2.1, the motion is actuated and sensed via direct current (DC) motors and built in encoders. The authors discussed other possible applications of the VGT structure, including support architectures for space stations and large actively controllable space structures. Further research on VGT configure topologies were presented in (Hughes, Sincarsin et al. 1991), a 20 cells model were investigated, considering configurational constrains, joint simplicity, and structure static and dynamic properties. The standard octahedral configuration was shown to be superior, especially on the simplicity of hinge articulation (including singularities considerations), among the four candidates as shown in Figure 2.2.

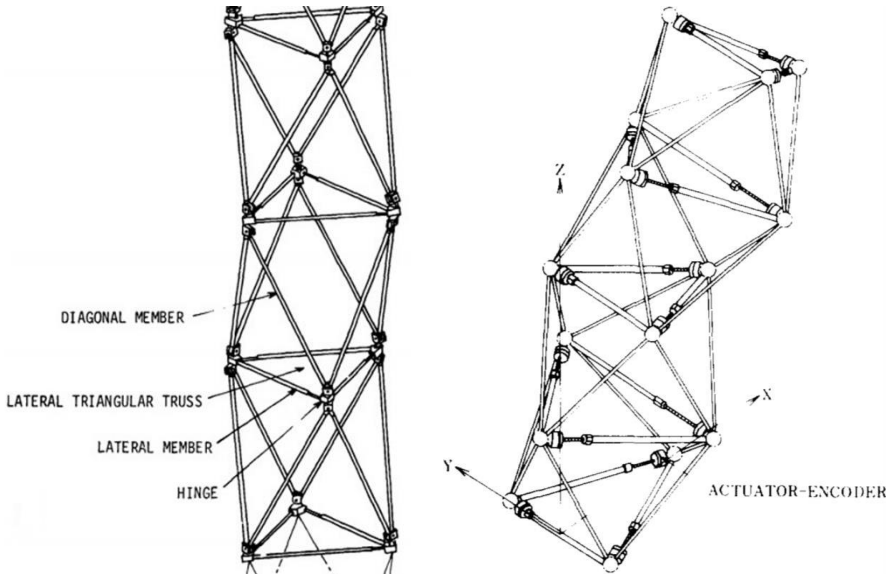

Figure 2.1 VGT structure modules (Left) (Miura 1984), and VGT manipulator actuated by DC motor (Right)(MIURA, FURUYA et al. 1985)

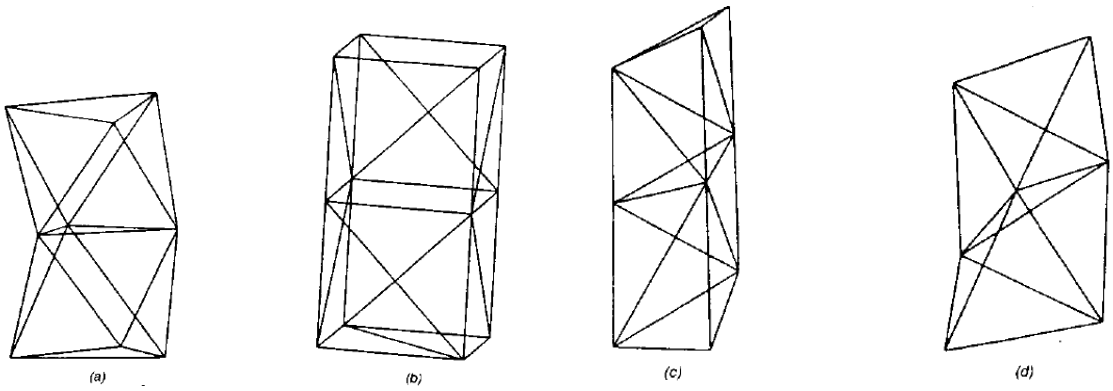

Figure 2.2 Four candidate VGT topologies: (a) stacked octahedral; (b) stacked cubic; irregular tetrahedral; (d) stacked regular tetrahedral. (Hughes, Sincarsin et al. 1991)

A compliant cellular truss was developed by Ramrakhyani et al (Ramrakhyani, Lesieutre et al. 2005), as shown in Figure 2.3, which used a cable-strut system to demonstrate actuation on the hyper-elliptic cambered span (HECS) wing. Tendon control was used to achieve a bending control of the wing. Theoretical research in clustered actuation for tensegrity structures was presented in (Moored and Bart-Smith 2009), using actuation via cables running through the structure, as illustrated structure in Figure 2.4.

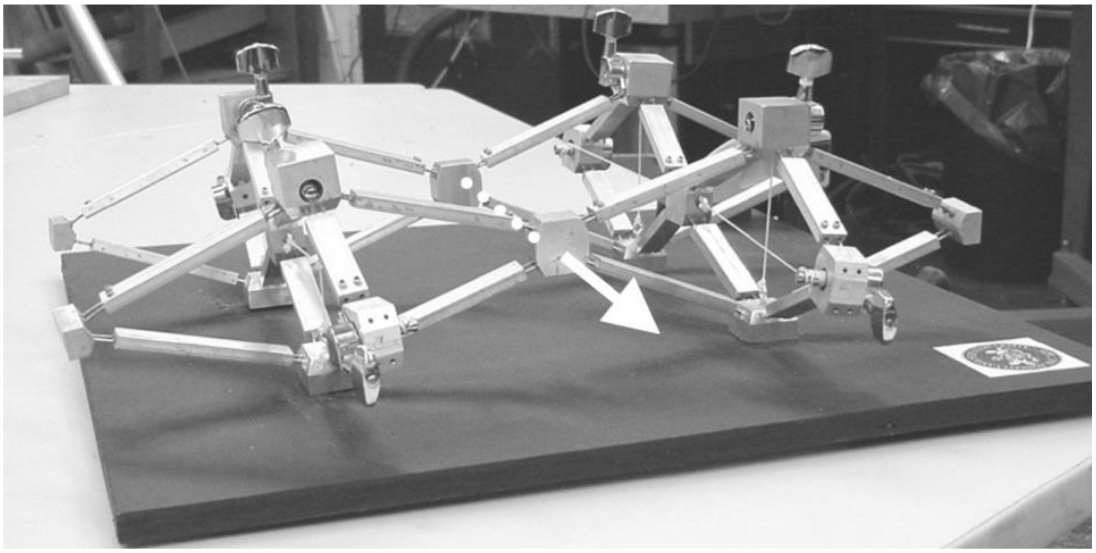

Figure 2.3 Tendon-actuated compliant truss (Ramrakhyani, Lesieutre et al. 2005)

A shape morphing hinged truss structure capable of bending, twisting and undulating was latterly developed by Sofla et al.(2009). Shape memory wire actuators were used antagonistically to change the shape of tetrahedral truss unit cells as shown in Figure 2.5. Prior research by Sofla et al. (2007) presented a novel spherical-pivotal joint, which allows up to 18 struts to be connected at each node as though they met at one point.

Recently, Moosavian et al (2013, 2014) presented a novel design of under-actuated parallel mechanism for application to a morphing wingtip. The structure of a conventional wingbox was replaced by active and passive linearly adjustable members, which would allow the structure to move in all six spatial degrees of freedom, with four actuators. A prototype was built and actuated with embedded hydraulic cylinders and active/passive flow control valves as shown in Figure 2.6.

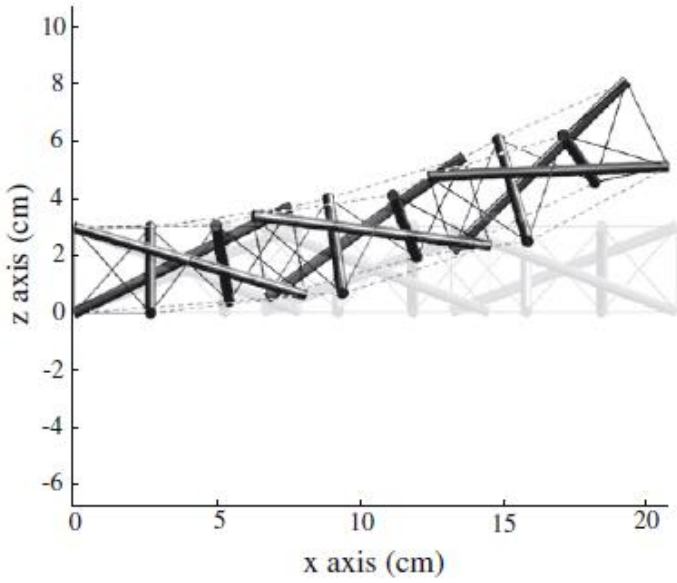

Figure 2.2.4 Clustered actuated tensegrity structures(Moored and Bart-Smith 2009)

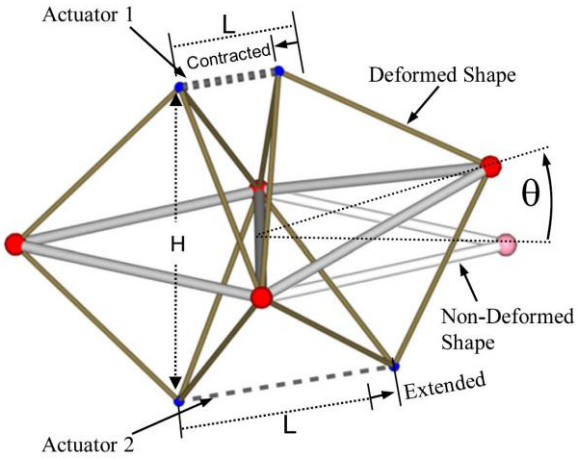

Figure 2.5 A tetrahedral truss unit actuated by shape memory wire actuators (Sofla, Elzey et al. 2009)

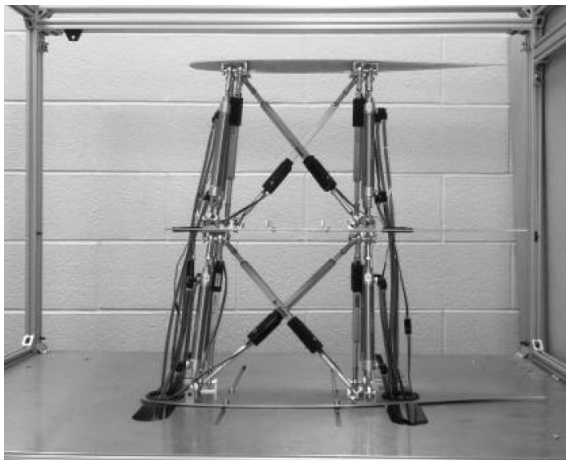

Figure 2.6 VGWingbox prototype with hydraulic actuators (Moosavian, Xi et al. 2014)

Among the modular designed examples of smart structure above, the motion control for a single unit cell has only been studied in detail by Moosavian, other studies are intended to verify the feasibility of shape morphing without much consideration of physical constraints (e.g. dimension for structure components, payload needed to be carried by the structures, etc.). In the work by Moosavian (2014), which is one of the very few examples where a full scale prototype was built, motion control examples were presented without carrying a payload, and the structural stiffness was only tested in the mid-position. Current research on smart structures lacks examples of the study

of kinematics, which is a vital step for motion control, and dynamic behaviour of such structures, especially under high-load conditions. It may be difficult to achieve a precise motion control of smart structures with high stiffness and for high load applications. Thus research on developing smart structures with high stiffness and motion capability is required, and it should be associated with the development of motion control methods.

2.1.2 Tensegrity structure concept

A tensegrity structure is a good candidate for smart structures due to its potentially excellent stiffness and strength-to-weight ratio, and as a multi elements structure the natural ease for embedded actuation.

The first reported tensegrity structure was a sculpture built by Snelson in 1948 (Sultan 2009). Snelson later defined the structure as a ‘Continuous tension, discontinuous compression structure’ (Snelson 1965) which is a closed structural system composed of a set of three or more compression struts within a continuous network of cables in tension, combined in such a way that the struts do not touch one another, but press outwardly against nodal points in the tension network to form pre-stressed units. Emmerich independently developed “self-tensioning structures” from the late 1950s (Emmerich 1996). Buckminster Fuller didn’t invent the structure (Emmerich , Sadao , Snelson 1996), but he did invented the word ‘tensegrity’ as a contraction of “tensional-integrity” (Buckminster 1962), and made the idea popular though his series of lectures in the late 1950s. Several tensegrity structures were built and presented in the1960s with a focus on geometric methods to find equilibrium form of tensegrity structures.

Pugh (1976) wrote a book on practical rules of building simple tensegrity structure, and he gave a definition: "*A tensegrity system is established when a set of discontinuous compression components interacts with a set of continuous tensile components to define a stable volume in space*,". Motro (2003) presented a definition which includes structures with interconnected compressive members into tensegrity structures: "*A tensegrity system is a system in a stable self-equilibrated state comprising a discontinuous set of compressed components inside a continuum of tensioned components*.", Skelton has further developed the definition in his book (2009): "*A tensegrity configuration that has no contacts between its rigid bodies is a class 1 tensegrity system, and a tensegrity system with as many as k rigid bodies in contact is a class k tensegrity system*.", examples are given in the book as shown in Figure 2.7.

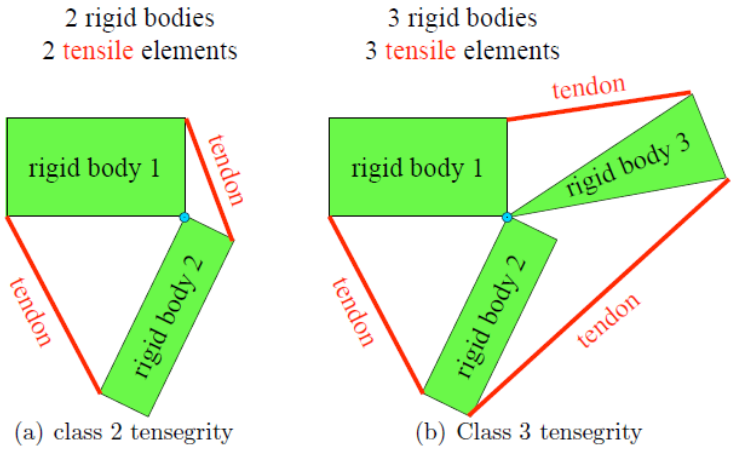

Figure 2.7 A class 2 and a class 3 tensegrity system (Skelton and Oliveira 2009)

With the wide range definitions, tensegrity structures could also be classified as a type of truss structures (Nishimura and Murakami 2001), or a pin-jointed framework composed of struts and cables of the statically indeterminate type (PELLEGRINO and

CALLADINE 1986). It could be concluded that any structures which are not stabilized by pre-stressed cables (i.e. tensile members) without external load are not tensegrity structures. The cable members are only able to withstand tensile forces, while the struts are intended to be in compression when the structure is in static equilibrium. The struts are able to exert tensile loads and may do so in dynamic scenarios or with altered external loading. The cables are tensile members, with no need to resist buckling, so they can be lighter, and gives high strength-to-weight ratios by reducing the structural mass, which reduces the energetic cost for motion control of conventional pin-jointed frameworks like a trusses.

Kenner(1976) initiated systemic research on tensegrity structures and introduced Newtonian analysis into tensegrity structures statics. They were modelled as diagrams of equilibrated forces, and simple geometry was used to find equilibrium configurations. Form-finding research was carried out since then to determine geometries and pre-stress distributions which give stable tensegrity structures, and this is well studied in the following two decades. Different approaches were presented. Analytical methods are largely used on symmetric tensegrity frameworks (Connelly and Back 1998, Sultan, Corless et al. 2001, Zhang, Guest et al. 2009, Koohestani and Guest 2013). Numerical methods and computational algorithms, e.g. the dynamic relaxation method which is capable of finding highly irregular prestressable configurations, in which each element could be a different length (for regular configurations, lengths of all cables are the same, and lengths of all struts are the same), can be found in (Zhang, Maurin et al. 2006, Koohestani and Guest 2013, Tran and Lee 2013).

For engineering applications, the tensegrity needs to have a stable configuration and high stiffness to mass ratio at the same time. The response of tensegrity structures under external load is important and was investigated widely (Stamenovic, Fredberg et al. 1996, Kebiche, Kazi-Aoual et al. 1999, Murakami 2001). As a self-stressed reticulated spatial systems, the mechanical behaviour of a tensegrity structure is non-linear due to their flexibility, also the displacement responses are different with external loads in same direction but with different distributions (i.e. uniformly distributed or concentrate) (Kebiche, Kazi-Aoual et al. 1999). The stiffness of a tensegrity structure increases when external load is applied (Motro, Najari et al. 1987). It is also shown(Oppenheim and Williams 2000), that the stiffness of a tensegrity structure increases when the pre-stress of its members increase. An algorithm optimizing a 2D structure under compressive and bending load was presented by Skelton (2009). A static prototype recently built (Lai 2017), addressed more engineering issues in tensegrity modelling and application, including the consequence of finite nodes (i.e. members which do not meet at an infinitesimal point) and therefore nodal angular stiffness considerations.

2.1.3 Active tensegrity structure studies

Common approaches for active tensegrity structures are replacing some members with actuators. These can be single-acting actuators, either contracting actuators to replace cables, or extending actuators to replace struts, approaches can be found in (Djouadi, Motro et al. 1998, Aldrich, Skelton et al. 2003, Chan, Arbelaez et al. 2004, Paul, Valero-Cuevas et al. 2006, Raja and Narayanan 2007). Averseng's group (2004,

2005, 2013) used hydraulic jacks placed outside of the structure as actuators (Figure 2.8).

Fine shape morphing and adjustment may be easier for tensegrity structures than for conventional structures(Skelton and Oliveira 2009), with the development of multi variables control, the active control for tensegrity structures has been the subject of several studied since the 1990s. The need to combine dynamics and control considerations with structural optimisation presents added complexity to the design of active tensegrity structure.

The nonlinear equations of motion for tensegrity structures were derived in the early 2000's by (Murakami 2001, Skelton, Pinaud et al. 2001, Sultan, Corless et al. 2002) using the Lagrangean approach. Conventional truss structures which are composed purely by struts are complex in member properties, therefore dynamic modelling requires infinitely dimensional partial differential equation (PDEs) sets.

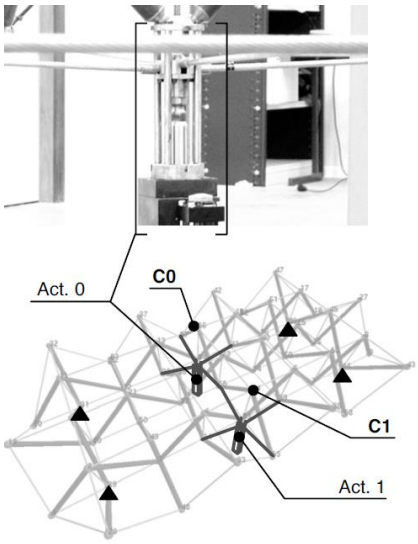

Figure 2.8 Integration of actuators (Averseng, Dubé et al. 2005)

For tensegrity structures, because of the clear separation of member properties, the

structures can be modelled as a set of rigid bodies (struts) subjected to a potential elastic field of soft bodies (cables). For the dynamic model, the motion can be determined by a finite number of ordinary differential equations (ODEs)(Sultan 2009). Few closed loop control study for active control have been presented, and these could be categorized by the feedback parameters. Nodal displacements were used by (Djouadi, Motro et al. 1998, Averseng and Crosnier 2004, Averseng, Dubé et al. 2005), nodal position and velocities were used by (Raja and Narayanan 2007). And tension force measurement were used in (Aldrich, Skelton et al. 2003, Chan, Arbelaez et al. 2004, Paul, Valero-Cuevas et al. 2006). Averseng et al.(2004, 2005) have divided the control law for the proposed tensegrity grids into two parts: Static control, where the high frequency displacements due to the vibration of the structure are filtered out and a simple PI controller is used, and dynamic control, which requires a robust control strategy to minimize the influence of un-modelled dynamics and external perturbations; (a H_∞ controller is suggested.).

A tensegrity flight simulator with 6-DOF was presented with a proposed controller, using the framework as shown in Figure 2.9 (Sultan, Corless et al. 2000), Skelton and Oliveira(2009) also investigated the dynamics and presented a control strategy for three-dimensional active tensegrity structures, with limited experimental results.

The research cited in this section is mostly theoretical and with some simulation results, however, experimental studies are particularly lacking at present. Only Averseng and Chan tested their algorithms using experimental prototype.

Locomotion is another application for active tensegrity structures. Paul (2006)

presented via simulations that actuator damage in a tensegrity robot can be accommodated, which showed a promising approach to building active structures with redundancy, but he encountered experimental issues in application to crawling locomotion robot research. NASA also developed a locomotion tensegrity for planetary exploration, known as Reservoir Compliant Tensegrity Robot (ReCTeR) (Caluwaerts, Despraz et al. 2014)and Spherical Underactuated Planetary Exploration Robot ball (SUPERball) (Sabelhaus, Bruce et al. 2015), Pictures of rolling motions are shown in Figure 2.10. In both cases, DC motors located at the end of struts were used to control the length of cables to actuate the structures.

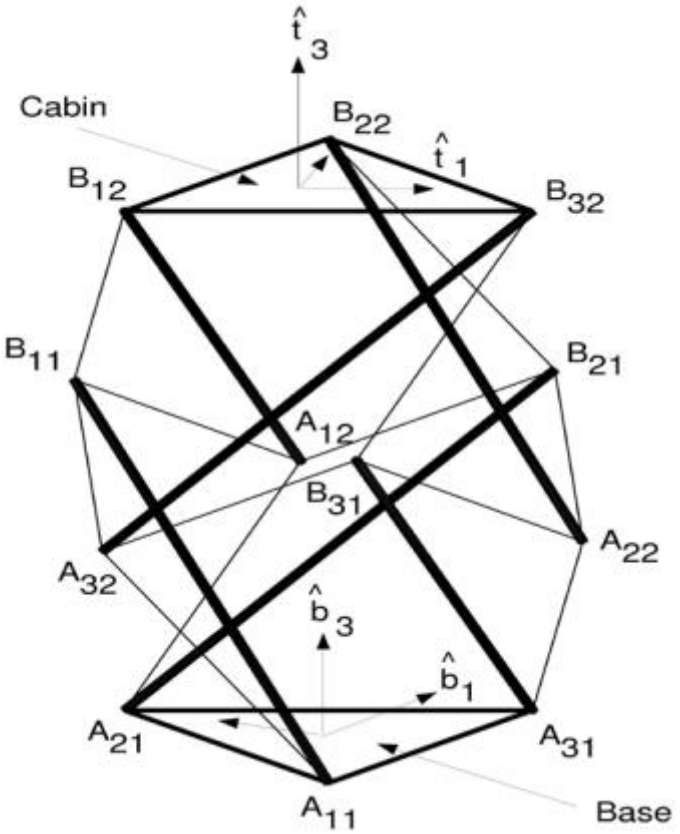

Figure 2.9 A Tensegrity flight simulator (Sultan, Corless et al. 2000)

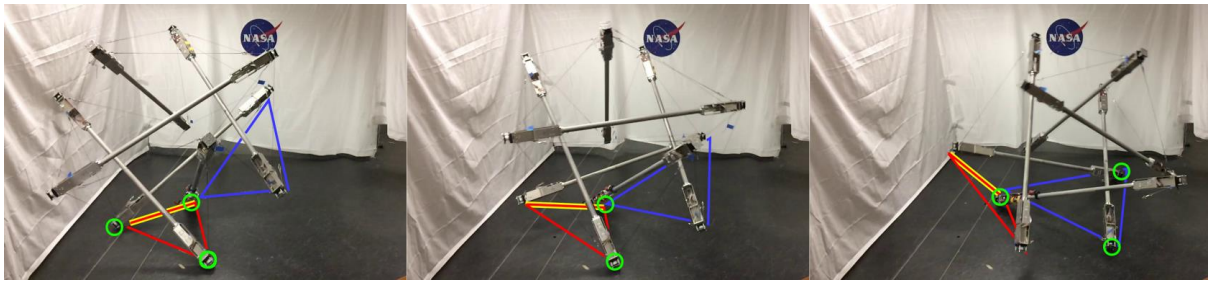

Figure 2.10 SUPERball performing a single punctuated roll or face-change movement (Sabelhaus, Bruce et al. 2015)

2.2 Morphing aircraft wings

The morphing wing is a concept which is far from new, it has been used since the first manned flight. The Wright Flyer embedded twisting of the wing directly actuated by cables operated by pilot, which controlled the roll of the plane as shown in Figure 2.11 .(Wright and Kelly 1988).

In modern aircraft, a high stiffness wing structure is commonly used, which is a result of the need to withstand higher aerodynamic loads and lift a higher payload. Conventional aerodynamic control mechanisms such as slats and flaps are adopted in civil aircraft to provide geometric change of its wings. They are only effective in a limited flight condition, and often have neutral or negative effect outside that range. Rotational hinges and sliding surfaces used in the conventional mechanisms are effective in controlling airflow, but not efficient as they create discontinuous surfaces and therefore causing unwanted fluid dynamic phenomena. (Barbarino, Bilgen et al. 2011)

Shape changing concepts have often used complex mechanics to achieve the wanted morphing, which bring penalties such as extra weight. A study by Bowman et al.(2007),

suggested that for most applications, there were crossover points where the weight penalties for morphing wings overtook the fuel efficiency penalties for not morphing. Some believe the morphing concept can only provide limited improvements in specific vehicles. Some also believe that morphing can only be successful if the new device is lighter than the conventional mechanism it is replacing. This is unlikely to be true, as morphing design should be considered from whole system level, rather than considering a specific aspect (Weisshaar 2013).

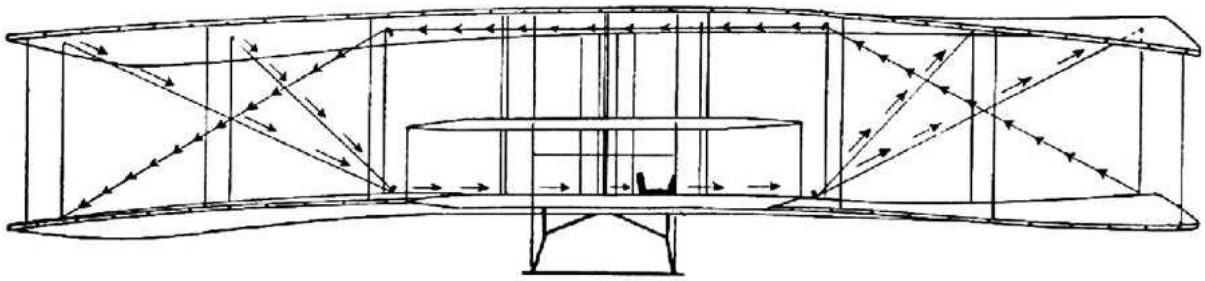

Figure 2.11 Wright Flyer wing control method (Wright and Kelly 1988)

2.2.1 Morphing wing categories and research

Based on the controlled motion, morphing might be categorized into two major parts as shown in Figure 2.12: i) airfoil morphing ii) wing morphing. Airfoil morphing includes camber adjustments, chord and thickness change, and wing morphing may be further divided into two sub sections: planform morphing (i.e. span and sweep change), out-of-plane morphing (i.e. twist, dihedral and spanwise bending). Table 2.1 summarises the wing parameters and how they generally affect aircraft performance, which are the major motivations for morphing aircrafts.

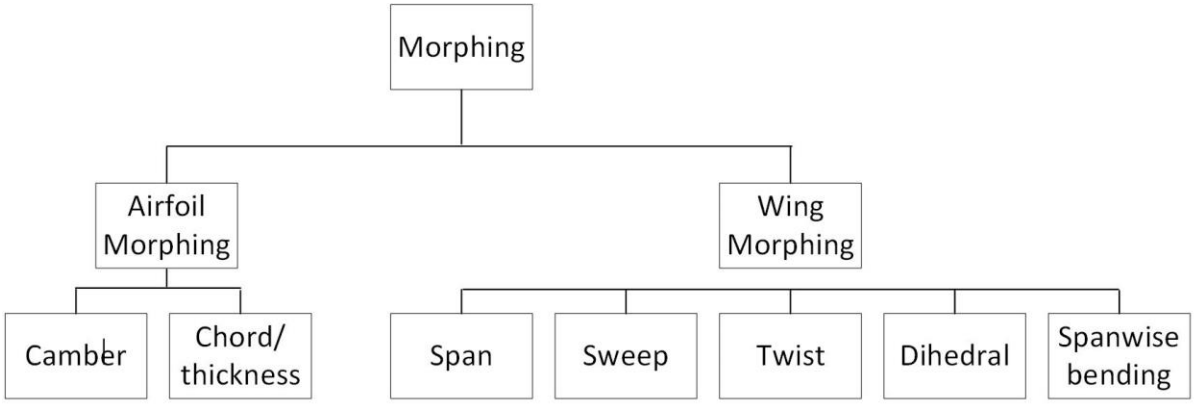

Figure 2.12 Morphing wing categories

Table 2.1 Effects of wing geometric parameters on aircraft performance

(Jha and Kudva 2004)

Parameters	Effects of variability -with other parameters unchanged
Wing Plan Area	↑ Increased: lift and load factor capability ↓ Decreased: parasitic drag
Wing Aspect ratio	↑ Increased: lift/drag ratio, loiter time, cruise distance and turn rates; Decreased: engine requirements ↓ Increased: maximum speed; Decreased: parasitic drag
Wing dihedral	↑ Increased: rolling moment capability and lateral stability ↓ Increased: maximum speed
Wing sweep	↑ Increased: critical Mach number and dihedral effect; Decreased: high-speed drag ↓ Increased: maximum lift coefficient
Wing taper ratio	Wing efficiency (span-wise lift distribution) and induced drag
Wing twist distribution	Span-wise lift distribution and prevention of tip stall behavior
Airfoil camber	Zero-lift angle of attack, airfoil efficiency and separation behavior

Airfoil thickness/chord ratio	↑ ↓	Improved: low-speed airfoil performance Improved: high-speed airfoil performance
Leading edge radius	↑ ↓	Improved: low-speed airfoil performance Improved: high-speed airfoil performance
Airfoil thickness distribution		Airfoil characteristics and laminar/turbulent transition

2.2.1.1 Span morphing

The variable span idea is used in a morphing wing to change the aspect ratio and wing plan area, to optimize the wing lift and induced drag in specific flight conditions.

Telescope wings have been a popular approach for span morphing, an early example of span morphing is MAK-10, which first flew in 1931, with a telescope wing capable of adjusting the span between 13m to 21m, the wing was activated with pneumatic actuators (Weisshaar 2006, Barbarino, Bilgen et al. 2011). Other examples are shown by (Neal, Good et al. 2004) and (Samuel and Pines 2007).

The scissor mechanism is another approach for span morphing, and it is usually coupled with sweep, examples are show in works by (Joo, Sanders et al. 2006) (Bharti, Frecker et al. 2007)(Figure 2.13).

Ajaj et al. (2013) proposed a zigzag structure to build a wingbox that could vary the wing span by 44%. Unlike the previous scissor examples, this design did not couple with sweep change.

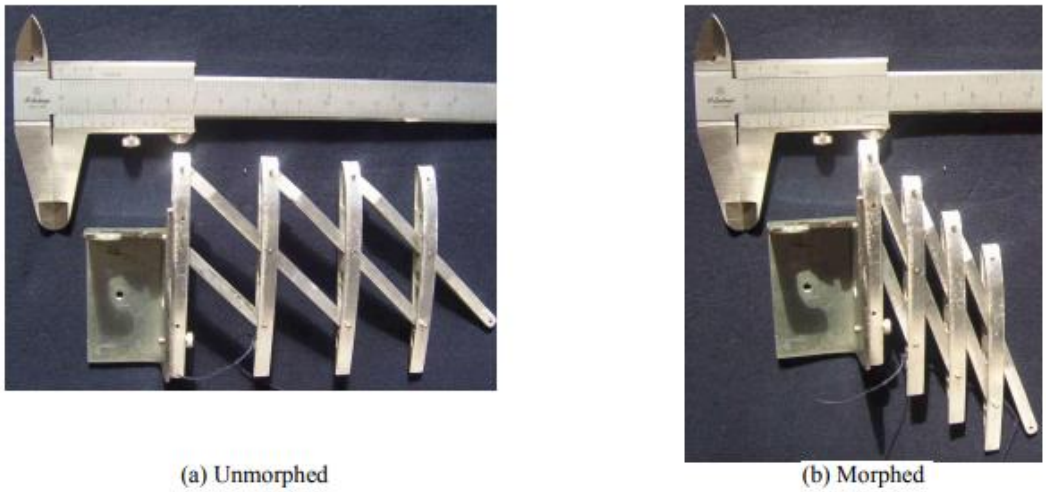

(a) Unmorphed (b) Morphed

Figure 2.13 Scissor wing section: un-morphed and morphed configurations

(Bharti, Frecker et al. 2007)

2.2.1.2 Sweep morphing

Variable sweep wings allow aircraft to fly efficiently at both low and high speed, other reasons for sweep morphing are: improving longitudinal stability by adjusting the aerodynamic centre and gravity centre, providing longitudinal and directional stability for tailless planes, and reducing compressibility induced drags at transonic speed (Weisshaar 2013). The typical design for sweep morphing is allowing the wing to pivot around the wing root, and controlling the sweep angle via a gearbox, which requires the gearbox bearings to carry all the aerodynamic forces and moments. The design brings complexity and therefore weight penalty, with an intensive maintenance requirement (Barbarino, Bilgen et al. 2011).

Various military aircrafts have deployed variable sweep wings, starting from the 1950's, including the Bell X-5, F-111, F14, Su-17, Mig-23, B-1 bomber, and Tu-160. With the development of flight control systems in 1970's, the stability advantages for variable

sweep aircraft were eliminated, which makes Tu-160 (which first flew in 1981) the last (and reputed to be the largest) major military variable sweep aircraft built.

The Boeing 2707 Supersonic Transport (SST)(Figure 2.14), proposed in 1964 was the first variable-sweep application in commercial aircraft, but the project was called off with wing/tail integration difficulties in 1968. (Weisshaar 2013)

The recent researches on sweep morphing wings are focused on multi mission UAVs, and good examples are presented in (Bowman, Sanders et al. 2007, Ivanco, Scott et al. 2007). Example configurations and prototypes are shown in Figure 2.15 and 2.16 (Bowman's (2007)).

Boeing SST (Model 2700-200) variable-sweep wing version

Figure 2.14 Boeing 2707-200 variable-geometry supersonic transport (Weisshaar 2013)

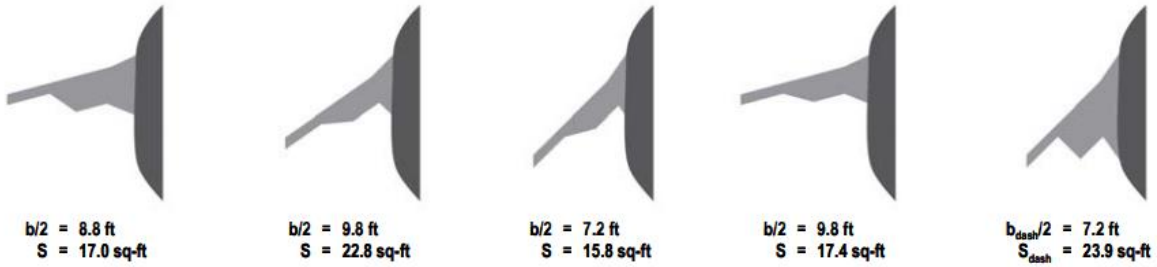

Figure 2.15 Morphing wing configurations for (left to right) high-lift, climb, cruise, loiter, and maneuver. *b* is wing span and *S* is wing area. (Bowman, Sanders et al. 2007)

Figure 2.16 Batwing model in the NASA Langley wind tunnel(Bowman, Sanders et al. 2007)

2.2.1.3 Twist morphing

Twist may be the most common wing morphing idea, due to the great aeroelastic benefits it carries. Twisting the structure changes the shape of aerodynamic surface therefore reducing drag and enhancing roll and load control, with a relatively simple configuration.

One of the most popular examples is the NASA Active Aeroelastic Wing (AAW) project on F/A-18 as shown in Figure 2.17 (Clarke, Allen et al. 2005), which morphed by wing warping to improve aircraft roll control.

Previously presented research (Chen, Sarhaddi et al. 2000) contributed to the AAW projected. In the approach, variable stiffness spars (VSSs) (Figure 2.18) were used to change the wing torsional stiffness, and therefore improve the aircraft roll performance.

Figure 2.17 Active aeroelastic wing F/A-18 airplane on flight test program(Clarke, Allen et al. 2005)

The spar segments are connected with articulated joints, and when the joints are in a horizontal orientation the segments are fully uncoupled and offer zero stiffness. The spar segments are joined and gain stiffness when rotated, and reach a maximum stiffness in the vertical orientation with all segments continuously connected. An electrical actuator was used to rotate the spar for stiffness change. Detailed research was done using the baseline of F/A-18PRM flight data. The VVSs were embedded in the aircraft wings by replacing conventional spars (Figure 2.19), and two approaches were given in the paper. In the first approach (single VVS), the sixth spar, which had the maximum roll rate sensitivity among all the spars, was replaced by a VVS, resulted in 6-22% increased roll rate. In the second approach, a torsion free (TF) wing concept was applied, which was a wing with very low torsional stiffness. The wing bending moments were mostly carried by two very strong and stiff spars closely placed near to

the centre of the chord (spars three and four), spars two and five were removed to reduce the wing torsion stiffness, and spars one and six were selected as VVSs to control the wing stiffness as a function of Mach number and altitude. The VVS/TF design amplified the aeroelastic effect, resulted in a 29-126% increasing on roll rate, and also generated additional lift.

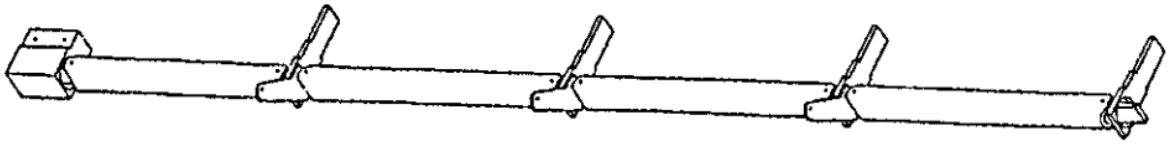

Figure 2.18 VSS mechanism (Chen, Sarhaddi et al. 2000)

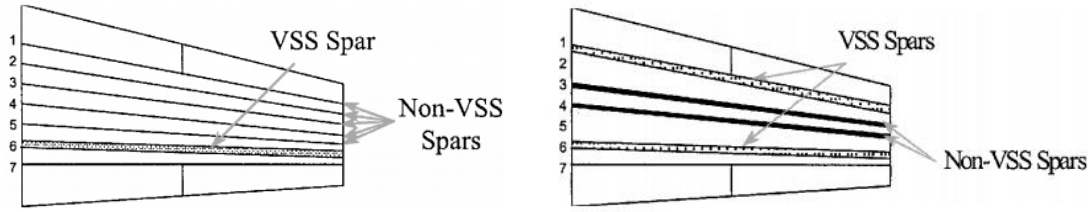

Figure 2.19 Single VVS (left) and VVS/TF design(right) (Chen, Sarhaddi et al. 2000)

Twist demonstrations for roll control were given (Garcia, Abdulrahim et al. 2003, Stanford, Abdulrahim et al. 2007), using servo actuated membrane morphing wings. Servo controlled torque rods were fitted in metal sleeves orientated spanwise near to the leading edge, and were allowed to twist. A torque rod was embedded in the membrane wing as shown in Figure 2.20.

Shape Memory Alloys (SMA) are also used in twisting morphing research. A torsion free wing approach with SMA spars was presented by (Nam, Chattopadhyay et al. 2002), in this approach the VVS spars were replaced with variable stiffness SMA spars to control the aeroelastic characteristics. An approach for wing twist control via SMA wire was presented in (Rodrigue, Cho et al. 2016), as illustrated in Figure 2.21.

Modular design is also used in the twist approach. A twisting wing prototype built by NASA mission adaptive digital composite aerostructure technologies group (Jenett, Calisch et al. 2017) used carbon fiber materials and building blocks for the wing construction, as shown in Figure 2.22.

Most examples presented for twist morphing also controlled the washout of the wing which modified the spanwise lift distribution to reduce lift induced drag, and offered some spinning resistance.

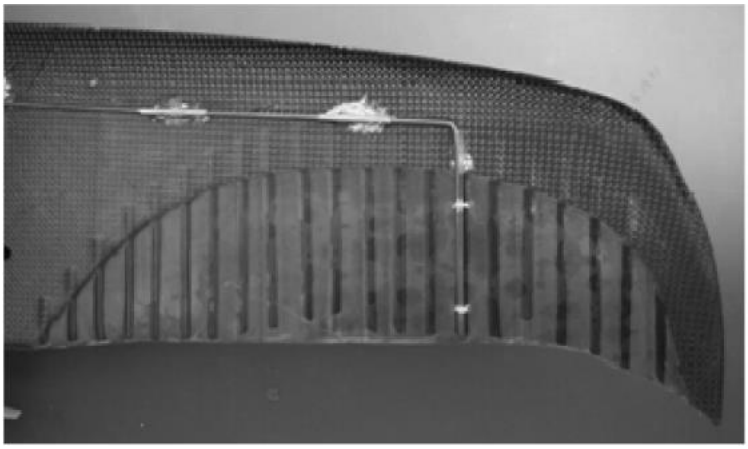

Figure 2.20 A torque rod embedded within the membrane wing (Stanford, Abdulrahim et al. 2007)

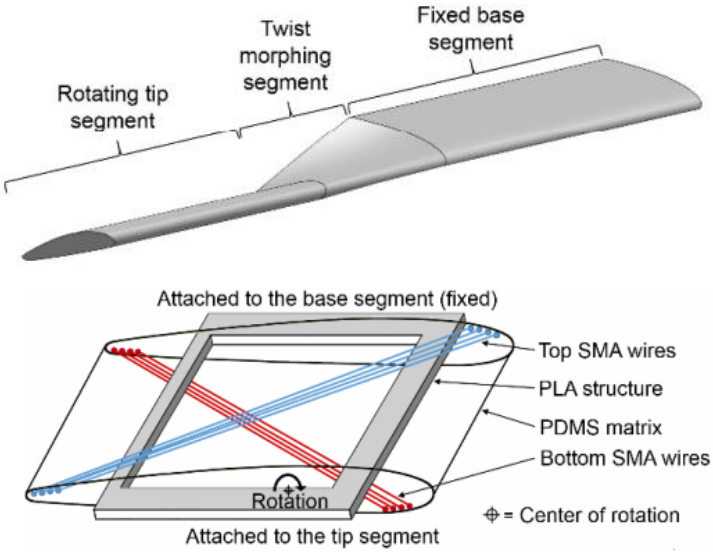

Figure 2.21 Shape of morphing wing (Top), position of the SMA wires within the morphing wing section (bottom) (Rodrigue, Cho et al. 2016)

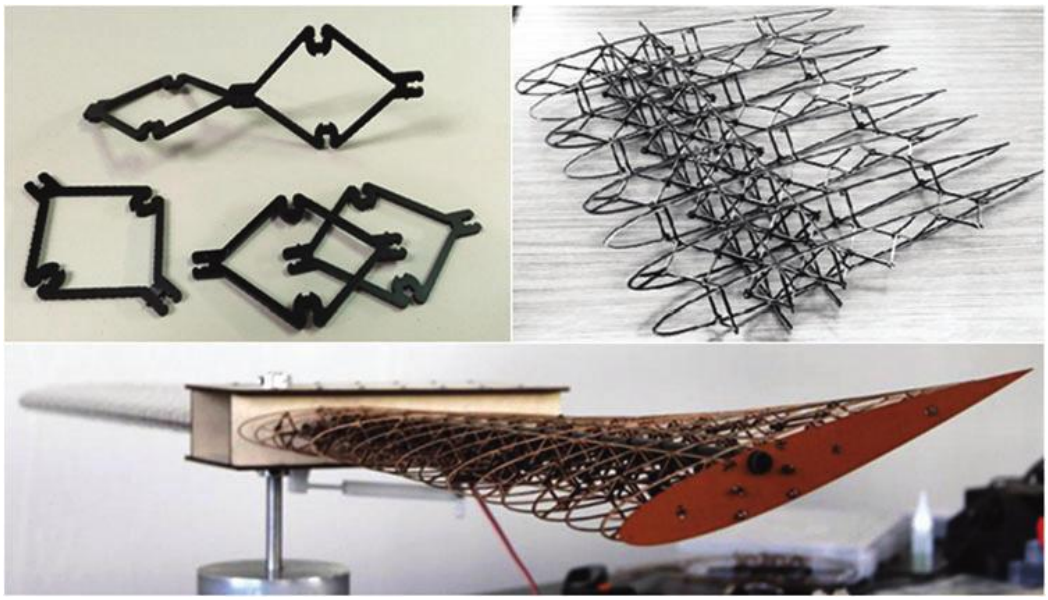

Figure 2.22 Construction of shape-changing structures from discrete lattice building-block elements (Jenett, Calisch et al. 2017)

2.2.1.4 Dihedral and span-wise bending

Dihedral is the upward angle from horizontal of the wings or tail plane of an aircraft. Dihedral affects stability and manoeuvrability of an aircraft about the roll axis. Variable dihedral at a wing tip may also be defined as span-wise bending, and can reduce the wingtip vortices. Being able to changing vorticity distribution may reduce the induced drag.

The XB-70 Valkyre (Figure 2.23) supersonic bomber designed in 1960s was a very special example of spanwise bending. With large wing panels, bending towards the ground ta up to 65°, the lift-to-drag ratio was increased by compression lift generated by shock waves generated at transonic and supersonic speeds.

More recently, a variable gull wing was analysed and demonstrated (Abdulrahim and

Lind 2004). The dihedral angle was controlled by a telescope spar connected to the fuselage. Lockheed Martin developed the folding wing (Love, Zink et al. 2007), as part of the Morphing Aircraft Structures (MAS) project. Two actuation approaches were investigated: i) Thermopolymer actuators driving a helical spline gear ii) electric driven servo. The electric driven design was finally used and tested with a semi-span half-scale representation in wind tunnel (Figure 2.24).

An active winglet was analysed and wind tunnel tested (Bourdin, Gatto et al. 2008). In this approach, servo-driven winglets were used for flight control of a flying wing, with the help of conventional flaps and elevators. The experimental model is shown in Figure 2.25.

SMA actuators were also used for active winglet, and approaches are discussed and tested by Manzo et al.(2005, 2010). A honeycomb structure design for an active winglet, which is actuated by a pressure tube is also presented with basic demonstration by (Sun, Gao et al. 2014).

Figure 2.23 The North American XB-70A Valkyrie (s/n 62-0207)(U.S. 1966)

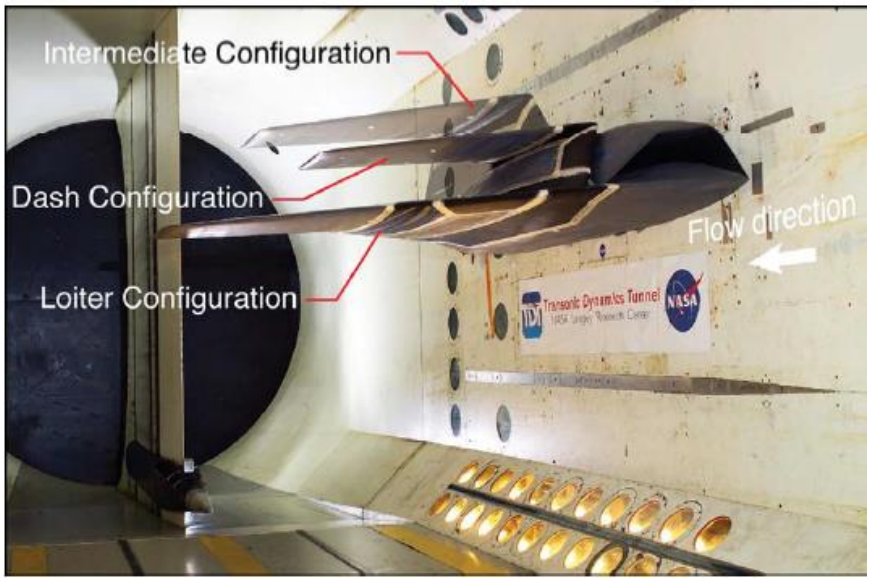

Figure 2.24 Multiple exposure photograph of Lockheed Martin MAS wind tunnel model during a morphing sequence (Ivanco, Scott et al. 2007)

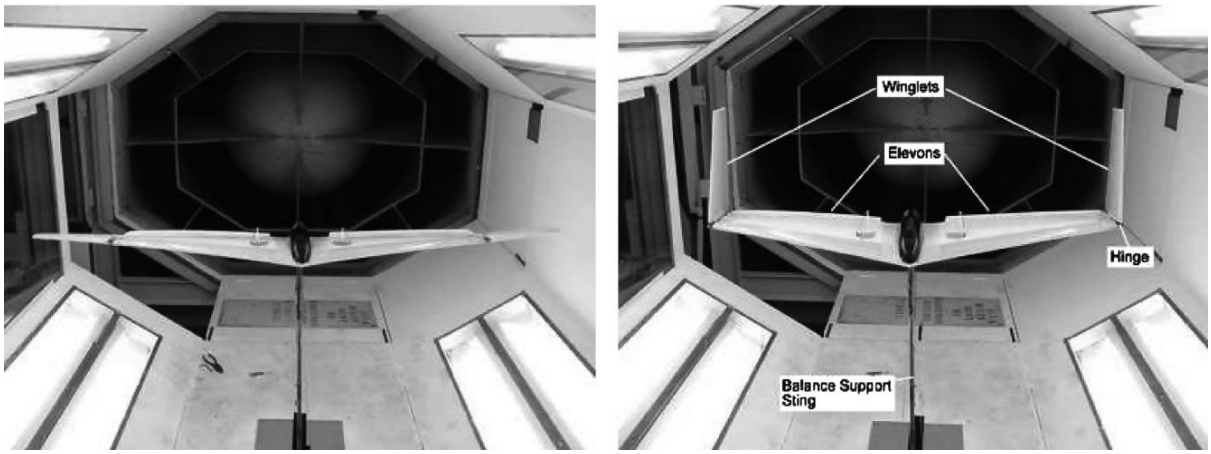

Figure 2.25 Experimental model as mounted in the wind tunnel; left: both winglets planar; right: both winglets upright (Bourdin, Gatto et al. 2008)

2.2.1.5 Airfoil morphing

Airfoil morphing research has mainly focused on camber variations, with relatively little concerned with airfoil thickness and chord change. The camber change includes locally morphing (i.e. leading edge and trailing edge morphing), or globally morphing, that is change the camber of the whole. The morphing may be realised by a

mechanism (actuated by conventional actuators, e.g. hydraulic, pneumatic and electromagnetic), or by smart materials (e.g. piezoelectric,SMAs). Examples are categorized in the review paper (Barbarino, Bilgen et al. 2011)

Enhancement of aerodynamic performance is the motivation for most various camber research. Being able to adjust the airfoil shape continuously during the flight, would result in increasing the lift/drag (L/D) ratio (Spillman 1992). There are also possibilities for airfoil morphing to enhance control for aircraft. A simulation research (Gern, Inman et al. 2005) pointed out that by replacing the conventional flaps with morphing a airfoil, the roll performance could be improved.

More recently, a fish-bone trailing approach was investigated (Woods and Friswell 2012) and including wind tunnel testing (Woods, Bilgen et al. 2014) (Figure 2.26), which is an elastomer seamless skin covered fish bone structure, actuated by electric power tendons. The wind tunnel test result shows a noteworthy increase in lift-to-drag ratio of 20%–25% compared to the conventionally flapped airfoil over the range of angles of attack typical of fixed wing and rotary wing applications.

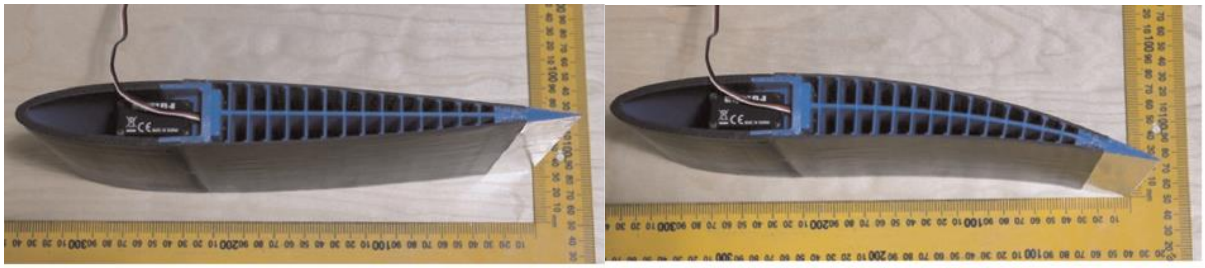

Figure 2.26 FishBAC wind tunnel model: (a) baseline state (b) deflected

2.2.2 Poly-morphing and smart structures

Most approaches introduced in section 2.2.1 only focused on one type of morphing, as categorized, only a few examples considered the combination of two or more morphing types, thus poly-morphing. One poly-morph approach combining dihedral, twist, taper and span morphing was proposed by (Ursache, Melin et al. 2007), called MORPHLET, which is a morphing winglet concept, as shown in Figure 2.27. A mechanical demonstration platform was built based on the concept (Ursache, Melin et al. 2008), as shown in Figure 2.28, and further analysis was presented by(Smith, Isikveren et al. 2010). There are no clear details in the papers of the actuation system and the capability of controlling the four proposed motions individually. An UAV design for three motion control variables was presented in (Neal, Good et al. 2004), the actuation systems were fully separated as shown in Figure 2.29.

A fully variable morphing wing using the VGT concept was presented (Moosavian, Xi et al. 2013), and a prototype with hydraulic actuator was built for motion validation, shown in Figure 2.30. Some basic tests with external loads conditions were performed on the prototype using pulleys and weights, but no further experiments on the wing construction with flexible skin for wind tunnel testing are presented. A bio-inspired morphing wing for underwater use was presented (Moored and Bart-Smith 2007), and a cluster actuation method was discussed (Moored and Bart-Smith 2009) (Figure 2.31), which maybe a useful concept, but no experiments have been presented.

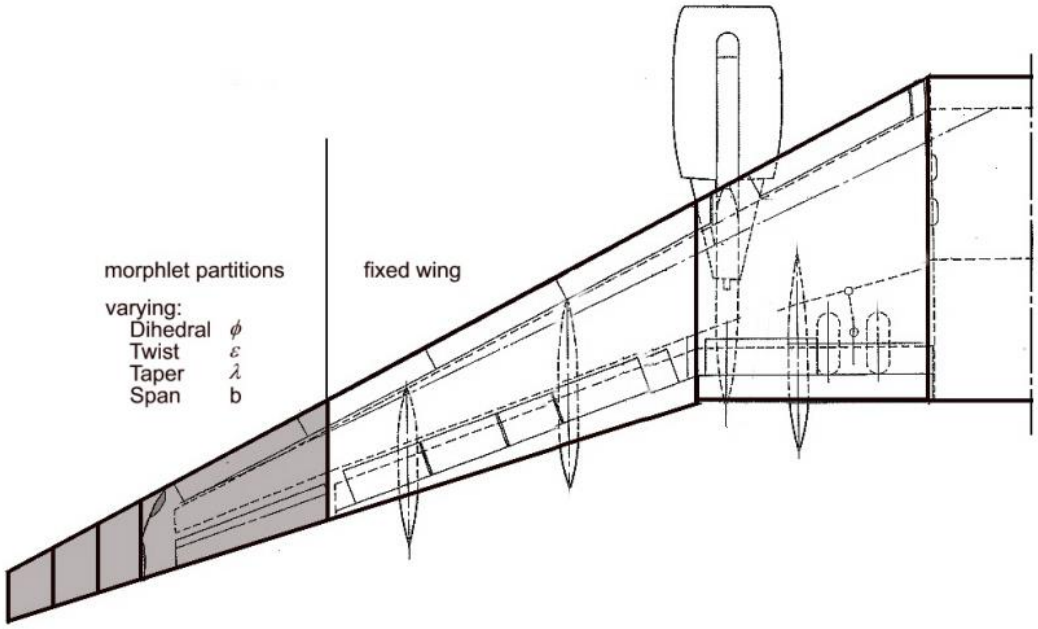

Figure 2.27 Wing planform schematic of baseline and MORPHLET

(Ursache, Melin et al. 2007)

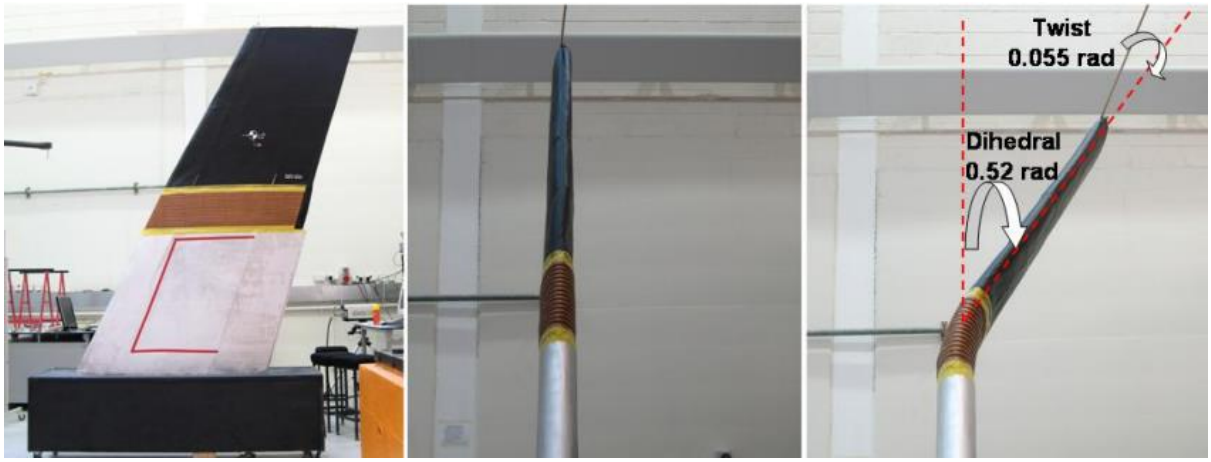

Figure 2.28 Rolled out and canted mechanical demonstrator (30 deg dihedral and 5 deg twist) (Ursache, Melin et al. 2008)

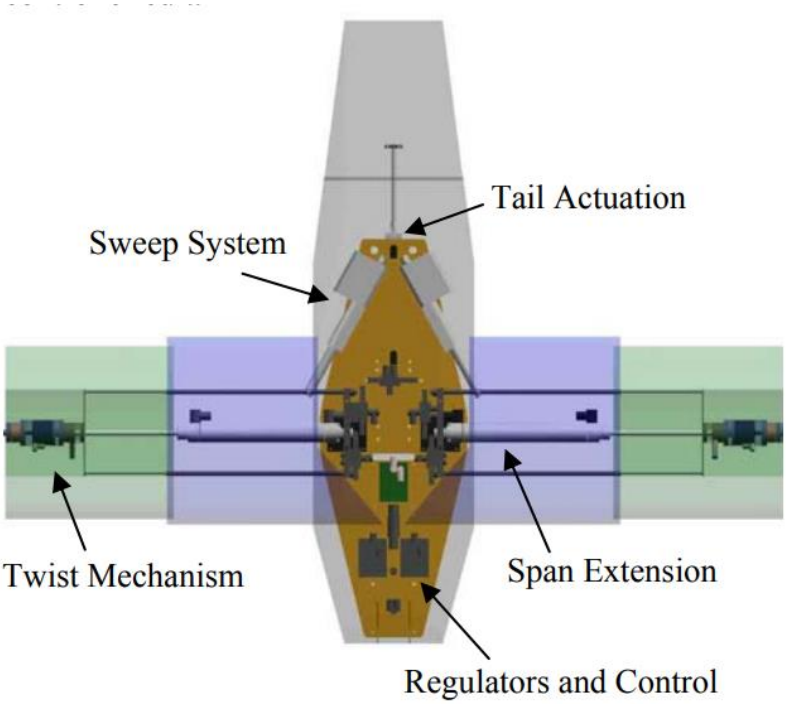

Figure 2.29 Overview of internal vehicle structure for a 3DOF morphing wing(Neal, Good et al. 2004)

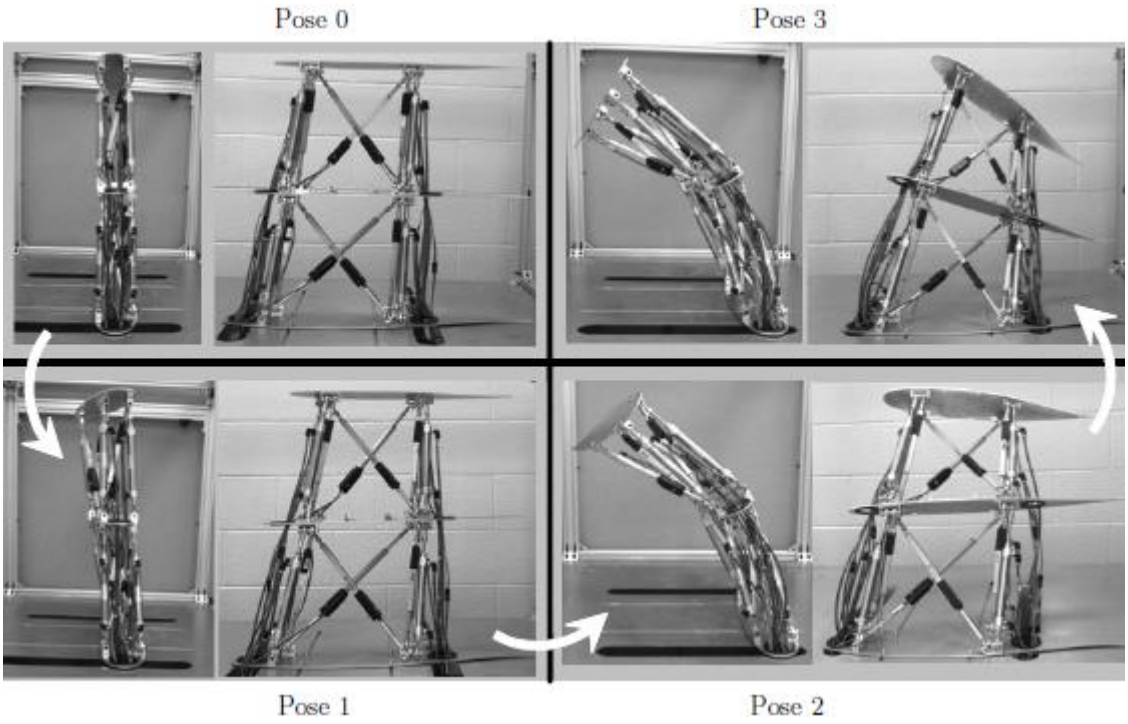

Figure 2.30 Side and front views of the prototype showing poses 0, 1, 2, and 3. (Moosavian, Xi et al. 2013)

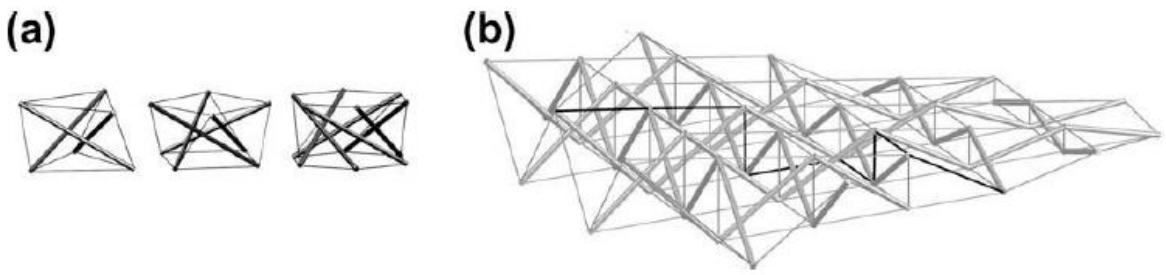

Figure 2.31 (a) A three-strut, a four-strut and a six-strut tensegrity prism (b) a tensegrity wing structure with a cable actuation cluster (black) (Moored and Bart-Smith 2009)

2.2.3 Flexible skin for morphing aircraft wings

The skin for a morphing aircraft wing needs to deform with the morphing wingbox structure, while be stiff enough to bear local aerodynamic pressure and transmit the load to the wingbox. The contradictory requirements bring challenges to skin design. SMAs may be a good candidate for the morphing skins, but the current SMAs have limitations, such as low deformation speed, poor fatigue properties and normally low energy efficiency. Approaches and applications for SMA skins are reviewed in (Barbarino, Bilgen et al. 2011). Research approaches and current applications in passive skin design are reviewed in this section

Flexible skin approaches using rubber or silicone elastomers have been wind tunnel tested and applied on aircraft. These usually require external pressure or vacuum to help maintain the airfoil shape. A seamless skin approach with a vacuum system was proposed and tested in the Lockheed Martin MAS project (Ivanco, Scott et al. 2007) (Figure 2.32). The vacuum pressure was determined depending on the flight condition, and loss of suction during some conditions resulted in significant skin dynamics. The

inflated air bags were used to fill the gap between the fuselage and main wing in F-14 fighter, as shown in Figure 2.33.

A segmented stiff skin design, which was composed with a set of stiff skin panels, and allowed non-interference sliding between skin panels to deform with wing box structure, was proposed by (Guo, Qiang et al. 2016). As a discontinuous approach, there were gaps between skin panels, especially on the leading edge (smaller radius and higher curvature), which affected aerodynamic smoothness. Further investigations are in needed for segmentation design optimization for various DOF and better aerodynamic smoothness.

Honeycomb structures have high out-of-plane stiffness and very low in-plane stiffness, and can be air tight with a smooth surface when covered with flexible face sheets. A topologies study on 1-D morphing honeycomb structure was presented by (Olympio and Gandhi 2012). A design and finite element simulation for an auxetic honeycomb design, was proposed by (Huang, Zhang et al. 2017). Thin plates were added between honeycomb columns to offer extra out-of-plane flexibility. A finite element model is shown in Figure 2.35.

Flexible Matrix Composite (FMC) is a kind of elastomer matrix material, which is reinforced with embedded stiff fibers, a concept introduced in (Murray, Gandhi et al. 2010). The direction of fiber reinforcement was perpendicular to morphing, which offered high out-of-plane stiffness, as shown in Figure 2.36. The matrix-dominated direction was aligned with the morphing direction, and provided large strain capability and low in-plane stiffness. FMC can be used individually or with honeycomb structures

to further increase out-of-plane stiffness. A shape changing example of FMC and honeycomb structure combination was presented in (Bubert, Woods et al. 2010), which was actuated with pneumatic artificial muscles (PAMs), as shown in Figure 2.37. Camber morphing research by (Woods, Bilgen et al. 2014) has shown that pre-tensioning the FMC skin will result in better surface smoothness and also increasing local out-of-plane stiffness.

Corrugated structures are drawing interest due to the high stiffness in the longitudinal direction and compliance in the transverse direction. A prototype showing a camber morphing concept using the corrugated structures can be found in (Thill, Etches et al. 2010) (Figure 2.38), with numerical studies presented in (Dayyani, Khodaparast et al. 2015). An example for span-wise bending application was presented in (Ursache, Melin et al. 2008).

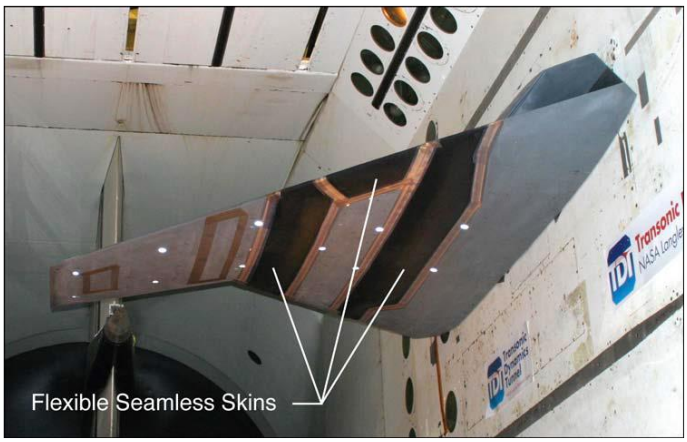

Figure 2.32 Lockheed Martin MAS model with flexible seamless skins (Ivanco, Scott et al. 2007)

Figure 2.33 An F-14 “Tomcat” fighter aircraft with black inflated air bag at wing root (O'Connor 2003)

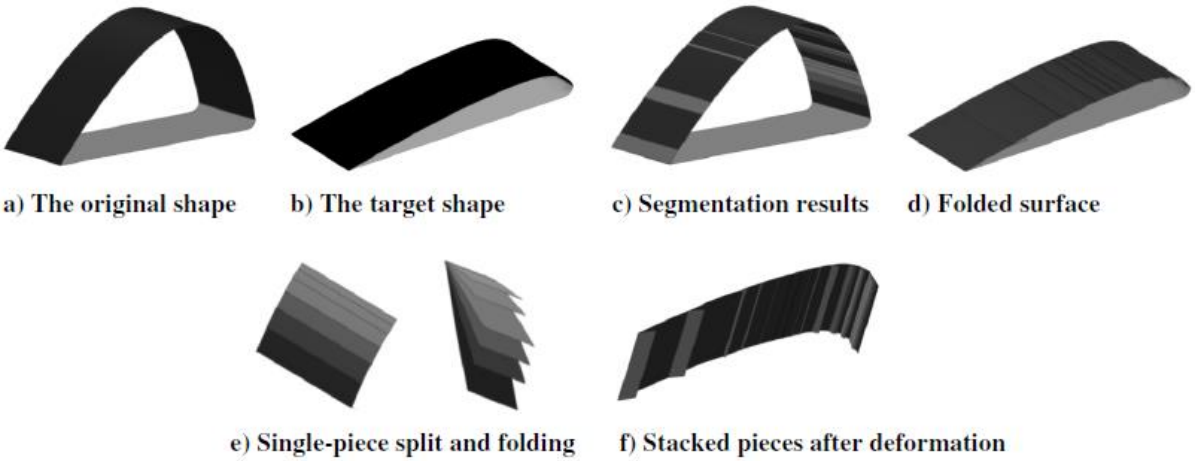

Figure 2.34 Simulation of surface segmentation and morphing.(Guo, Qiang et al. 2016)

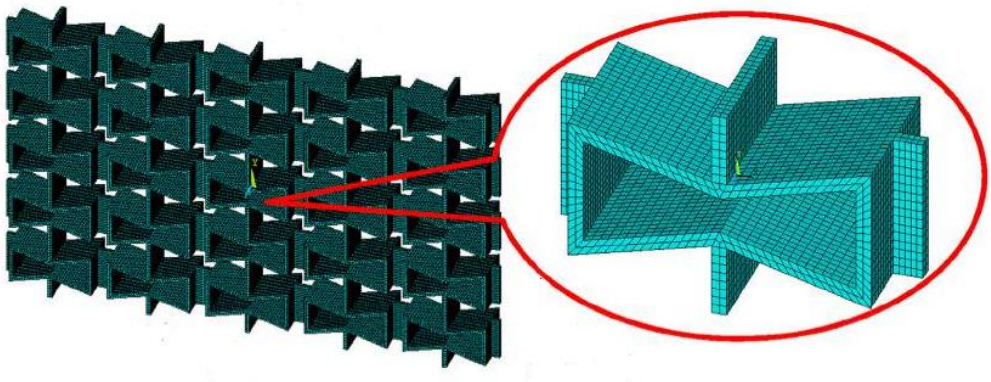

Figure 2.35 FE models for auxetic honeycomb design(Huang, Zhang et al. 2017)

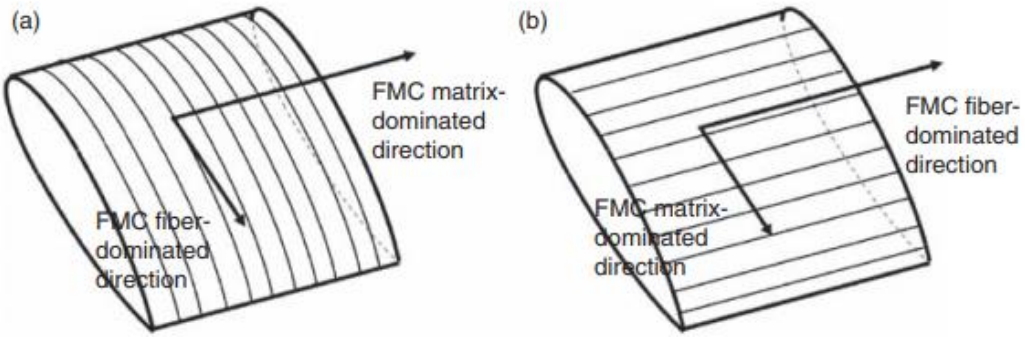

Figure 2.36 Schematics of FMC fiber orientation for (a) span morphing and (b) camber or chord morphing.(Murray, Gandhi et al. 2010)

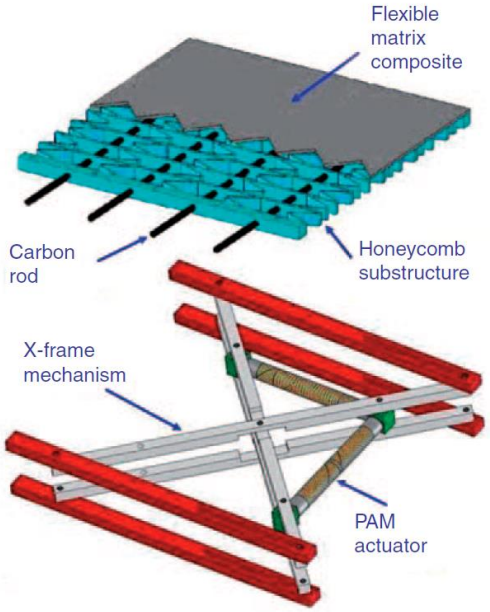

Figure 2.37 Proposed morphing skin prototype including PAM actuation system. (Bubert, Woods et al. 2010)

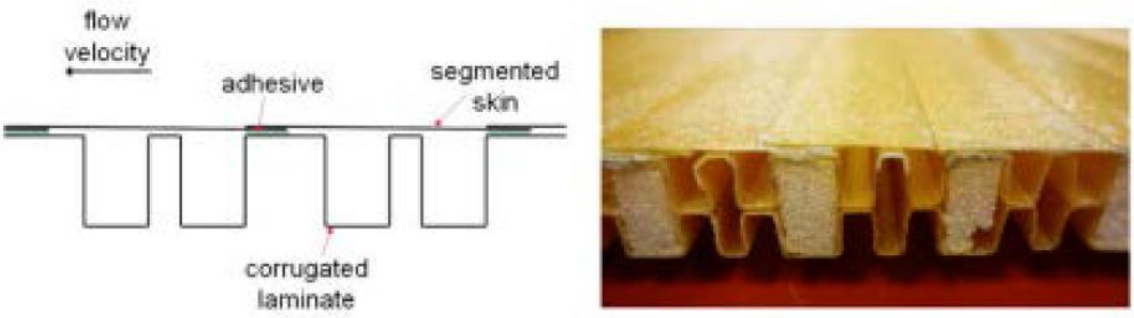

Figure 2.38 Schematic (left) and picture (right) of segmented skin bonded to the corrugated laminate (Thill, Etches et al. 2010)

2.3 Conclusions

In this chapter, research on smart structures, especially active tensegrity and truss structures was reviewed. Conceptual design and theoretical studies show great potential for such structures for future shape changing and load-bearing applications. Morphing aircraft wings is an area where stiffness, weight, effective shape changing DOF, and redundancy potentials are all essential characteristics. Morphing aircraft wing approaches are reviewed by DOF categories, and actuation methods in each category are described.

In conventional aircraft wings, shape changing mechanisms need to bear bending load (aerodynamic load, i.e. lift), so they are designed to be stiff, result in a weight penalty and high maintenance requirements. Compared to conventional structures, tensegrity structures can resolve external load to pure axial load on members with some members only experiencing tension load, and can have low mass, with no stiffness penalty.

These characteristics make the active tensegrity structure concept a strong candidate for future morphing aircraft wings. Tensegrity structure design, investigation of motion and stiffness control, especially with high external loads, would be valuable for developing a successful morphing aircraft wing. The following research issues should be addressed:

- Active structure design, build, based on shape changing DOF requirement and dimension constraint.

- Finding effective approaches to calculate shape changing forward kinematics, i.e. the transformation between actuated member displacements to specific DOF position change.
- Establishing and validating control schemes for closed loop motion and internal load control on proposed structure.
- Active wing construction and validation by precise motion control under external load (wind tunnel test).

3 Active structure design and kinematics

3.1 Introduction

A tensegrity structure is a subset of a pin-jointed truss, stabilised by balancing the tensile forces in some elements (usually cables) and the compressive forces in struts The structure can provide a high strength-to-weight ratio, which minimizes its weight and inertia, and hence reduces the power needed to actuate the structure. Tensegrity structures are well suited as active structures and, more specifically, they are advantageous for large amplitude, low inertia applications(Lai, Plummer et al. 2016).

In this chapter the design of an active tensegrity structure for application in an experimental morphing wing is described. The wing dimensions were dictated by the capacity limit of the University of Bath's large wind tunnel which was to be used for aerodynamic testing. The design allows the tensegrity structure to be integrated into a flexible wing, and keeps the morphing pivot axis on the aerodynamic centre of the airfoil. The configuration of the morphing tensegrity structure is introduced. A wing analysis to estimate the aerodynamic load was performed, and actuators in the morphing structure were selected based on the analysis results.

Direct kinematic analyses of the tensegrity structure were also performed, focusing on the shape change in twist and span-wise bending, as these are important for aerodynamic control of a morphing wing.

3.2 Wing morphing structure concept design

The octahedron (six vertices, twelve members and eight faces) truss frame as shown

in Figure 3.1a, is the basis of this research for active tensegrity in wing morphing structures. A topology study for VGT structures (Hughes, Sincarsin et al. 1991) has shown that a VGT structure with octahedron cells has superior overall performance. It is a platonic solid, which potentially makes the structure stiffer and stronger. An octahedron frame could be form the basis of a tensegrity by replacing eight of the struts with flexible tensile members, i.e. cables, and add another strut to keep the structure integrity, as shown in Figure.3.1b; blue lines indicates the members replaced by cables. A tensegrity unit has six vertices and thirteen members, in which five of them are struts and eight are cables.

However, the members in a tensegrity structure are connected to each other in a different way than in a conventional truss. Spherical joints are commonly used in the tensegrity structure, which allows the connected members to rotate in all rotational degrees of freedom, as illustrated in Figure 3.2. This guarantees there is no bending moments transmitted between members, thus all the members only take either compression or tensile forces in axial direction. Spherically-jointed members are also necessary for morphing.

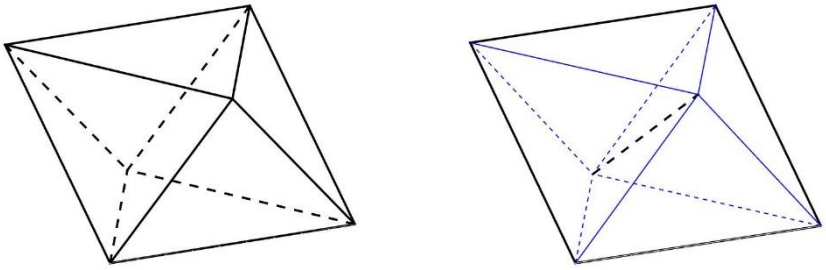

Figure 3.1 a) octahedron frame b) unit tensegrity. (Dashed lines are members which are behind the imagined front faces of the structure; blue lines are cables)

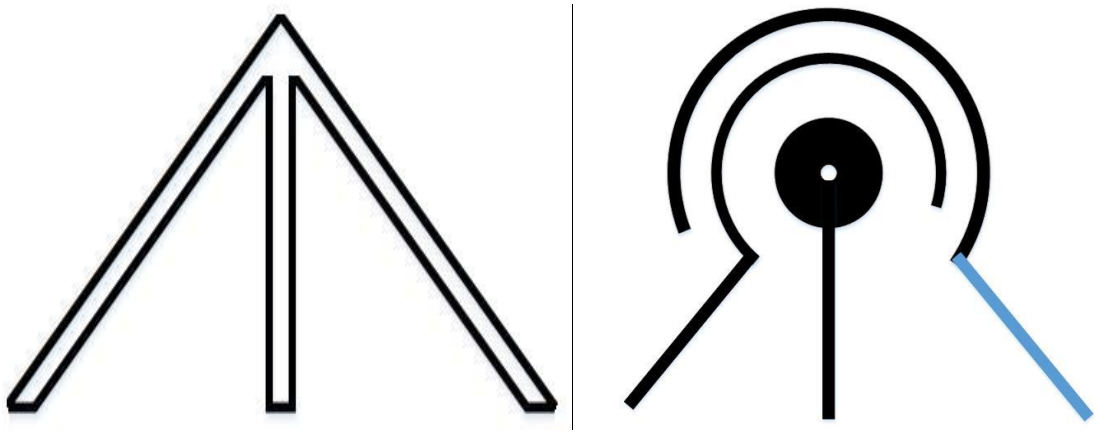

Figure 3.2 Frame (left) and tensegrity (right) joints

With proper internal load applied, the tensegrity unit could be stiff and bear external loads from all directions. The stiffness-mass ratio is likely to be higher than a similarly jointed truss structure without preload, due to low stiffness (or even backlash) at the joints in the unloaded condition.

Conceptually, single-acting actuators can be incorporated in the structure replacing some of the elements to achieve multi-axis morphing. The elements to be replaced by actuators are selected depending on the morphing requirement. In this project 4 single-pulling actuators were embedded in a unit tensegrity cell. The structure can achieve 3DOF as shown in Figure 3.3, in which red lines indicate actuators. The front plane remains fixed and only the red lines change length to give three independently controllable shape changes (morphing modes).

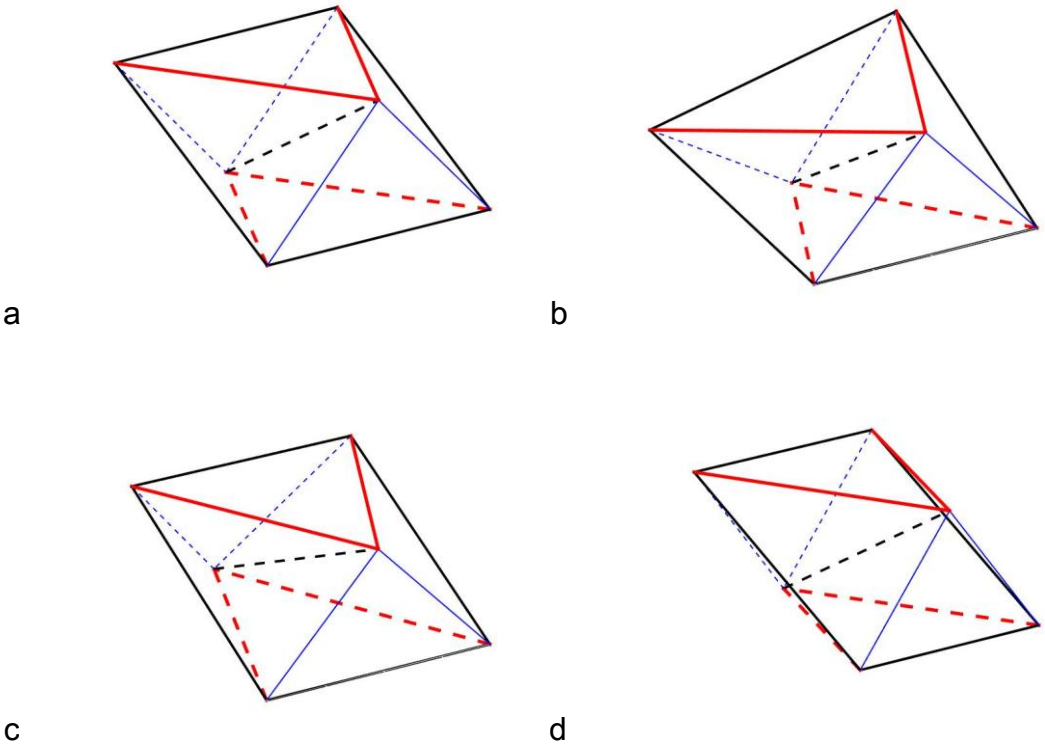

Figure 3.3 Tensegrity in morphing modules a) neutral b) twist c) bend d) shear. Black lines are struts, blue lines are cables, and red lines are actuators.

The unit cells could be stacked together from either side, giving more complex morphing results. The major requirement for this research is twisting and span wise bending of the wing, achieved by independent control of the rotational DOF along one axis, which is twisting, and another rotational DOF perpendicular to that same axis. An example is given with two unit cells sharing a common side strut in Figure.3.4.

The two octahedron cells sharing only one strut is not stable, so two tensile members were added to close the loop, and the middle cell could be seen as an octahedron cell only with three struts, sharing two actuators with the right cell.

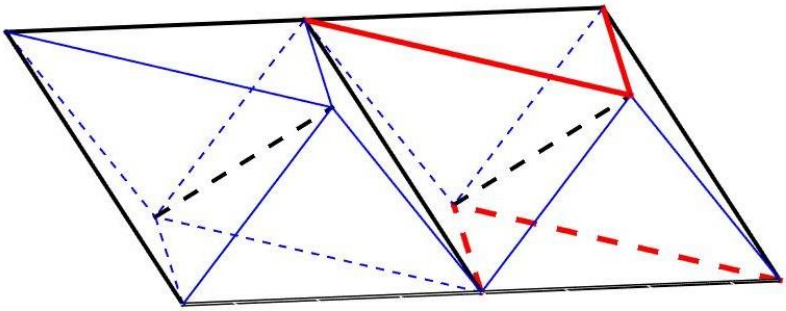

Figure 3.4 Pair of unit cells sharing a side strut

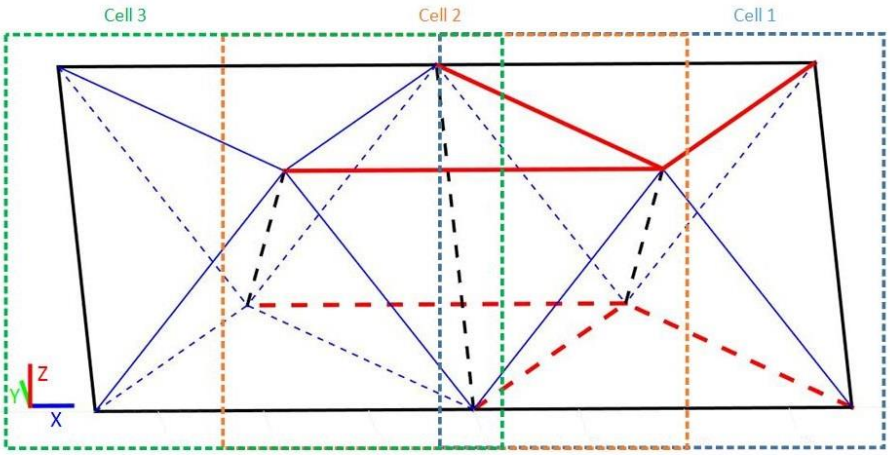

Figure 3.5 fully integrated cell with additional actuators

The cells could be stacked along the x-axis by duplicating the same expansion method and produce a smooth morphing result. The structure is able to meet the requirements for the proposed wing morphing, and the detailed kinematics are discussed in section 3.4.

3.3 Wing load simulation and actuator selection

The prototype wing dimension is determined based on the capacity of the large wind tunnel in the University of Bath, with test section dimensions of 2.13 x 1.51 x 2.70 m.

A NACA0015 airfoil profile was chosen due to its symmetry and reasonable thickness for accommodating the embedded actuators. The aim of the morphing wing is to achieve twisting and span wise bending simultaneously, and in such morphing conditions the trailing vortices are not negligible, which means the prototype has to be a 3D finite wing. A chord length, b=1.0m, was chosen offering sufficient gap to the wind tunnel wall, which allowed the air to flow around the tips. Ideally the chord length should be selected to ensure the aspect ratio is in a proper range, while in this case, the chord length is determined by the thickness of the wing, which needs to be enough for actuators to be embedded without any interference.

Actuators need to be selected for the active tensegrity. Tendons powered by electric motors have been suggested previously (Caluwaerts, Despraz et al. 2014), and for multi-axial application this design would require a complex tendon routing, with increasing risks of friction and malfunction. A fluid powered actuator is another choice. Hydraulic actuators have been widely used for flight control of commercial aviation since the 1950s, and they have proved to be robust and high in power density. The small size of the prototype wing makes hydraulic components selection a challenge in this project, and off-the-shelf solutions are not available currently. Pneumatic cylinders were selected as the actuation method in this research instead. They were suitable for embedding in the structure, while providing useful research results on the control of fluid power actuators in such preloaded multi axis systems. Note however that the effect of friction is known to be significantly larger in pneumatics compared with hydraulics.

3.3.1 Aerodynamic load simulation

The wing span is set as b=1.0m, as mentioned, while the chord length will be determined by the actuator force capability and other dimensions. Thus it is essential to estimate the external aerodynamic load (lift and drag) that the wing will experience in the wind tunnel:

$$L = \frac{1}{2} C_l \rho v^2 S \tag{3.1}$$

$$D = \frac{1}{2} C_d \rho v^2 S \tag{3.2}$$

where, L and D are lift and drag, ρ is the air density at the specific testing temperature, v is the test wind speed and S is the relevant surface area, in this case the product of chord length, c, and span, b.

The wing area changes proportional to the chord length, and the lift or drag coefficient varies with different aspect ratio b/c, which is not linear. A simulation was carried out to investigate the relationship between aerodynamic load and chord length with parameters values shown in Table 3.1.

Table.3.1 Parameters for wing load simulation

Parameter	Value	Units
Span, b	1.0	m
Chord, c	0.2, 0.4, 0.6, 0.8, 1.0	m
Wind speed, v	15	m/s
Air density, ρ	1.204	kg/m^3
Wingtip Angle of attack, α_{tip}	0~36	Degree (°)

The simulation was run with inviscid assumptions. The lift and drag coefficient results are shown in Figure 3.6 and Figure 3.7. Substituting the results into Eq.3.1 and Eq.3.2, lift and drag for the wing can be estimated, as shown in Figure 3.8 and Figure 3.9.

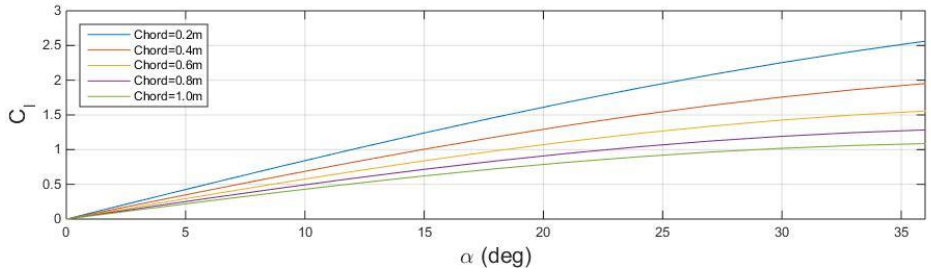

Figure 3.6 Lift coefficient vs angle of attack: simulation result for different chord lengths

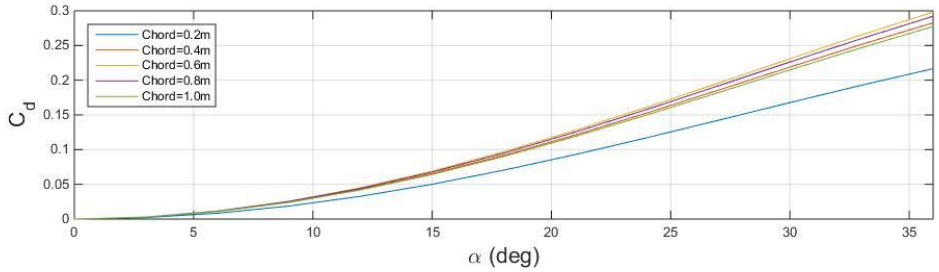

Figure 3.7 Drag coefficient vs angle of attack: simulation result for different chord lengths

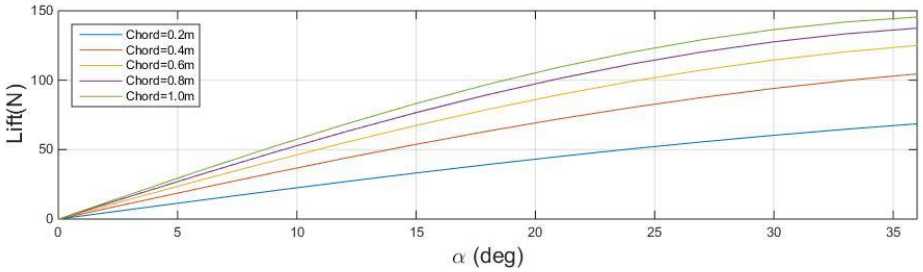

Figure 3.8 Lift *L* vs angle of attack: simulation result for different chord lengths

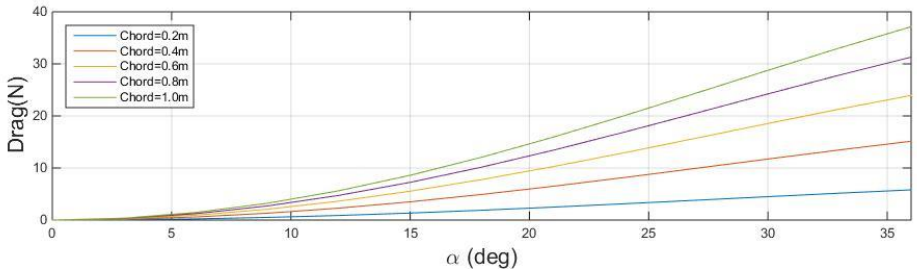

Figure 3.9 Drag *D* vs angle of attack: simulation result for different chord lengths

3.3.2 Tensile force estimation under external loads

The tensile force required under external load is calculated based on the structure shown in Figure 3.10. The tensegrity structure is in its neutral position, in which all actuators are the same length. Only lift is accounted for in this section, which is the major load on the wing for the upcoming wind tunnel test. Preloads in all cables are assumed to be zero in this section. The external loads are assumed to be point forces applied on nodes, and are distributed as follows to balance the moment, an internal preload (F_5) half of the external load (lift) was assumed for the following actuator force estimation.

$$L = F_1+F_2+F_3 \tag{3.3}$$

$$F_2=F_3=0.5F_5=0.5F_1 \tag{3.4}$$

The angles in the structure, α, β and γ, can be calculated from the element lengths.

$$\alpha = \cos^{-1}\left(\frac{\sqrt{l_{ac}{}^2 - \left(\frac{l_{s1}}{2}\right)^2}}{l_{s2}}\right) \tag{3.5}$$

$$\beta = \sin^{-1}\left(\frac{0.5l_{s1}}{l_{ac}}\right) \tag{3.6}$$

$$\gamma = \sin^{-1}\left(\frac{0.5l_{s1}}{l_c}\right) \tag{3.7}$$

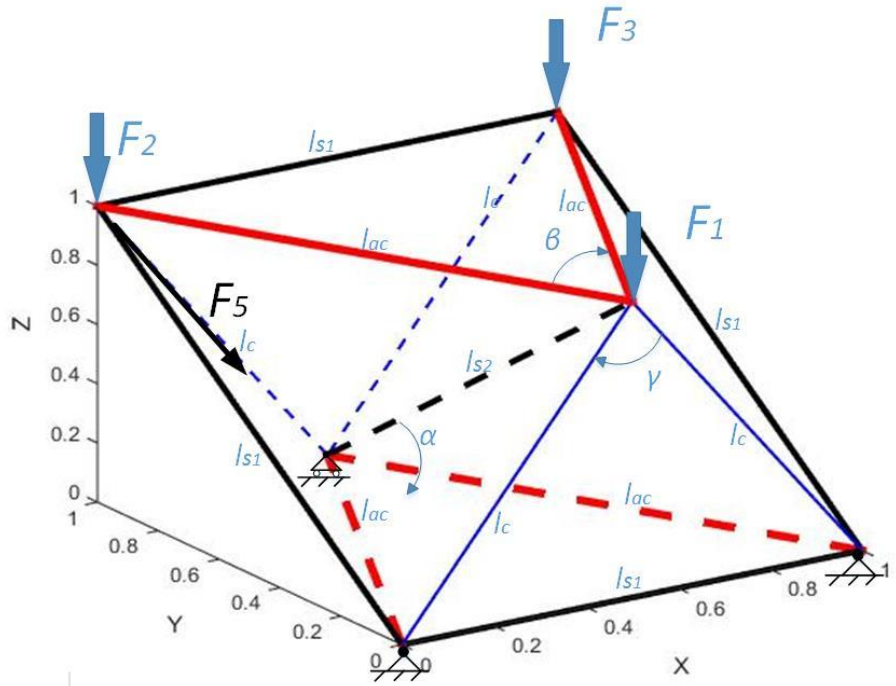

Figure 3.10 Structure and element parameter notations

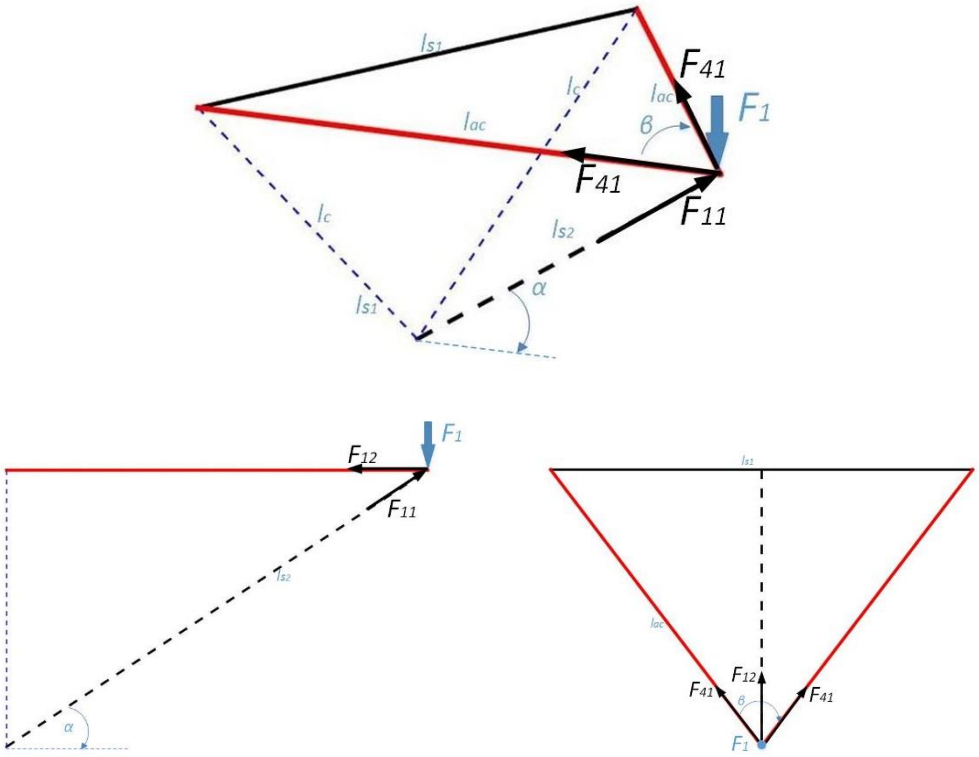

Figure 3.11 Load F_1 on actuators

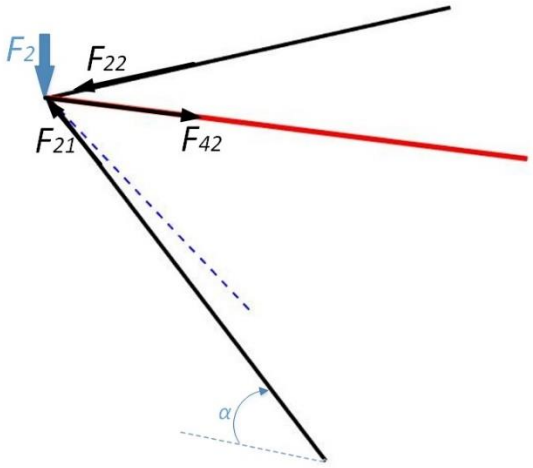

Figure 3.12 Load F_2 on actuators

Starting with load F_1, the cables cannot take any compression load, so for a vertical load like F_1, the required actuator tension can be calculated in a tetrahedron as shown in Figure.3.11.

$$F_{11} = \frac{1}{\sin(\alpha)} F_1 \tag{3.8}$$

$$F_{12} = \frac{1}{\tan(\alpha)} F_{11} \tag{.3.9}$$

$$F_{41} = \frac{1}{2\sin(\beta/2)} F_{12} \tag{3.10}$$

For F_2 the actuator tension should be the same (same actuator), and can be calculated:

$$F_{22} = \frac{1}{\tan(\alpha)} F_2 \tag{3.11}$$

$$F_{42} = \frac{1}{\sin(\beta/2)} F_2 \tag{3.12}$$

In the neutral tensegrity case, the actuator tensile forces associated with the expected lift force can be found, which depend on the size of the wing, and detailed results are shown in section 3.3.4. The tensile force also varies with the morphing mode direction

and amplitude, e.g. for a regular octahedron unit, under a certain external load the tensile force required at 15° twist morphing was 1.35 times that of the neutral position value.

3.3.3 Preload tension on actuators

Preloads in cables are essential to keep the structure stable, and adjusting the preload can directly control the tensegrity structure general and nodal stiffness. It is important to keep sufficient preload during the morphing, and this will require additional tensile forces to be provided by the actuators.

For a preload in cable F_5, the diagram for the force balance on a node is illustrated in Figure 3.13.

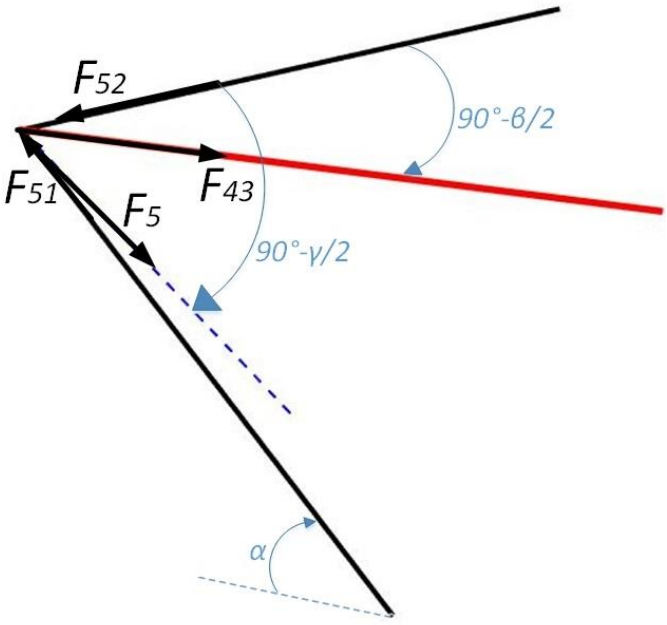

Figure 3.13 Cable preload on actuators

Eq.3.13-3.16 can be derived, thus the actuator tensile force F_{43} can be calculated from the preload F_5.

$$F_5 \cos(\gamma/2) = F_{51} \sin(\alpha) \tag{3.13}$$

$$F_{51} \cos(\alpha) = F_{43} \cos(\beta/2) \tag{3.14}$$

$$F_{52} = F_{43} \sin(\beta/2) \tag{3.15}$$

$$F_{43} = \frac{\cos(\gamma/2)}{\cos(\beta/2)\tan(\alpha)} F_5 \tag{3.16}$$

3.3.4 Actuator selection and dimension optimization

For a NACA0015 airfoil profile, the maximum thickness is 15% of the chord length, and the maximum thickness is at 30% of the length of the chord from the leading edge. It is ideal to lie the pivot axis of twist morphing at the aerodynamic centre, which will minimize the pitching moment variation for different angles of attack. For a subsonic airfoil, it has been found that the aerodynamic moment stays almost constant if the aerodynamic is applied on the point, which is at a quarter of the chord length from leading edge. In this case, a symmetrical airfoil generates almost zero moment on the aerodynamic centre. A tensegrity may be embedded into the airfoil as illustrated in Figure 3.14. Based on this figure, Table 3.2 gives some possible critical points, where the tensegrity may interfere with the skin. The actual space available for the actuators is smaller than this limit, because the structure holding the skin is not yet included. The required tensile forces for different chords are calculated and shown in Table 3.3, using a maximum AOA of α_{tip} = 24°, which is the maximum tip AOA would be used in the further wind tunnel tests.

Actuators must be selected which will fit in the structure and provide adequate force. Some critical dimensions of pneumatic cylinders from FESTO, are listed in Table 3.4;

both regular round cylinders and compact cylinders are included. Assuming the tensegrity cell used in the prototype wing is built with regular octahedron units, so every edge is the same length l, from simple geometric math, the diameter of an inscribed sphere is approx.0.816l, which is the maximum thickness allowed for the structure. To avoid any interference, any parts of the structure should stay within the critical points provided in Table 3.2, the allowed axial length l_{ac} of an actuator can be calculated as 3.17 (fitting and connectors included). Rod-end eye and clevis fittings would be used on both ends of the actuator, it would be safe to have l_{ac} at least 1.5 times of the actuator's built-in length l_{ac}' at maximum stroke l_{as}.

$$0.816l_{ac} \leq 2 \times (0.06682c\text{-}r_{ac}) \tag{3.17}$$

$$l_{ac} \geq 1.5\times (l_{ac}'+2l_{as}) \tag{3.18}$$

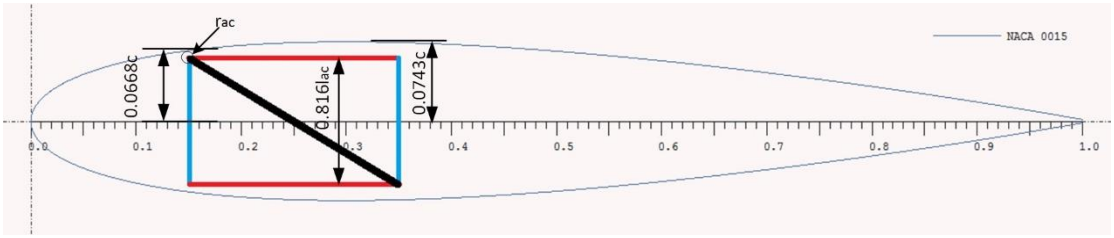

Figure 3.14 Illustrated tensegrity embedded

Table 3.2 Critical points on the airfoil where interference might happen

Horizontal (fraction of chord)	Vertical (fraction of chord)
0.15	±0.0668
0.35	±0.0743

Table 3.3 Actuator tensile force requirement for different chord at angle of attack a = 24°, regular octahedron units.

Chord (m)	Maximum thickness (m)	Tensile force required (N)
0.2	0.03	49.44
0.4	0.06	78.05
0.6	0.09	96.93
0.8	0.12	109.17
1.0	0.15	117.59

Table 3.4 Dimensions of pneumatic cylinders of different retraction force. (FESTO 2018, FESTO 2018)

Piston diameter(mm)	Max retraction force(N) @6bar	Axial length l_{ac}'(mm) (stroke excluded)	Cylinder diameter or width, r_{ac}(mm)
10	40	62	19
12	51	72	24
12(compact)	51	39.2	27.5×27.5 square
16	104	78	24
16(compact)	104	39.7	29×29 square
20	158	92	32
20(compact)	158	42.5	35.5×35.5 square
25	247	97.5	32
25(compact)	247	44.5	39.5×39.5 square

For chord length c= 0.2 and 0.4, the wing thickness was too thin to embed two sets of actuators in parallel. For larger chord length, greater retraction forces were required for actuation, which resulted in larger actuator dimensions. With maximum axial lengths limitations as stated in 3.17, actuator length selection were main challenges for large chord length wings. According to the estimation, no off-the-shelf actuators can be properly fitted in to a regular octahedron unit, so the unit needs to be flatter and wider, i.e. small α and larger β and γ.

Iterations are made for an optimized dimension set, in which a large aspect ratio of the wing is chosen for better wind tunnel performance. The final dimensions and parameters for the unit tensegrity are presented in Table 3.5.

Table.3.5 Dimensions of optimized tensegrity

Parameter	Value	Unit
Long Strut length (l_{s1})	191.6	mm
Short Strut length (l_{s2})	148	mm
Cell Actuator overall length at neutral (l_{AC})	159.9	mm
Intermediate actuator overall length at neutral (l_{IA})	191.6	mm
Cable length (l_c)	121	mm
Thickness (node-node)	74	mm
Maximum Thickness	113.5	mm

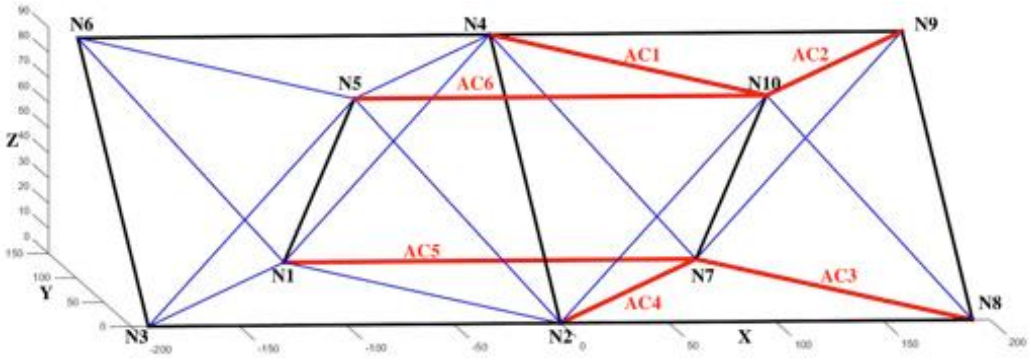

Figure 3.15 Active tensegrity structure in its neutral position

The geometrical configuration presented in Table 3.5 is used as the basis of the further research of this project. The structure has 9 struts (black lines), 12 cables (blue lines), and 6 actuators (red lines, labelled AC1 to AC6) as illustrated in Figure 3.15.

The chord length 0.8m is selected for the prototype wing. Compact cylinders with 25mm piston diameter and 25mm stroke are selected as the four in-cell actuators (AC1-4), and standard cylinders with 25mm piston and 25mm stroke are selected as the two intermediate actuators (AC5 and AC6).

Substitute dimensions in Table 3.5 to use equation 3.12 and 3.16, actuation force required can be calculate, in which, $\alpha = 28.44°$, $\beta = 73.39°$, $\gamma = 102.29°$

For neutral tensegrity case:

$$F_{42} = 86.18\text{N},\ F_{43} = 80.58\text{N}$$

In the twist case, required tensile force could be higher:

$$F_{ac} = 1.3\times (F_{42} + F_{43}) = 225.12\text{N} \qquad (3.19)$$

The selected actuators provide 247N retraction force as stated in Table 3.4.

3.4 Direct kinematics of proposed structure

3.4.1 Configuration of the structure

As illustrated in Figure 3.15, the members are pin jointed to 10 dimensionless nodes, thus the assumption that the members meet at the centre of the nodes was made, and all joints are spherical joints.

3.4.2 Kinematic analysis

In the kinematic study in this section, all passive members are assumed to be rigid, i.e. lengths of the members do not change. The motions defined for the structure are not directly measured, instead actuator position measurements are used and a transformation between actuator and structure positions needs to be established in order to perform closed loop motion control. Notation and numbering for nodes and actuators are shown in Figure 3.15

The left cell is a passive cell, thus N_2 (x_2, y_2, z_2) and N_4 (x_4, y_4, z_4) are fixed points, and dl_i (i= 1, 2, 3, 6) is the displacement for an actuator from its neutral position, with extension as positive. Based on the pin joint assumption, equations can be found for the tensegrity model:

$$(x_{10}-x_4)^2+(y_{10}-y_4)^2+(z_{10}-z_4)^2=(l_{AC}+dl_1)^2 \tag{3.20}$$

$$(x_{10}-x_7)^2+(y_{10}-y_7)^2+(z_{10}-z_7)^2=l_{s2}^2 \tag{3.21}$$

$$(x_{10}-x_2)^2+(y_{10}-y_2)^2+(z_{10}-z_2)^2=l_c^2 \tag{3.22}$$

$$(x_7-x_4)^2+(y_7-y_4)^2+(z_7-z_4)^2=l_c^2 \tag{3.23}$$

$$(x_7-x_2)^2+(y_7-y_2)^2+(z_7-z_2)^2=(l_{AC}+dl_4)^2 \tag{3.24}$$

$$(x_{10}-x_9)^2+(y_{10}-y_9)^2+(z_{10}-z_9)^2=(l_{AC}+dl_2)^2 \tag{3.25}$$

$$(x_9-x_7)^2+(y_9-y_7)^2+(z_9-z_7)^2=l_c^2 \tag{3.26}$$

$$(x_8-x_9)^2+(y_8-y_9)^2+(z_8-z_9)^2=l_{s2}^2 \tag{3.27}$$

$$(x_8-x_2)^2+(y_8-y_2)^2+(z_8-z_2)^2=l_{s1}^2 \tag{3.28}$$

$$(x_9-x_4)^2+(y_9-y_4)^2+(z_9-z_4)^2=l_{s1}^2 \tag{3.29}$$

$$(x_{10}-x_8)^2+(y_{10}-y_8)^2+(z_{10}-z_8)^2=l_c^2 \tag{3.30}$$

$$(x_{10}-x_5)^2+(y_{10}-y_5)^2+(z_{10}-z_5)^2=(l_{1A}+dl_6)^2 \tag{3.31}$$

The tensegrity structure is naturally over constrained, with 4 DOF to control, so four of six actuator displacements are given and the other two can be determined.

3.4.3 Structure deformation modes

In this section the motion modes of the active structure are introduced, including the definition of the motions and how the displacement of the actuators will affect the motion of the structure.

For a tensegrity structure embedded in an active wing, the x-axis is the span wise, and y as the chord wise direction. Defining the controlled positions in Cartesian coordinates as: twist (θ, angular deformation about the x-axis), bend (ϕ, angular deformation about the y-axis), sweep (ψ, angular deformation about the z-axis), and introducing a general control variable (φ), the structure displacement vector $\mathbf{y_c}$ will be:

$$\mathbf{y}_\mathbf{c}=\begin{pmatrix}\theta & \phi & \psi & \varphi\end{pmatrix}^T$$

The nodes N_8 and N_9 are on the wing tip side of the structure, and the coordinates of N_8 and N_9, which can be found from the equation set 3.20-3.31, are used to define the motion modes.

N_{81} (x_{81}, y_{81}, z_{81}) and N_{91} (x_{91}, y_{91}, z_{91}) are the initial node coordinates while dl_i (i= 1, 2, 3, 6) = 0. With given dl_i the morphed node position are N_{82} (x_{82}, y_{82}, z_{82}) and N_{92} (x_{92}, y_{92}, z_{92}). Motion modes are defined as follows.

Twist angle θ is the angle between $\overrightarrow{N_{81}N_{91}}$ and $\overrightarrow{N_{82}N_{92}}$ projected on the Y-Z plane,

$$\theta = \cos^{-1}\left(\frac{(x_{91}-x_{81})(x_{92}-x_{82})+(y_{91}-y_{81})(y_{92}-y_{82})}{\sqrt{(x_{91}-x_{81})^2+(y_{91}-y_{81})^2}\sqrt{(x_{92}-x_{82})^2+(y_{92}-y_{82})^2}}\right) \quad (3.32)$$

Bend angle ϕ is the angle between $\overrightarrow{N_{91}N_4}$ and $\overrightarrow{N_{92}N_4}$ projected on the X-Z plane,

$$\phi = \cos^{-1}\left(\frac{(x_{91}-x_4)(x_{92}-x_4)+(z_{91}-z_4)(z_{92}-z_4)}{\sqrt{(x_{91}-x_4)^2+(z_{91}-z_4)^2}\sqrt{(x_{92}-x_4)^2+(z_{92}-z_4)^2}}\right) \quad (3.33)$$

Sweep angle ψ is the angle between $\overrightarrow{N_{91}N_4}$ and $\overrightarrow{N_{92}N_4}$ projected on the X-Y plane,

$$\psi = \cos^{-1}\left(\frac{(x_{91}-x_4)(x_{92}-x_4)+(y_{91}-y_4)(y_{92}-y_4)}{\sqrt{(x_{91}-x_4)^2+(y_{91}-y_4)^2}\sqrt{(x_{92}-x_4)^2+(y_{92}-y_4)^2}}\right) \quad (3.34)$$

Substituting the geometric dimensions in Table.3.5, equation set 3.20-3.31 can be solved numerically, giving a relationship between the actuator displacements dl_i and the structure DOF modes:

$$\begin{pmatrix} -0.4545 & 0.4545 & 0.4545 & -0.4545 & 0 & 0 \\ -0.1667 & 0.1667 & -0.1667 & 0.1667 & 0 & 0 \\ 0.1365 & 0.1365 & -0.1365 & -0.1365 & 0 & 0 \\ 0 & 0.1667 & -0.1667 & 0 & 0.1872 & -0.1872 \end{pmatrix} \begin{pmatrix} dl_1 \\ dl_2 \\ dl_3 \\ dl_4 \\ dl_5 \\ dl_6 \end{pmatrix} = \begin{pmatrix} \theta \\ \phi \\ \psi \\ \varphi \end{pmatrix} \quad (3.35)$$

This is the linearized result around the neutral position, i.e. it shows the Jacobian matrix which relates small changes in actuator length to small changes is mode position. The twisted and bended examples are illustrated as Figures 3.16 and 3.17

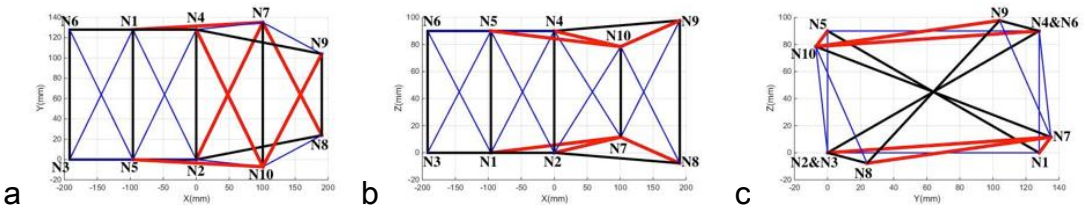

Figure 3.16 Twist actuation example: a) top view b) front view c) end view

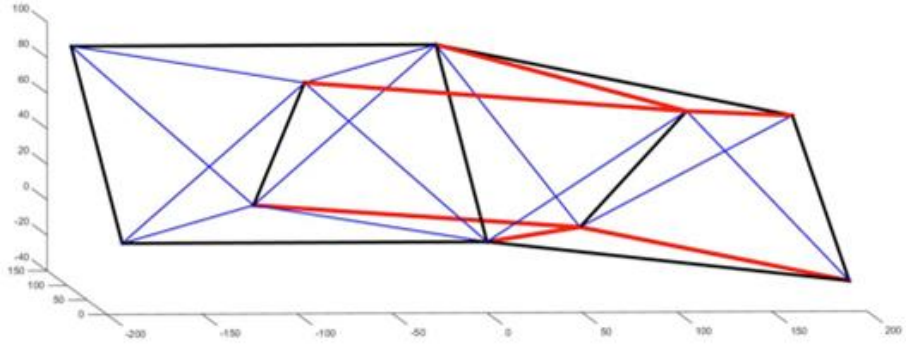

Figure 3.17 Bend actuation example (downward)

Figure 3.16 illustrates an example of twisting actuation using orthogonal views. When AC1 and AC4 are retracted by 6.31mm, AC2 and AC3 extended by 6.31mm, and AC5 and AC6 retracted by 5.61mm, the structure will be at a twisting angle of 12°. An example of span-wise bend is shown in Figure 3.17, in which AC1 and AC3 are extended by 11.1mm, AC2 and AC4 contracted by 11.1mm, and AC5 extended by 9.87mm and AC6 retracted by 9.87mm, giving the structure a bending angle of 8°

3.5 Conclusions

A concept design of smart structures with octahedral tensegrity cells is proposed in this chapter. The design is refined with consideration of estimated external load, dimension constraints and kinematic requirements. A forward kinematics analysis is presented, which helps to understand the relationship between actuator length change

and structure shape change, and can be used as the basis of precise motion control.

The detailed design of the proposed structure is introduced in Chapter 4.

4 Experimental systems

The conceptual design and actuator selection for the tensegrity structure was introduced in Chapter 3, and the dimensions for the optimized tensegrity were included in Table 3.5. It was not possible to perfectly implement the concept design in the physical experiment, especially in terms of the node joint design, where up to 7 members are designed to meet at exactly one point. A node and strut design which fits the morphing requirement is introduced in this chapter. The following sections describe the experiment physical and sensing system in detail, including the pneumatic actuation system, displacement and motion tracking, extension wing and flexible skin design, aero load measurement and data acquisition (DAQ) system.

4.1 Structural components and node design

The general dimensions for an optimized tensegrity were determined in Chapter 3, and an example of a physical single-unit tensegrity structure is shown as Figure 4.1, in which tension springs are used instead of actuators.

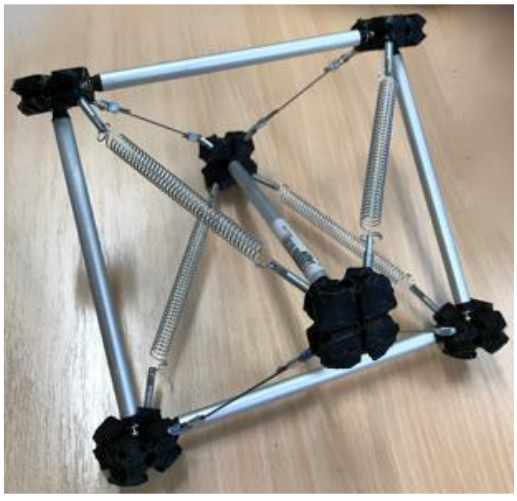

Figure 4.1 A single-unit tensegrity structure with springs instead of actuators

The load on nodes may not be symmetrical, which can make the nodes at the same wing section twist in different directions (e.g. top left and bottom left nodes in Figure 4.1). Initial experiments showed that non-even twisting also made it challenging for the airfoil shaped sections to be attached to the tensegrity structure. A morphing tensegrity structure of class two and higher would require an efficient joint, which could offer adequate degrees of freedom. Previous research was done on rotational joints for shape morphing trusses (Sofla, Elzey et al. 2007). For the morphing tensegrity application in this project, up to seven members are connected to one node, and each of them requires all three rotational degrees of freedom, in which three of them are compression members, and this brings more complexity to the design. The nodes and joints used in the experiments have finite volume, which are different from the dimensionless node assumptions in ideal tensegrity theory, where members meet at a single point. An alternative design was proposed to balance the torque on node members for a tensegrity structure in its neutral position, by making the load vectors (or their extensions) meet at a virtual point, which may be located outside the node. When the structure is in a morphed position, this design also minimized the unbalanced torque, and guaranteed a positive rotational stiffness on node elements. Kinematic analysis shows that a local DOF for the nodes is not necessary to achieve the global deformation DOF, which makes it possible to have a design in which the chord-wise struts and nodes are rigidly connected.

Figure 4.2 shows the left unit cell from the prototype, which contains no actuation; the node-to-node dimensions are consistent with Table 3.5, while outer dimensions are

larger. As described above, a change has been made to the nodes and struts compared to the original pin-jointed design, by replacing the struts parallel to the Y-Z plane with bespoke aluminium frames, to increase the node twisting stiffness of the connected nodes and to give interfaces for attaching aerofoil shaped ribs. As a rigid member in a tensegrity structure, the original strut carries compression load only. The diagonal element beams on each frame are designed to have similar mechanical properties in compression load, compared to the original struts design. The supporting outer frames are designed as mounting interfaces, and the pocket shapes are different to allow the wires and pipes to run through the structure and to avoid any interference with other elements (e.g. struts, actuators).

Figure 4.3 shows the original node design and the refined design with cable and struts attached, allowing pairs of nodes at the same wing section to be rigidly connected together. Frames are milled from 8mm thickness aluminium tooling plate, and weigh from 72 to 90g each depending on the design details.

In the original structure nodes are 3D printed PLA blend with 100% in fill. The refined nodes are machined form aluminium blocks, and threaded holes were drilled and tapped for the tensile members to meet the requirements of angles (α, β and γ) in Chapter 3 as illustrated in Figure 4.4. Spherical joint sockets are milled out from the block, and lined with PTFE film for lubrication.

The struts are made from 8mm diameter aluminium tube with 1mm wall thickness, stainless steel ball studs of 4.8mm diameter were fitted to both ends, with a centre-centre dimension of 191.6mm, offering buckling resistant of 2500N (safety factor

around 10) in this case. The ball studs are fitted to the milled sockets to complete the spherical joint as shown in Figure 4.3 c).

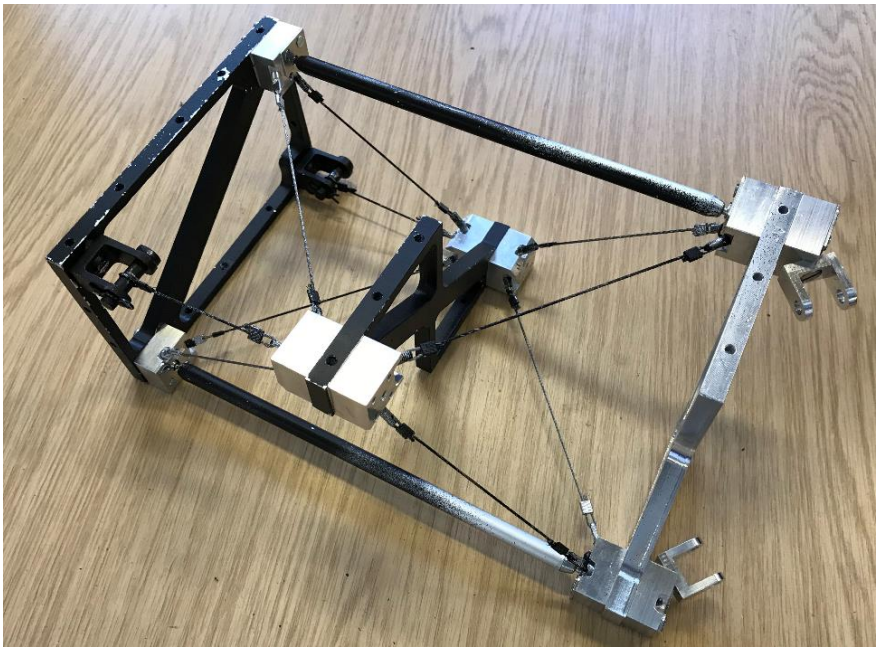

Figure 4.2 Unactuated tensegrity structure cell (210×150×94mm outer dimension)

a) 

b) 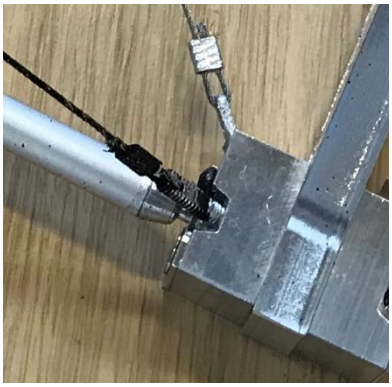

c) 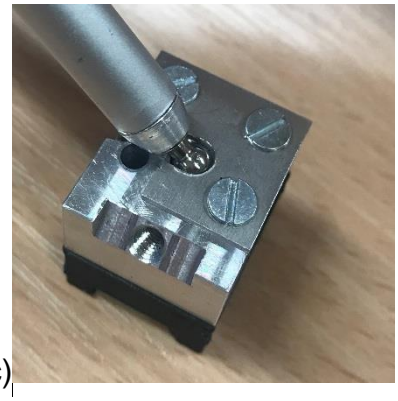

Figure 4.3 Node design before (a) and after (b) refinement (c) ball joint

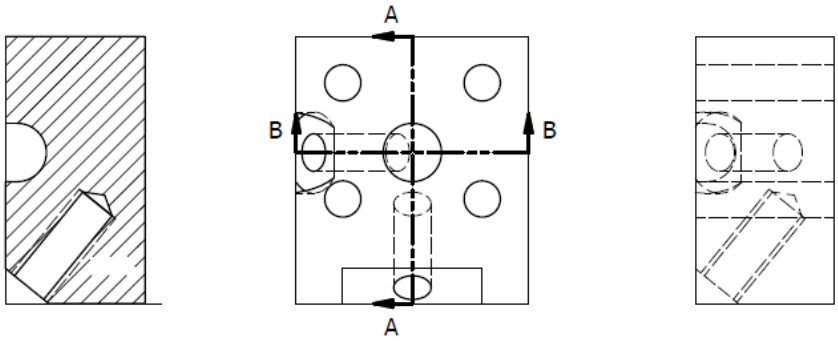

Figure 4.4 Node design example

4.2 Pneumatic actuation

4.2.1 Actuator and valves

Single-acting (pull only) pneumatic actuators are embedded in the tensegrity structure and are sized by considering outer dimensions and the theoretical retraction force at 6 bar supply pressure. Actuators are selected as discussed in Chapter 3.3. Low friction seals are selected in order to perform smoother transient motion and more precise adjustments.

SMC V100 series 3 port solenoid valves are selected. Each cylinder is controlled by two 3/2-switch valves: V114 valves are used to pressurize the actuators and V124 valves are used to exhaust them. Each actuator is connected in the circuit as shown in Figure 4.5. Valve type V114 is normally closed and V124 is normal open(SMC 2015). For each valve, only ports 1 and 2 are used, and port 3 is blocked. The flow characteristics are given in Table 4.1, in which C is the sonic conductance, b is the critical pressure ratio, and C_V is the flow coefficient which gives a maximum 13.32 L/min inlet flow rate for V114 and 19.44 L/min exhaust flow rate for V124, at the

maximum operation pressure of 6 bar. The maximum operating frequency of the valve is 20Hz, with a response time T_s of 5ms for opening and 4ms for closing. The valves are mounted on manifolds as shown in Figure 4.6 and Figure 4.7.

Festo piezo resistive pressure transmitters (type SPTE) are mounted with push-in sleeves on the manifold as seen along the bottom of Figure 4.7, and these are used to measure the actuation force. The pressure transmitters have a measurement range of 0-10 bar, with accuracy of ±0.3 bar, and repetition accuracy of ±0.03 bar (at room temperature of 23 °C). Outputs are analogue voltage signals of 0-10V, with a rise time of 1ms(FESTO 2018).

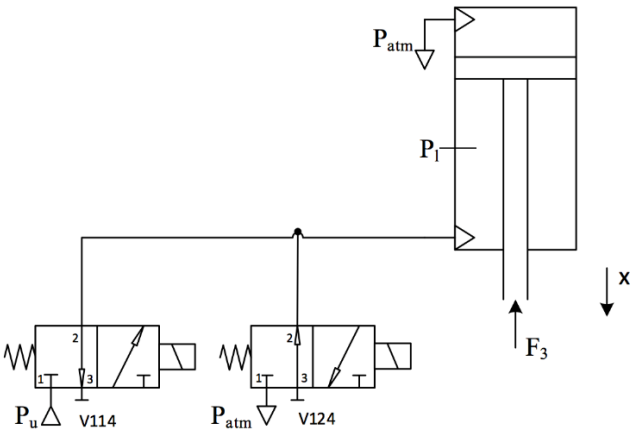

Figure 4.5 Circuit diagram for a single actuator

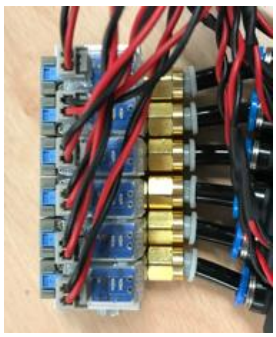

Figure 4.6 V124 exhaust valve group on manifold

Figure 4.7 V114 supply valve group with pressure transmitters

Table 4.1 Flow characteristics for valves

Valve Model	Port 1-Port2		
	Sonic conductance C [dm^3/(s bar)]	Critical pressure ratio b_v	Flow coefficient C_v
V114	0.037	0.11	0.008
V124	0.054	0.35	0.015

4.2.2 Assembly of actuators

The tensegrity concept requires all joints to be able to rotate in all three rotational degrees of freedom. For actuators like a pneumatic cylinder, which is rigid in radial directions, the joints need to fulfil the requirements and with very low in friction.

In the prototype built for this project, rod-end bearings are used on both ends of all cylinders. As shown in Figure 4.8, the compact cylinder selected has a flat end cap (left side), and a piston rod with female thread (right side). Extra space between two clevis forks is designed, which grants the rod end joint extra rotation range on two DOF, as shown in Figure 4.9. A flange plate is designed to mount the rod end bearing on the cylinder end cap though a pin and R-clip, the stud of the rod end joint is directly fitted into the node. At the piston rod end of the compact cylinder, the rod end bearing is attached to the node with a clevis. For intermediate actuators, which are standard

round cylinders, both ends are attached to the nodes with a clevis and pin, as shown in Figure 4.10.

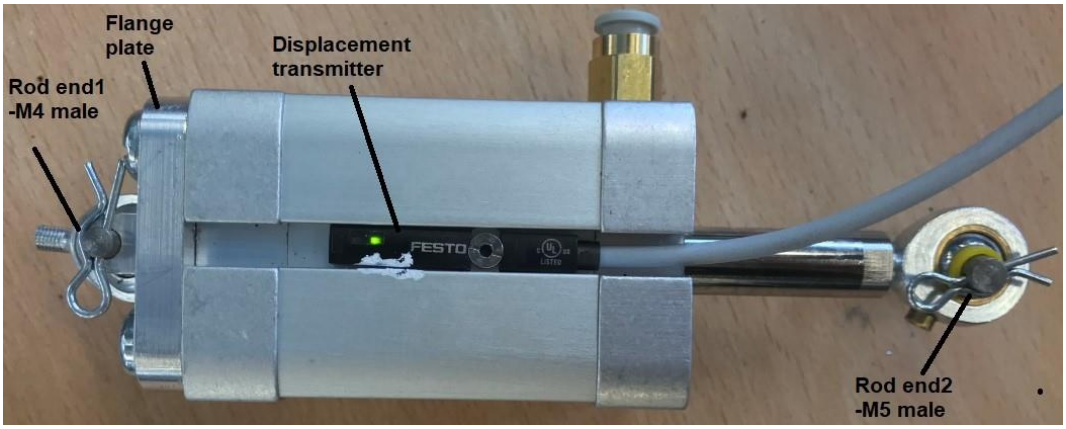

Figure 4.8 Compact cylinder and fittings

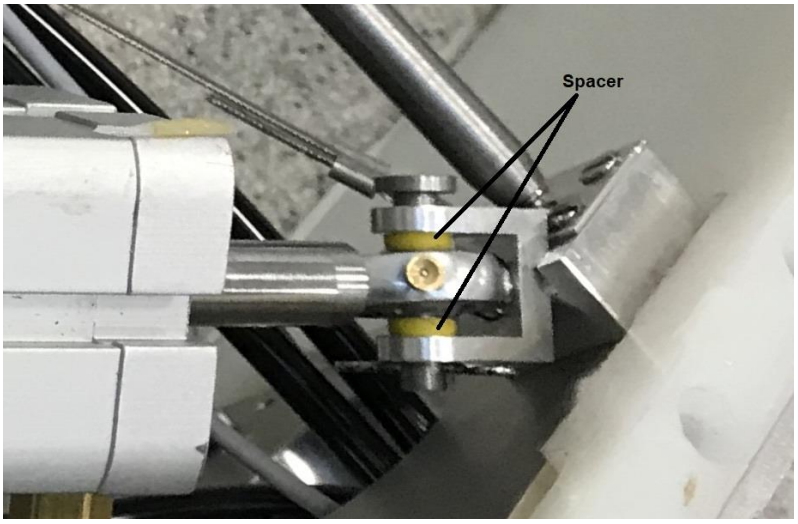

Figure 4.9 Clevis with spacer

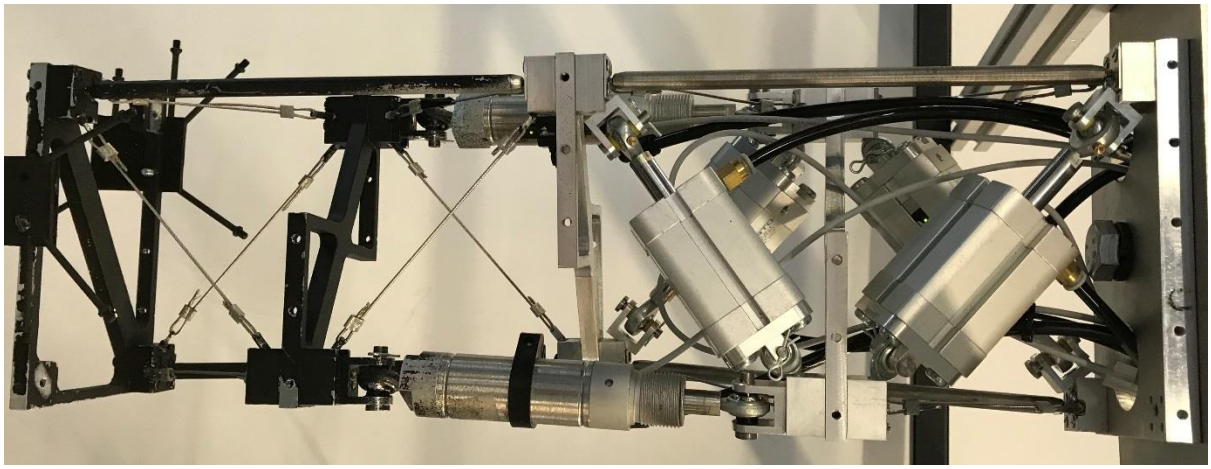

Figure 4.10 Structure full assembly

4.3 Displacement and motion tracking

The deformation of the wing is tracked locally by measuring each actuator displacement and calculated through the kinematic transformation discussed in Chapter 3. These displacement feedbacks are used in the real-time motion and force control loop.

The deformation is also tracked by an optical motion capture system, OptiTrack, and results are compared with the actuator displacement measurements, to provide an independent verification.

Contactless actuator position transmitters are used for the displacement measurement. The Festo SMAT-8M position transmitters are mounted on circular clips on standard DSNU round cylinders (Figure 4.10) and in the T-slot for ADN compact cylinders (Figure 4.8). They are Hall Effect sensors so the piston displacement are measured magnetically, with a measurement range s of 28mm for standard cylinder and 27mm for compact cylinder (FESTO 2018). The displacement sensor has regulated voltage output, which is linear in the measuring range. The repetition accuracy is ±0.1 mm; The repetition accuracy in the centre of the measuring range is lower than at the edge, which is caused by the nature of magnetic field distribution. The repetition accuracy is ±0.06 mm at a distance of ±5 mm from the centre as illustrate in Figure 4.11. In the prototype the transmitters are mounted on the mid-stroke point for each cylinder, which is the piston position for the structure in neutral state.

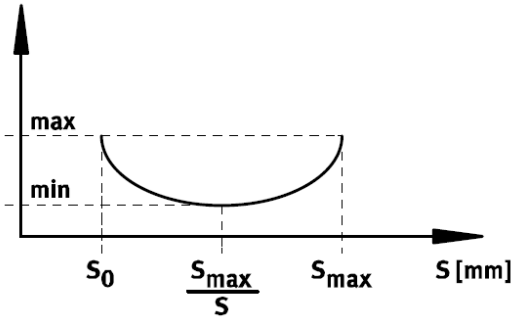

Figure 4.11 Repetition accuracy as a function of position measuring range *s* (FESTO 2018)

For the bench top test, three Prime 13 cameras and 5 markers are used to the track the end of the structure. The motion data is recorded in a software package Motive as Cartesian coordinates and Euler angles. The motion of the rib nearest to the wing tip is tracked. All five markers are rigidly mounted on the rib; the camera and marker arrangement is shown in Figure 4.12. A capture volume of 1.0 m×1.0 m×1.0m was used, and about 3000 sample points were captured by each camera, giving a mean 3D measurement re-projection error of 0.193mm. All motions are tracked at a frame rate of 120 fps.

The camera and marker arrangement in the wind tunnel is shown in Figure 4.13. The tracking markers are closely mounted on the wingtip of the prototype wing for a rigid connection and to minimize the extra drag in the test. The tracking markers do not project out from the wingtip plate, so all cameras are placed on a lower level to avoid losing track during deformation. In order to provide a steady flow for the wing test, camera 1 is placed underneath the glass floor, camera 2 is placed on the wind tunnel

floor on the trailing edge side, camera 3 on the edge of octagon test section, in front of the leading edge.

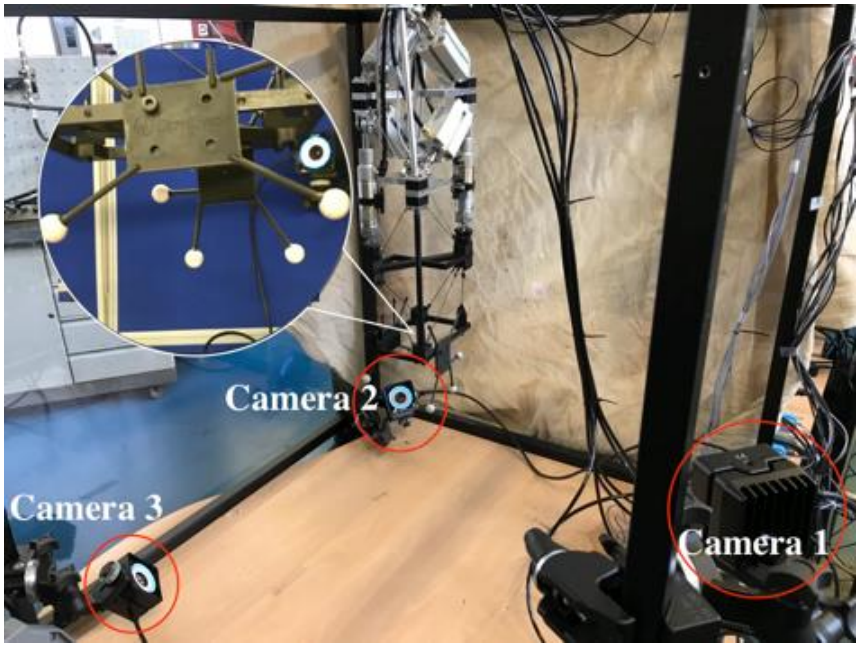

Figure 4.12 Cameras and markers arrangement on test rig

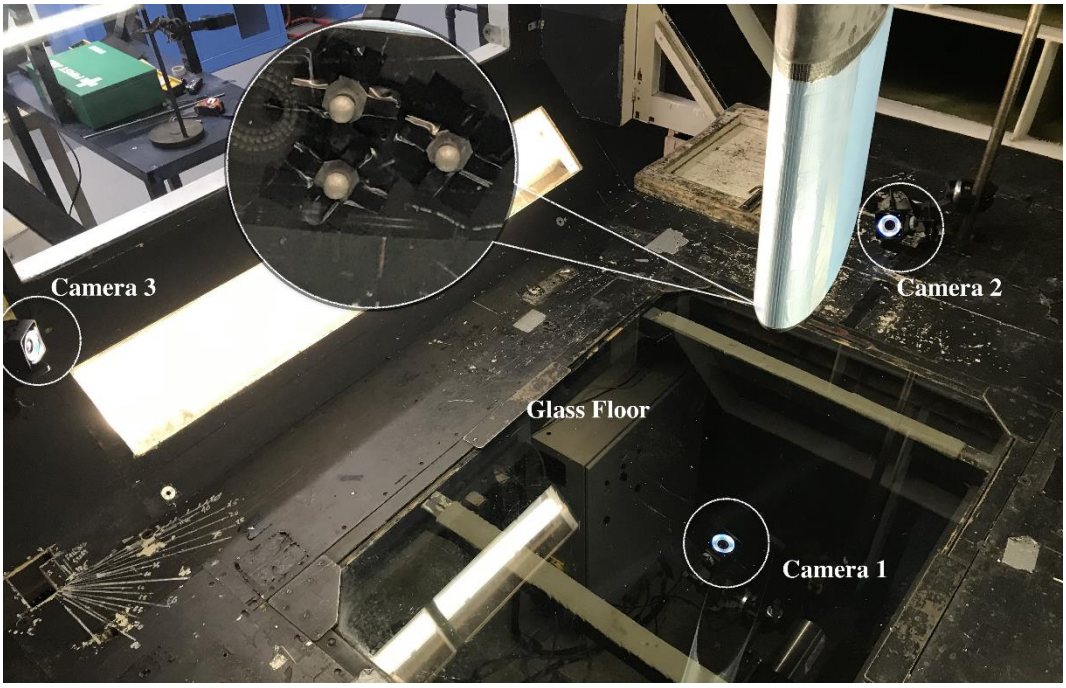

Figure 4.13 Cameras and markers arrangement in wind tunnel

4.4 Force measurement in wind tunnel

Aerodynamic force changes corresponding to the structure deformation are the main interest for the wind tunnel test. A two-axis 2014T6 Aluminium binocular strain gauge force balance was employed to measure the aerodynamic forces directly, as shown in Figure 4.14. The two axes of the force balance were arranged at 90° to one another and were aligned in directions parallel (drag *D*) and perpendicular (lift *L*) to the flow direction of the wind tunnel test section. Four strain gauges were deployed on the binoculars for each axis, at the stress concentrations, and the gauges were arranged in a Wheatstone bridge, thus generating a voltage difference corresponding to the force applied. The symmetric design also balanced out the moment load applied, which is not the main interest in this part of the test.

The force balance is attached to the wing via a shaft, allowing the baseline AOA to be adjusted manually and checked using a laser indicator and optical tracking system before each test. A calibration was done prior to the test to determine the relationship between the load applied and voltage generated. Load was directly applied on the shaft by hanging weights for calibration. The measured force values are transferred to force coefficients for further analysis. Lift coefficient C_l and drag coefficient C_d are calculated using eq. 4.1 and 4.2.

$$C_l = \frac{L}{\frac{1}{2}\rho v^2 S} \tag{4.1}$$

$$C_d = \frac{D}{\frac{1}{2}\rho v^2 S} \tag{4.2}$$

where, L and D are lift and drag in measured by the balance, ρ is the air density at the specific testing temperature, v is the test wind speed and S is the relevant surface area. In this case S is 0.8m^2 (0.8m chord length by 1m span).

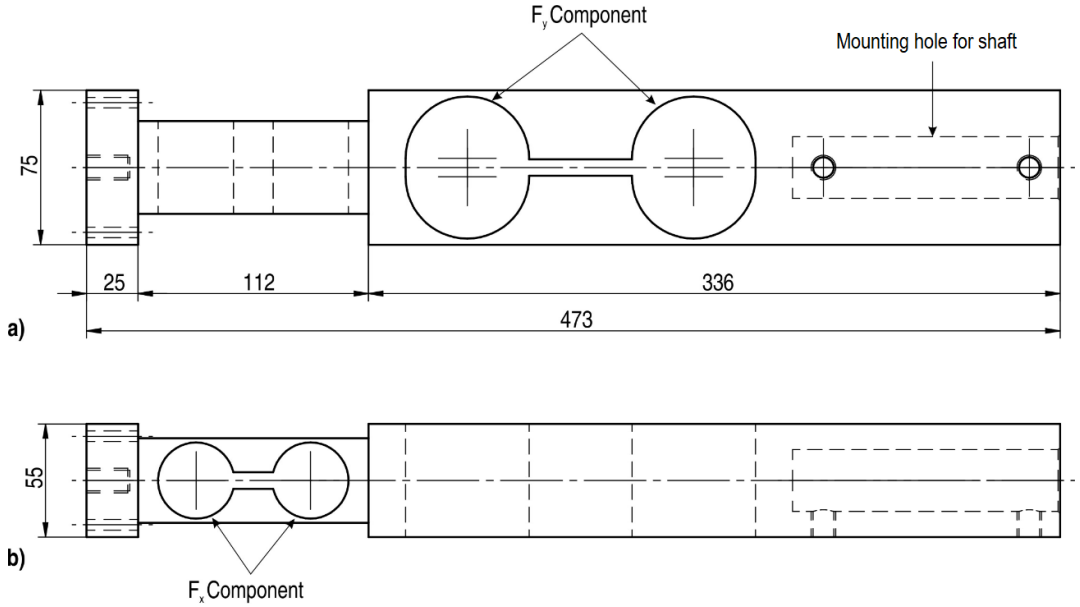

Figure 4.14 Force measurement balance a) front view b) top view

4.5 Extension wing and skin

4.5.1 Wing rib and extension wing

Wing ribs are manufactured and assembled to expand the truss-like structure to a morphing wing. Five ribs are milled from nylon66 sheet of 12mm thickness, with outer 0.8m chord length and a NACA0015 airfoil profile, and inside cut-outs matching the five frames in the tensegrity structure. The ribs are attached to the tensegrity structure with countersunk bolts to give a smooth surface finish.

The prototype tensegrity structure shown in Figure 4.12 has an overall length of 440mm when pre-stressed. A solid extension wing is hot wire cut from Styrofoam blocks, with same outer profile with the ribs. The two bottom ribs will not deform relative

to each other, the skin in this area will not be tensioned, and a Styrofoam filling is attached to help holding a smooth airfoil shape, as shown in Figure4.15.

Figure 4.15 Nylon ribs and foam in-fill before skin attached. Ribs held at correct spacing by temporary fixture.

4.5.2 Flexible skin

The flexible skin for the morphing wing should always be in tension, so it can bear aerodynamic loads and remain in approximately the correct airfoil shape. Various flexible skin approaches were reviewed in Chapter 2, and a pre-tensioned elastomer skin was considered the most appropriate due to its surface smoothness and ease of manufacture, as the flexible skin is not the key research aim of this thesis. It is important to determine the pre-strain needed to achieve the deformation, as well as the associated pre-stress.

The flexible skin used in the test is black natural latex film with 0.2mm thickness. The basic properties are shown in Table 4.2. The skin is glued to the edge of the ribs using Ethylene-Vinyl Acetate thermal glue ‘Tecbond 132’.

A stress-strain test was carried out to check the adhesive strength between the latex skin and airfoil ribs, and determine the proper strain range for the morphing wing. A stress-strain test specimen made of nylon66 was milled out, to represent the essential features of the airfoils ribs, including leading edge, trailing edge and countersunk holes for assembly. The perimeter of the specimen is 440mm (about 1/4 of the prototype wing perimeter) as shown in Figure 4.16. A single piece of latex film is wrapped around and glued on the two specimen ribs, leaving 60mm gap between the two ribs, as shown in Figure 4.17. The screw at the centre of the leading edge arc is used to hold the specimen during the test, as shown in Figure 4.18.

Table 4.2 natural latex film physical properties (FULLCHANCE-INDUSTRIAL 2018)

	Value	Unit
Tensile strength	25	MPa
Modulus at 500% Extension	3	MPa
Elongation at break	850	%
Tear Strength (Crescent)	70	N/mm
Hardness (Shore M)	35	°
Specific Gravity	0.95	-

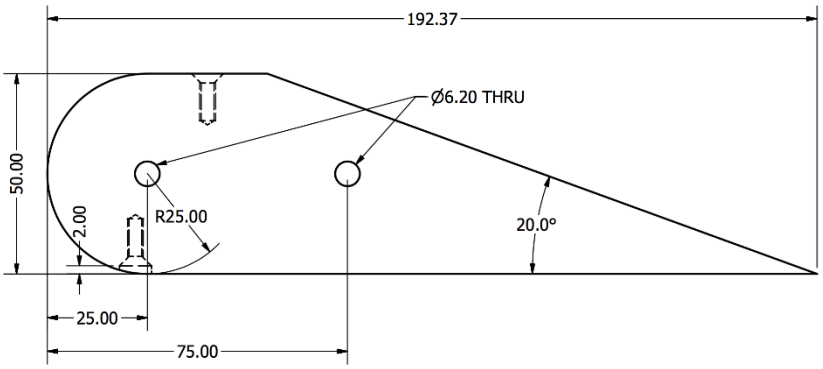

Figure 4.16 Test specimen section (dimensions in mm)

a)  b) 

Figure 4.17 Stress-strain test specimen a) top view b) back view

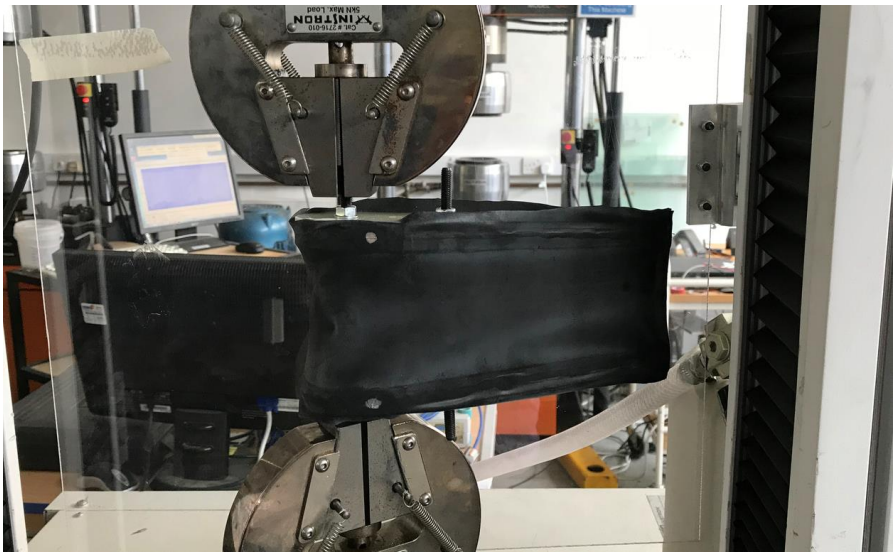

Figure 4.18 Tensile test specimen clamped with V-jaws

The tensile test is carried out on an Instron universal testing machine (Type 5965), with a test speed of 5mm/min. The test is conducted in position control; the film was extended by certain amount, and released back to zero extension. Four cycles were used in the test, 3mm (5% strain), 6mm (10% strain) and 9mm (15% strain) and 12mm (20% strain), each performed five times. Test results are shown in Figure 4.19. Certain stress relaxations can be observed from the test results, but the linearity of the load-extension curve is acceptable, which means the latex chosen can maintain elasticity within the envisaged load range and is suitable for this application.

According to the kinematic analysis in Chapter 3, a minimum strain of 8% is required to keep the skin in tension during deformation in the wind tunnel test. In this experiment, a 12% strain is selected for the skin pre-strain. The latex skin was glued to the rib set shown in Figure 4.15, and pre-tensioned while the wing shaped structure was mated to the tensegrity structure. The morphing structure with tensioned skin mounted on the force balance is shown in Figure 4.20.

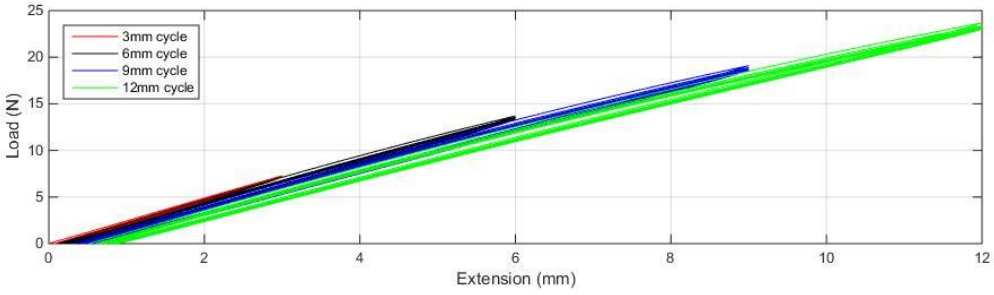

Figure 4.19 Tensile test result for the specimen

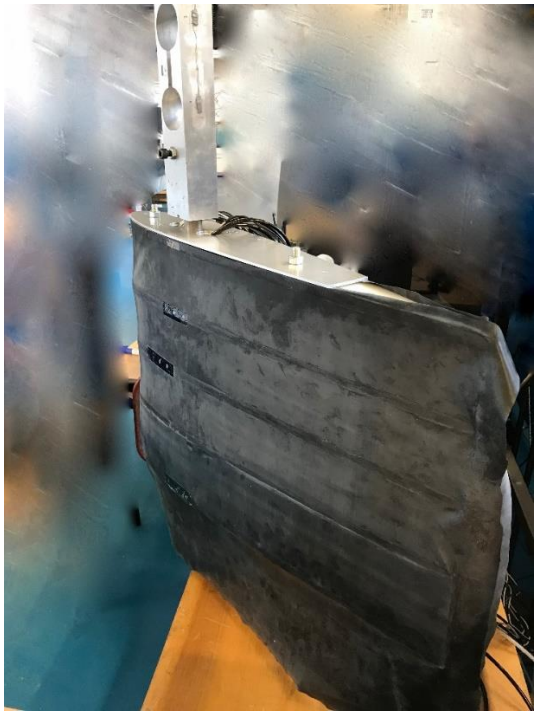

Figure 4.20 Wing morphing part with skin attached (trailing edge not trimmed yet)

4.5.3 Wing design scaling

The prototype wing presented in this thesis is designed and tested at a condition which is close to a small UAV with relatively low air speed (the Reynolds number of 6.61×10^5 and freestream velocity of 12.5m/s used in the tests are close to the small UAV wind tunnel test examples given in (Bourdin, Gatto et al. 2008) which have a Reynolds number of 2.3×10^5 and freestream velocity of 10m/s).

For larger scale applications, to a first approximation the mass of the aircraft will change with an exponent of three over dimension change, i.e. ten times bigger, a thousand times heavier. The forces acting on the aircraft change at a similar rate to the mass change, as the wing lift change needs be close to the aircraft weight change. Detailed parameters are different due to specific design and mission requirements, e.g. the Boeing 737-800 has a wingspan of 34.32m and maximum takeoff weight of

79 tons, and the Airbus A380 has a wingspan of 79.8m and maximum takeoff weight of 560 tons (Tennekes 2009). The two airliners have wing span ratio of 2.33 and takeoff weight ratio of 7.09, which corresponds to an exponent of 2.31.

When evaluating the scaling outcome, it is important that structural strength grows at about the cube of the linear dimension growth, which is required for the wing to support the aircraft to fly. And strength-to-mass ratio determines how effective the scaled structure is. The relationship between overall wing size scaling, structural component dimensions and weight scaling, total aircraft mass scaling and the actuation system size are discussed in this section.

In this section, the baseline structure (one unit) used for the scaling investigation is shown in Figure 3.15. All struts are assumed to be tube members. Note however that the conclusions will apply to any strut cross-section which has a second moment of area which changes to the power of 4 with the linear dimension scaling factor. Structural strength of a tensegrity structure is highly dependent on the buckling resistance of its struts, so this is investigated thoroughly in this section.

Node and actuator masses are not considered to be a dominant factor, and are assumed to scale in the same way as strut mass. Cables are light weight members, and only have a minor contribution to the mass of the structure, so they are assumed to be massless in this section.

According to Euler's formula for a pin-jointed column, given in eqn. (4.3), the buckling load of the struts in the morphing structure can be calculated.

$$F_c = \frac{\pi^2 EI}{L^2} \tag{4.3}$$

Where, F_c is the critical axial load for buckling, E is the modulus of elasticity, I is the second moment of area given in eqn. (4.4), and L is the length of a strut.

$$I = \frac{\pi(d_1^{\,4} - d_2^{\,4})}{64} \tag{4.4}$$

Where, d_1 is the outer diameter of the strut and d_2 is the inner diameter of the strut. In this section a constant ratio $d_2 / d_1 = r_d$ is assumed. Thus, eqn.4.3 can be written as:

$$F_c = \frac{\pi^3 E}{64} \frac{d_1^{\,4}(1 - r_d^{\,4})}{L^2} \tag{4.5}$$

The mass of a tubular strut is calculated based on its geometry, given in eqn.4.6:

$$m_{strut} = \frac{\rho\pi}{4} L d_1^{\,2}(1 - r_d^{\,2}) \tag{4.6}$$

The mass of the morphing structure unit (the full structure in Figure 3.5) can be calculated as in eqn. 4.7, which includes nine struts, ten nodes and six actuators:

$$M = 9m_{strut} + 10m_{node} + 6m_{actuator} \tag{4.7}$$

Struts are believed to be the major contributor to mass change for the scaled morphing structure. The node mass and actuator mass change are assumed to be proportional to strut mass change and generally have less effect on total mass, which is discussed later. So the scaling in the total mass of the struts is used in the analysis to represent the total mass change of the morphing structure.

The scaling analysis in this section only considered wing shear force (lift) changes with plane scale. The bending moment at root changes at a higher exponent because the

center of the lift is moved further away from root when scaled. The wing considered in this section only has a part which is morphing, and that part is assumed to be in the vicinity of the center of the lift.

Case 1: If the linear dimensions of all components of the morphing structure are scaled in the same proportion, *K*, the mass and strength relationship could be estimated by scaling the eqn.4.5-4.7. Strut strength (i.e. failure load) is calculated by eqn.4.8, and total mass for all struts is calculated by eqn.4.9:

$$F_{cs} = \frac{\pi^3 E}{64} \frac{(Kd_1)^4 (1 - r_d{}^4)}{(KL)^2} \tag{4.8}$$

$$M_s = 9 \frac{\rho \pi}{4} (KL)(Kd_1)^2 (1 - r_d{}^2) \tag{4.9}$$

And canceling all constant values, the scaling outcomes are:

$$\frac{F_{cs}}{F_c} = K^2 \tag{4.10}$$

$$\frac{M_s}{M} = K^3 \tag{4.11}$$

where F_{cs} is the critical axial load for buckling after scaling, and M_s is the mass after scaling. The strength of the struts grows with the square of *K,* and mass grows with the cube of *K*. The outcome shows that the structural strength is not enough to support the scaled aircraft weight when all dimensions are scaled in the same factor.

Case 2: As shown in eqn.4.5, the diameter and length of strut members' contribute in different exponents for structural strength. Different scaling factors can be used: *K* for the diameter of the struts *d,* and scaling factor *J* for strut length *L*. Consider a

wing *K* times larger (in both chord, thickness and span directions) than the prototype wing in this thesis. And canceling all constant values, eqn.4.12 is found from eqn.4.5:

$$\frac{F_{cs2}}{F_c} = \frac{K^4}{J^2} \tag{4.12}$$

Eqn.4.12 determines the structural strength change when scaled. The RHS of eqn.4.12 should be similar to K^3, so structural strength grows in a similar rate with the required lift, i.e., $J = K^{0.5}$ is required for sufficient structural strength. Because each unit is smaller, the factor $(\frac{K}{J})^3$ more units are required to fill the same volume as Case 1, and the total mass change for all struts can be calculated from eqn.4.13.

$$\frac{M_{s2}}{M} = K^2 J(\frac{K}{J})^3 = \frac{K^5}{J^2} \tag{4.13}$$

Case 1 can be considered as a special example of case 2, where $J = K^1$. When a strut length scaling factor of $J = K^{0.5}$ is used, adequate strength is maintained, with an increase in structure mass by a factor of *K*. From eqn.4.12 and 4.13, the strength-to-mass ratio of the morphing will always decrease when the wing gets larger (i.e. increased K).

Case 3: The prototype wing proposed and tested in this research has an aspect ratio (AR) of 1.25, which is far smaller than a typical airliner's wing aspect ratio (e.g. 737-800 has an AR of 9.45, A380 has an AR of 7.5). A further scaling case is considered based on Case 2: The chord and thickness of the wing are scaled by *K*, and the span length is scaled by an additional factor K_1 (i.e. span scaled by KK_1), so the scaled wing can have an aspect ratio closer to the typical value. This could be achieved by stacking

K_1 units of the morphing structure along the span, as illustrated in Figure 4.21. The simple example shown has $K_1 = 3, J = K$.

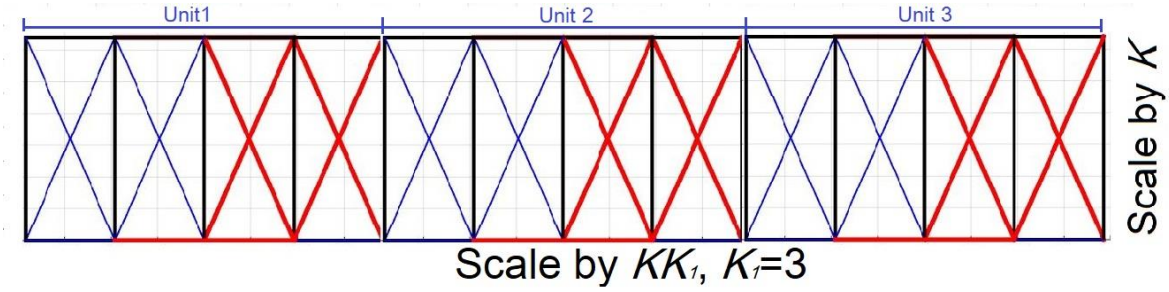

Figure 4.21 Scale using a different span wise factor, top view.

The scale factor K for each unit in case 2 and case 3 are kept the same (i.e. each unit in the two cases is the same size, and case 3 has K_1 times the number of units than case 2). The wing area in case 3 is K_1 times of the wing area in case 2, and as a first approximation, the lift generated is also increased by K_1 times. The structural strength requirement changes in proportion to lift change, so in case 3, the strength also needs to change by a factor K_1, so eqn.4.14 can be written.

$$\frac{F_{cs2}}{F_{cs3}} = \frac{1}{K_1} \tag{4.14}$$

For a strut length scale $J=1$, substitute eqn.4.8 and eqn.4.12 into eqn.4.14. The strut outer diameter change is calculated in eqn.4.15:

$$d_1^{'} = KK_1^{0.25} d_1 \tag{4.15}$$

Where, $d_1^{'}$ is the strut outer diameter in case 3. The total strut mass change is calculated, by substituting eqn.4.15 into eqn.4.13:

$$\frac{M_{s3}}{M} = (KK_1^{0.25})^2 J(\frac{K}{J})^3 = K_1^{0.5} K^5 \tag{4.16}$$

A conclusion can be drawn at this point, that without additional scaling on chord and thickness, only span wise scale change, this results in a total mass change for struts

with exponent of 0.5 of additional span wise scale (a comparison can be made between eqn.4.13 and eqn.4.16). This result cannot be expanded to additional chord and thickness scale, because their behaviors with lift are different.

Apart from structural dimension scaling, the actuation system also needs to be amended for the larger scaled applications. The actuation method should meet aviation industry standards (e.g. 5000psi supply pressure hydraulics), which has a power density far greater than the tested prototype. The relationship between actuator diameter and force is shown in eqn.4.17.

$$F_a = 344.7\pi(\frac{d_a}{2})^2 \times 10^5 \tag{4.17}$$

Where F_a is the maximum force of the actuator in newtons, d_a is the actuator piston diameter in metres, and 5000psi (344.7bar) supply pressure is assumed. A simple example to check the feasibility of hydraulic actuation at 5000psi: an actuator with 120mm bore size has maximum output force of 392kN (40 tons, 1/2 of the maximum takeoff weight of Boeing 737-800), this actuator diameter dimension is feasible to support the whole wing from the wing root, although this would never be necessary in practice. Eqn.4.12 addressed the upper limit for scale factor J of strut length to provide sufficient structural strength. And the lower limit of scale factor J is determined by the actuator axial length, which will be embedded in to the morphing structure. As many as $(\frac{K}{J})^2$ morphing units may be used in the wing root cross section, each of their actuators can be smaller than the one in given in the example as they would not be expected to exert the full shear load at the wing root, making it possible to have smaller dimensions for a single embedded actuator. The actuator selection and design will be

discussed in the future work section in Chapter 8.

The dimensions of the nodes should be kept to a minimum, and not necessarily scaled with the dimensions of the wing, i.e. nodes should be designed for a minimum volume to hold a spherical joint of adequate size for the expected load.

The cable strength is proportional to its cross-sectional area (for the same type of cable), and cable length is determined by strut length. Cables are light weight members compared with struts, and they have minor contribution in the weight change when scaled.

In this section, three scaling cases are investigated: proportional scaling, scaling with different strut lengths, and scaling with additional span length. Generally, when the morphing structure is scaled-up by the same amount in all dimensions, the strength-to-mass ratio reduces, as a result of buckling of the longer struts. Compromises need to be made between the strut diameter scaling and length scaling, so the strength is sufficient to withstand all the scaled lift without too much weight penalty. Also, the result indicates that to build a full morphing wing (capable of morphing from wing root to wingtip) for a large aircraft may not be a good choice. A wing which has a part which is morphing is likely to be the future application for this technology, and the morphing part is suggested to be in the vicinity of the centre of lift (or closer to the wingtip). Morphing control close to the wingtip regions would have a higher efficiency, because they are relatively small size and have good capabilities to change aerodynamic performance. And they are not expected to exert shear force and bending moment of the full wing, which makes it possible for them to be light weight. Detailed scaling and

design issues need to be addressed by future research.

4.6 Signal processing and real-time control environment

The experimental system uses an xPC target environment to implement real-time closed loop control. A National Instruments PXIe-8821 controller is used as the target PC, the experiment was run in the NI VeriStand environment. A control model was built in Simulink and compiled on a host PC then deployed to the target PC. Signals used in the model are listed in Table 4.3. There are 14 analogue input signals and 12 digital output signals used in the model. To generate an accurate PWM signal at 20Hz which is the recommended maximum frequency of the valves, a controller sample rate of 1000Hz was used.

A NI PXIe-6341 data acquisition board (DAQ) is used,with16 analogue input ports (16 bits, range: ±10 V, ±5 V, ±1 V and ±0.2 V), 24 digital I/O ports and 2 analogue ports (range: ±10 V, not used), with a maximum multichannel sample rate of 500kS/s. (National-Instruments 2016)

Table 4.3 specification for signals used in the experiments

Signal	Component	No.	Form
Actuator Displacement	SMAT-8M position transmitters	6	Analogue voltage input
Actuator Pressure	SPTE pressure transmitters	6	Analogue voltage input
Aerodynamic Force	Strain gauges	2	Analogue voltage input
Inlet Valve PWM	V114 valve group	6	Digital voltage output
Exhaust Valve PWM	V124 valve group	6	Digital voltage output

4.7 Wind tunnel

Wind tunnel morphing experiments were carried out in the University of Bath's Large Wind Tunnel, which is a closed loop design, with an octagonal test section, maximum dimensions 2.13 ×1.51 ×2.71m, as shown in Figure 4.21. A Digitron 2020P7 Digital Pressure meter was used to measure the dynamic pressure in the test section through a pitot-static tube. The free stream velocity v can be calculated from:

$$p - p_{\infty} = \frac{1}{2}\rho v^2 \tag{4.3}$$

In which, p is the static atmospheric pressure in lab, p_{∞} is the static pressure in the test section free stream, and ρ is air density. The uncertainty in the velocity measurement was ±0.3 m/s, and the freestream turbulence level at the prototype stand was approximately 0.46%. The prototype wing is mounted on the top frame of the wind tunnel via the force balance introduced in section 4.4, as shown in Figure 4.22. The cables are taped in position to ensure there is no contact between cables and the force balance during the test.

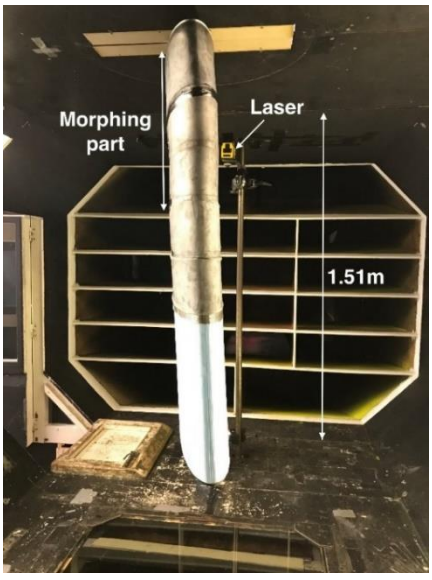

Figure 4.22 Wind tunnel test section and wing

Figure 4.23 Force balance mounted on the wind tunnel frame

4.8 Conclusions

The design of the experimental prototype morphing wing system is introduced in this chapter. This includes, morphing tensegrity design and manufacturing, wing structure construction, and monitoring and controlling hardware. Detailed node and joint design is presented. The new design has increased the tensegrity structure node twisting stability, and created a mounting interface for the wing structure. The structure morphing part is covered with flexible skin, which is load bearing and keeps its aerodynamic shape.

A simulation and multi-body analysis based on the prototype tensegrity structure is presented in Chapter 5. The results for bench-top dynamic tests of the tensegrity structure and wing wind tunnel tests are presented and discussed in Chapter 6 and Chapter 7.

5 Simulation and control scheme

This chapter introduces the modeling of the prototype active tensegrity structure. The modeling contains three parts: pneumatic system, mechanical system and control scheme. The pneumatic valves and actuators were modelled in Matlab®/Simulink®, and the 3D mechanical kinematics modelling was carried out in Matlab®/Simmechanics®. The method for motion and internal load control is also discussed.

5.1 Modeling of Pneumatic Valve and Actuator groups

5.1.1 Modeling of SMC V114/124 3 port solenoid valve

The objective of this section is to calculate the mass flow rate $\dot{m}$ as a function of the valve opening orifice A_t, as A_t is a control variable. The valves modeled in this section are three port solenoid valves. V114 valves will be used to charge the actuators and V124 are used to exhaust. A diagram of a single actuator set-up is shown in Figure 5.1. For each valve, only port 1 and 2 are used in the design, the flow characteristics was given in Chapter4 as seen in Table 4.1.

Both of the valves are used as on/off valves, A_{ti} is valve opening and A_{0i} is the max orifice area of each valve, i = 114 or 124, indicating the valve type. Valves V114 are normally closed and V124 are normal open.(SMC 2015) Port 3 for both V114 and V124 are physically blocked by epoxy adhesive so they will function like on/off valves.

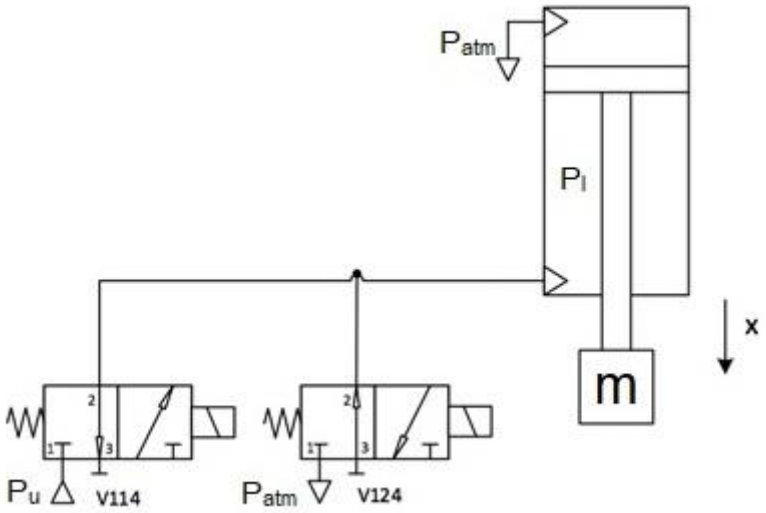

Figure 5.1 Circuit diagram for an actuator pulling a mass block

The maximum orifice areas A_{oi} can be approximated from the flow coefficient C_v (Liptak).

$$C_v = \frac{46250.9}{\sqrt{1-n^4}} C_d D_o^2 \tag{5.1}$$

Where n is the ratio of orifice to pipe size, $n=D_o/D_l$, and C_d is the discharge coefficient, for an orifice plate C_d= 0.61. D_o is the valve orifice diameter and D_l is the pipe diameter (in mm). D_o is normally a small number compared with D_l so n = 0 is assumed in this section. By applying the parameters in table 4.1 to equation (5.1), the approximated circular orifice area of the valves can be calculated:

$$A_{o114} = 0.2227 mm^2$$

$$A_{o124} = 0.4174 mm^2$$

As suggested by Tressler (2002), mass flow rate of air going into a pneumatic cylinder can be expressed as a function of the upstream pressure P_u which is the supply pressure, the downstream pressure P_l which is the pressure in the chamber, and the

valve opening A_t. This could be written as:

$$\dot{m}_1 = \gamma_{114}\sqrt{\frac{k}{RT}}P_u A_{t114} \tag{5.2}$$

For air, heat capacity ratio k =1.4, Individual Gas Constant R = 287J/kgK, and in this case an isothermal process is assumed, so the system temperature is constant, and assumed to be T= 298K.

Now two cases should be considered: whether the flow is choked or not choked. For the inflation valves the situation is determined by comparing the chamber pressure to supply (upstream) pressure ratio, with the valve critical pressure ratio b:

While $\frac{P_l}{P_u} > b$, the flow is not choked, and γ in equation 5.2 is:

$$\gamma_{114} = \sqrt{\frac{2}{k-1}}\left(\frac{P_l}{P_u}\right)^{\frac{k+1}{2k}}\left[\left(\frac{P_l}{P_u}\right)^{\frac{1-k}{k}} - 1\right]^{\frac{1}{2}} \tag{5.3}$$

The flow is choked when $\frac{P_l}{P_u} \le b$, and the pressure at the orifice P_l will stay constant and equal to bP_u. In this case γ is a constant, which only depends on the valve property, and it can be determined by substituting $\frac{P_l}{P_u} = b$ into equation 5.3.

$$\gamma_{114} = 0.3161 \tag{5.4}$$

For air exhausting from the cylinder, consider the pressure in the cylinder chamber P_l as the upstream pressure, and atmospheric pressure P_{atm} as downstream pressure. Equation 5.2 can be written as:

$$\dot{m}_2 = \gamma_{124}\sqrt{\frac{k}{RT}}P_u A_{t124} \tag{5.5}$$

If $P_{atm} > bP_l$ then the flow is not choked;

$$\gamma_{124} = \sqrt{\frac{2}{k-1}\left(\frac{P_{atm}}{P_l}\right)^{\frac{k+1}{2k}}\left[\left(\frac{P_{atm}}{P_l}\right)^{\frac{1-k}{k}} - 1\right]^{\frac{1}{2}}} \tag{5.6}$$

If $P_{atm} \leq bP_l$ then the flow is choked;

$$\gamma_{124} = 0.5378 \tag{5.7}$$

The total mass flow rate going into the cylinder is:

$$\dot{m} = \dot{m}_1 - \dot{m}_2 \tag{5.8}$$

A first order lag is used to simulate the response of the valve, and a time constant T_c=0.003s is assumed based on the valve response time given in the data sheet(SMC 2015),

$$G(s) = \frac{1}{T_c s + 1} \tag{5.9}$$

Valve control signals are PWM signals, $r_i(t)$, for which 0 indicates off, and 1 indicates on. Dynamic valve opening orifice area could be approximated as a function in time domain, for example the inlet valve orifice area is modelled:

$$A_{t114} = r_{114}(t)\left(1 - e^{-t/T_c}\right)A_{o114} \tag{5.10}$$

5.1.2 Modeling of FESTO DSNU25-25 Pneumatic Actuator

In section 5.1.1 equations for the mass flow rate going in and out of the pneumatic cylinder are established. In this section, equations for actuator forces are summarized. The actuator model described in this section is a FESTO DSNU standard round cylinder, with inner diameter 25mm, and stroke l_s = 25mm. The piston area A_1= 4.91cm^2, and annulus area A_2= 4.11cm^2. The ADN compact cylinders, which are also

used in the prototype (details introduced in Chapter 3 and 4) have same working principle as the standard round cylinder, only different in outer dimensions and connectors, and will be discussed in the next section. A block diagram of cylinder modelled in this section is shown in Figure 5.2, assuming an extending situation. The center of the stroke is defined as x=0, and extension is positive. Assuming ideal gas behavior,

$$\dot{P}_l = \frac{kRT}{V_2}\dot{m} - \frac{kP_l A_2}{V_2}\dot{x} \tag{5.11}$$

where V_2 is the volume of the annulus chamber:

$$V_2 = \left(\frac{l_s}{2} - x\right) A_2 \tag{5.12}$$

and T will be assumed to be constant.

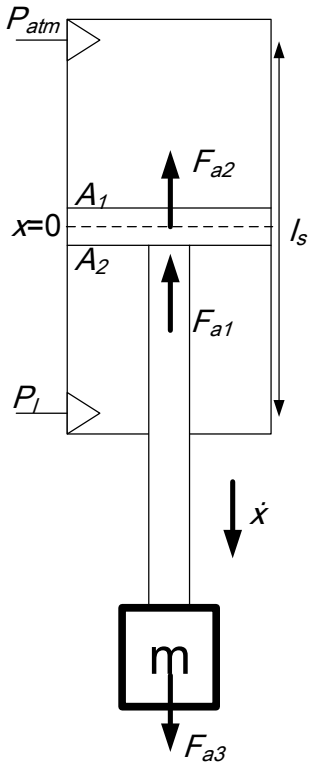

Figure 5.2 Actuator diagram defining notation

In this section, three kinds of force are considered affecting the displacement.

First, consider the force due to the pressure difference in the two chambers. Since the actuator is used as single acting for pulling, we have:

$$F_{a1} = -P_l A_2 \tag{5.13}$$

Second we have the Coulomb friction force and viscous forces

$$F_{a2} = \mathrm{sgn}\left(\dot{x}\right) k_c + k_v \dot{x} \tag{5.14}$$

The coulomb friction is k_c= 3N found through the experiment results, and the viscous friction coefficient of piston k_v = 180 N/(m/s). And F_{a3} is the external load applied on the piston rod.

Newton's law is applied to complete the actuator model:

$$\ddot{x} = \frac{1}{m}\left(-F_{a1} - F_{a2} + F_{a3}\right) \tag{5.15}$$

5.2 Multi-body modeling for active tensegrity structure

In this section, a simulation of the proposed active tensegrity structure is presented. The dynamic model of the mechanical system is built in Matlab®/SimMechanics®. The simulation was carried out with the ODE15s variable-step solver at early stages of this research, when joint friction was not taken into consideration. The solve duration had become infeasible with variable-step solvers when friction was added (e.g. 10min simulation duration only simulated 0.002s in SimMechanics). The fixed-step solver was selected as an alternative option. For frictionless models, the fixed-step solvers and variable-step solvers successfully solved the model, and generated similar results.

For the model with friction, the fixed-step solvers were giving credible results compared with experimental results. The numerical integration presented in this Chapter uses the ODE1 Euler solver with a time step of 0.00005s, for a stable solution, fast progress and reasonable accuracy.

The actuator degrees-of-freedom are modelled as a cylindrical joint, which enables two solids to move both prismatically along an axis and revolve around the same axis. The actuator joint was actuated by an input force form the valve and actuator model introduced in section 5.1, and motion outputs were derived by SimMechanics, which include the axial displacement (x) and axial velocity. Rod end bearings and crimped cables are modelled as frictionless spherical joints.

The ball-in-socket spherical joints between struts and nodes are modeled as spherical joints with friction (shown in Figure 5.3), friction torques are given as shown in Table 5.1, which are determined individually by empirical methods. In this case joint friction is assumed to be proportional to the compression force on joint.

Solid bodies are designed in Inventor 2018 as introduced in Chapter 4, and imported into SimMechanics, thus the inertial properties of all components are given by the CAD design. Detailed inertia parameters for major components are listed in Table 5.2. Figure 5.4 is a visualization of the tensegrity structure simulated in SimMechanics.

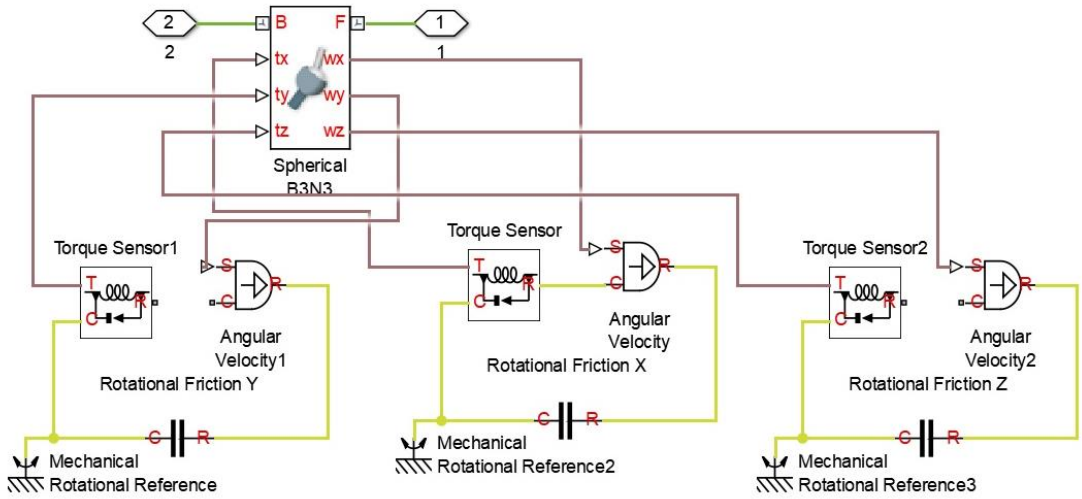

Figure 5.3 Spherical joint for strut-to-node joint

Table 5.1 Joint friction torque on node joints

	140N internal load	70N internal load	Unit
Breakaway (Same for X, Y and Z axis)	4	2	Nm
Rotational X	0.15	0.075	Nm
Rotational Y	0.15	0.075	Nm
Rotational Z	0.5	0.25	Nm

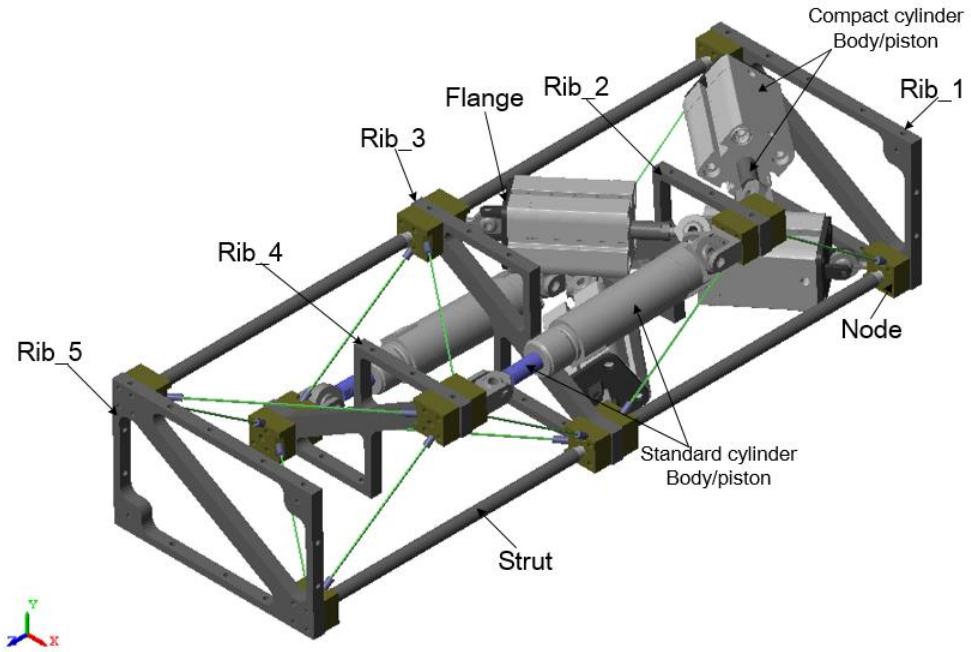

Figure 5.4 Simulated structure in neutral position isometric view

Table 5.2 Physical parameters in multi-body simulations

Part	Mass (g)	Moment of Inertia $[I_{xx}, I_{yy}, I_{zz}]$ $(g \cdot cm^2)$	Product of Inertia $[I_{yz}, I_{zx}, I_{xy}]$ $(g \cdot cm^2)$
Rib_1	255.5	[2200,4696,6787]	[0, 0, -31.4]
Rib_2,Rib_4	71.4	[674,1159,1802]	[0, 0, -720]
Rib_3	74.5	[713,1187,1869]	[0, 0, 706]
Rib_5	104.5	[1141, 2691, 3788]	[0, 0, 220.36]
Strut	11.6	[1.42, 370, 370]	[0, 0, 0]
Compact cylinder body/piston	180.2 53.5	[514, 2723, 2739] [23.1, 798, 798]	[0, 28, 0] [0, 0, 0]
Standard cylinder body/piston	182.3 74.2	[173, 9573, 9577] [25.6, 2591, 2591]	[0,0,-3.72] [0, 0, 0]
Node	4.9	[4.73, 4.07, 3.95]	[-0.5, 0, 0]
Flange	12.4	[14.4, 15.0, 26.1]	[0, 0, 0]

5.3 Control scheme

For the active tensegrity structure proposed in, a closed loop control method for motion and pre-stress control is presented in this section. The multi-axis control scheme is shown in Figure 5.5. It has been developed according to a general co-ordinate transformation framework for multi-axis motion control (Plummer 2010), which was proposed for application to active tensegrity structures in (Plummer and Lai 2015).

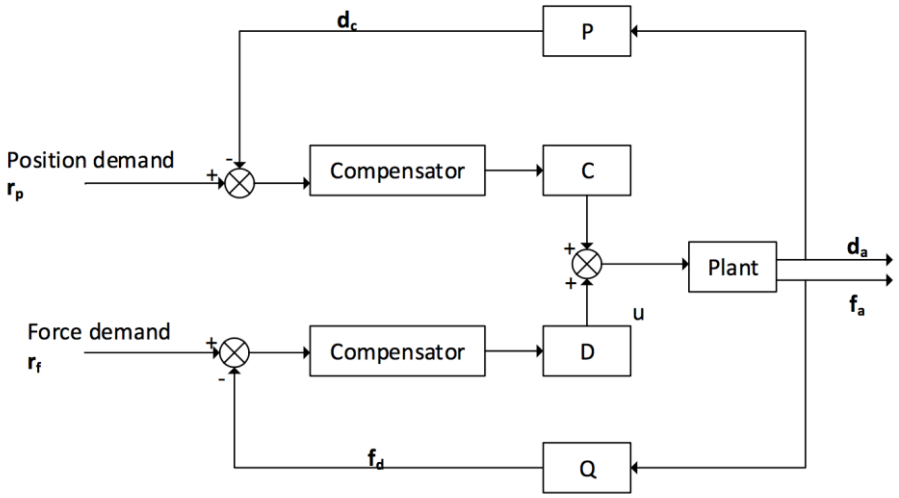

Figure 5.5 Control scheme for the discussed structure

All actuators are single acting actuators working antagonistically as groups, which makes it possible to control both motion and the internal force (i.e. pre-stress) independently. A total of *d* closed loop position loops is necessary, and (*a-d)* force control loops, where *a* is the number of actuators and *d* is the number of independent degrees-of freedom.

For position control, the position demand is in workspace co-ordinates, and defines the desired deviation from the structure's neutral position with a vector $\mathbf{r}_p \in \Re^{d\times 1}$. Position feedback is measured via the position transmitters on the actuators, given vector $\mathbf{d}_a \in \Re^{a\times 1}$ .The transformation matrix $\mathbf{P} \in \Re^{d\times a}$ defines the workspace position control coordinates, so the measured displacements are transformed thus:

$$\mathbf{d}_c = \mathbf{P}\mathbf{d}_a \tag{5.16}$$

where,

$$\mathbf{d_c} = \begin{pmatrix} \theta \\ \phi \\ \psi \\ \varphi \end{pmatrix} \quad \mathbf{d_a} = \begin{pmatrix} x_1 \\ x_2 \\ x_3 \\ x_4 \\ x_5 \\ x_6 \end{pmatrix}$$

In this case sets of weighted actuator position differences are used to define the matrix **P**, substituting the dimensions of the prototype into a linearized form of the equations introduced in Chapter 3 (equation 3.35), P can be written as:

$$\mathbf{P} = \begin{pmatrix} -0.4545 & 0.4545 & 0.4545 & -0.4545 & 0 & 0 \\ -0.1667 & 0.1667 & -0.1667 & 0.1667 & 0 & 0 \\ 0.1365 & 0.1365 & -0.1365 & -0.1365 & 0 & 0 \\ 0 & 0.1667 & -0.1667 & 0 & 0.1872 & -0.1872 \end{pmatrix} \tag{5.17}$$

The first row of **P** defines the twist motion θ of the structure, the second row defines the bending motion ϕ, the third row defines the sweep motion ψ, and the last row is the remaining degree of freedom φ. In all experiments the demand for φ is set to 0, and the lengths of AC_5 and AC_6 are therefore determined using the last row of **P**. Each column controls an actuator, actuators are numbered as shown in Figure 5.6.

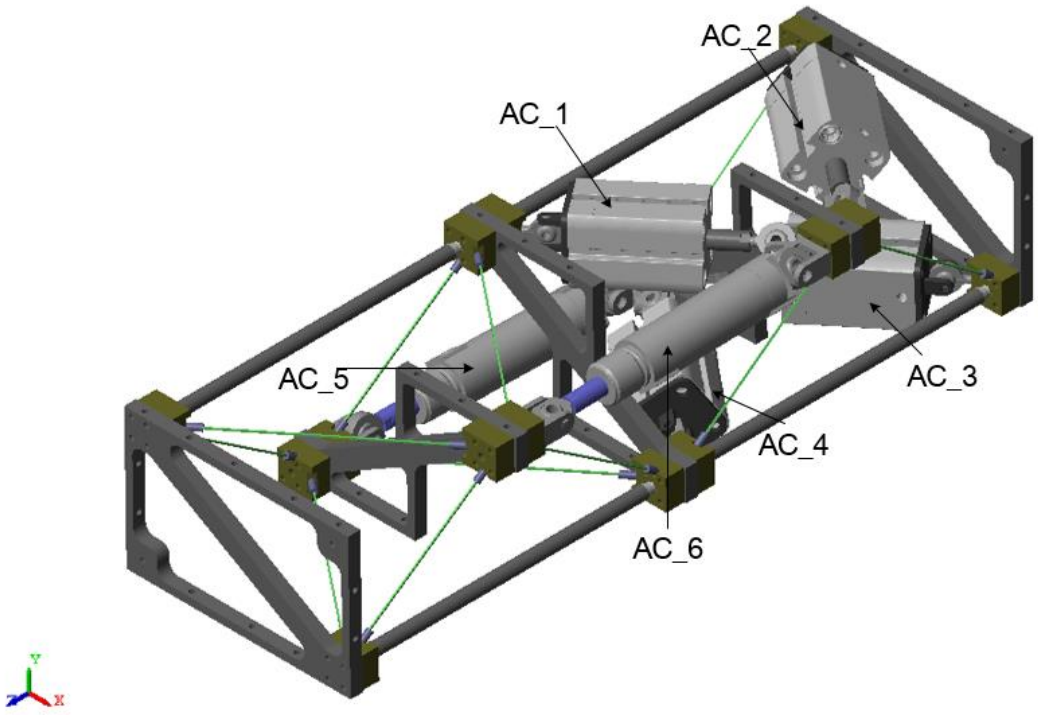

Figure 5.6 Actuator orientation in model

As shown in Figure 5.5, $\mathbf{d_c}^{d\times 1}$ is the virtual feedback transformed from $\mathbf{d_a}$. The conversion from structure position control variables back to actuator coordinate space can be achieved by using a matrix **C**, which satisfies:

$$\mathbf{PC} = \mathbf{I_d} \tag{5.18}$$

Where $\mathbf{I_d}$ is the identity matrix of dimension *d*. One solution is to choose **C** to be the pseudo inverse of **P**:

$$\mathbf{C} = \mathbf{P}^{\mathrm{T}}\left(\mathbf{P}\mathbf{P}^{\mathrm{T}}\right)^{-1} \tag{5.19}$$

Which gives in this case:

$$\mathbf{C} = \begin{pmatrix} -0.5501 & -1.4997 & 1.8315 & 0 \\ 0.5501 & 1.4997 & 1.8315 & 0 \\ 0.5501 & -1.4997 & -1.8315 & 0 \\ -0.5501 & 1.4997 & -1.8315 & 0 \\ 0 & -1.3355 & -1.6309 & 2.6709 \\ 0 & 1.3355 & 1.6309 & -2.6709 \end{pmatrix} \tag{5.20}$$

As previous stated, (*a-d)* force loops are necessary for a closed loop control, therefore the force demand vector is $\mathbf{r_f} \in \Re^{(a-d)\times 1}$. Force feedback is estimated via the pressure sensor on the actuator, so $\mathbf{f_a} \in \Re^{a\times 1}$. A transformation matrix $\mathbf{Q} \in \Re^{(a-d)\times a}$ for the force control loop is required, to average the tension force of selected groups of antagonistic actuators, so:

$$\mathbf{f_d} = \mathbf{Q}\mathbf{f_a} \tag{5.21}$$

Where,

$$\mathbf{f_d} = \begin{pmatrix} f_{d1} \\ f_{d2} \end{pmatrix} \quad \mathbf{f_a} = \begin{pmatrix} P_{l1}A_2 \\ P_{l2}A_2 \\ P_{l3}A_2 \\ P_{l4}A_2 \\ P_{l5}A_2 \\ P_{l6}A_2 \end{pmatrix}$$

Q should be the null space of **P** (Plummer and Lai 2015), which is not unique, and in this case **Q** is chosen as:

$$\mathbf{Q} = \begin{pmatrix} 1/4 & 1/4 & 1/4 & 1/4 & 0 & 0 \\ 0 & 0 & 0 & 0 & 1/2 & 1/2 \end{pmatrix} \tag{5.22}$$

With this choice the first row of **Q** controls the average tension force in the unit cell containing actuators 1 to 4. The second row controls the average force in AC_5 and AC_6. Also the conversion from force control components to actuator coordinate can be achieved using D:

$$\mathbf{D} = \mathbf{Q}^{\mathrm{T}} \tag{5.23}$$

Diagonal PID (proportional-integral-derivative) compensators are used, giving control signals regulated between -1 and +1. Signal values from 0 to 1 indicate the duty cycle of the supply valve opening where 1 is 100% open for V114. Signal values from -1 to 0 indicate the duty cycle of the exhaust valve opening, where -1 is 100% open for the V124 valve.

Two Pulse-Width-Modulation (PWM) generators give on/off signals at 20Hz frequency, which is the maximum operation frequency for the valves. Proportional and integral gains are tuned experimentally.

5.4 Simulation results

In this section simulation results under different motion demands are given (square and sine) to validate the control method proposed in this chapter, and further investigate the dynamic performance of the morphing structure under different internal load (140N and 70N). To be consistent with the bench top test conditions, twist signals of 0° to 12° are given, and bend demands are from 0° to 8°. Settings for the PID controller used in the simulation are shown in Table 5.3

Table 5.3 Controller settings for simulation

	Values	Unit
Proportional gain in motion loop K_p	8	1/deg
Integral gain in motion loop K_i	0.001	1/(degs)
Derivative gain in motion loop K_d	0.045	s/deg
Proportional gain in force loop K_{pf}	0.1	1/N
Integral gain in force K_{if}	0.0001	1/(Ns)

5.4.1 Motion control with square wave demand

In this series of experiments the structure motions were controlled by a square wave demand signal of 0.2Hz, between twist angles of 0° and 12°, and bend angles of 0° and 8°. Figure 5.7 and 5.8 illustrates the simulated model in twist and bend. Figure 5.9 illustrate the twist deformation with 140N and 70N average internal load for each set of actuators, and Figure 5.10 illustrates the bend deformations.

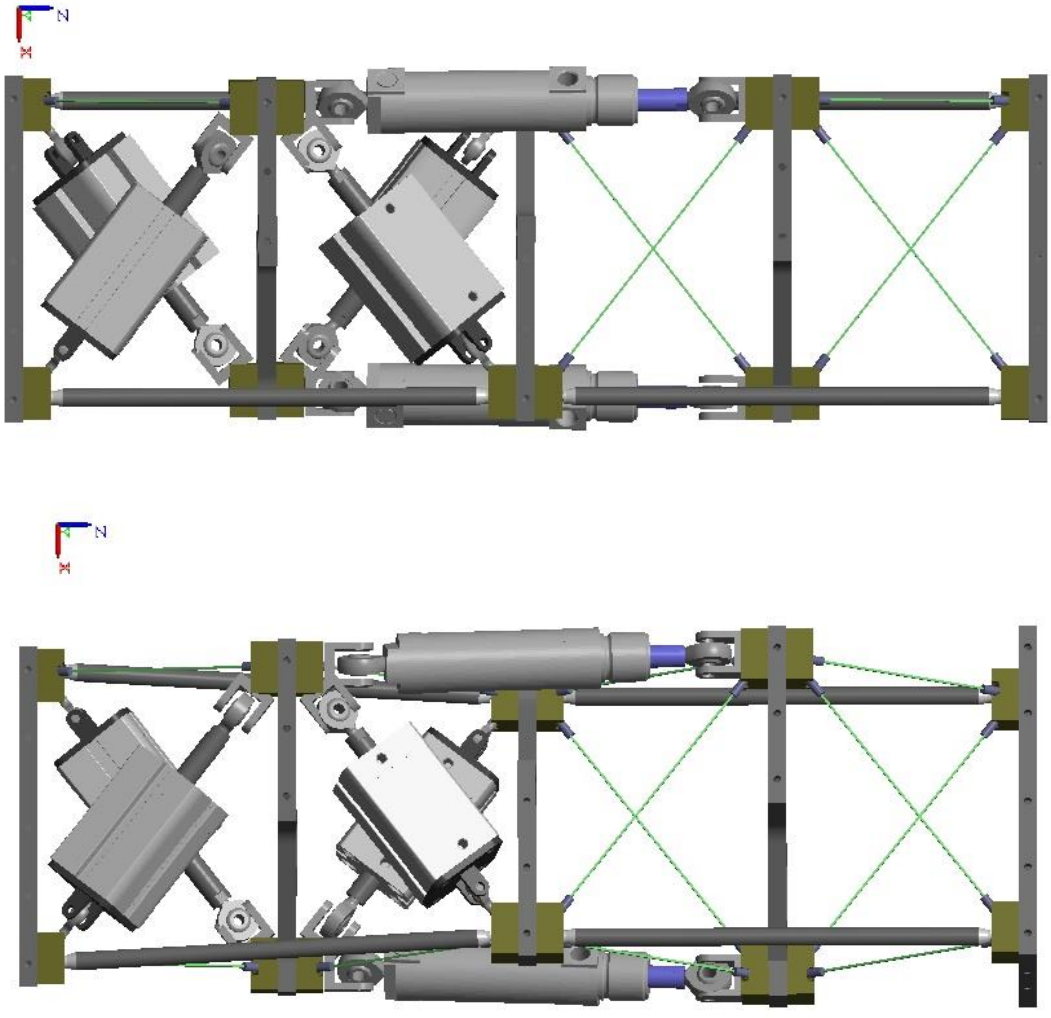

Figure 5.7 Simulated structure top view with neutral (top) and 12° twist (bottom)

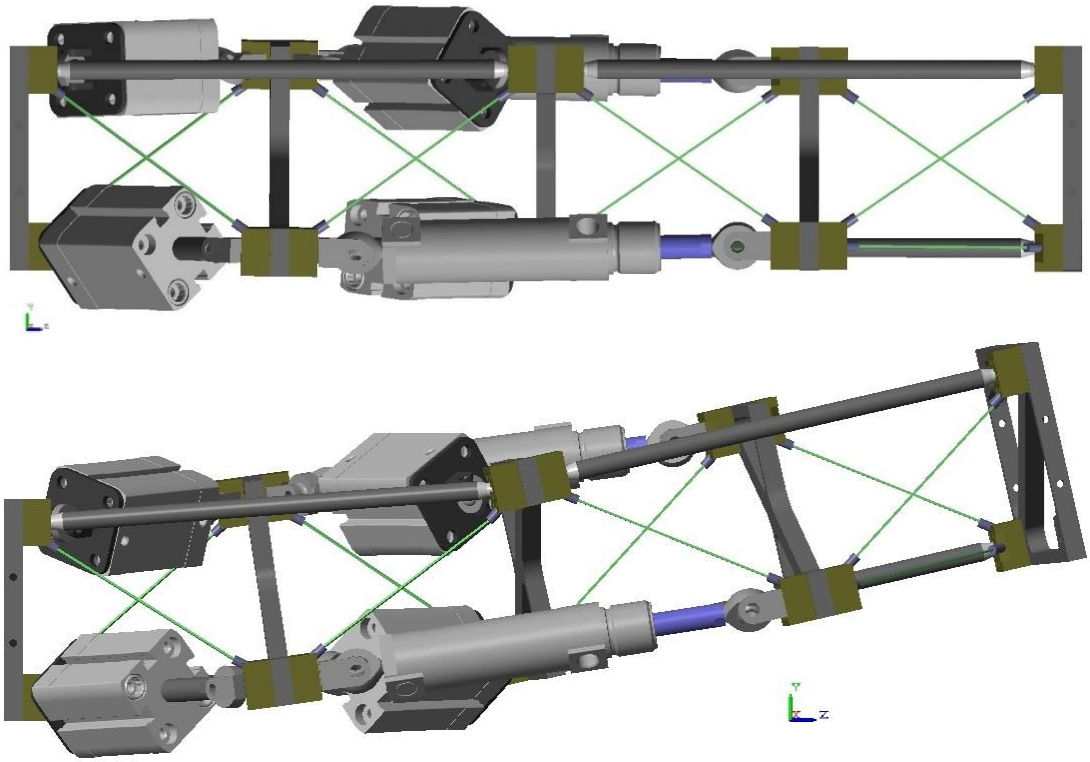

Figure 5.8 Simulated structure front view with neutral (top) and 8°bend(bottom)

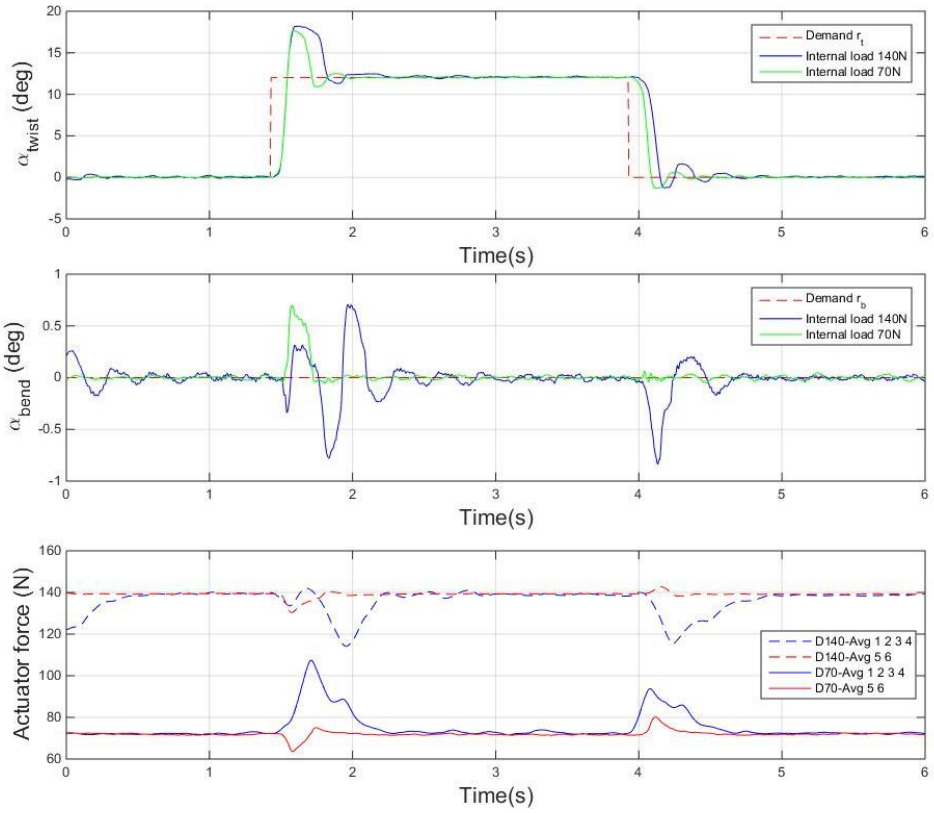

Figure 5.9 Simulation results with square wave twist demand of 12°

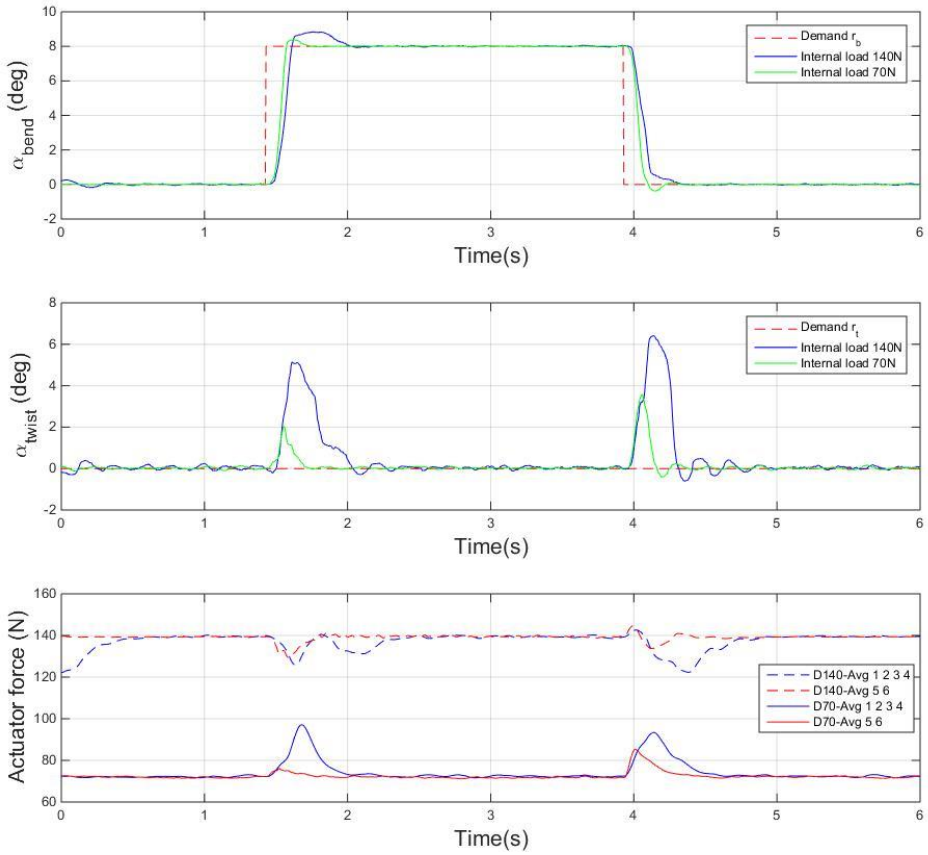

Figure 5.10 Simulation results with square wave bend demand of 8°

The motion responses are reasonably fast and accurate for both internal load cases. For twist motion responses, the rise time (10%-90%) is the same for both internal load cases, with 0.05s rising time and 200°/s twist rate. Overshoot is 47% for the 70N internal load case and 52% for 140N case which is also close, but the dynamics of the response was different, in some results (Figure 5.9, 1.6-1.9s). In the backward twist stage (Figure 5.9, 3.9-4.5s), the structure takes more time to settle down in the high internal load case, and there is also a phase delay of 0.45s, though the twist rates are the same for the two cases. It is believed that the joint friction is the major factor cause the dynamic difference. The cross coupled bend during transit is greater in the140N case, which is also a result of the long settling time.

For the bend motion response, the rising time (10%-90%) is slightly different for different internal load, results in 0.067s rising time and 95.5°/s bend rate for 70N internal load case and 0.009s rising time and 70.9°/s bend rate for 140N internal load. Overshoot is at maximum 4.94% for 70N internal load case and 10.46% for 140N case, and the dynamic behaviour for the overshoot part is similar to the twisting response, with the higher load cases giving longer settling time. For the backward bend stage, the bend rate for the lower load case is greater, and there is no major phase delay observed in bend motion control.

The force control loop has successfully maintained the demanded average actuator force in both cases. There is some disturbance on the averaged actuator force, when the structure is deforming. The disturbance tends to be a rising for the 70N case and a sinking for the 140N case. The acceleration of the structure is determined by the tensile force difference in the actuators. For 140N load case, the higher tensile force actuator pair is reaching maximum tensile at 247N, while the controller is still demanding larger force difference, the low tensile force actuator pair is further exhausting for lower pressure, results in averaged actuator force dropping. It is only possible for the controller to maintain the demanded average actuator force precisely when the structure is in steady state or slow motion, or at a cost of compromising the dynamic performance of the structure.

5.4.2 Motion control with sine wave demand

A sinusoidal position demand was given to the structure, to investigate the dynamic behaviour of continuous motion at a slow deformation rate, as well as the ability of

maintaining demanded internal load in such conditions.

The sinusoidal position demand was 0.1 Hz for all simulations, with amplitude of 6° for twist, and 4° for bend. Internal loads are set to 140N and 70N to test the ability for the control system to maintain the load in continuous motion. Figure 5.10 illustrates the twist deformation with 140N and 70N average internal load, and Figure 5.11 illustrates the bend deformations. Results on different internal levels are plotted with 1s phase lag to avoid over lapping and give a clear view.

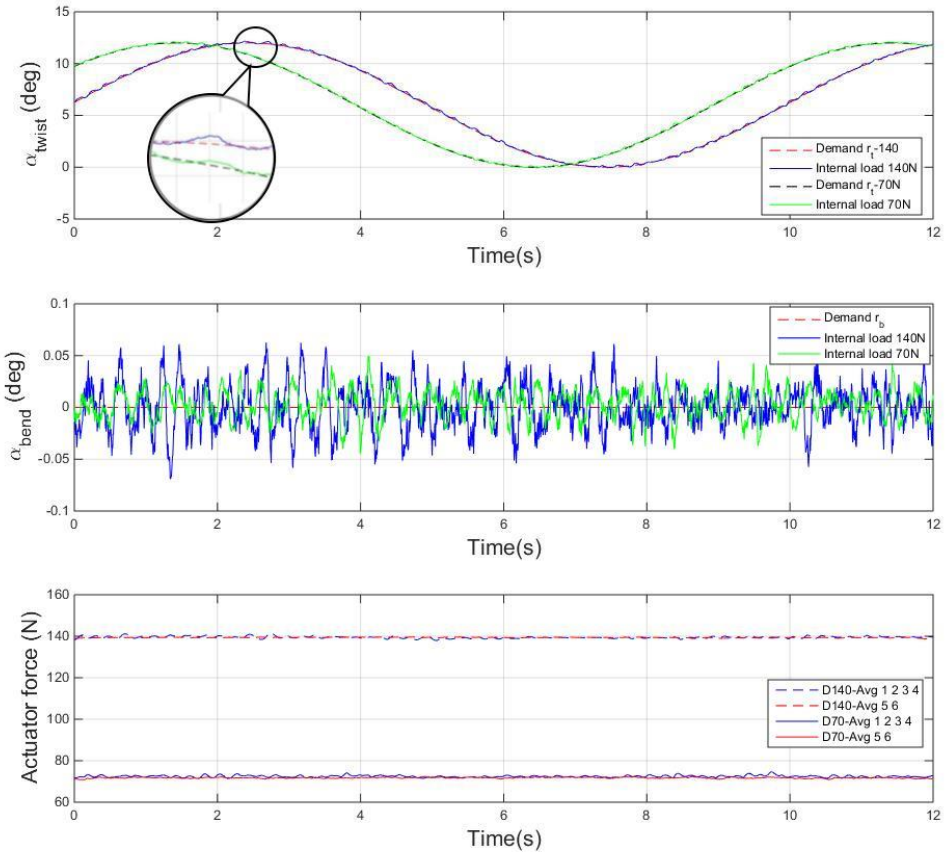

Figure 5.11 Simulation results with sine wave twist of 6° (around 6° baseline)

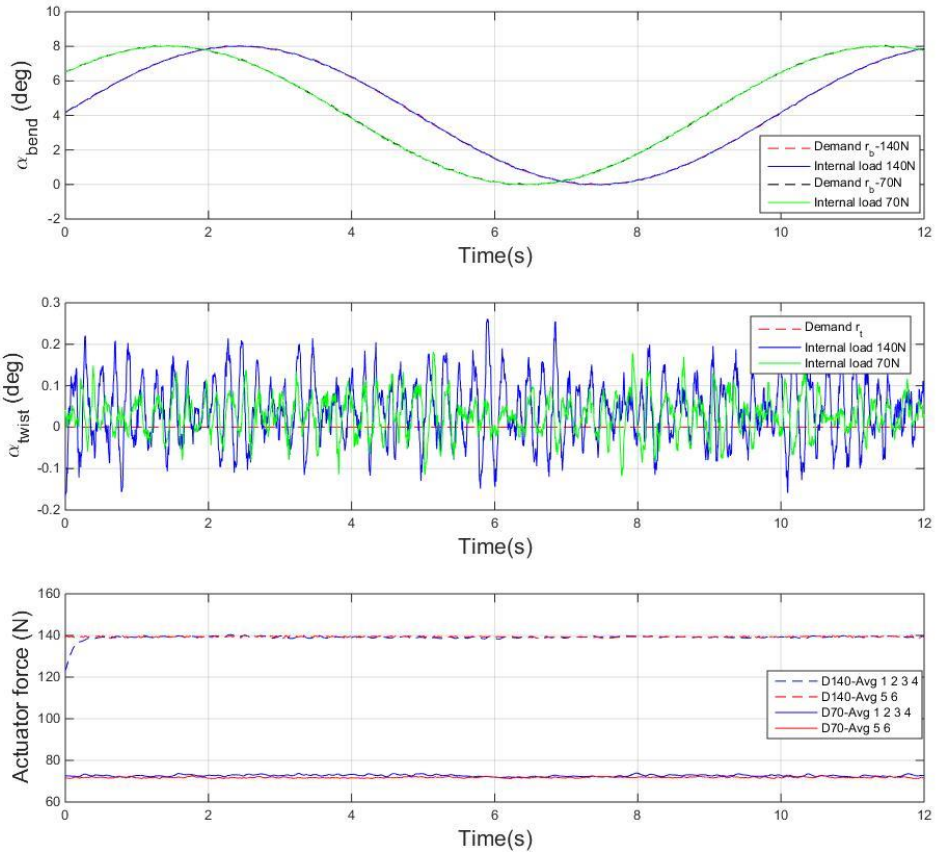

Figure 5.12 Simulation results with sine wave bend of 4° (around 4° baseline)

The simulation result gives a good matching with the demand in both cases. In the twist cases un-smoothness could be observed (detailed view in Figure 5.11), and in high internal condition case (blue line), the un-smoothness is more obvious than the low load case (green line). The twist response acts like a stick-and-slip motion which is typically caused by friction. In the bend case, there's no obvious un-smoothness in the main controlled DOF, for both internal load levels.

Continuous motion with sine wave also causes continuous cross coupled motions in small amplitude. The cross coupled bending (Figure 5.11 mid), lies between ±0.05°, and higher load level results in higher cross coupled motion. The cross coupled twisting (Figure 5.12 mid), lies between ±0.2°, compared with the step response result,

(Figure 5.9 and 5.10 mid), the cross coupled motions amplitude has a positive correlation with motion rate (slope). The coupled twist has a larger amplitude than bend in overall.

As introduced in last subsection, the disturbance on the averaged actuator force is determined by the deformation rate of the structure (motion error in this case), and the saturation limit for the actuator (0-247 N tensile force limit). In the sine wave motion case, the deformation rate is generally low, which results in a nearly constant averaged actuator force level.

5.4.3 Comparison between simulation and experimental motion control results

The simulation results are compared with samples of experimental results (sensor measured displacement) in this section. Detailed experimental results are introduced in Chapter 6.

Figure 5.13 compares the step twist response simulation and experimental results, with 140N internal load demand, and Figure 5.14 compares the results with 70N internal load. For the prefix in the legends, S stands for simulation, B stands for bench top test.

For the step twist response the experimental and simulation result matches reasonable well at both internal load levels. It is believed that the errors are caused by the imperfection of joint friction model. In the simulation the struts-to-node joint friction are pre-determined constant values, while in experimental practice the joint could be very dynamic, which changes the friction with the compression force vector applied on the socket. Figure 5.15 compares the step bend response simulation and experimental

results, with 140N internal load demand.

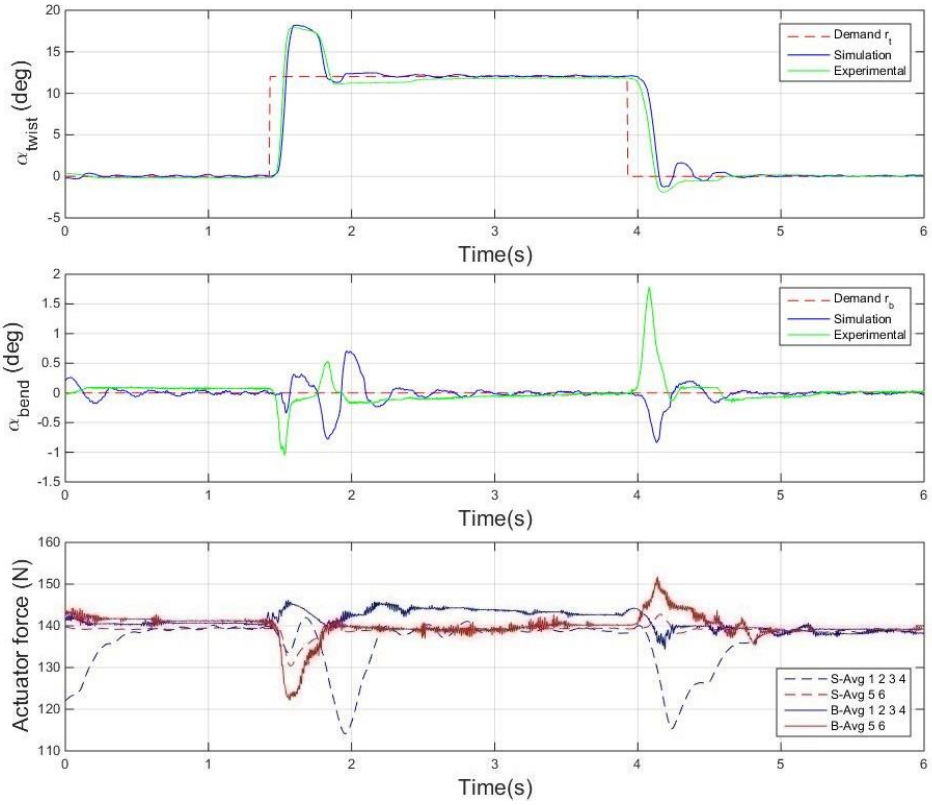

Figure 5.13 Results with step twist demand and 140N internal load

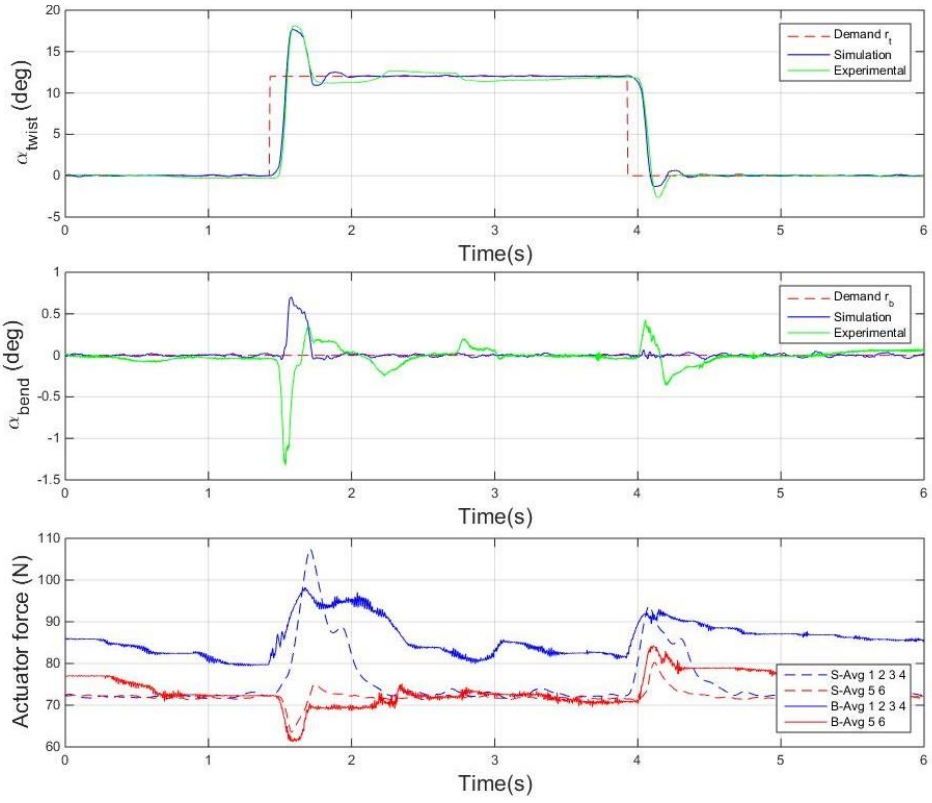

Figure 5.14 Results with step twist demand and 70N internal load

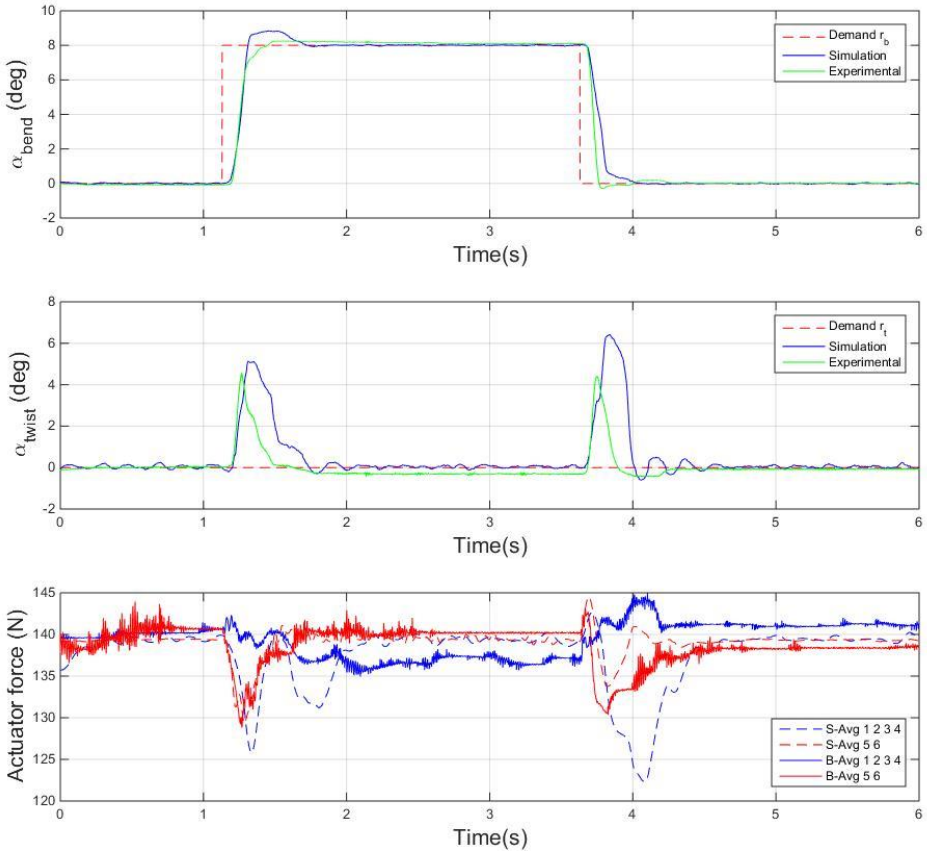

Figure 5.15 Results with step bend demand and 140N internal load

The simulated bend motion matches the experimental result reasonable well as shown in Figure 5.15. The comparison between Figure 5.13 and 5.15 provides further evidence for the previous hypothesis, that joint friction torques are affecting the twist and bend motion differently, as the dynamics on increasing displacement are very different for the two deformation modes. The cross coupled twist is greater in amplitude in both simulation and experimental results, which agrees with the previous results. This might be caused by the natural difference of two deformations; for the twist the pivot axis lies close to the centre of gravity and the product of inertia is low

on that axis, for bend motion the centre of gravity shifts significant with the motion, and product of inertia is higher, which makes the disturbance of coupled motion larger. The twist and bend deformation with sine wave demands are shown in Figures 5.16 and 5.17.

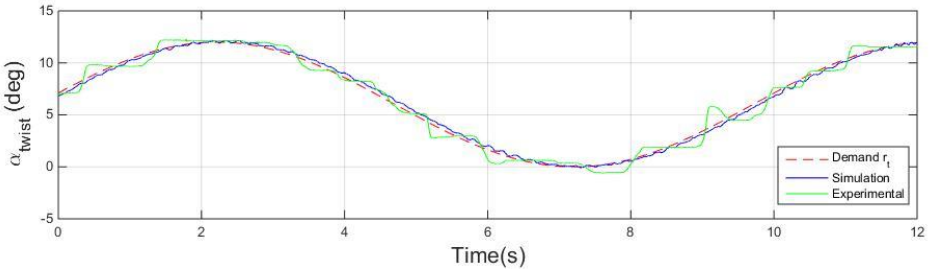

Figure 5.16 Simulation and experimental results with sine wave twist demand and 140N internal load

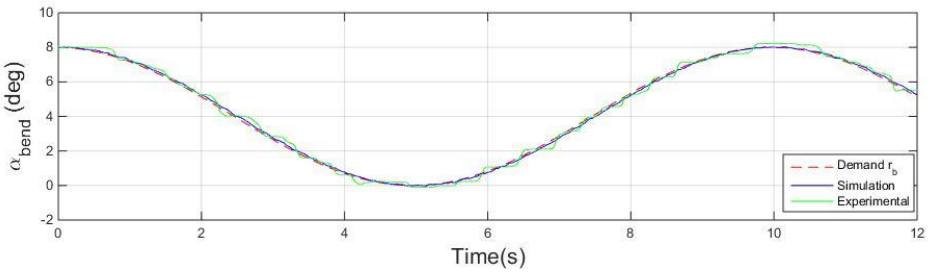

Figure 5.17 Simulation and experimental results with sine wave bend demand and 140N internal load

The experimental response shows signs of the stick-and-slip motion in Figure 5.11, but at a much larger scale. As discussed in section 5.1, the valve model used in this simulation does not include a detailed dynamic model. The valve dynamic response is approximated by a first order lag with time constant of 3ms, which is the response time of the valve as stated in documentation(SMC 2015), as no further information on opening response is provided by the manufacturer. The approach agrees well with

step or square wave experimental results of large amplitude, but for the continuous slow motion of the sine wave, the model does not work as well. The valves should rapidly switch on/off, as commanded by the PWM signals, when the error between demand signal and motion response is tiny, which makes the valve stay in a dynamic 'half open' stage. The intermediate stage is not included in the simulation. Also the time needed for a valve to fully open or close may be larger than the given response time of 3ms, making the experimental system respond slower as well. Comparison with a simulation using a valve time constant T_c=10ms is presented in Figure 5.18 and 5.19, to investigative the effect of the valve response lag on the motion. The result proves that continuous slow motion is more sensitive to the valve response change. Future research will be focused on the effect of dynamic behaviour of the valve on the motion of the tensegrity structure.

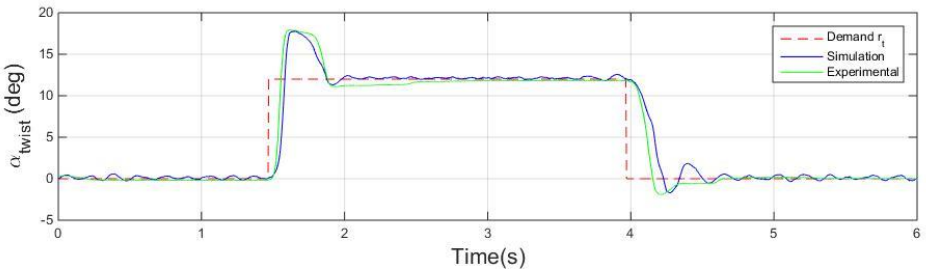

Figure 5.18 Results with step twist demand and 140N internal load, T_c=10ms

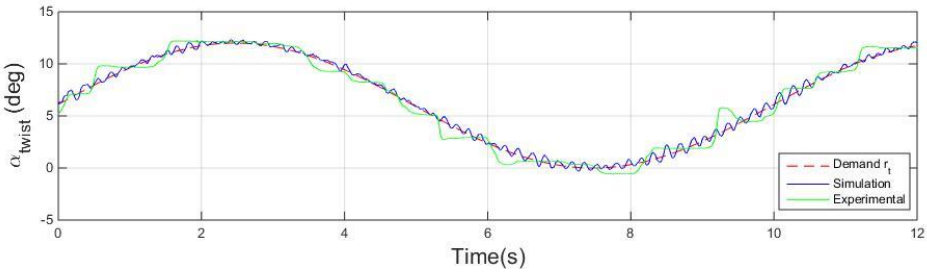

Figure 5.19 Results with sine twist demand and 140N internal load, T_c=10ms

5.5 Conclusions

The structure proposed and built in Chapter 3 and 4 was modelled in this chapter. A detailed 3D simulation model is built in Matlab®/SimMechanics® to study and verify the control scheme proposed in this chapter. Simulations are carried out with step and sine wave motion demands on different internal load levels. Results are compared with experimental result samples, with a generally good agreement. Detailed experimental results are introduced in Chapter 6.

6 Motion and internal load control of active structure

The experimental results from testing the morphing of the proposed tensegrity structure will be shown and discussed in this chapter. The experiments were carried out to justify the kinematic module and control methods presented in Chapter 3 and Chapter 5. An investigation of the dynamic performance of the pre-loaded structure and control method refinement are also included.

Twisting and bending motions were tested separately to validate the actuator behaviour in different modes. Based on the initial results, a study on the effect of member elasticity on motion was presented. The kinematic model was refined and tested, and the structure was reinforced with higher grade tensile members for subsequent wind tunnel testing. Figure 6.1 shows the prototype structure on demanded twist (15°) and bend (8°) positions.

Figure 6.1 the prototype structure with neutral (left) twist (mid) and bend (right)

6.1 Motion control with fixed internal load

A supply pressure of six bar was used for all the experiments. Zero dead-band was given for both deformation modes, and 5N dead-band was given for both force loops, to avoid continuous adjusting due to internal load error, control parameters were selected as shown in Table 6.1. For the gain tuning method for motion control; a fast response was preferred, so proportional gain was increased, until there was no significant change on rising time. Proportional gain tuning resulted in a fast response with large overshoot, so derivative gain was increased to decrease the overshoot. The derivative gain was increased until a significant high frequency oscillation happened, and was tuned around that point. Integral gain was introduced to produce small steady-state-error within short enough time. Fine tuning was done empirically following the described method. Gains for the force control loop were selected to ensure that both loops contributed similarly to the final controller output signal. Results determined in the control loop from transformed actuator positions (see equation 5.16), are compared with results from the independent motion tracking system (labelled Opti-track).

Table 6.1 Controller settings for benchtop test

	Values	Unit
Proportional gain in motion loop K_p	8	1/deg
Integral gain in motion loop K_i	0.03	1/(degs)
Derivative gain in motion loop K_d	0.01	s/deg
Proportional gain in force loop K_{pf}	0.1	1/N
Integral gain in force K_{if}	0.0001	1/(Ns)

6.1.1 Motion control with square wave demand

Figure 6.2 to Figure 6.4 show results for a square wave demand of 0° to 15° in twist, with constant demands of 150N tension for both force loops. The first two figures show the twist displacement and bend disturbance; Figure 6.4 shows the internal force values, i.e. elements from vector $\mathbf{f_d}$, transformed from the actuator forces calculated from pressure measurements.

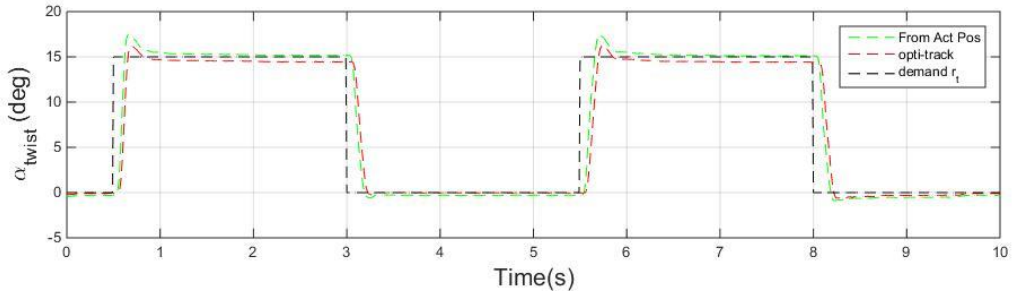

Figure 6.2 Twist angle from actuator position measurements and optical tracker, with a square wave twist demand r_t

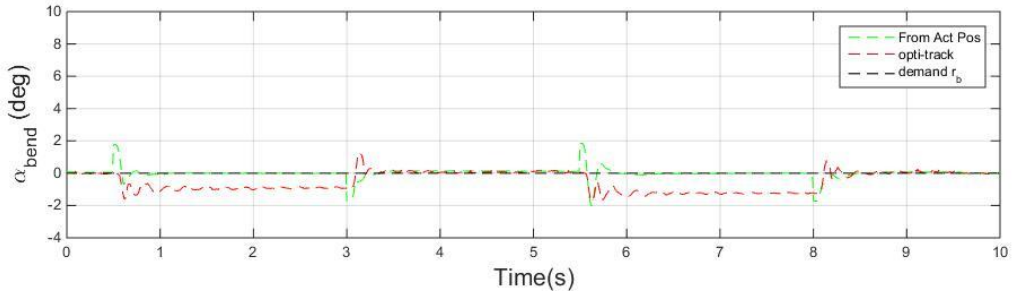

Figure 6.3 Bend angle from actuator position measurements and optical tracker, with a square wave twist demand r_t

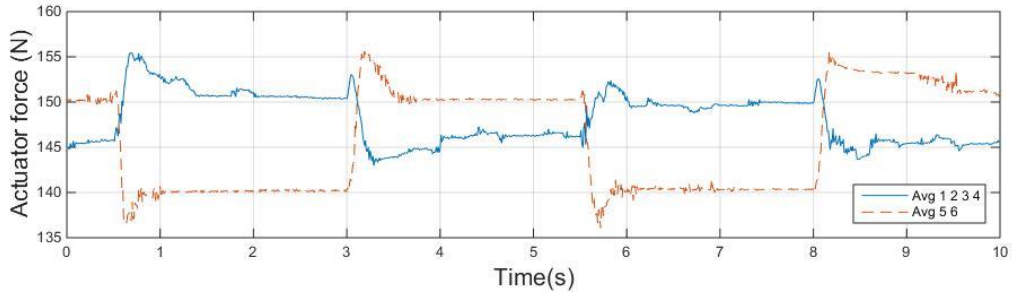

Figure 6.4 Controlled actuator force result during square wave twist demand

Figure 6.5 to Figure 6.7 show results for a square wave demand of 0° to 8° in bend, again with constant demands of 150N tension for both force loops. Zero dead-band was given for both deformation modes, and 5N dead-band was given to both force loops. Similarly, the first figure shows the twist disturbance, the second shows bend displacement, the results being compared between the transformed actuator positions and the independent motion tracking result; the third figure shows the internal forces.

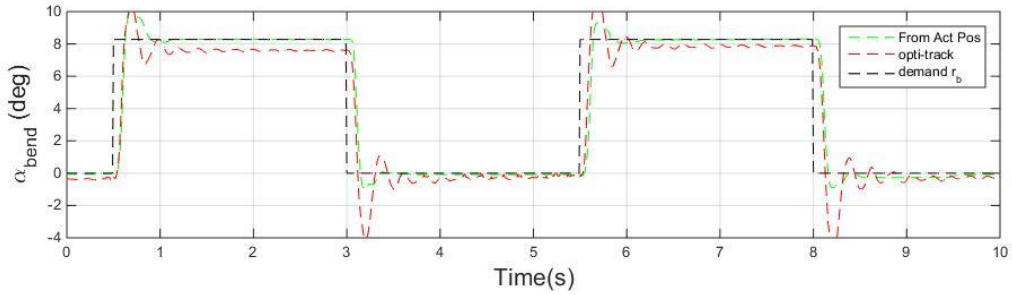

Figure 6.5 Bend angle from actuator position measurements and optical tracker, with a square wave demand r_b

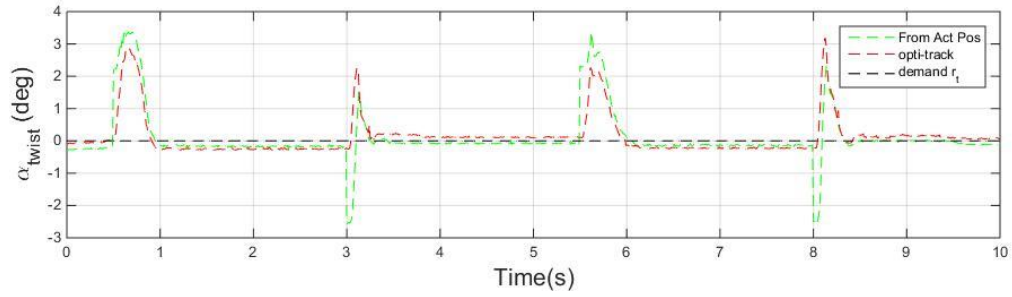

Figure 6.6 Twist angle from actuator position measurements and optical tracker, with a zero demand r_t

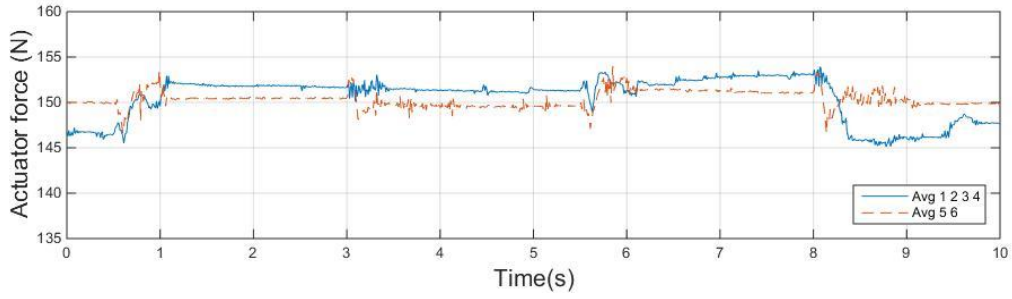

Figure 6.7 Controlled actuator force result during bending

Table 6.2 Motion control performance (considering transformed actuator positions as output unless otherwise stated)

	Overshoot (%)	Rise time 10%-90%(s)	Steady State error (%)	Opti-track s. state error (%)
Bend 8°	18.8	0.06	0.8	6.5
Twist 15°	27.3	0.05	1	4

6.1.2 Discussion of step response results

The results show rapid response to the step demand in both the twist and bend cases, and reasonably accurate steady state position control. There is some cross-coupling between degrees-of-freedom, particularly transients in bend disturbing the twist angle (Figure 6.6). The optical tracking results match those based on the actuator position measurements quite closely. Controller step-response characteristics are shown in Table 6.2.

There is some difference between tracked motion and actuator-measured motion during transients, particularly in the bend direction, probably due to compliance in the passive elements of the structure and the structure mounting. In the twisting case, a steady state error is observed in both twist and bend (Figure 6.2/6.3), but the control errors measured by sensors on the actuators are approaching zero. This is due to the elasticity of the passive tensile members. With changing geometry the individual cable forces change, even though the average actuator forces are controlled to a constant value, and the cable lengths change slightly when a different tension is applied, as discussed in Ch.6.2. Adding some compensation, which is a function of the internal force, to the transformation matrix P could improve this, or in hardware, changing to a

stiffer cable or stiffer crimp connection would also help, further investigation is presented in Ch.6.3.

On average the force controller achieves the desired values, and the disturbances during motion are quite small. There is a small step error in force with position change, which is due to the geometric change of the structure. The actuation force disturbance during twisting was significantly larger than the disturbance on bending.

6.2 The effect of tensile member elasticity on motion control

When the twist motion demand is15° in Figure 6.2, with actuator internal force demand of 150N, a steady state twist error of 1.2° is observed with the optical tracker, while such an error does not show up from displacement measurements. The displacement error varies when different internal forces are applied.

As discussed in Ch.3, the kinematics model was established with the assumption that all members in the structure were non-elastic. In experimental practice this assumption is not always accurate. The elastic deformation of tensile members would be noticeable under large internal load, which would affect the kinematic model's accuracy.

An example of the tensile member used in the prototype is shown in Figure 6.9, which is a stainless steel wire rope, type 7×7 with 1mm diameter and minimum breaking load of 0.56kN. Cables in the morphing region (C1 to C4 as shown in Figure 6.8 pin joint model), were all the same length, 97mm, between ends bent to form eyes.

A tensile test was carried out to study the tensile member deformation under static load, which is very close to the working condition of the cable in the proto type structure.

The test was done on an Intron universal testing machine (Type 5965), with test speed of 0.5mm/min, up to a load of 300N. The experiment setup as shown in Figure 6.10, and the result of load applied vs cable extension was recorded, as shown in Figure 6.11.

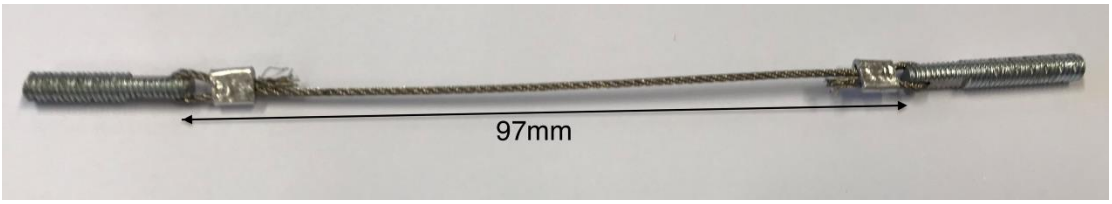

Figure 6.8 Tensile member example used in prototype

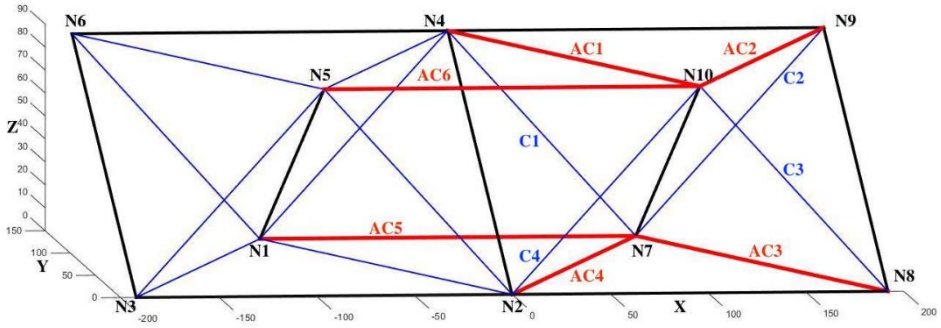

Figure 6.9 Pin joint model of the prototype

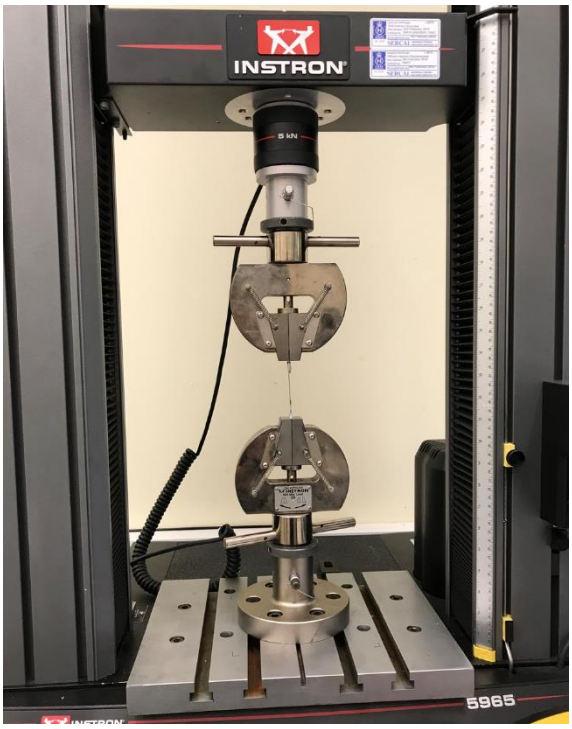

Figure 6.10 Tensile test set up

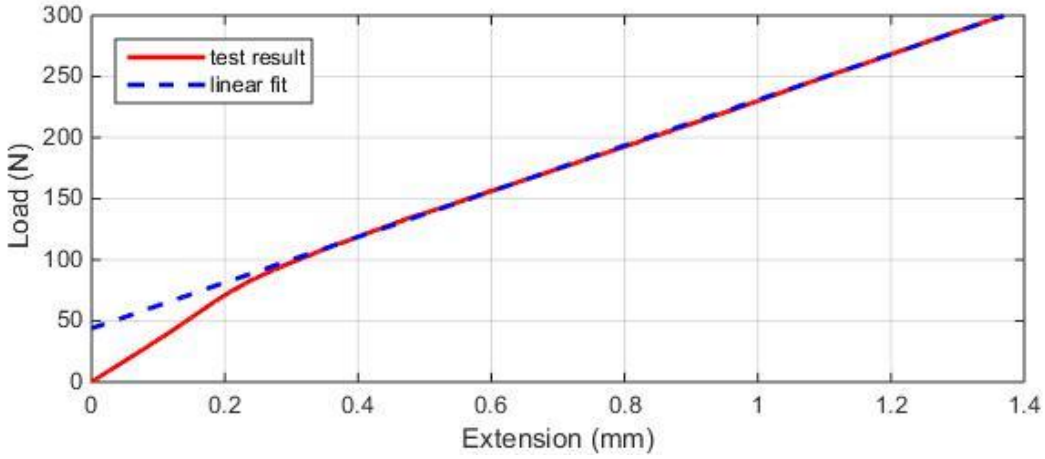

Figure 6.11 Cable tensile test result

The cable tensile test gives a 1.37mm elastic stretch with 300N load, and the load-extension relationship is linear in the normal working range (90N and up).

$$dl_c = 0.00535W - 0.235 \tag{6.1}$$

Where dl_c is the length change of cable, and W is the applied load.

The tensile forces in each cable are different, depending on their location and the structure displacement. For twisting motion at 15°, and average actuator force demand of 150N, the tensile cable forces are approximately: 140N for C1, C4 and 200N for C2, C3. From the tensile test result, the cable elastic deformation dl_{c1}=0.51mm. dl_{c2}=0.84mm.

6.2.2 Kinematics refinement and results

When elastic deformation of tensile members is taken into account, the kinematic equation introduced in Chapter 3 could be written as follows:

$$(x_{10}-x_2)^2+(y_{10}-y_2)^2+(z_{10}-z_2)^2=(l_c+dl_{c4})^2 \tag{6.2}$$

$$(x_7-x_4)^2+(y_7-y_4)^2+(z_7-z_4)^2=(l_c+dl_{c1})^2 \tag{6.3}$$

$$(x_9\text{-}x_7)^2+(y_9\text{-}y_7)^2+(z_9\text{-}z_7)^2=(l_c+dl_{c2})^2 \tag{6.4}$$

$$(x_{10}\text{-}x_8)^2+(y_{10}\text{-}y_8)^2+(z_{10}\text{-}z_8)^2=(l_c+dl_{c3})^2 \tag{6.5}$$

Substituting the dimensions from Table.3.5 into the kinematic equations (6.2 – 6.5), the results as shown in Table.6.3.

Table.6.3 calculated twisting results using different kinematic model

Twist Demand	Twist angle (inelastic)	Bend angle (inelastic)	Twist angle (elastic)	Bend angle (elastic)
0°	0.0654°	-0.0004°	0.4295°	-0.0004°
15°	15.006°	-0.0660°	14.168°	-0.7032°

When elastic deformation of passive tension members is taken into account, with the same actuator length change, the kinematic calculation result shows an offset on both bend and twist angles. The calculated results show a good match with the experimental result for twisting motion.

As the elastic deformation is approximately proportional to the tensile force applied, a 1st order correction term can be added to the transformation matrix **P**:

$$\mathbf{P}=\begin{pmatrix} -0.4545-k_1F_1 & 0.4545+k_1F_2 & 0.4545+k_1F_3 & -0.4545-k_1F_4 & 0 & 0 \\ -0.1667-k_2F_1 & 0.1667+k_2F_2 & -0.1667-k_2F_3 & 0.1667+k_2F_4 & 0 & 0 \\ 0.1365 & 0.1365 & -0.1365 & -0.1365 & 0 & 0 \\ 0 & 0.1667 & -0.1667 & 0 & 0.1872+k_4F_5 & -0.1872-k_4F_6 \end{pmatrix} \tag{6.6}$$

In this matrix, F_i is the tensile force in each actuator, k_i is the correction factor for structure deformation modes, with k_1 for twist deformation, k_2 for bend deformation, k_3 for sweep deformation, which is not used in this part as sweep is not of interest in the test, and k_4 for extra deformation mode. Values of k_i were found empirically, in this

case:

k_1= -1.515×10^{-4} deg/N, k_2=5.5567×10^{-5} deg/N, k_4=-4.875×10^{-5}deg/N.

New motion control results obtained with the revised transformation matrix which includes the correction factors are shown in Figures 6.12 to 6.17, for twist and bend square wave demands respectively.

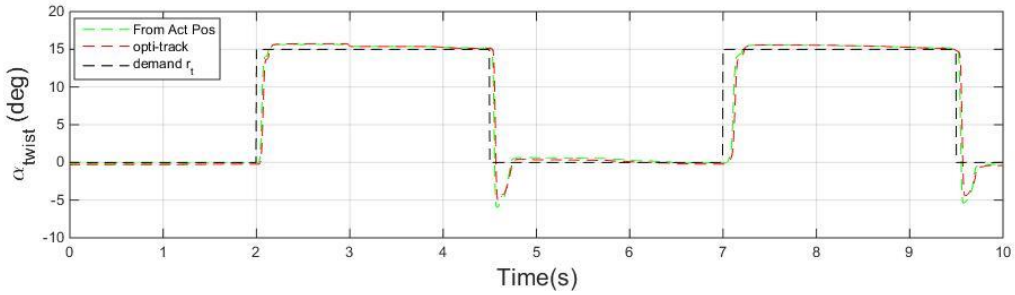

Figure 6.12 Twist angle from actuator position measurements and optical tracker, kinematics refined.

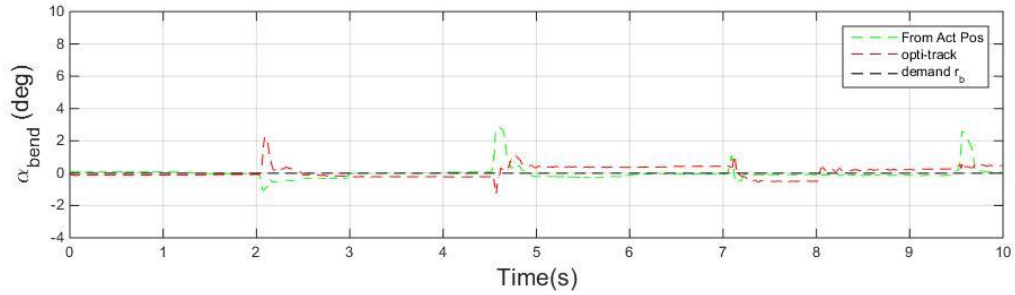

Figure 6.13 Bend angle from actuator position measurements and optical tracker, with a zero bend demand r_b, kinematics refined.

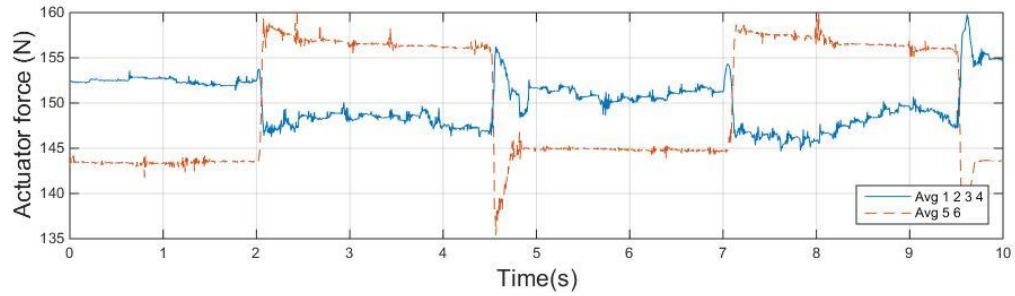

Figure 6.14 Controlled actuator force result during twisting

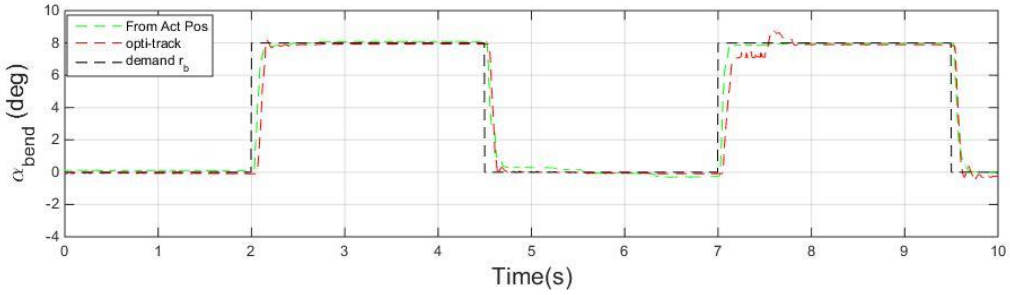

Figure 6.15 Bend angle from actuator position measurements and optical tracker, with a square wave demand r_b, kinematics refined.

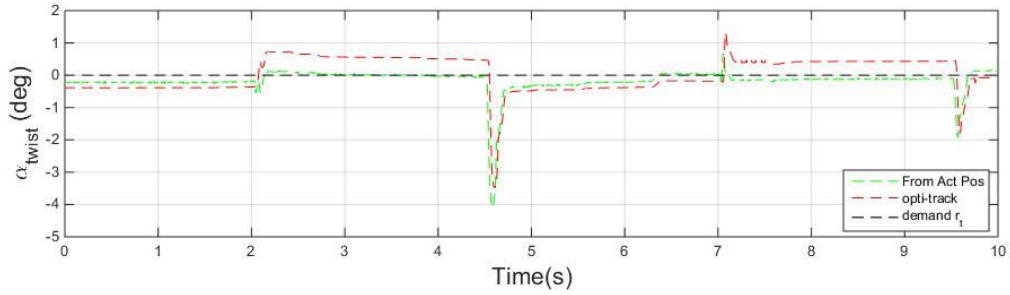

Figure 6.16 Twist angle from actuator position measurements and optical tracker,, with a zero demand r_t, kinematics refined.

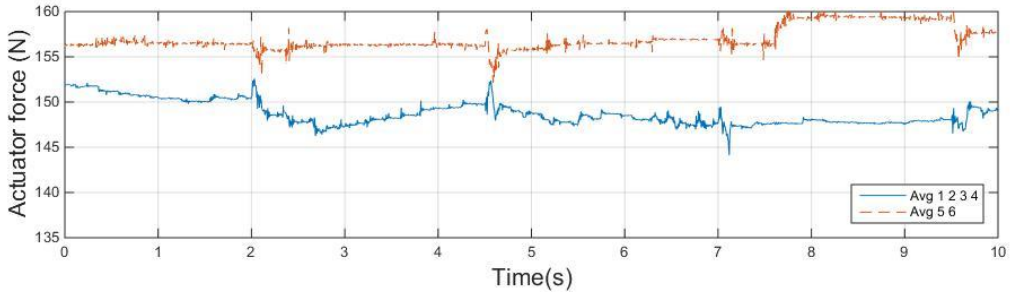

Figure 6.17 Controlled actuator force result during bending

Compared with previous results, the results with refined kinematics show a better match between optical tracker motion and actuator displacement based motion for both deformation modes. The internal load is mostly in or close to the 150±5N dead band range. The results shows a clear relationship between tensile members' elastic deformation and the shape of the structure.

In this set of bench top tests, with an internal load of 150N the static cable tensile force

in the neutral position is approx. 40% of its minimum breaking load, which gives a safety factor of 2.5. This causes a significant length change, and a potential danger of breaking when tensions increase due to the presence of an external load. With a step command as shown in bench top tests, inertia-related dynamic loads are generated which can also increase tension. Two types of cable failure happened during the subsequent wind tunnel testing as shown in Figure 6.18: mechanical damage due to cable movement over a sharp edge whilst under load, and tensile failures around the crimped point of the cables.

a)  b) 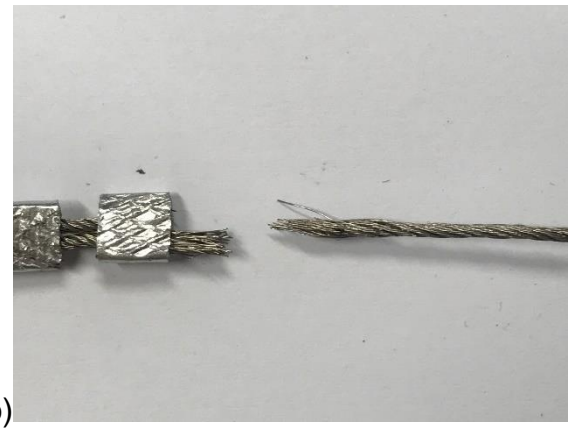

Figure 6.18 a) Mechanical damage b) Tensile failure

6.3 Motion and internal load control with reinforced tensile members

The elastic effect was discovered and analysed on the structure with thin and flexible cables. Due to the failure cases, cables are changed from type 7×7 stainless steel cable at 1mm diameter, to type 1×19 stainless steel cable at 1.25mm diameter (cross-sections as shown in Figure 6.19). The new cable has a minimum breaking load of 1280N, which more than doubles the cable strength, and the tensile stiffness of the cable is also substantially higher. And they are less flexible compared with the original

ones, which makes the crimped eye ring stiffer.

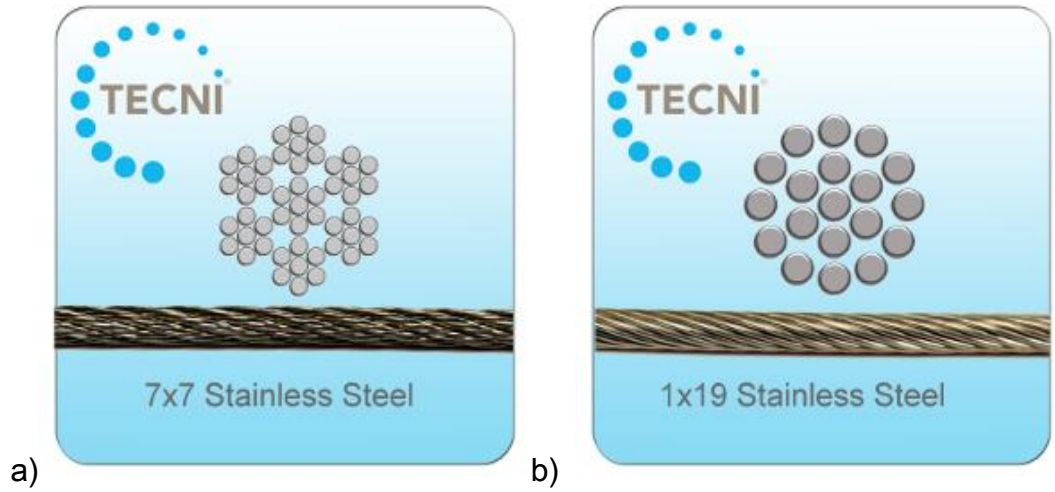

a) b)

Figure 6.19 Cable types a) 7×7strands b) 1×19 strands (TECHNI-CABLE 2019)

In this section different motion demands are given (square, sine and ramp) to investigate the dynamitic performance of the morphing structure under different internal load (140N and 70N). To be consistent with the wind tunnel test conditions, twist signals of 0° to 12° are given, and bend demands are form 0° to 8°. Zero dead-bands are given for both motion and force control to give more precise tracking. Structure deformation results are also verified with optical tracker results. The transform matrix used in tests in this section is the original matrix (3.35) as the cable stretch is now much smaller.

6.3.1 Motion control with square wave demand

In this series of experiments the structure motions were controlled by a square wave demand signal of 0.2Hz, between twist angles of 0° and 12°, and bend angles of 0° and 8°. From this section on, α_{tip} is used to denote the twisting angle on the wing tip, to be consistent with the wind tunnel test result. And α_{root} is 0° in this section.

$$\alpha_{tip} = \alpha_{twist} + \alpha_{root} \tag{6.7}$$

Figures 6.20 and 6.21 illustrate the twist deformation with 140N and 70N average internal load for each set of actuators.

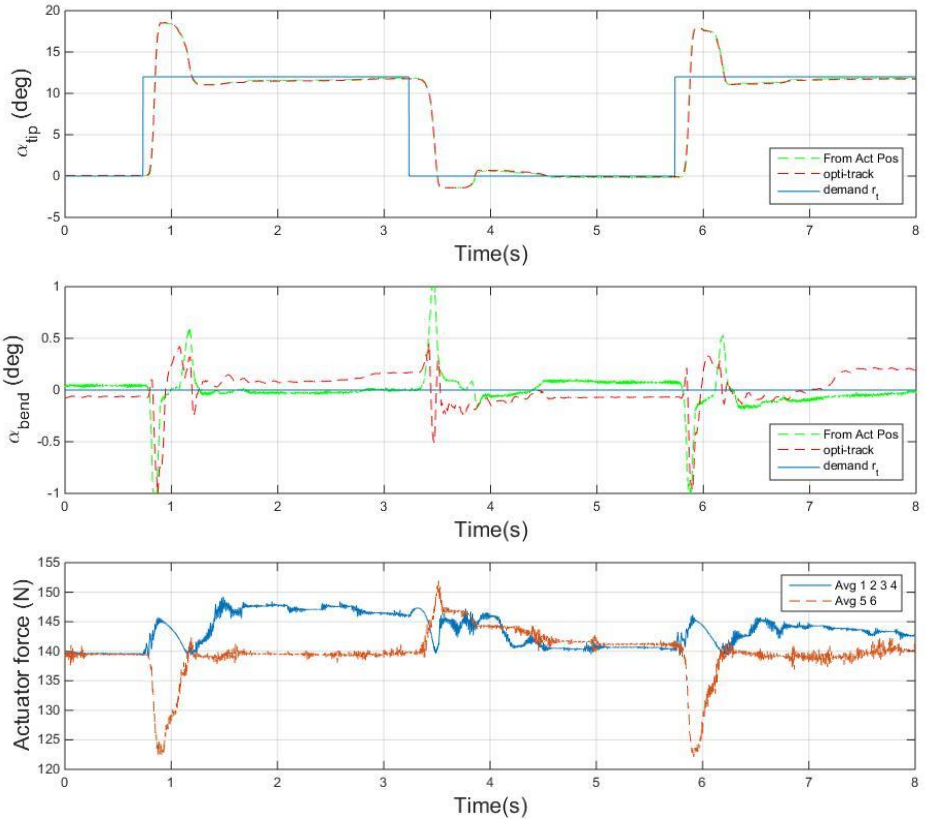

Figure 6.20 Results with square wave twist demand of 0° to 12°, 140N internal load.

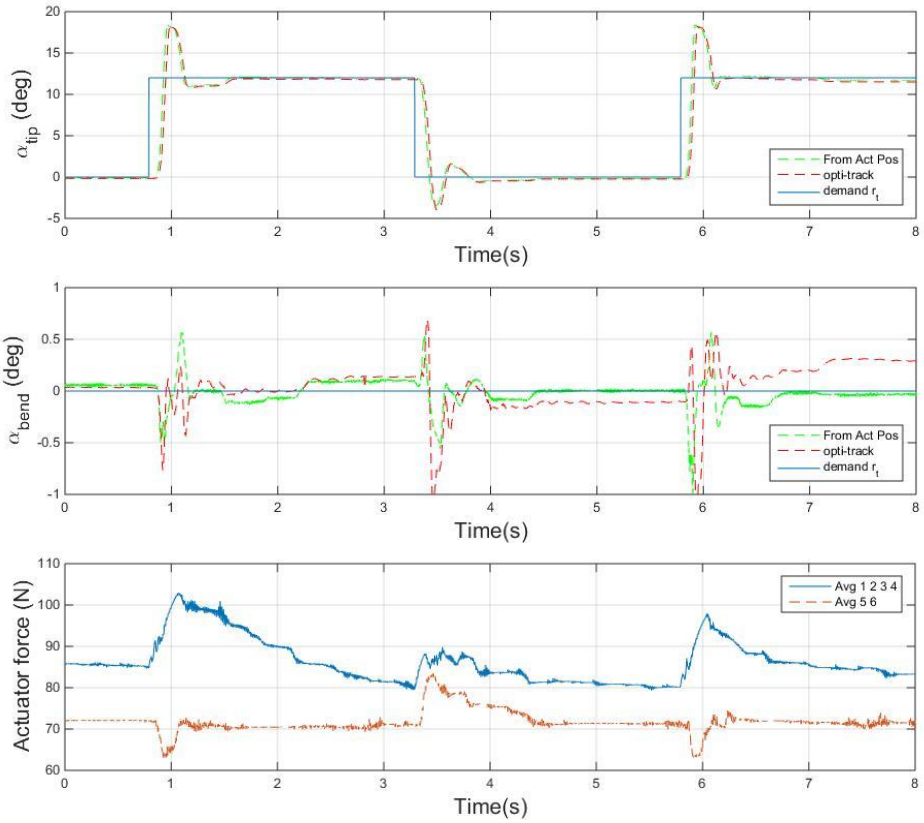

Figure 6.21 Results with square wave twist demand of 0° to 12°, 70N internal load.

Compared with initial results with the original transformation matrix (Figure 6.2), the agreement between actuator displacements based motion and optical tracker motion with reinforced cables is better. It indicates that with this level of preload, only minor deformation of passive members happened, and its effect on motion can be neglected. The motion responses are reasonably fast and accurate for both internal load cases, while the dynamic behaviours are different. Friction has a significant effect on the dynamics of the structure twist motion, as seen in Figures 6.20 and 6.21, in both the outward twisting stage (0.8-2s), and the twisting back stage (3.2-4.5s), the motions with lower internal load are smoother. For higher internal load applied in the actuators, the friction in the joint between the aluminium socket on the node and the strut tip

stainless steel sphere grows significantly. The friction of metal-to-metal contact joint is highly sensitive to the compression force applied, and with the steel to aluminium design the wear rate is further increased. The friction of the sealing in the pneumatic cylinders is also increased when the chamber pressures rise, but this has only a minor effect on the structure motion compared with the mechanical joint friction.

For the internal load control results, the controller has successfully maintained the demanded 140N internal load with up to 5N steady state error. From the 70N internal load control result, with the same proportional and integral gain, the error is 10N. The response speed is also not as fast as in the high internal load experiment.

Figures 6.22 and 6.23 illustrate the bend deformation with 140N and 70N average internal load for each set of actuators.

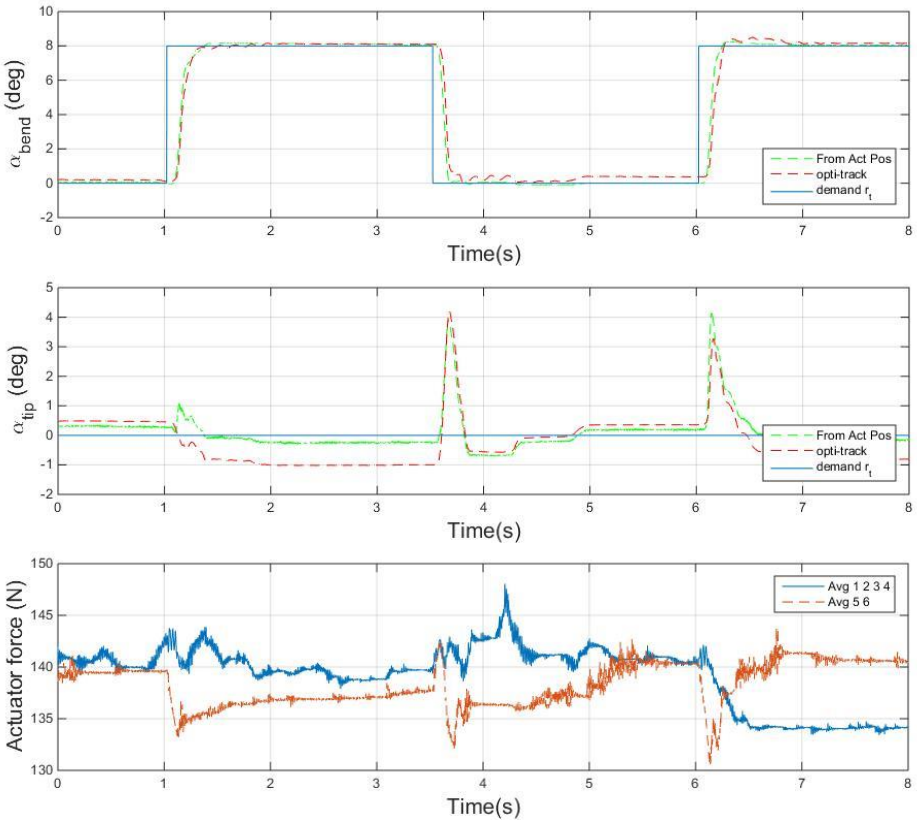

Figure 6.22 Results with square wave bend demand of 0° to 8°, 140N internal load.

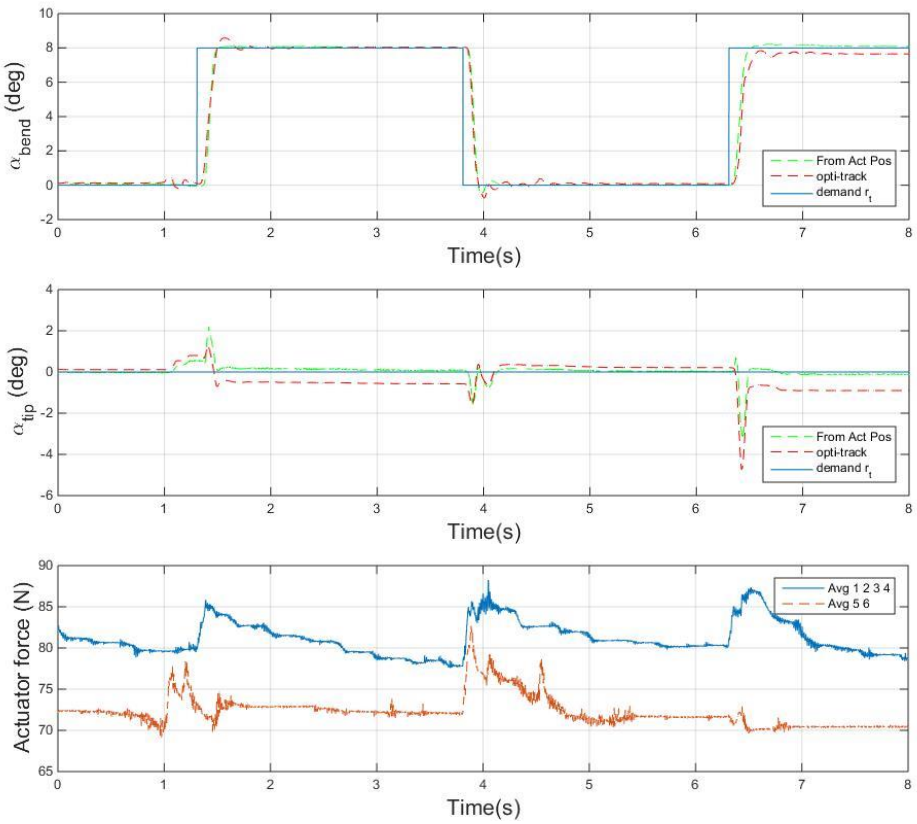

Figure 6.23 Results with square wave bend demand of 0° to 8°, 70N internal load.

The step response of the bend motion is reasonably fast with low overshoot rate compared with the twist motion. The friction effects on bending are also less obvious in both 140N and 70N internal cases. At large amplitudes cross coupling of twist happens, because of the non-smooth motion caused by the coulomb friction effect (clearly seen at 3.5-5s Figure 6.22). A 1° error on twist can be observed when the bend angle is 8°, with 140N internal load, and 0.5° error with 70N internal load, which suggests that transformation matrix inaccuracy is evident in this case.

For internal load control, the bend motion produces less actuation force disturbance during the transient than the twist motion. The force control loops can successfully maintain a 140N average load as shown in Figure 6.22, with errors within about 5N. Similarly with twist motion, with 70N force demand, the four in-cell actuators internal

load has a slower response and larger error as a result, because it is not able to reach the steady state before next cycle starts.

The motion control results with step demands shows that the friction effect on motion varies with the internal load applied and the different deformation in DOF. This is also further proved in later subsections.

6.3.2 Motion control with sine wave demand

Unlike the conventional pneumatic two-point control, the proposed tensegrity structure and control method is able to produce a more precise positon response on controlled DOF. A sinusoidal position demand was given to the structure, to investigate the dynamic behaviour of motion and ability to maintain the requested internal load.

The sinusoidal position demand was 0.1 Hz for all tests in this subsection, with amplitude of 6°(around 6° baseline) for twist, and 4°(around 4° baseline) for bend. Internal loads are set to 140N and 70N to test the ability for the control system to maintain the load with continuous motion.

Figures 6.24 and 6.25 give the results for twist motion control with the two internal load demands.

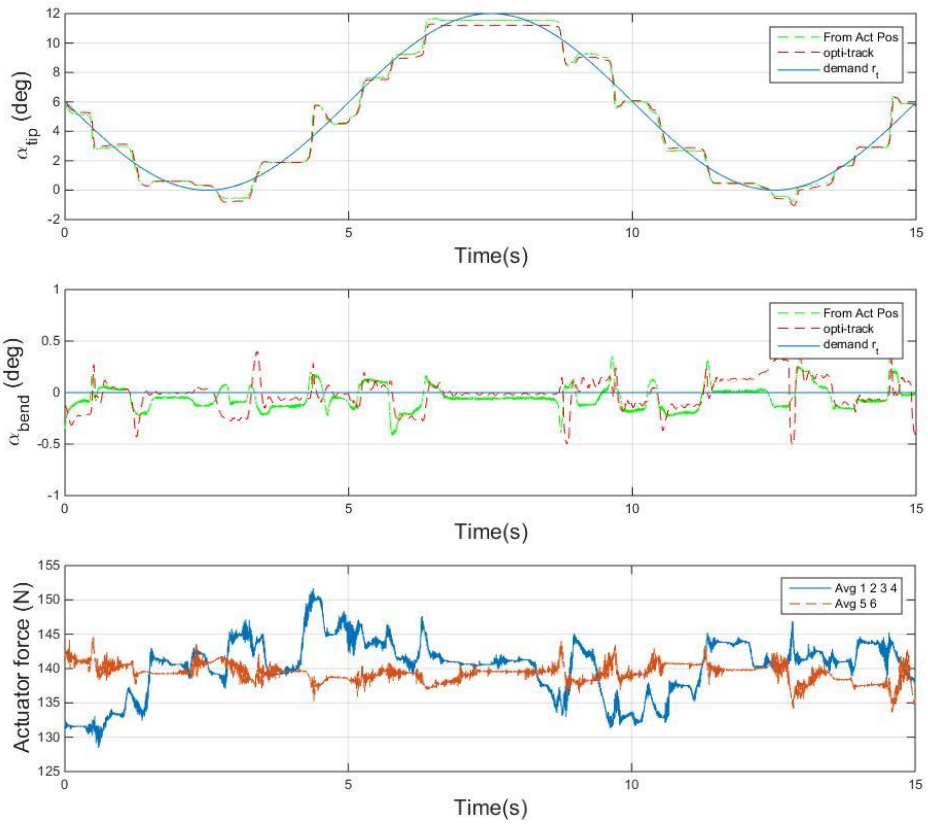

Figure 6.24 Results with sine wave twist demand, 140N internal load.

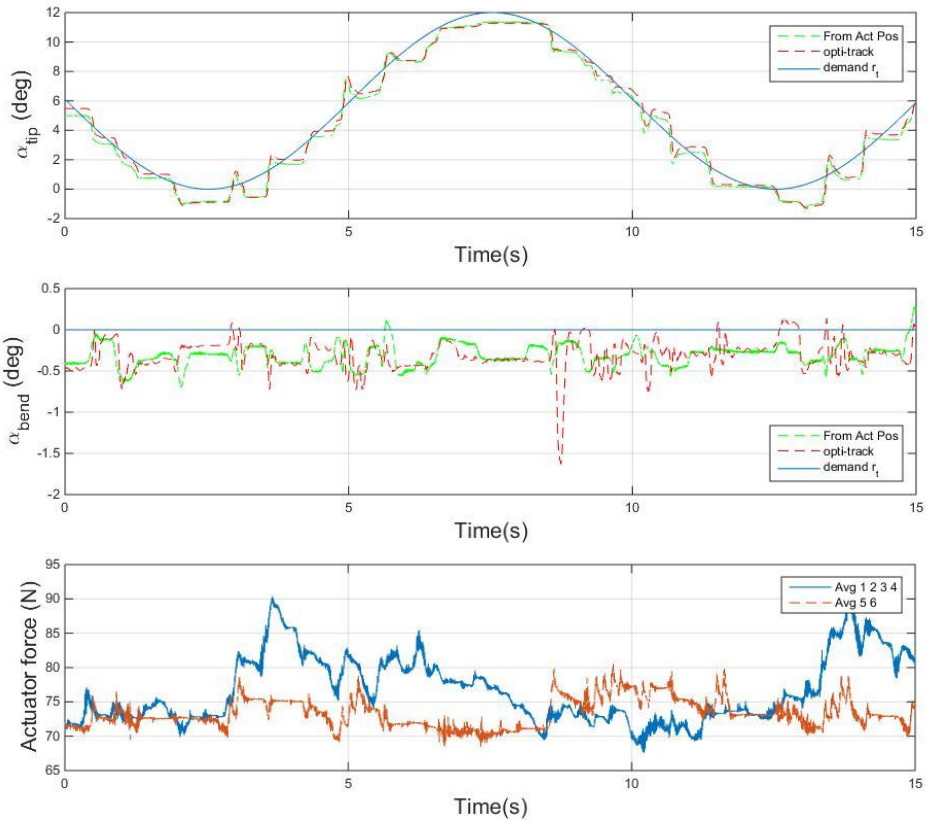

Figure 6.25 Results with sine wave twist demand, 70N internal load.

For the continuous sinusoidal twist demand, the structure successfully tracks the demand, but with up to 1.5° error in twist due to the stepwise motion profile that occurs. Stick-slip motion is a typical effect of friction. Oscillations within ±0.5° occur in the bending DoF, because of the cross coupling produced during the continuous deformation of the structure. As analysed in sub section 6.3.1, compared with the low internal load case, the friction effect is severe when the internal load is high.

With continuous deformation of the structure, the internal load responses are smoother, with less error. When the structure deviates away from its neutral position (Figure 6.21 1s and 6s, Figure 6.25 2.5s and 12.5s), the force disturbance was higher than when twisting it back towards that position (Figure 6.21 from 3.5s, Figure 6.25 from 7.5s), because the neutral position is the most symmetrical position, where load differences between the actuators are smallest.

Figures 6.26 and 6.27 give the results for bend motion control under 140N and 70N internal load demands.

For bend motion responses, the stepwise motion response is less obvious, and the structure satisfactorily tracks the sinusoidal bend demand, and has good agreement with the optical tracker results. The motion response proves that the friction has more effect in the bend DoF than the twist DoF, as mentioned earlier. The difference in the effective friction is believed to be caused by the nature of the joints; for a different motion, the joint friction has a different effect. Therefore it is likely that the spherical joints are the major source of the friction effect encountered in this section.

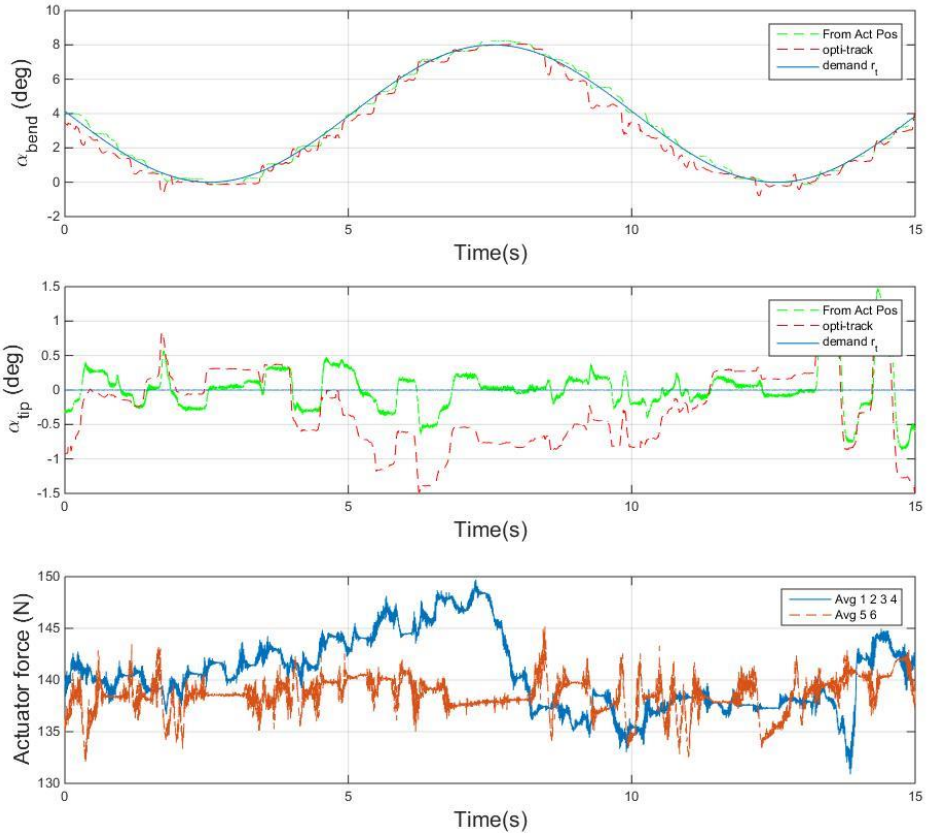

Figure 6.26 Results with sine wave bend demand, 140N internal load.

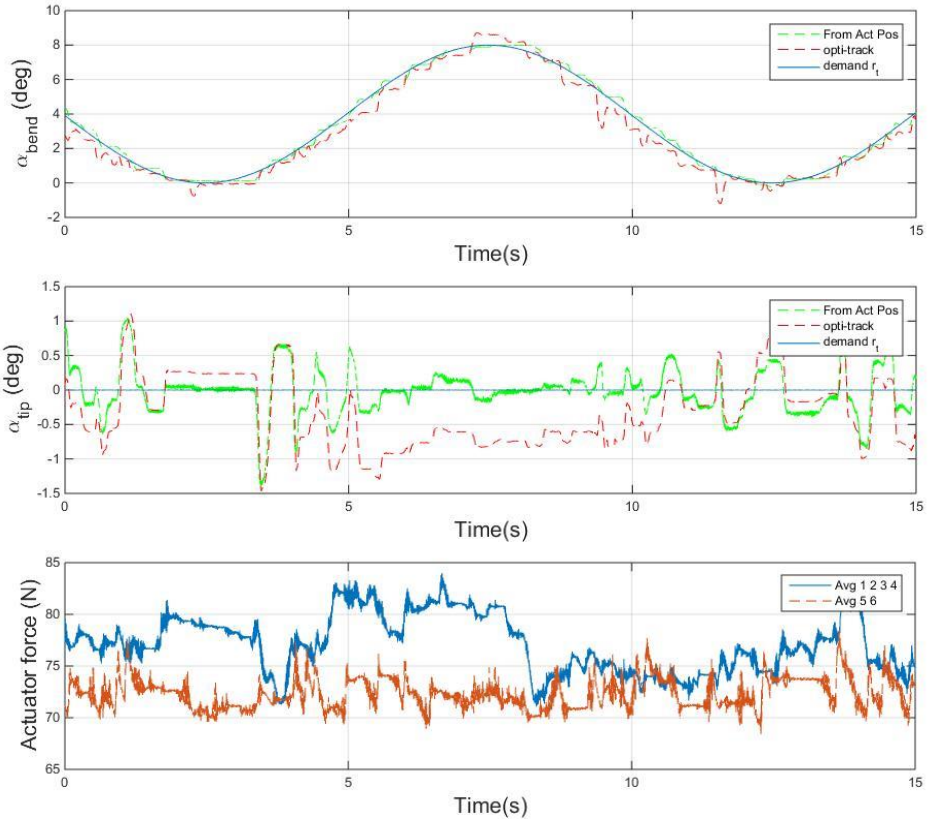

Figure 6.27 Results with sine wave bend demand, 70N internal load.

The error between actuator measured coupled twist motion and optical track results, further proves the existence of transformation matrix inaccuracy, and in experimental practice the two DOF are not fully independent. This happened in the coupled twist when bend is the main controlled motion (Figure 6.26 and 6.27), but was not observed in the coupled bend when twist is the main controlled motion (Figure 6.24 and 6.25). It is believed that the kinematic inaccuracy is caused by the inaccurate assembly of the prototype structure. The average actuator loads are kept around the demand value for both cases. The actuation force required to bend the structure back to neutral position is considerably smaller than an outward bend, as an actuation force drop can be observed (Figures 6.26 and 6.27 7.5s).

6.3.3 Motion control with ramp demand

The motion and force response for dynamic structure deformation of different motion demand and internal load levels were presented in section 6.3.1 and 6.3.2.

For the wind tunnel test, conditions are different than with the bench top test. A distributed external load is applied to the structure, the aerodynamic moment is balanced around the pivot axis of twist motion, but with the extra airfoil rib and extension wing attached, the centre of mass is not located on the same axis. The inertia of the full prototype wing is far greater than the tensegrity structure alone, which introduces large inertia forces when a step response demand is used. Rapid and large amplitude deformation will also change the external load dramatically, which potentially makes the controller unstable.

Thus, a ramp signal from 0° to 12° twist and 0° to 8° bend with constant ramp rates of

0.5°/s are used in the wind tunnel test to smooth out the deformation motion and corresponding external load change. The internal load is set to 140N, which is consistent with the lower limit of the internal load demand used in the wind tunnel test. The twist and bend results are illustrated in Figures 6.28 and 6.29.

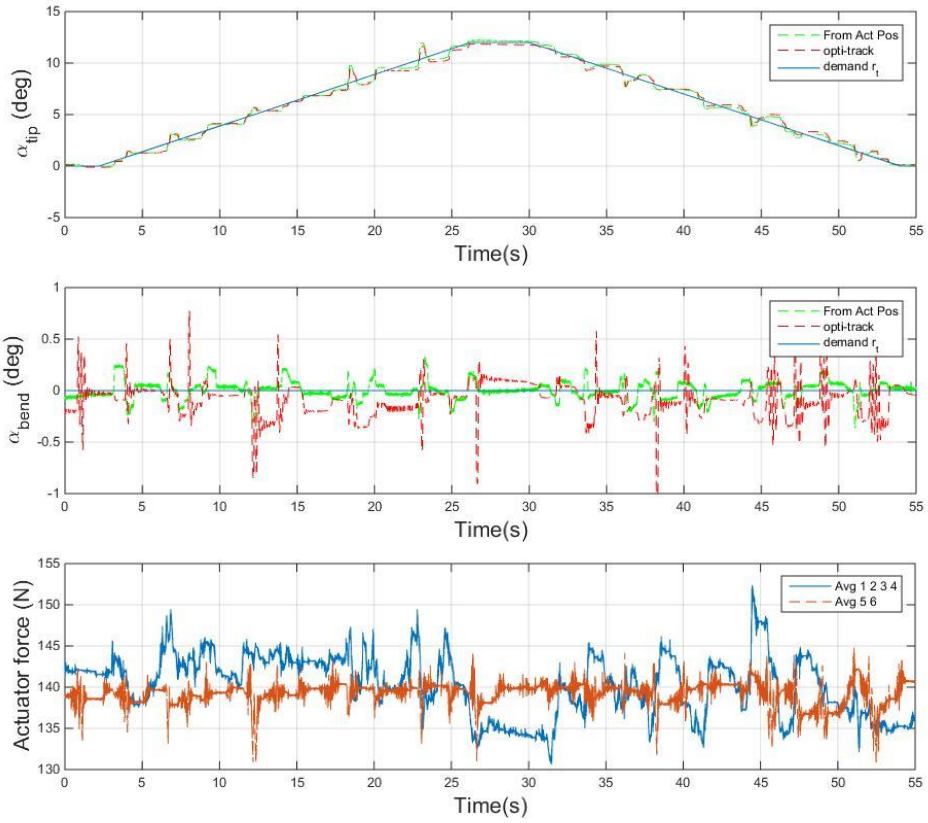

Figure 6.28 Results with ramp twist demand, 140N internal load.

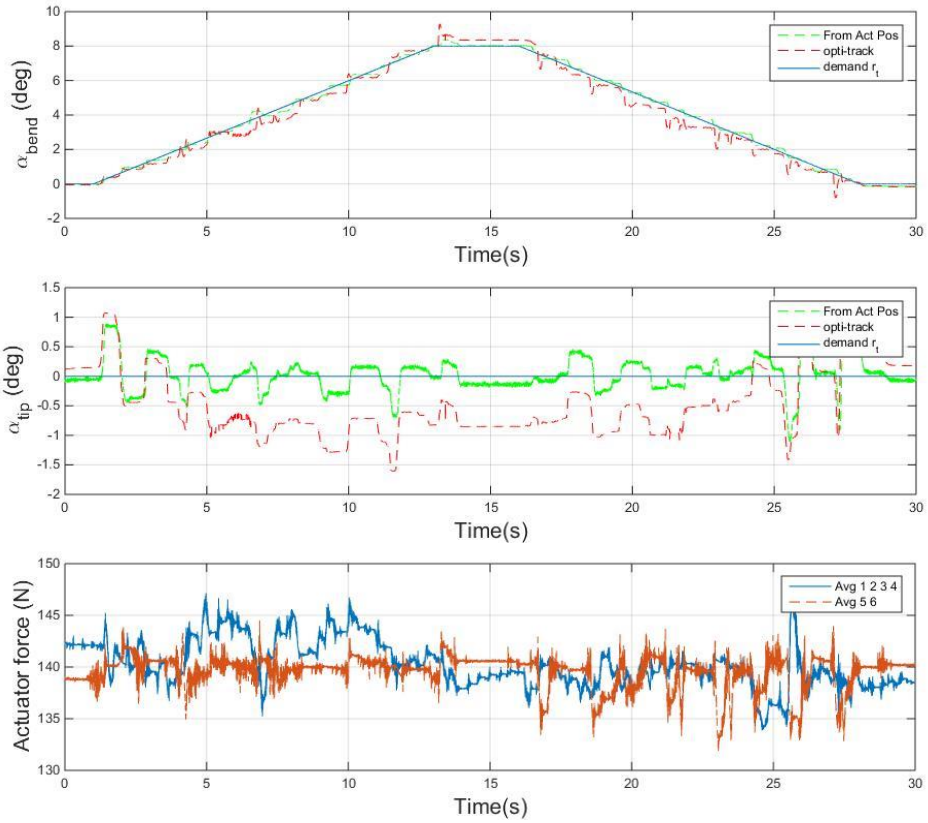

Figure 6.29 Results with ramp bend demand, 140N internal load.

As shown in Figure 6.28, the stepwise movement is on both rising and falling edge of twist, which is an obvious effect of friction. Cross-coupled bend happens with each stepwise twist, which can be observed as spikes in the optical tracked bend response. In Figure 6.29, again up to 1° error can be observed between the actuator measured result and the optical tracker result of coupled twist, which is consistent with the former results.

With a constant ramp motion demand, the force controller can keep the average actuator force closer to the demanded value than for the other motions presented.

6.4 Conclusions

The kinematics model of the proposed tensegrity structure is validated and refined in

this chapter. A series of bench top tests is carried out to study the dynamics of the morphing structure prior to the wind tunnel test. The result show a good match between the kinematic result (i.e. bend and twist calculated from measured actuator displacements) and the actual motion measured by the optical tracker. The twist angle is most accurate with zero bend, while a twist error of up to 1° exists during bending, which may suggest the two DOF are not fully independent in experimental practice, and also there's some inaccuracy in the Jacobian matrix introduced. The force controller has successfully maintained the internal load as demanded, with only modest deviation during the deformations transients

Stepwise movement response is observed with slowly varying demand signals, which is a typical effect caused by friction. Through experiments with different motion demands, it is concluded that the friction in node joints is the major factor rather than actuator friction.

Dynamic response of the structure under external load (aerodynamic load), is presented in next chapter. Ramp motion is selected for further experiments to reduce the load impact on the wing and turbulent flows generated with sudden movement, as well as achieve more accurately controlled internal load.

7 Morphing wing tests in a wind tunnel

This chapter will present and discuss the experimental and simulation results for the morphing wing in a wind tunnel as shown in Figure 7.1. The experiments were carried out to investigate the static and dynamic performance of the pre-loaded structure under distributed external load.

Figure 7.1 Full prototype wing in wind tunnel test section

Twisting and bending motions were tested separately to validate the actuator behaviour in different modes. Wing root angles of attack from 0° to 12° with steps of 3° were used to generate different aerodynamic loads, and these angles were adjusted manually between test cases. Air flow speeds of 10m/s and 12.5m/s were used for most tests, and higher flow speeds were used in extreme cases and will be discussed

later. Full data for 10m/s tests are shown in appendix 1.1. Additional tests at 15 m/s and 17.5 m/s wind speeds were carried out for α_{root} of 12° to investigate the performance in more extreme conditions. Ramp demands for twist and bend angles were used for all the experiments. The pre-load demands were set to 150±10N. Variables used in this chapter are presented in Table 7.1. Lift coefficient C_l and drag coefficient C_d are measured using the method introduced in Chapter 4.

Table 7.1 Variables for wind tunnel test

Parameters	Description	Units
v	Wind speed (10, 12.5, 15, 17.5)	m/s
r_t r_b	Twist, bend demand	Degree (°)
α_{root}	Pre-set wing root angle of attack (0-12)	Degree (°)
α_{twist}	Measured wingtip twist angle relative to wing root (0-12)	Degree (°)
α_{tip}	Measured wing tip angle of attack (0-24)	Degree (°)
α_{bend}	Measured wingtip bend angle relative to wing root (0-4)	Degree (°)
C_d	Drag coefficient	
C_l	Lift coefficient	

7.1 Twist motion

In this series of tests, the twist angle of the wing tip relative to the wing root was controlled. Starting from α_{twist} = 0°, the wing was twisted to 12° with a constant ramp rate of 0.5°/s, then held stationary for 12s and twisted back to α_{twist} = 0° at -0.5°/s.

Wind speeds of 10m/s and 12.5m/s were used with wing root angles of α_{root} = 0°, 3°, 6° , 9° and 12°. The values for α_{tip} and α_{bend} were directly measured using optical track as the validations.

7.1.1 Twist motion wind tunnel test results

The prototype wing in un-morphed and twisting position of 12° is shown in Figure 7.2. The set of data shown in Figure 7.3 to Figure 7.7 was recorded with an ambient temperature 20°C and wind speed of 12.5m/s (Reynolds Number 6.61×10^5), with α_{root} = 0°, 3°, 6°, 9°and 12°. Figure 7.8 to Figure 7.10 show the results for α_{root} = 12°, with wind speeds of 10m/s, 15m/s and 17.5m/s. Expected wing twist along span is shown in Figure 7.11 as a reference.

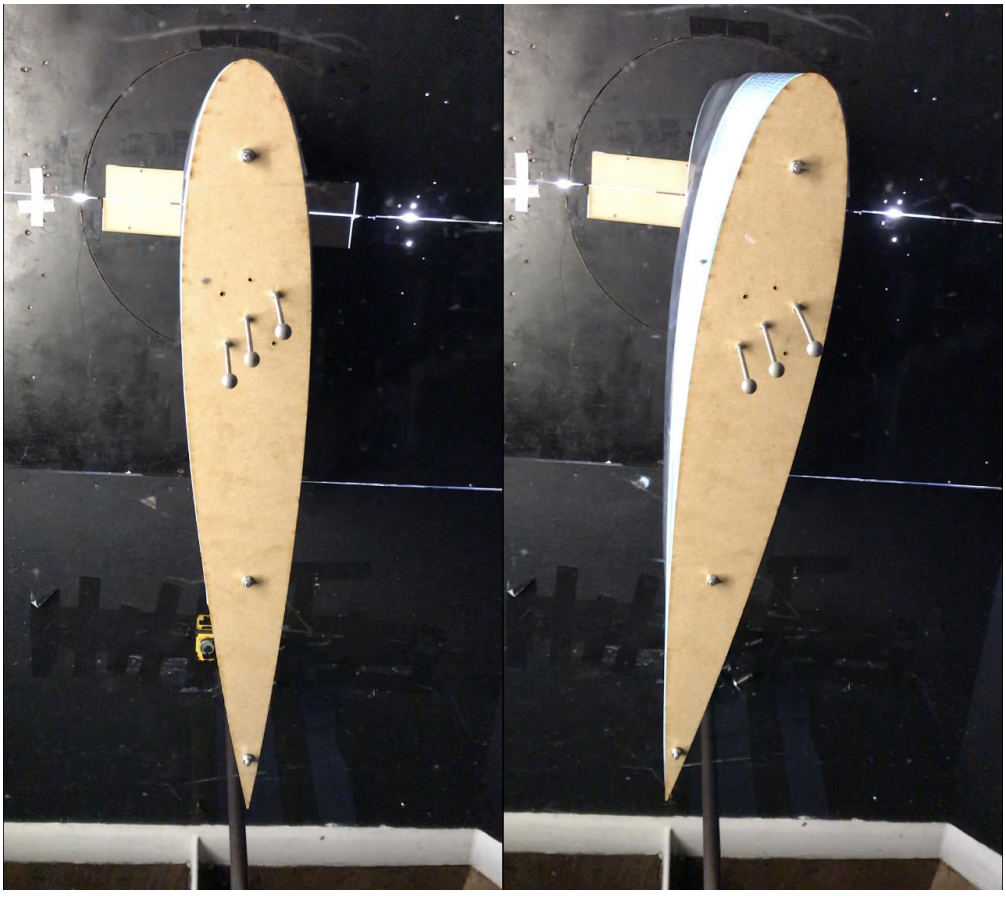

Figure 7.2 Prototype wing with neutral and 12°twist (bottom view through glass floor)

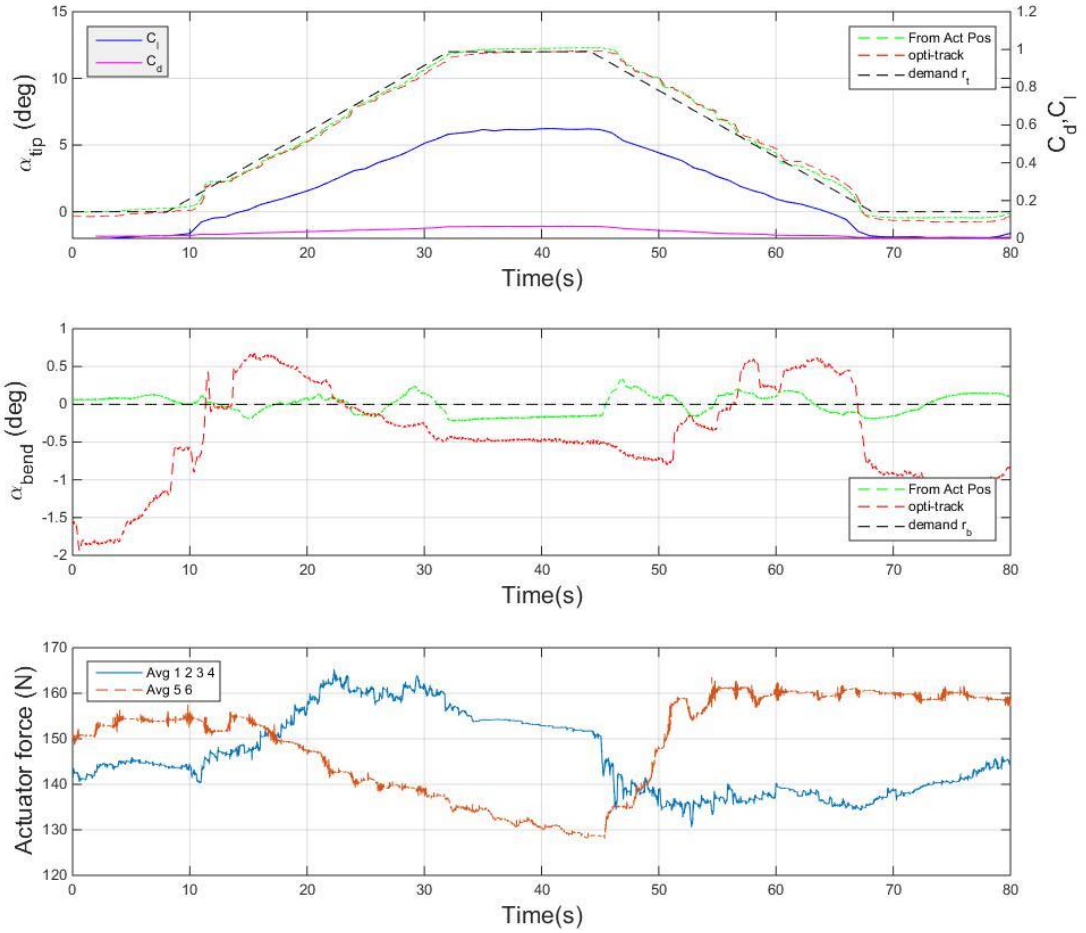

Figure 7.3 α_{tip} and α_{bend} optical tracker and actuator sensor angles, and actuation force, at α_{root} =0°, v=12.5m/s

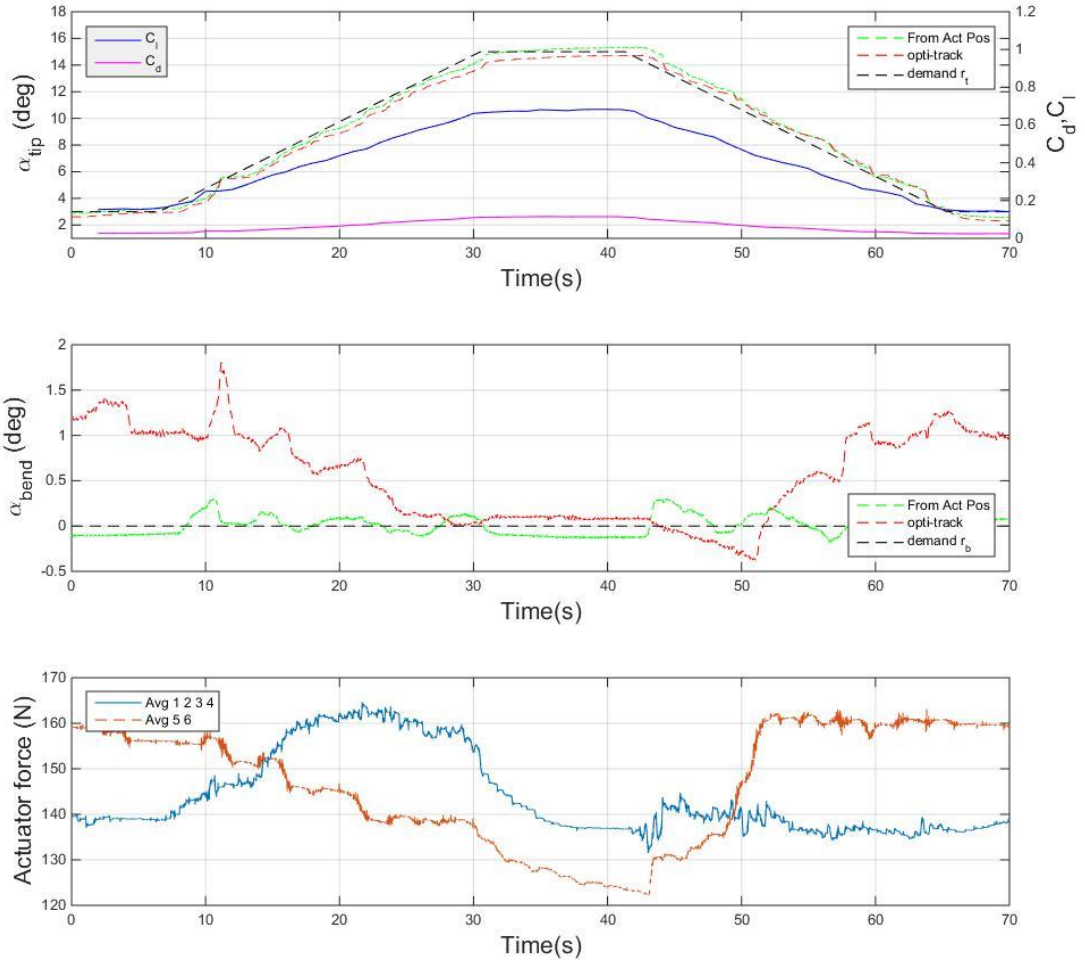

Figure 7.4 α_{tip} and α_{bend} optical tracker and actuator sensor angles, and actuation force, at α_{root} =3°, v=12.5m/s

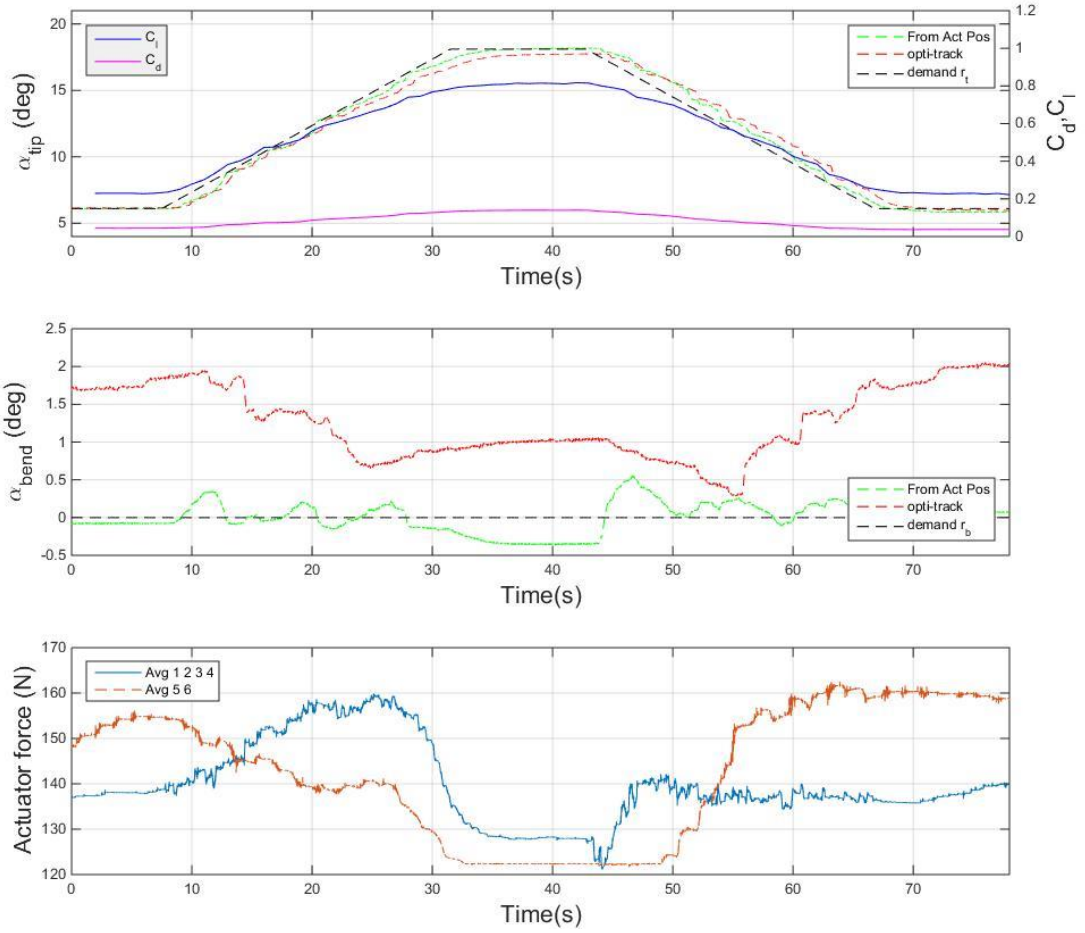

Figure 7.5 α_{tip} and α_{bend} optical tracker and actuator sensor angles, and actuation force, at α_{root} =6°, v=12.5m/s

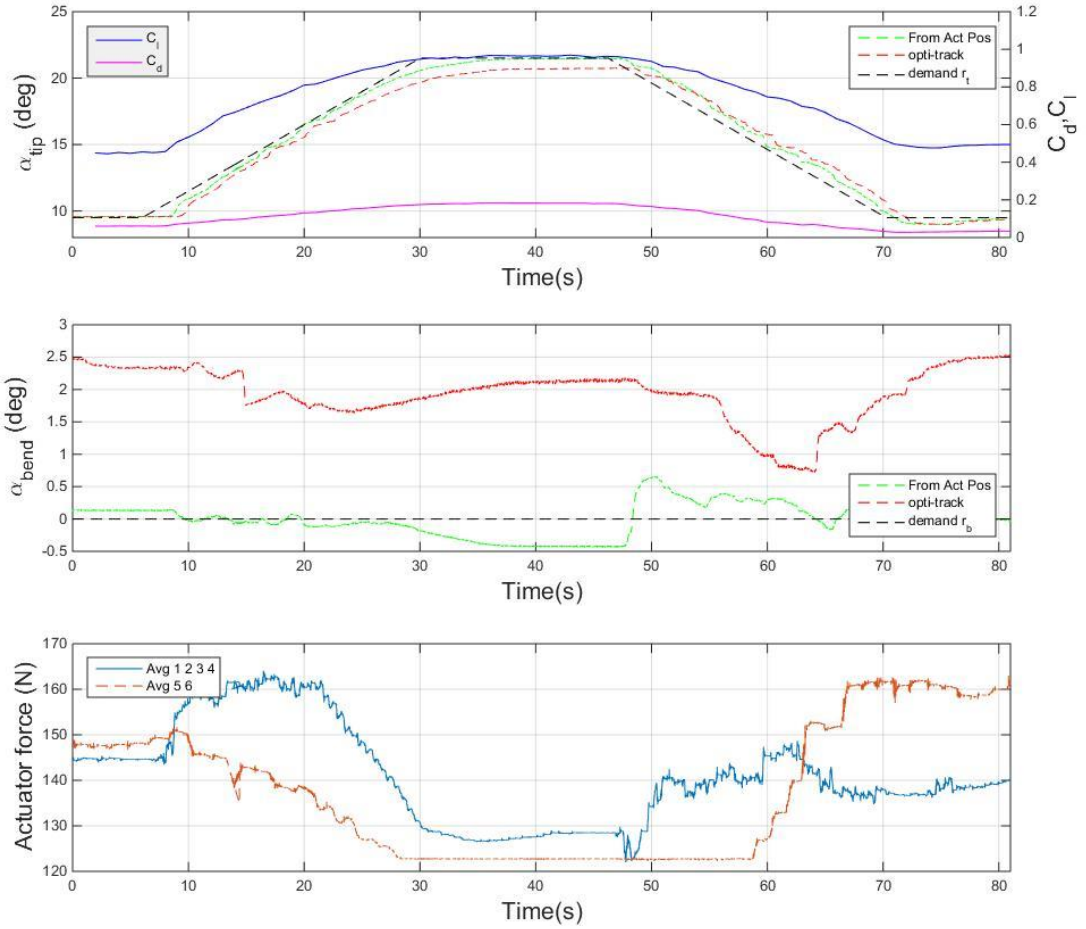

Figure 7.6 α_{tip} and α_{bend} optical tracker and actuator sensor angles, and actuation force, at α_{root} =9°, v=12.5m/s

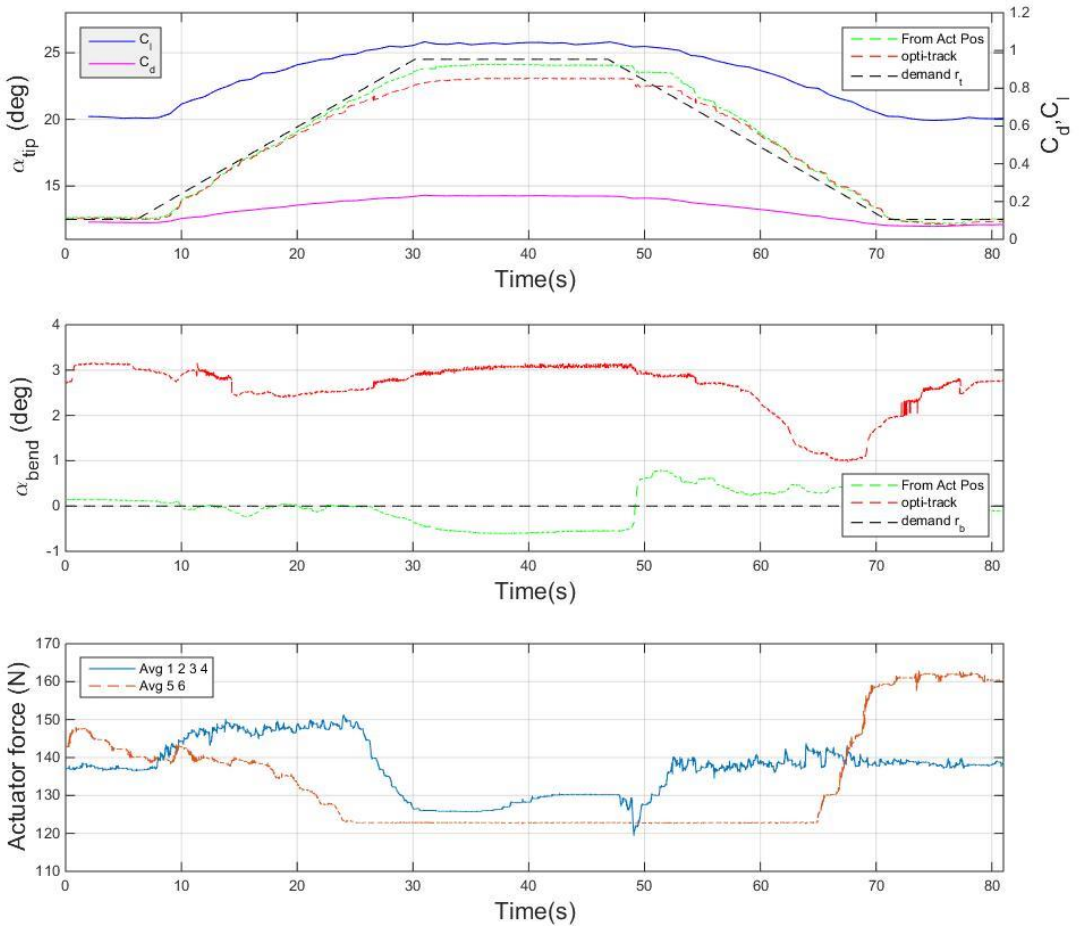

Figure 7.7 α_{tip} and α_{bend} optical tracker and actuator sensor angles, and actuation force, at α_{root} =12°, v=12.5m/s

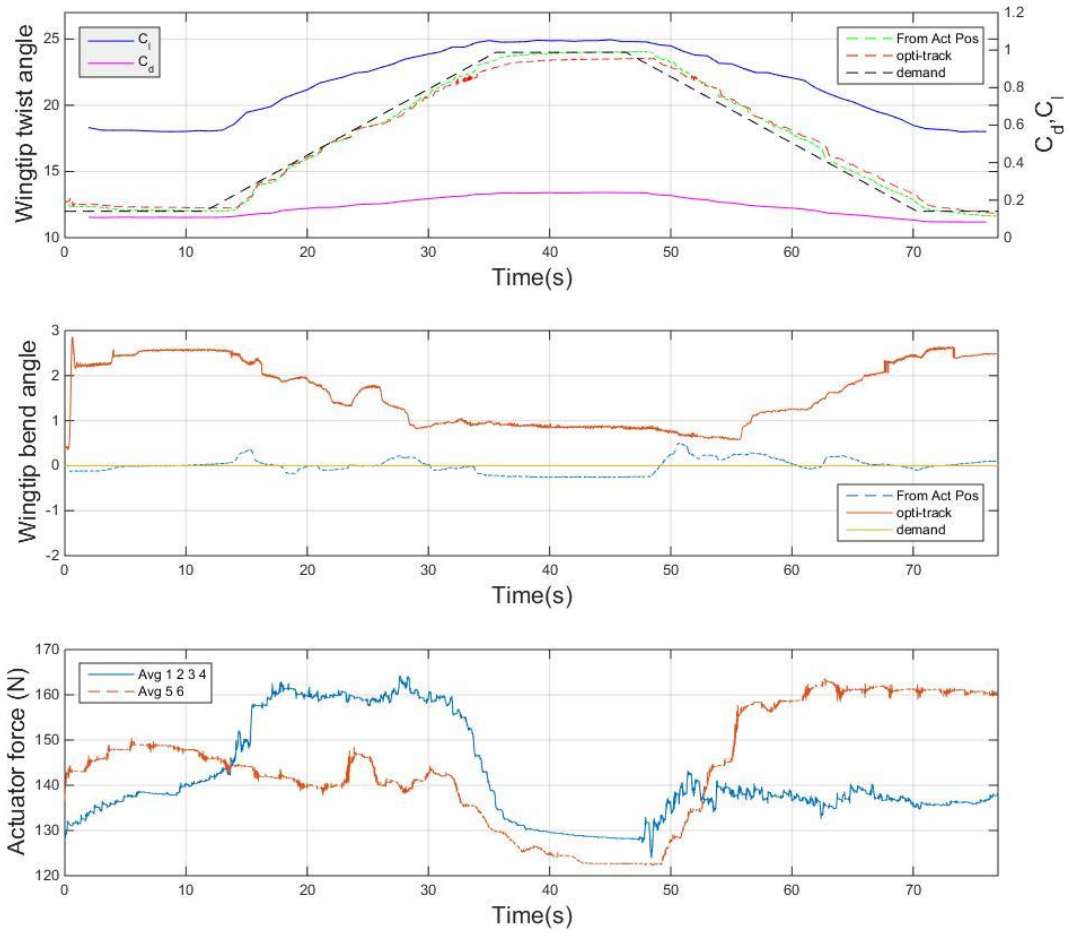

Figure 7.8 α_{tip} and α_{bend} optical tracker and actuator sensor angles, and actuation force, at α_{root} =12°, v=10m/s

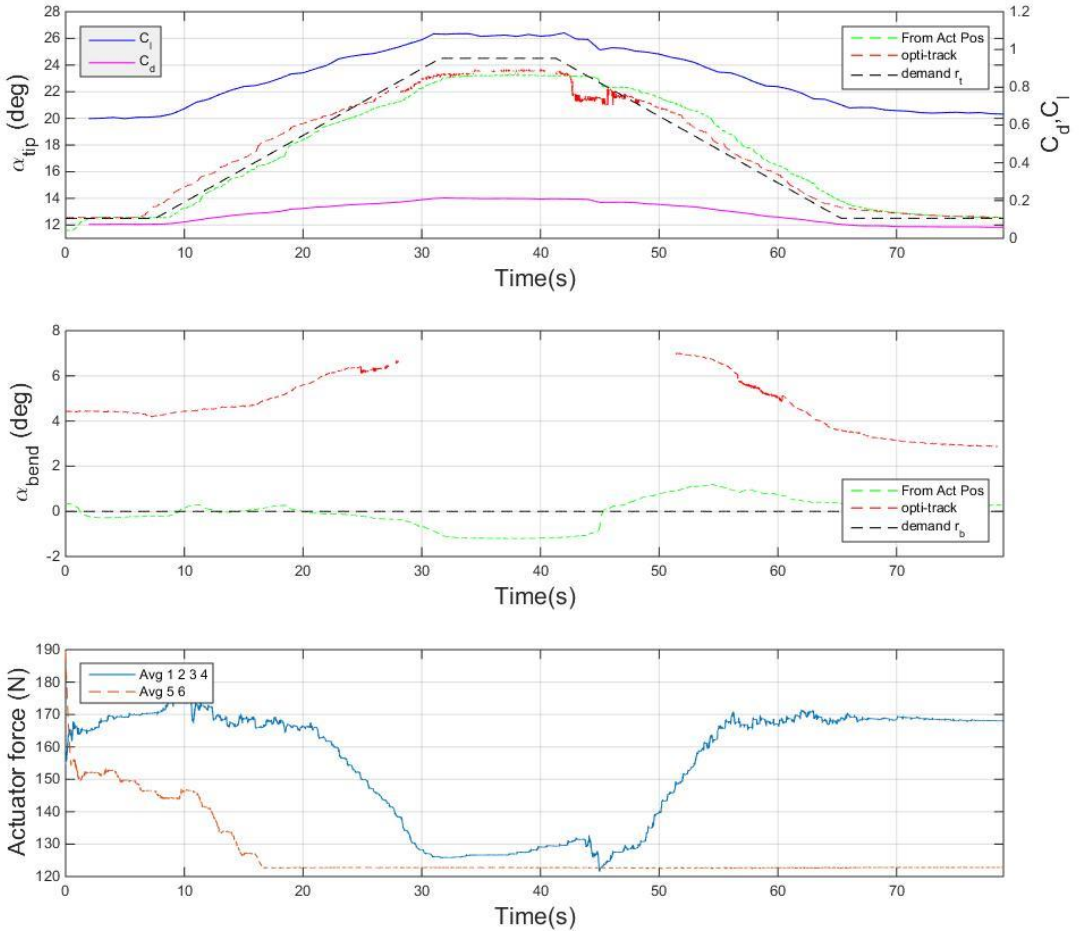

Figure 7.9 α_{tip} and α_{bend} optical tracker and actuator sensor angles, and actuation force, at α_{root} =12°, v=15m/s

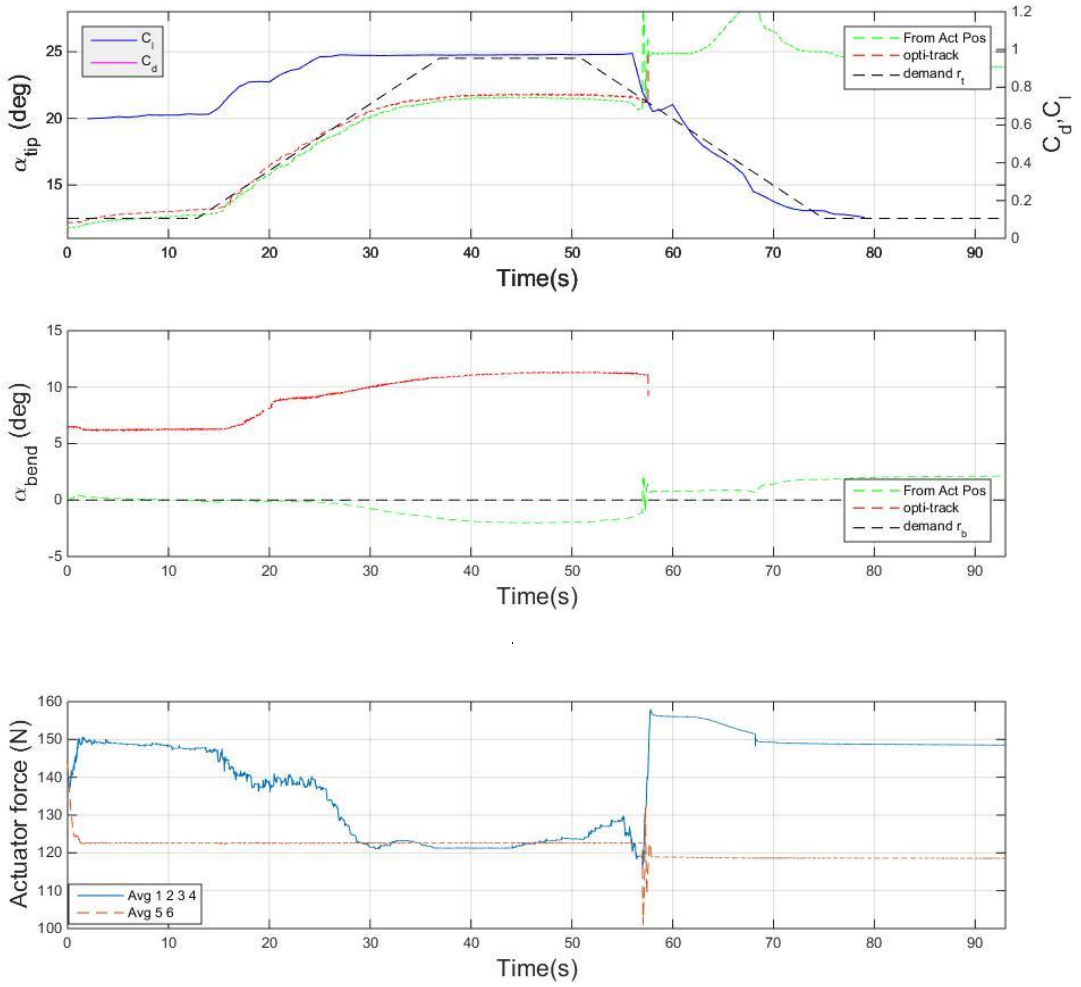

Figure 7.10 α_{tip} and α_{bend} optical tracker and actuator sensor angles, and actuation force, at α_{root} =12°, v=17.5m/s

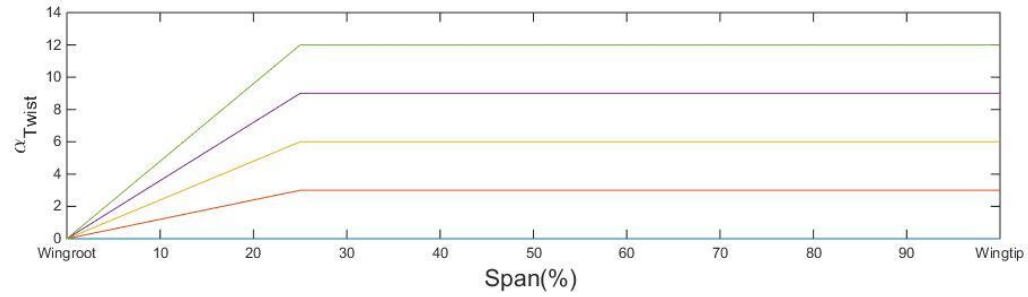

Figure 7.11 Expected wing twist distribution along span

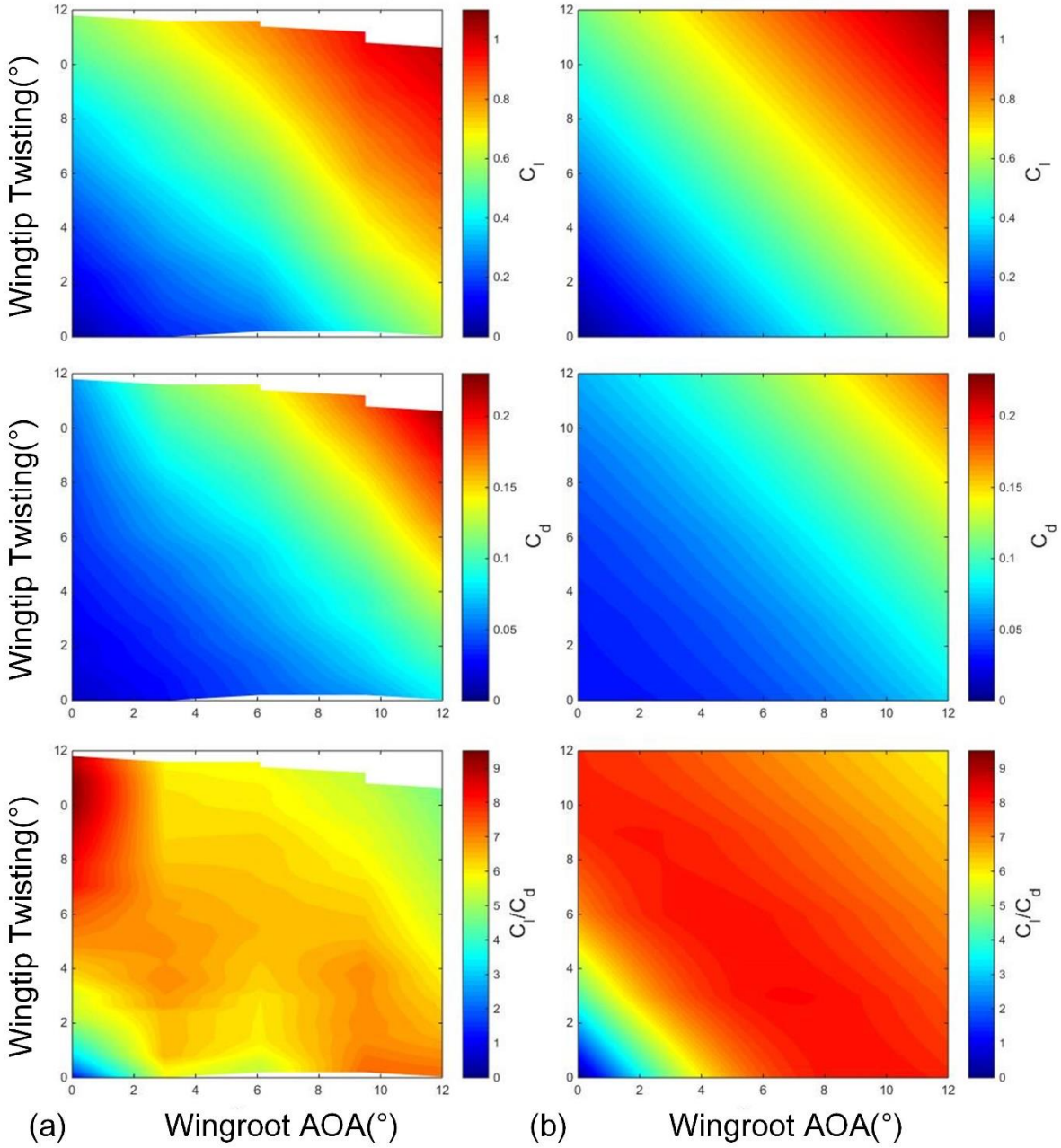

Figure 7.12 C_l, C_d and C_l/C_d contour for v=12.5m/s

(a): experimental, (b): simulation

7.1.2 XFLR5 simulation results

A wing simulation is performed using the XFLR5 software package, to compare with the wind tunnel results and show if the aerodynamic performance of the prototype

morphing wing is as expected. The simulation uses a fixed wind speed of 12.5m/s, and a 3D panels model with potential flow assumption, following the method introduced in (Maskew 1987). The panel method is selected due to its good performance when modelling high Reynolds Number (>10^5, in this case Reynolds Number is 6.61×10^5), subsonic conditions (Mach number<<1), and with no rotational flow conditions(Katz and Plotkin 2001).

The model is calculated by the constant-strengths doublet/source method with Dirichlet boundary condition; source and doublet densities are uniform on each panel. For better numerical precision, lift and drag are calculated on a far field plane using Kutta-Joukowski's theorem, instead of using summation of each panel force(Deperrois 2019), as illustrated in Figure 7.13. The lift is given by:

$$L = -b\rho v\Gamma \tag{7.1}$$

$$\Gamma = \oint_C v_l \bullet ds = \oint_C v_l \cos\theta ds \tag{7.2}$$

where b is the span, ρ and v are the freestream density and velocity, and Γ is the circulation defined as the line integral around a closed contour C, which encloses the airfoil in the anti-clockwise direction. And $v_l \cos\theta$ is the component of the local air velocity in the direction tangential to the curve C, and ds is an infinitesimal length on the curve C.

The predicted drag could be inaccurate using the Panel method, as only form drag has been considered in the model, and skin–friction drag is not taken into account, which could be significant in low AOA conditions. A constant extra drag coefficient component of 0.024 is added for compensation, which uses the experimental

measured C_d value with α_{root} = 0° and α_{twist} = 0°.

A mirrored wing was built for the simulation; each half had the same dimensions as the prototype wing. The twist angles α_{twist} distribution alone span as shown in Figure 7.11 was applied to the simulation model. Results for wing root angles α_{root} = 0, 3, 6, 9, 12° and twist angles α_{twist} = 0, 3, 6, 9, 12° were recorded. An example of α_{root} = 12°, α_{twist} = 9° is shown in Figure 7.14. The results of the simulations are shown in the C_l, C_d and C_l/C_d contour plots of Figure 7.12 (right).

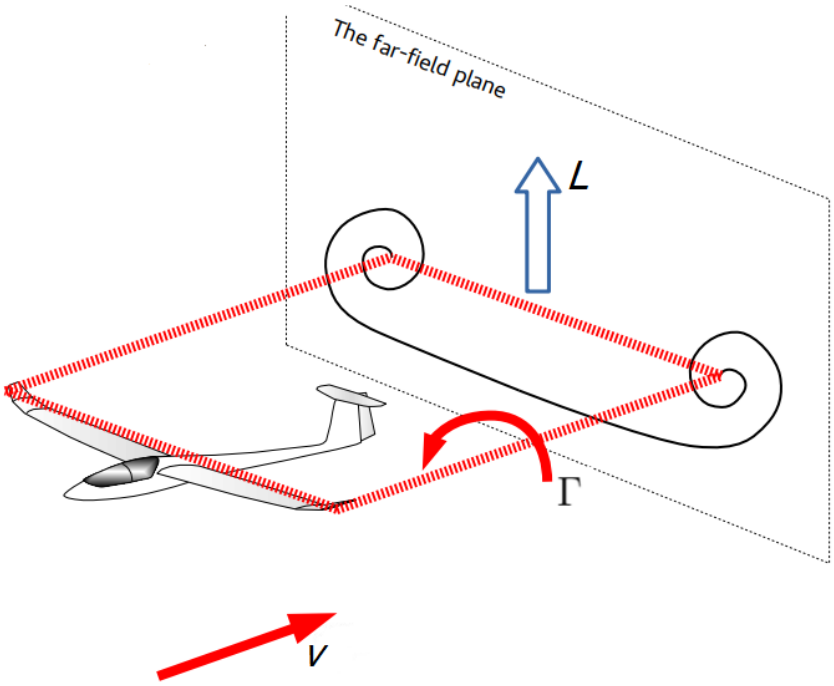

Figure 7.13 Far-field plane method for lift calculating(Deperrois 2019)

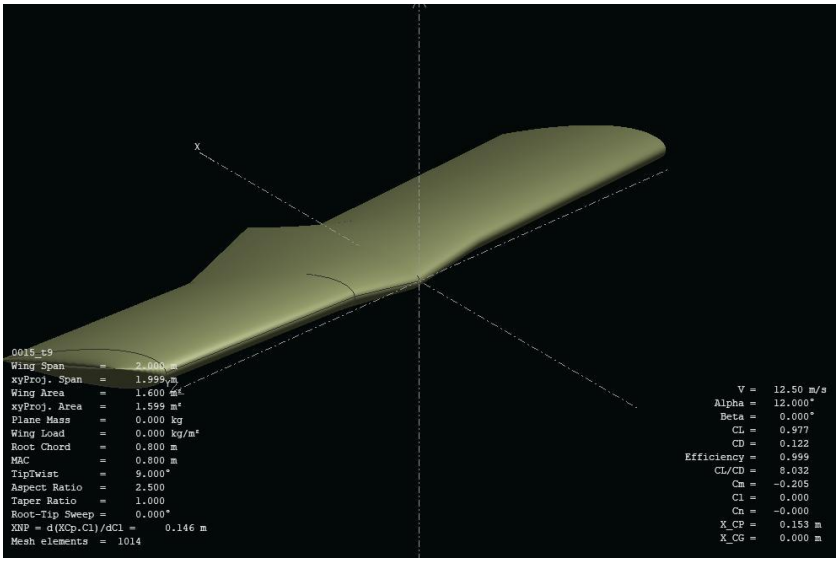

Figure 7.14 XFLR5 simulation panel with α_{root} = 12°, α_{twist} = 9°

7.1.3 Discussion of twist wind tunnel tests

In terms of motion control while under load, from Figures 7.3 and 7.4, the twist angle of the wing at small wing root angle ($\alpha_{root} \leq 3°$) followed the ramp demand signal r_t closely with very small steady state errors. From Figures 7.5, 7.6 and 7.7, with larger wing root angle ($\alpha_{root} \geq 6°$), the demand signal r_t is tracked quite well at small twist angles α_{twist}. When α_{twist} increased with the demand, the forces in actuators 5 and 6 reached their minimum (zero) and maximum values, and the twist angle no longer accurately tracked the demand. This is first observed in Figure 7.5 at 32s, and resulted in steady state errors seen in Figures 7.6 and 7.7.

The controller worked effectively through the actuator position sensor feedback, with a maximum error of ±1° during transients. The bending motion measured by the optical tracker shows there were offsets on initial wingtip bending. The bending happened at the wing root, indicating that the stiffness of the structure near the root in the bending direction was insufficient. There was a small amount of coupling between

wingtip twisting and bending as shown in Figures 7.4 and 7.5.

There was some disturbance in internal force control during the angle demand ramp period, but the controller has successfully maintained the internal force to keep the structure stable when the external loads were increasing, and to keep the internal load approaching the demanded values when the external loads were released. As already noted, the internal force feedback shows the actuation force was not enough to hold the demanded internal load as shown in Figure 7.5 at 32s, Figure 7.6 at 28s and Figure 7.7 at 24s. An averaged force of 125N is half of the maximum retraction force at 6 bar supply pressure, which indicates that one of the actuators in the 5/6 pair was pressurised to 6bar and the other was at 0 bar, giving the maximum force difference. The actuation force requirement is not only determined by the external load, but also the twist angle, and the further the structure is moved from the neutral position, the larger the required actuation force. As shown in Figures 7.9 and 7.10, the structure was still able to morph in high external load conditions, even though the actuators were force limited.

The relationships between wing aerodynamic performance, i.e. lift coefficient C_l, drag coefficient C_d and lift to drag ratio C_l/C_d, are plotted against α_{root} and α_{twist}. In the plots Figure 7.11 and contour Figure 7.12.

Figure 7.11 shows the expected twist angle distribution along the span; the twist was evenly distributed in the 0-25% span region from the wing root and the remained the same through to the wing tip as this is the rigid part of the test wing. The Figure 7.12 contour plot shows the aerodynamic characteristics of the wing as a result of the twist

morphing and different wing root angles. Theoretically the gradient of the C_l and C_d contours are 1:0.875, according to the integral of Figure 7.11, in which case the lift and drag are assumed to be evenly distributed along span. The gradient of the C_l from experiment is approximately 1:0.92, and C_d contours are approximately 1:0.9, with minor differences in the top-left corner. This indicates the twist and wing root angle offered about the same contributions to changing the lift and drag coefficients. This is expected as the majority of the wing area was at the maximum twist angle, while the wing tip region has a lower local lift coefficient in experimental practice, which will counteract the ratio to bring it closer to 1:1. The twist in wing shape gives an unneglectable effect on the aerodynamic characteristics as α_{twist} gets larger, as the twisting region offers noticeable lower lift and drag, and this explains the gradient change at the top-left corner in C_d and C_l / C_d contours. The C_l/C_d contour shows the efficiency of the wing at different α_{twist} and α_{root} combinations. The gradients show an approximate symmetry about the 45° axis, and the region of high values when the summation of α_{twist} and α_{root} is around 10.5°. The highest value point appears in the top-left corner when $\alpha_{twist} = 10.5°$

The gradients of the C_l contour is 1:0.862 and, the gradients for the C_d contour is 1:0.868 in the XFLR5 simulated results. The gradients at the top-left corners (i.e. high angle values) have minor differences but not as much as the experiment results. The lift coefficient values C_l match the test results well in all cases, while drag results from the simulation were considerably lower. This is clearly shown in the C_l/C_d contour, which has a good symmetry about the 45° axis, and the region of highest values when

the summation of α_{twist} and α_{root} is around 9.5°. The highest value point appears in the top-left corner when α_{twist} = 9.5° and α_{root} = 0°, which is 1° lower than in the experimental results. The simulation contour looks considerably warmer overall, while in extreme cases (highest C_l/C_d at α_{twist} = 10.5° and α_{root} = 0° in experiment result), the experiment and simulation result matches well.

And comparing the α_{root} = 0°, α_{twist} =12° case with α_{root} = 12°, α_{twist} =0° case, the former one has a higher lift-to-drag ratio, indicating that wing twist morphing is a higher efficiency solution compared to the wing root angle change in this case. It might be the outcome of wing wash-in effect. The flexible skin may also be a reason, a non-ideal airfoil profile due to the Poisson's ratio of the latex skin producing some distortion along the span.

The differences in two sets of contours were mainly caused by the difference in drag coefficient, i.e., the drag coefficient is generally higher by an average of 18% in the experiment than the simulations. There are three possible reasons for this: i) the inviscid method used in the simulation, the inaccurate viscous friction could be an important part of the drag; ii) the imperfections in the manufacturing process and materials used for the skin of the experimental wing give a non-smooth finish on the trailing edge, and a non-ideal airfoil profile as previously mentioned; iii) high uncertainty in the measurement of drag coefficient due to the small magnitude of the drag force relative to the moments and the cross-axis interaction from lift.

Some optical track data loss happened as shown in Figure 7.9, which was a non-extreme condition. A singular point caused by the arrangement of camera and

reflective pods might be reached, which causes the loss of tracking, it might be solved by adding additional cameras.

A structural failure happened as shown in Figure 7.10, when the prototype wing was starting to twist back from its max available twist angle, in the 17.5m/s wind speed test. A cable tensile failure happened at 56s, causing the structure to immediately become unstable and uncontrollable. The wind tunnel was stopped with emergency controls after the failure happened.

7.2 Bend motion

In this series of tests, the bend angle of the wing tip relative to the wing root was controlled. Starting from α_{bend} = 0°, the wing was bended to 4° with a constant ramp rate of 0.5°/s, then held stationary for 12s and twisted back to α_{bend} = 0° at -0.5°/s. Wind speed of 12.5m/s were used for all the cases with wing root angle αroot = 0°, 3° , 6° , 9° and 12°.

7.2.1 Bend motion wind tunnel test result

The prototype wing in un-morphed and twisting position of 12° is shown in Figure 7.15. The set of data shown in Figures 7.16- 7.20 was recorded with ambient temperature 20° and wind speed v =12.5m/s, with αroot = 0°, 3°, 6°, 9°and 12°.

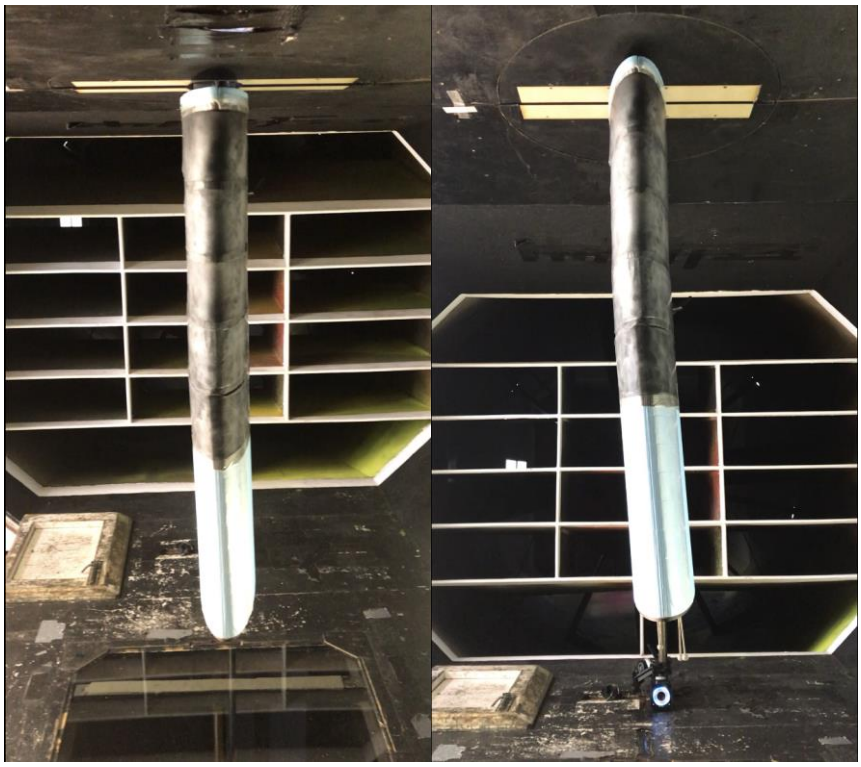

Figure 7.15 Prototype wing in neutral and 4°bend (front view from flow direction)

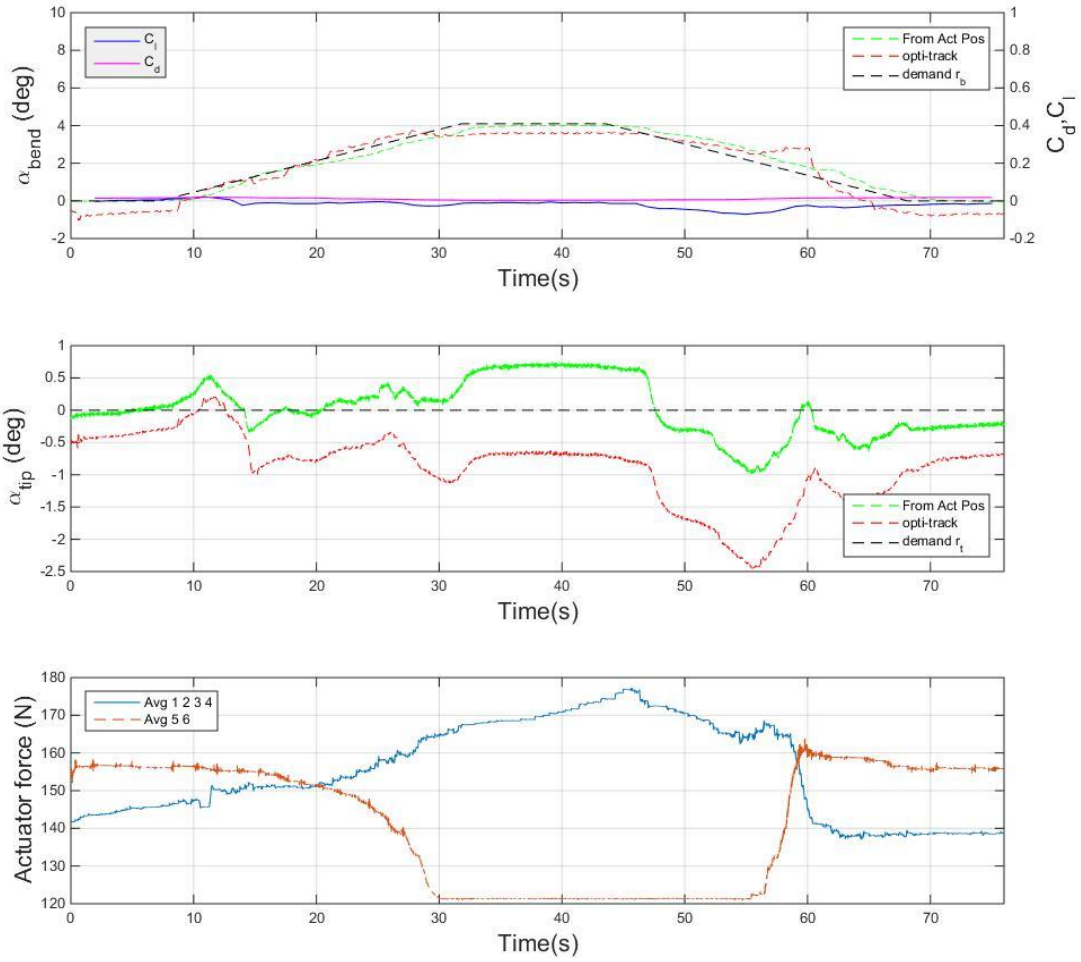

Figure 7.16 α_{bend} and α_{tip} optical track and sensor measure result with actuation force, at α_{root} =0°, v=12.5m/s

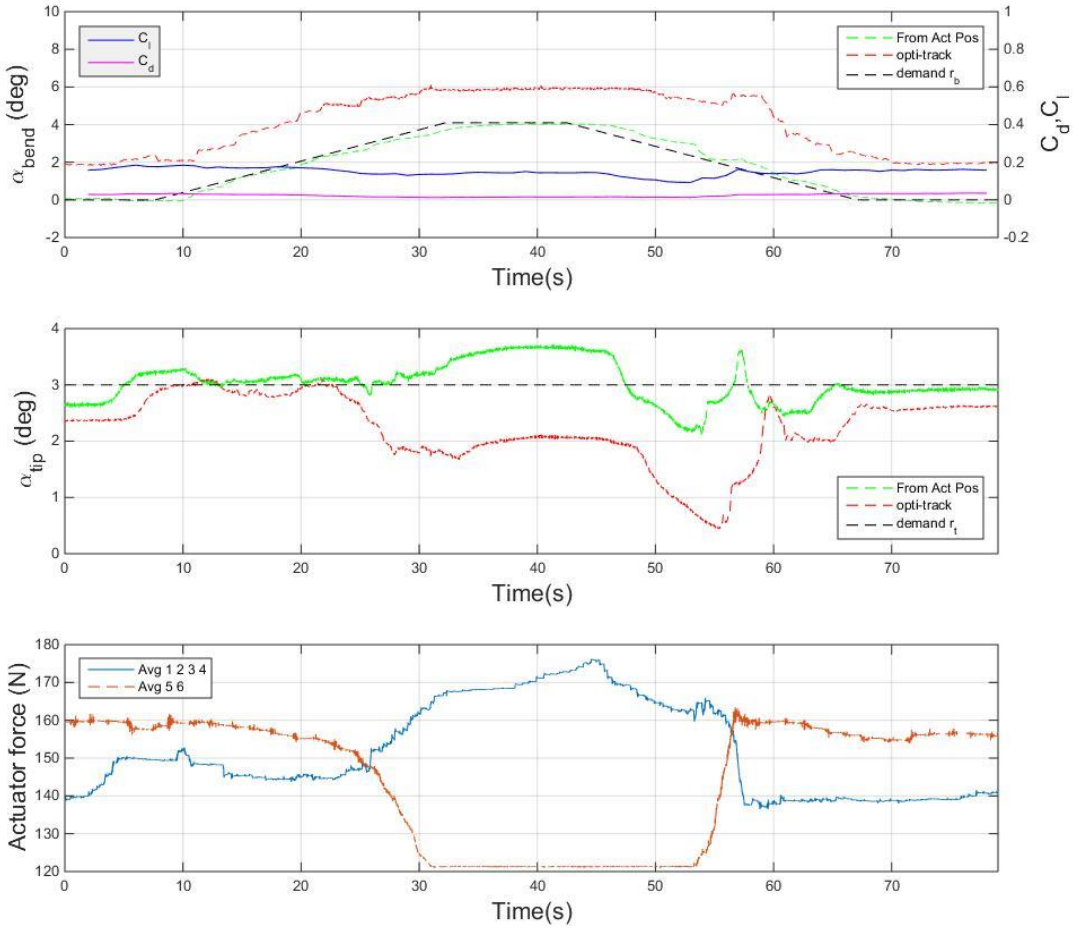

Figure 7.17 α_{bend} and α_{tip} optical track and sensor measure result with actuation force, at α_{root} =3°, v=12.5m/s

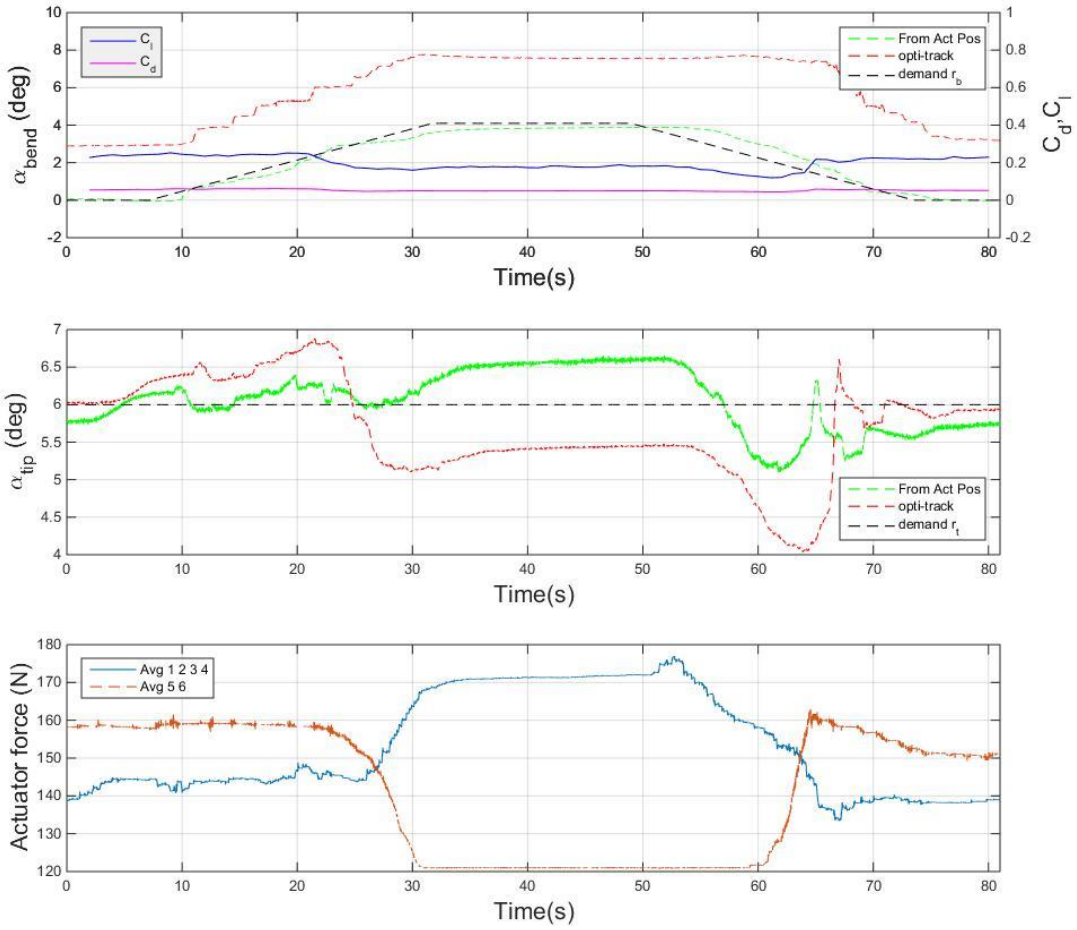

Figure 7.18 α_{bend} and α_{tip} optical track and sensor measure result with actuation force, at α_{root} =6°, v=12.5m/s

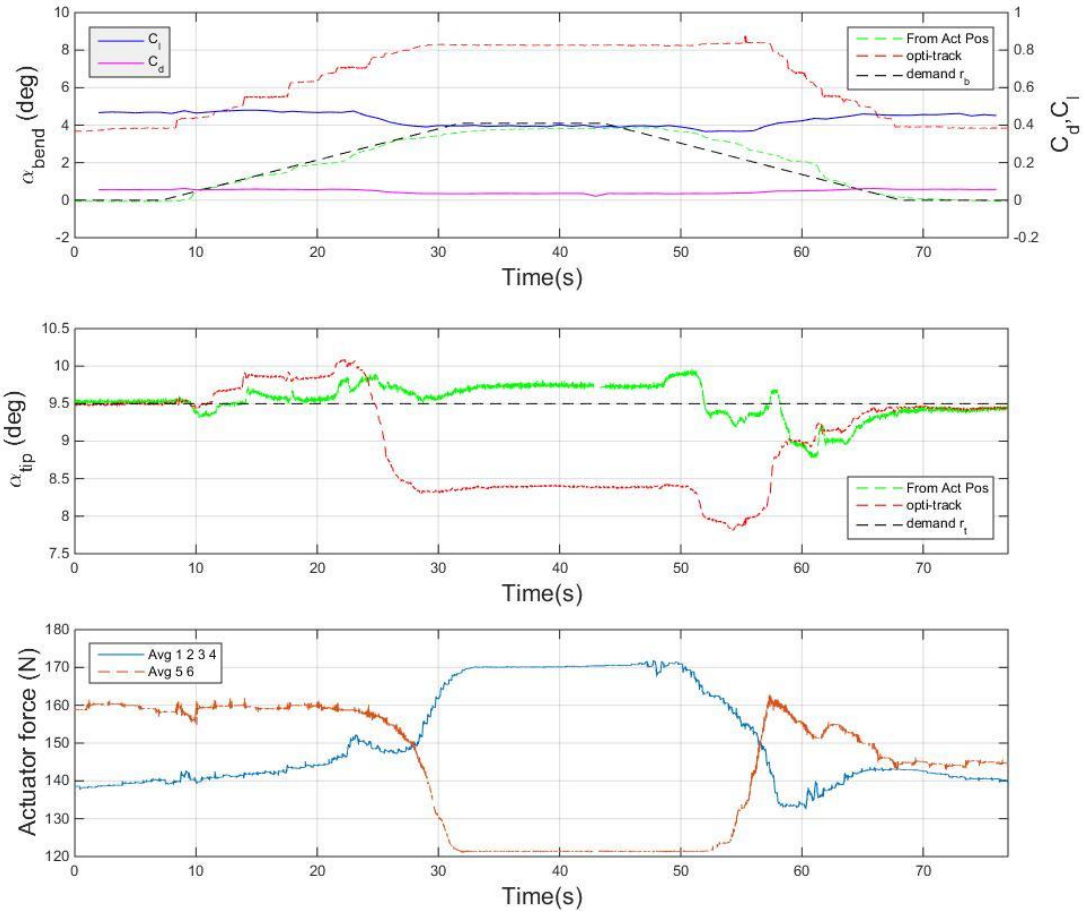

Figure 7.19 α_{bend} and α_{tip} optical track and sensor measure result with actuation force, at α_{root} =9°, v=12.5m/s

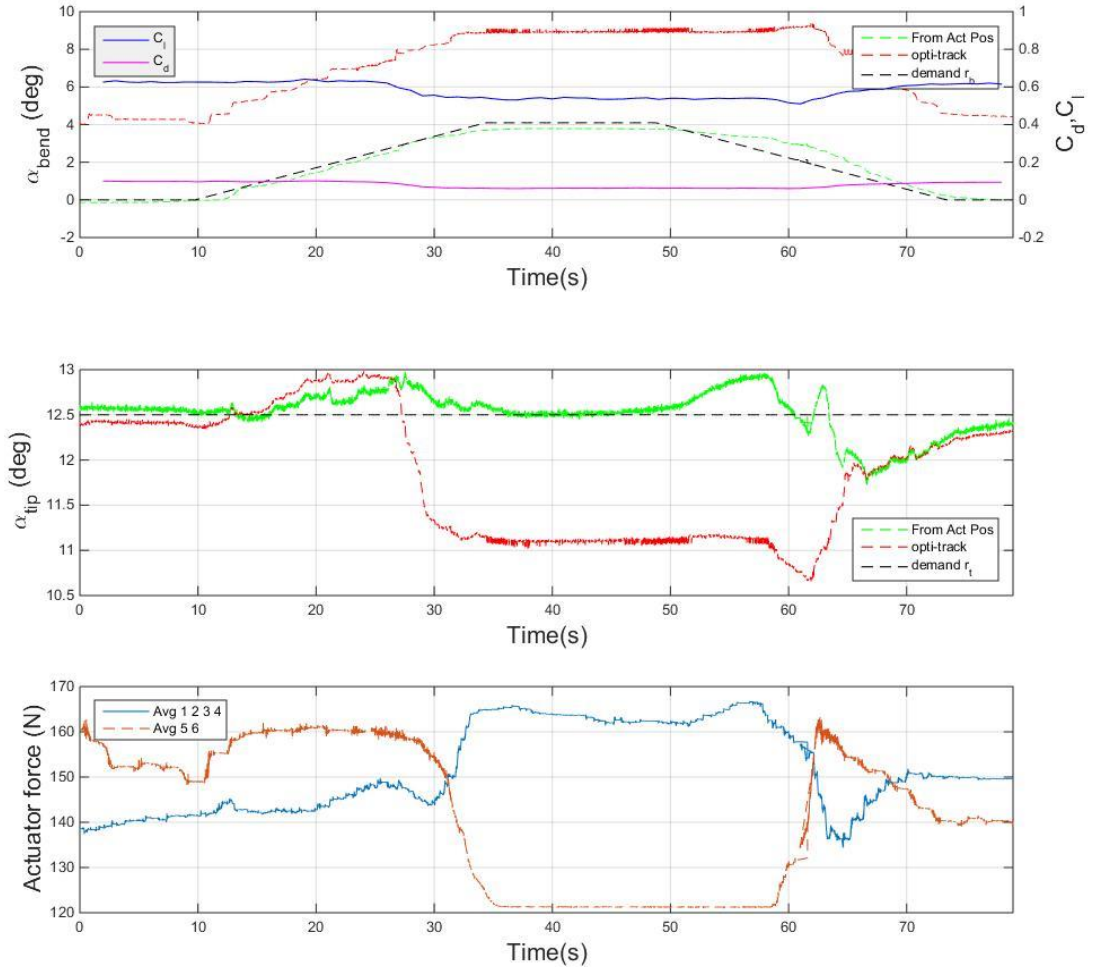

Figure 7.20 α_{bend} and α_{tip} optical track and sensor measure result with actuation force, at α_{root} =12°, v=12.5m/s

7.2.2 Discussions on bend wind tunnel tests

The morphing structure successfully tracked the ramp bend demand signal. The bend offsets observed in section 7.1 also appeared in bending tests, as indicated by the optical tracker measurements. The offset bending angles at the wing root were approximately the same values as in section 7.1. Based on the actuator position measurements the bend motion controller has successfully tracked the bend demand,

which is also indicated by the optical position sensing when the initial offset is accounted for. Note however that for α_{root} =6° (Figure 7.18) and larger, the response for reducing bend angle has a significant delay, discussed later.

The bending motions produced did not have a noticeable contribution on the lift and drag of the wing. The C_l and C_d changes during the morphing were produced by the cross coupled twisting motion. The twist disturbance was within about ±1° based on actuator position measurements, and slightly more from the optical tracker, and only brought minor lift and drag coefficient changes.

The actuation force required for bending was higher than the twisting, especially in actuator pair 5/6. From Figure 7.16, the actuator pair 5/6 was giving maximum force difference to achieve the bending morphing. The bending motion response was not affected by the lack of actuation force for increasing bend angle. For reducing angle, the controller needed more time to change the force, which resulted in a significant delay in motion response. The delay in force response was quite significant for actuator pair 5/6, due to the prolonged lack of actuation force for 15s creating a high integral component in the PID controller (i.e. integral wind-up), and this required a few seconds for the controller to override, causing the delay. Applying an anti-windup controller would solve this.

7.3 Comparison between bench top and wind tunnel test

Optical tracker and actuator sensor angles (α_{tip} and α_{bend}), as well as the actuation force results for wind tunnel test at α_{root} =0°, v=12.5m/s, and bench top test results are compared in Figure 7.21 (rising ramp) and Figure 7.22 (falling ramp), prefix 'W' stands for wind tunnel result, 'B' stands for bench test result. In the bench top tests, the prototype structure is not attached to the ribs, which results in lower inertia and total mass. The internal load demand for bench top test is 140N, and for wind tunnel test is 150N with ±10N dead band.

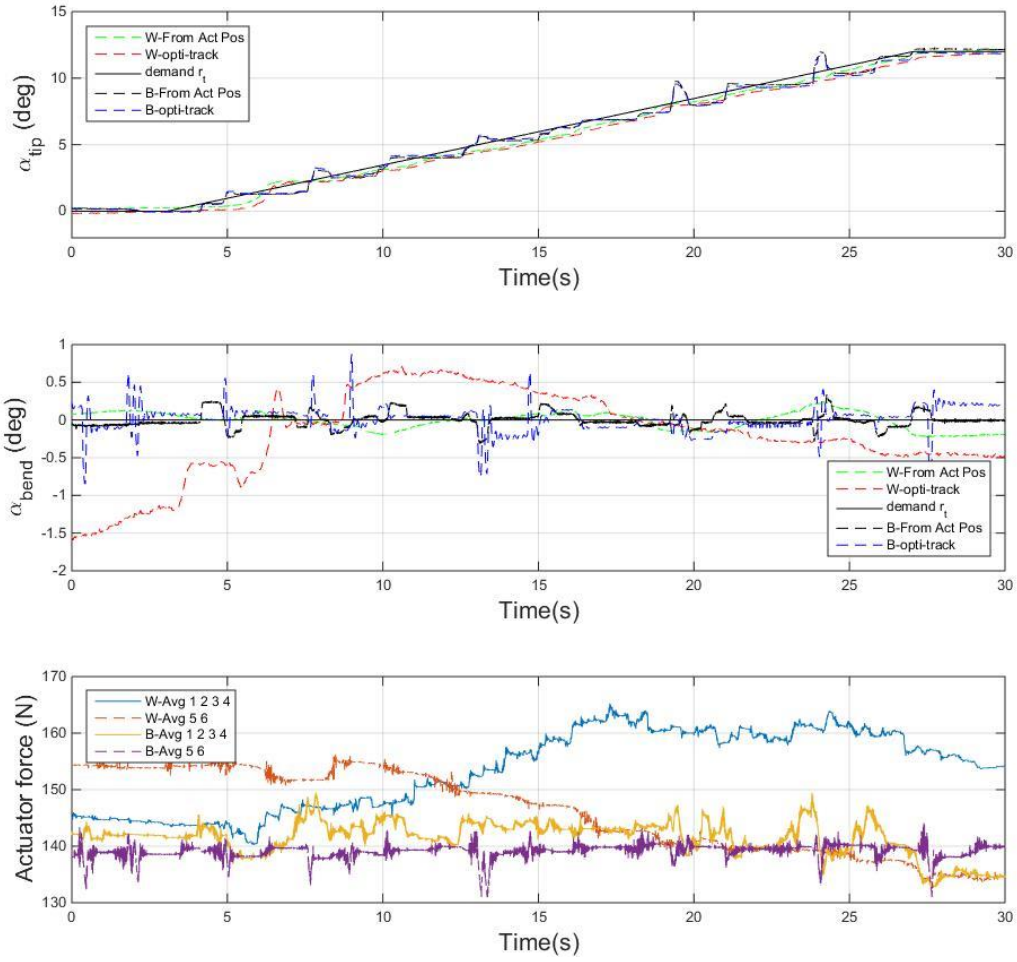

Figure 7.21 Optical tracker and actuator sensor angles with increasing twist, and actuation force, at α_{root} =0°, v=12.5m/s, compared with bench top test

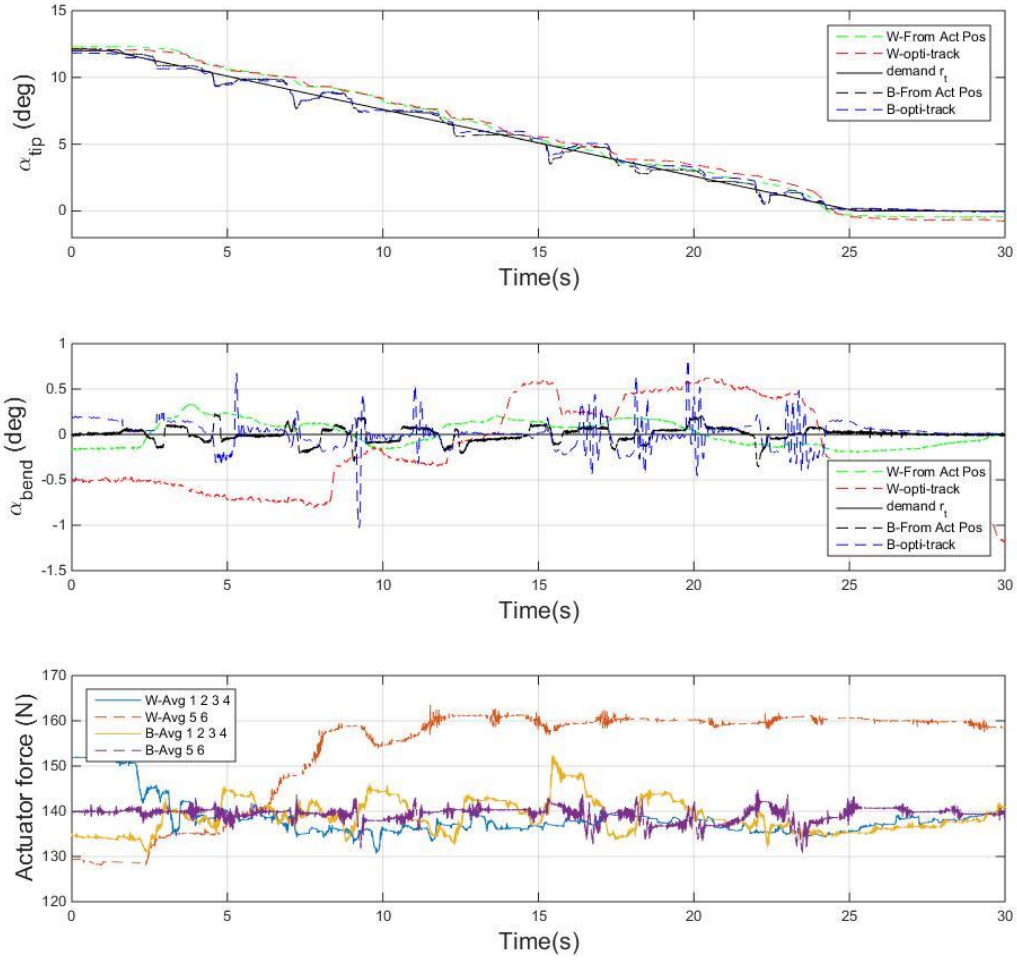

Figure 7.22 Optical tracker and actuator sensor angles with decreasing twist, and actuation force, at α_{root} =0°, v=12.5m/s, compared with bench top test

The structure deformation satisfactorily tracked the twist command signal in both cases. For the prototype wing in the wind tunnel test, the structure experienced external load, which is expected to be roughly proportional to α_{tip}. Compared with the core tensegrity itself, the wing has high inertia (with attached nylon ribs and extension wing), and also increased damping due to the pre-stressed latex skin.

It can be found that, there's a 1.2s delay on twist response of the wing in the wind tunnel test. This probably is caused by the unbalanced inertia and external load, which increases the start-up (static) friction. Also the motion of prototype wing in the wind

tunnel is much smoother; no stepwise motion is observed during wind tunnel test. With similar actuation force, the higher inertia of the wing appears to smooth the motion. For the bend response, there is a 0.5° error in the wind tunnel optical tracker result (dotted red line), which is caused by the lack of stiffness at the wing root mounting. For both cases, the force control loop has kept the averaged actuation force reasonable close to the demanded value. With external load applied the in-cell actuators (AC1-AC4), are likely to have a higher load during the rising ramp and lower load during the falling ramp. The inter-cell actuators (AC5 and AC6) act oppositely, the trend is to have a lower load in rising ramp, while keep a high load when the wing is approaching its neutral position.

For bend motion in the wind tunnel, the external load (aerodynamic load) generated during morphing is minor, so the results are not directly compared with the bench top test in this chapter.

7.4 Conclusions

The prototype wing has been tested for twist and bend morphing under different AOA and wind speed conditions. The wing was morphing as demanded with high accuracy for the main controlling degree of freedom, and for the other DoF there was cross coupling during deformation and up to ±1° error when the structure was approaching a steady state. The results suggest that in practice the DOF of the tensegrity structure were not fully independent, which might be partly the result of the finite-node design.

Comparisons are made between the prototype wing wind tunnel test results and the

tensegrity structure bench top test results. The structure moved in a smoother way in the wind tunnel, but had a small lag of 1.2s. The smoother motion is probably due to the higher inertia and damping of the full wing compared to the tensegrity structure alone.

Overall the motion and force control worked well in the wind tunnel test. There is a good match between the kinematic calculation and real world deformation. The experimental prototype wing is able to achieve demanded morphing and maintain internal load, while different external aerodynamic loads are applied.

8 Conclusions and future work

Design, analysis and prototype testing of a modular tensegrity based smart structure have been presented in this thesis. An example combination of modular cells is proposed, which has six actuators and controls four shape changing degrees of freedom. Stiffness of the morphing wing is also controlled by adjusting the internal load of the tensegrity structure, while achieving the kinematic requirements. The main feature of the proposed design is to replace a conventional wingbox with a smart structure morphing wingbox, therefore enhancing the wing performance and efficiency.

8.1 Conclusions

The research concerns the study of a smart structure configuration, which is an actuated tensegrity structure. A class three active tensegrity structure with octahedral modular cells is proposed based on the previous examples of Variable Geometric Trusses, due to the stability and stiffness advantage. Unlike truss members, the load conditions for tensegrity structure members are simpler, with cables subjected to tensile load only, and struts only subjected to compression load in static equilibrium conditions (struts may exert tensile load in dynamic conditions or with changing external load). Compared with conventional truss members, tensegrity structure members can potentially be designed to be lighter, because they do not have to take bending loads. This feature gives tensegrity structures great potential for achieving a high stiffness-to-mass ratio. A case study of modular geometric refinement and complete design is presented, with considerations of external load, dimension

constraints and kinematic requirements. Kinematics analyses are focused on wing twist and spanwise bend DOF, which significantly improves the wing performance and efficiency in subsonic conditions. The relationship between tensegrity structure element axial length changes and structure shape changing is determined, which is an important step for a motion control research.

An experimental smart structure system has been designed and built. Struts and node geometries are specially adapted to connect to ribs for morphing wings. Six single-acting pneumatic cylinders are embedded for distributed actuation, and each cylinder is controlled by two solenoid on/off valves. A detailed dynamic model of the experimental smart structure system is developed, including the pneumatic system and multi-body simulation model for the structure. While the pneumatic system is modeled mathematically and programmed using Matlab®/Simulink®, the multi-body simulation model is developed with Matlab®/SimMechanics® to solve the multi-body motion equations. A multi-axis control scheme for motion and internal load control has been proposed, in which morphing motion demands are directly given in DOF form. The dynamic behavior of the proposed smart structure is investigated with motion control simulations with different shape demand signals and internal force levels.

Benchtop tests are carried out to justify the kinematic analysis and proposed control scheme and validate the simulation models. Motions of the smart structure are measured via two approaches: actuator embedded position transmitter measuring local displacement on each actuator then calculating with the proposed kinematics, and a commercial optical tracking system measuring the structure directly in Cartesian

coordinates. The effect of tensile member compliance on kinematics are discussed based on experimental results. Comparison between benchtop experimental results and corresponding simulation results are performed to further investigate structure dynamics. A good agreement is reached with step motion control, but for the slow and continuous motion, the stick-slip form of motion in simulations are not as obvious as observed in experiments. The possible reasons have been discussed, including inaccuracy in valve dynamic modeling and complexity in strut-to-node joints friction characteristics.

Wind tunnel tests are carried out to investigate the capability of morphing with external load conditions. In addition, the aerodynamic behavior of the morphing wing is also validated. The prototype wing system has shown that it is able to precisely control motion with different external load conditions. With a continuous motion demand, the motion response in the wind tunnel is much smoother than benchtop results, which may be a result of higher inertia (with extended wing and ribs) and distributed external load. Wing morphing has been shown to improving wing efficiency (higher lift/drag ratio at same wingtip AOA), compared to a conventional stiff wing.

The overall concept of developing a load-bearing smart structure with shape-changing capability used a modular active tensegrity structure approach has been successfully justified. The multi-axis control scheme is capable of fulfilling the kinematic requirements while maintaining the demanded internal load. And the proposed smart structure has shown good performances in both benchtop tests and wind tunnel tests.

8.2 Future work

As an extension of the presented research, further investigations are recommended in the following aspects:

1. More modular cells and morphing DOF should be considered, which is not limited to plane form morphing (i.e. variation in camber may be considered), and the associated kinematics needs to be developed. Single cell geometry could be optimized for specified application (e.g. tapered cells for wingtips or finer mesh for more precise morphing). Improvements in structural stiffness, or minimizing weight, or increasing the capability for morphing may be considered, but optimization between these parameters would be challenging.
2. More research on dynamics of the multi-axis and multi DOF system needs to be undertaken. The control method should be refined for better response with continuous motion demands. It would be a challenge to develop a robust controller for structure shape changing with various internal and external load conditions.
3. From the actuation perspective, pneumatic actuation is good enough for concept validation. A compact actuation system needs to be developed for future application, as the sizing problems of the embedded actuator is one of the major challenges (finding actuators small enough for embedding) at the design stage for the presented prototype size. For larger scaled applications, it may be easier to have actuators with adequate stroke, and within the limited axial length. Actuation solutions should meet aviation standard (e.g. Electro-Hydrostatic actuators) for higher power density and

robustness. Or for UAVs, electric motor powered tendons, may be suitable, because the payload requirement is lower.

4. More requirements need to be addressed in the early design stage, with considerations for specific applications. For large aircraft morphing wings, the dimensions of embedded actuation systems should be taken into account, when scaling design of the morphing structure units is considered. An optimization should be made between target wing load, actuation system selection, increased mass, and structure stiffness. Detailed design considerations should be based on case studies, and will be discussed in future research.

5. For detailed structure design, friction on struts-to-node joints have a significant effect on precise motion control, and some low friction solutions should be considered. Similarly, cable soft-eye rings are used in this research due to dimension constraints and low payload requirements, but rose joints are recommended for larger scale applications.

6. Flexible skin design needs to be further developed. The proposed structure is load-bearing, which does not require aircraft skin to provide additional rigidity, so the pre-tensioned skin is designed independently. The presence of pre-tension in the flexible skin could be integrated into structural design as a tension member. The pre-tensioned latex skin worked fine in the wind tunnel test, but as an isotropic material with Poisson's ratio of approximate 0.5, the airfoil shape is not perfectly maintained as the wing changes shape, which will affect airfoil performance (especially on leading edge).

Some anisotropic or low Poisson's ratio materials should be considered in future research.

Publications:

1. Zhou, H., Plummer, A., & Cleaver, D. (2018). Closed Loop Position and Pre-Stress Control for a Morphing Aircraft Wing With Distributed Multi-Axis Pneumatic Actuation. Paper presented at the BATH/ASME 2018 Symposium on Fluid Power and Motion Control.

2. Zhou, H., Plummer, A., & Cleaver, D. (2018). Distributed Actuation of Tensegrity Structures for Morphing Aircraft wings. Paper presented at the MECHATRONICS 2018 - Reinventing Mechatronics, University of Strathclyde, Glasgow, UK.

3. Lai, G., Plummer, A., Cleaver, D., & Zhou, H. (2016). Parallel kinematic mechanisms for distributed actuation of future structures. Paper presented at the Journal of Physics: Conference Series.

References

Abdulrahim, M. and R. Lind (2004). Flight testing and response characteristics of a variable gull-wing morphing aircraft. AIAA guidance, navigation, and control conference and exhibit.

Ajaj, R., E. S. Flores, M. Friswell, G. Allegri, B. Woods, A. Isikveren and W. Dettmer (2013). "The Zigzag wingbox for a span morphing wing." Aerospace Science and Technology **28**(1): 364-375.

Aldrich, J., R. Skelton and K. Kreutz-Delgado (2003). Control synthesis for a class of light and agile robotic tensegrity structures. Proceedings of the 2003 American Control Conference, 2003., IEEE.

Amouri, S., J. Averseng and J.-F. Dubé (2013). Active control design of modular tensegrity structures. Proceedings of IASS Annual Symposia, International Association for Shell and Spatial Structures (IASS).

Averseng, J. and B. Crosnier (2004). "Static and dynamic robust control of tensegrity systems." Journal of the International Association for Shell and Spatial Structures **45**(3): 169-174.

Averseng, J., J.-F. Dubé, B. Crosnier and R. Motro (2005). Active control of a tensegrity plane grid. Proceedings of the 44th IEEE Conference on Decision and Control, IEEE.

Barbarino, S., O. Bilgen, R. Ajaj, M. Friswell and D. Inman (2011). "A Review of Morphing Aircraft." Journal of Intelligent Material Systems and Structures **22**(9): 823-877.

Bharti, S., M. Frecker, G. Lesieutre and J. Browne (2007). Tendon actuated cellular mechanisms for morphing aircraft wing. Modeling, Signal Processing, and Control for Smart Structures 2007, International Society for Optics and Photonics.

Bourdin, P., A. Gatto and M. Friswell (2008). "Aircraft control via variable cant-angle winglets." Journal of Aircraft **45**(2): 414-423.

Bowman, J., B. Sanders, B. Cannon, J. Kudva, S. Joshi and T. Weisshaar (2007). Development of next generation morphing aircraft structures. 48th AIAA/ASME/ASCE/AHS/ASC Structures, Structural Dynamics, and Materials Conference.

Bubert, E., B. Woods, K. Lee, C. Kothera and N. Wereley (2010). "Design and Fabrication of a Passive 1D Morphing Aircraft Skin." Journal of Intelligent Material Systems and Structures **21**(17): 1699-1717.

Buckminster, F. R. (1962). Tensile-integrity structures, US Patent 3,063,521, 1962.

Caluwaerts, K., J. Despraz, A. Iscen, A. Sabelhaus, J. Bruce, B. Schrauwen and V. SunSpiral (2014). "Design and control of compliant tensegrity robots through simulation and hardware validation." Journal of the Royal Society Interface **11**(98).

Chan, W. L., D. Arbelaez, F. Bossens and R. E. Skelton (2004). Active vibration control of a three-stage tensegrity structure. Smart Structures and Materials 2004: Damping and Isolation, International Society for Optics and Photonics.

Chen, P., D. Sarhaddi, R. Jha, D. Liu, K. Griffin and R. Yurkovich (2000). "Variable stiffness spar approach for aircraft maneuver enhancement using ASTROS." Journal of Aircraft **37**(5): 865-871.

Clarke, R., M. Allen, R. Dibley, J. Gera and J. Hodgkinson (2005). Flight test of the F/A-18 active aeroelastic wing airplane. AIAA Atmospheric Flight Mechanics Conference and Exhibit.

Connelly, R. and A. Back (1998). "Mathematics and tensegrity." American Scientist **86**(2): 142-151.

Dayyani, I., H. Khodaparast, B. Woods and M. Friswell (2015). "The design of a coated composite corrugated skin for the camber morphing airfoil." Journal of Intelligent Material Systems and Structures **26**(13): 1592-1608.

Deperrois, A. (2019). "Why does a plane fly: the inviscid potential flow." 1.1. Retrieved 5/27, 2019, from http://www.xflr5.com/docs/Part%20II:%20The%20inviscid%20problem_rev1.1.pdf.

Djouadi, S., R. Motro, J. Pons and B. Crosnier (1998). "Active control of tensegrity systems." Journal of Aerospace Engineering **11**(2): 37-44.

Emmerich, D. G. (1996). "Emmerich on self-tensioning structures." International Journal of Space Structures **11**(1-2): 29-36.

European Commission. Group of Personalities. and European Commission. European Commissioner for Research. (2001). European aeronautics : a vision for 2020 : meeting society's needs and winning global leadership. Luxembourg, Office for the Official Publications of the European Communities.

FESTO. (2018). "Compact cylinders ADN/AEN, to ISO 21287." Retrieved 5/24, 2019, from https://www.festo.com/cat/en-gb_gb/data/doc_engb/PDF/EN/ADN_EN.PDF.

FESTO. (2018). "Position transmitters SMAT-8M, for T-slot." Retrieved 5/10, 2019, from https://www.festo.com/cat/en-gb_gb/data/doc_engb/PDF/EN/SMAT-8M_EN.PDF.

FESTO. (2018). "Pressure transmitters SPTE." Retrieved 05/10, 2019, from https://www.festo.com/cat/en-gb_gb/data/doc_engb/PDF/EN/SPTE_EN.PDF.

FESTO. (2018). "Round cylinders DSNU/ESNU." Retrieved 5/24, 2019, from https://www.festo.com/cat/en-gb_gb/data/doc_engb/PDF/EN/DSNU_EN.PDF.

FULLCHANCE-INDUSTRIAL. (2018). "Latex Rubber Sheeting Grade S(Normal)- Technical Data Sheet." Retrieved 5/24, 2019, from http://www.rollsheetrubber.com/file/7338d4d6-e3b1-4143-87cf-e4022b7806a9.pdf.

Garcia, H., M. Abdulrahim and R. Lind (2003). Roll control for a micro air vehicle using active wing morphing. AIAA Guidance, Navigation, and Control Conference and Exhibit.

Gern, F., D. J. Inman and R. K. Kapania (2005). "Computation of actuation power requirements for smart wings with morphing airfoils." AIAA journal **43**(12): 2481-2486.

Guo, X., Z. Qiang and F. Xi (2016). "Design Segmented Stiff Skin for a Morphing Wing." Journal of Aircraft **53**(4): 962-970.

Huang, J., Q. Zhang, F. Scarpa, Y. Liu and J. Leng (2017). "In-plane elasticity of a novel auxetic honeycomb design." Composites Part B-Engineering **110**: 72-82.

Hughes, P. C., W. G. Sincarsin and K. A. Carroll (1991). "Trussarm—a variable-geometry-truss manipulator." Journal of Intelligent Material Systems and Structures **2**(2): 148-160.

Ivanco, T., R. Scott, M. Love, S. Zink and T. Weisshaar (2007). Validation of the Lockheed Martin morphing concept with wind tunnel testing. 48th AIAA/ASME/ASCE/AHS/ASC Structures, Structural Dynamics, and Materials Conference.

Jenett, B., S. Calisch, D. Cellucci, N. Cramer, N. Gershenfeld, S. Swei and K. C. Cheung (2017). "Digital morphing wing: active wing shaping concept using composite lattice-based cellular structures." Soft robotics **4**(1): 33-48.

Jha, A. K. and J. N. Kudva (2004). Morphing aircraft concepts, classifications, and challenges. Smart Structures and Materials 2004: Industrial and Commercial Applications of Smart Structures Technologies, International Society for Optics and Photonics.

Joo, J. J., B. Sanders, T. Johnson and M. I. Frecker (2006). Optimal actuator location within a morphing wing scissor mechanism configuration. Smart Structures and Materials 2006: Modeling, Signal Processing, and Control, International Society for Optics and Photonics.

Katz, J. and A. Plotkin (2001). Low-Speed Aerodynamics, Cambridge University Press.

Kebiche, K., M. Kazi-Aoual and R. Motro (1999). "Geometrical non-linear analysis of tensegrity systems." Engineering Structures **21**(9): 864-876.

Kenner, H. (1976). Geodesic math and how to use it. Berkeley ; London, University of California Press.

Koohestani, K. and S. Guest (2013). "A new approach to the analytical and numerical form-finding of tensegrity

structures." International Journal of Solids and Structures **50**(19): 2995-3007.
Krein, A. and G. Williams (2012). "Flightpath 2050: europe's vision for aeronautics." Innovation for Sustainable Aviation in a Global Environment: Proceedings of the Sixth European Aeronautics Days: 63.
Lai, G. (2017). "Distributed Actuation and Control for Morphing Structures."
Lai, G., A. Plummer, D. Cleaver and H. Zhou (2016). Parallel kinematic mechanisms for distributed actuation of future structures. Journal of Physics: Conference Series, IOP Publishing.
Liptak, B. G. Instrument Engineers' Handbook, Volume Two : Process Control and Optimization.
Love, M., P. Zink, R. Stroud, D. Bye, S. Rizk and D. White (2007). Demonstration of morphing technology through ground and wind tunnel tests. 48th AIAA/ASME/ASCE/AHS/ASC Structures, Structural Dynamics, and Materials Conference.
Manzo, J. and E. Garcia (2010). "Demonstration of an in situ morphing hyperelliptical cambered span wing mechanism." Smart Materials and Structures **19**(2): 025012.
Manzo, J., E. Garcia, A. Wickenheiser and G. C. Horner (2005). Design of a shape-memory alloy actuated macro-scale morphing aircraft mechanism. Smart Structures and Materials 2005: Smart Structures and Integrated Systems, International Society for Optics and Photonics.
Maskew, B. (1987). "Program VSAERO theory Document: a computer program for calculating nonlinear aerodynamic characteristics of arbitrary configurations."
Miura, K. (1984). "Design and operation of a deployable truss structure."
MIURA, K., H. FURUYA and K. SUZUKI (1985). "VARIABLE GEOMETRY TRUSS AND ITS APPLICATION TO DEPLOYABLE TRUSS AND SPACE CRANE ARM." Acta Astronautica **12**(7-8): 599-607.
Moored, K. and H. Bart-Smith (2007). "The analysis of tensegrity structures for the design of a morphing wing." Journal of Applied Mechanics-Transactions of the Asme **74**(4): 668-676.
Moored, K. and H. Bart-Smith (2009). "Investigation of clustered actuation in tensegrity structures." International Journal of Solids and Structures **46**(17): 3272-3281.
Moosavian, A., F. Xi and S. Hashemi (2013). "Design and Motion Control of Fully Variable Morphing Wings." Journal of Aircraft **50**(4): 1189-1201.
Moosavian, A., F. Xi and S. Hashemi (2014). "Optimal Configuration Design for the Variable Geometry Wing-Box." Journal of Aircraft **51**(3): 811-823.
Motro, R. (2003). Tensegrity: structural systems for the future, Elsevier.
Motro, R., S. Najari and P. Jouanna (1987). Static and dynamic analysis of tensegrity systems. Shell and Spatial Structures: Computational Aspects, Springer**:** 270-279.
Murakami, H. (2001). "Static and dynamic analyses of tensegrity structures. Part 1. Nonlinear equations of motion." International Journal of Solids and Structures **38**(20): 3599-3613.
Murakami, H. (2001). "Static and dynamic analyses of tensegrity structures. Part II. Quasi-static analysis." International Journal of Solids and Structures **38**(20): 3615-3629.
Murray, G., F. Gandhi and C. Bakis (2010). "Flexible Matrix Composite Skins for One-dimensional Wing Morphing." Journal of Intelligent Material Systems and Structures **21**(17): 1771-1781.
Nam, C., A. Chattopadhyay and Y. Kim (2002). Application of shape memory alloy (SMA) spars for aircraft maneuver enhancement. Smart structures and materials 2002: smart structures and integrated systems, International Society for Optics and Photonics.
National-Instruments. (2016). "DEVICE SPECIFICATIONS NI 6341." Retrieved 5/24, 2019, from http://www.ni.com/pdf/manuals/374566d.pdf.
Neal, D., M. Good, C. Johnston, H. Robertshaw, W. Mason and D. Inman (2004). Design and wind-tunnel analysis

of a fully adaptive aircraft configuration. 45th AIAA/ASME/ASCE/AHS/ASC Structures, Structural Dynamics & Materials Conference.

Nishimura, Y. and H. Murakami (2001). "Initial shape-finding and modal analyses of cyclic frustum tensegrity modules." Computer Methods in Applied Mechanics and Engineering **190**(43-44): 5795-5818.

O'Connor, R. (2003). An F-14 “Tomcat” fighter aircraft prepares for launch from the flight deck of the nuclear powered aircraft carrier USS Harry S. Truman (CVN-75). 030225-N-4308O-028. U. N.-N.-O.-A. F.-f. a. p. f. l. f. t. f. d. o. t. n. p. a. c. U. H. S. T. C. 75).jpg.

Olympio, K. and F. Gandhi (2012). "Optimal Cellular Core Topologies for One-Dimensional Morphing Aircraft Structures." Journal of Mechanical Design **134**(8).

Oppenheim, I. and W. Williams (2000). "Geometric effects in an elastic tensegrity structure." Journal of Elasticity **59**(1-3): 51-65.

Paul, C., F. Valero-Cuevas and H. Lipson (2006). "Design and control of tensegrity robots for locomotion." Ieee Transactions on Robotics **22**(5): 944-957.

PELLEGRINO, S. and C. CALLADINE (1986). "MATRIX ANALYSIS OF STATICALLY AND KINEMATICALLY INDETERMINATE FRAMEWORKS." International Journal of Solids and Structures **22**(4): 409-428.

Plummer, A. (2010). "A general co-ordinate transformation framework for multi-axis motion control with applications in the testing industry." Control Engineering Practice **18**(6): 598-607.

Plummer, A. and G. Lai (2015). New concepts for parallel kinematic mechanisms using fluid actuation. 7th International conference on Fluid Power and Mechatronics. Harbin.

Pugh, A. (1976). An introduction to tensegrity. Berkeley ; London, University of California Press.

Raja, M. and S. Narayanan (2007). "Active control of tensegrity structures under random excitation." Smart Materials & Structures **16**(3): 809-817.

Raja, M. G. and S. Narayanan (2007). "Active control of tensegrity structures under random excitation." Smart Materials and Structures **16**(3): 809.

Ramrakhyani, D., G. Lesieutre, M. Frecker and S. Bharti (2005). "Aircraft structural morphing using tendon-actuated compliant cellular trusses." Journal of Aircraft **42**(6): 1615-1621.

Rodrigue, H., S. Cho, M.-W. Han, B. Bhandari, J.-E. Shim and S.-H. Ahn (2016). "Effect of twist morphing wing segment on aerodynamic performance of UAV." Journal of Mechanical Science and Technology **30**(1): 229-236.

Sabelhaus, A. P., J. Bruce, K. Caluwaerts, P. Manovi, R. F. Firoozi, S. Dobi, A. M. Agogino and V. SunSpiral (2015). System design and locomotion of SUPERball, an untethered tensegrity robot. 2015 IEEE international conference on robotics and automation (ICRA), IEEE.

Sadao, S. (1996). "Fuller on tensegrity." International Journal of Space Structures **11**(1-2): 37-42.

Samuel, J. B. and D. J. Pines (2007). "Design and testing of a pneumatic telescopic wing for unmanned aerial vehicles." Journal of Aircraft **44**(4): 1088-1099.

Skelton, R., J. Pinaud and D. Mingori (2001). "Dynamics of the shell class of tensegrity structures." Journal of the Franklin Institute-Engineering and Applied Mathematics **338**(2-3): 255-320.

Skelton, R. E. and M. C. d. Oliveira (2009). Tensegrity systems. Dordrecht ; London, Springer.

SMC. (2015). "Series V100." Retrieved 11/19, 2018, from http://www.smcpneumatics.com/assets/images/pdf/V100.pdf.

Smith, D., A. Isikveren, R. Ajaj and M. Friswell (2010). Multidisciplinary design optimization of an active nonplanar polymorphing wing. 27th International Congress of The Aeronautical Sciences (ICAS).

Snelson, K. (1996). "Snelson on the tensegrity invention." International Journal of Space Structures **11**(1-2): 43-48.

Snelson, K. D. (1965). Continuous tension, discontinuous compression structures, US Patent 3,169,611, 1965.
Sofla, A., D. Elzey and H. Wadley (2007). "A rotational joint for shape morphing space truss structures." Smart Materials and Structures **16**(4): 1277-1284.
Sofla, A., D. Elzey and H. Wadley (2009). "Shape morphing hinged truss structures." Smart Materials & Structures **18**(6).
Spillman, J. (1992). "The use of variable camber to reduce drag, weight and costs of transport aircraft." The Aeronautical Journal **96**(951): 1-9.
Stamenovic, D., J. Fredberg, N. Wang, J. Butler and D. Ingber (1996). "A microstructural approach to cytoskeletal mechanics based on tensegrity." Journal of Theoretical Biology **181**(2): 125-136.
Stanford, B., M. Abdulrahim, R. Lind and P. Ifju (2007). "Investigation of membrane actuation for roll control of a micro air vehicle." Journal of Aircraft **44**(3): 741-749.
Sultan, C. (2009). "Tensegrity Structures: Sixty Years of Art, Science, and Engineering." Advances in Applied Mechanics **43,69-145**.
Sultan, C., M. Corless and R. Skelton (2000). "Tensegrity flight simulator." Journal of Guidance Control and Dynamics **23**(6): 1055-1064.
Sultan, C., M. Corless and R. Skelton (2001). "The prestressability problem of tensegrity structures: some analytical solutions." International Journal of Solids and Structures **38**(30-31): 5223-5252.
Sultan, C., M. Corless and R. Skelton (2002). "Symmetrical reconfiguration of tensegrity structures." International Journal of Solids and Structures **39**(8): 2215-2234.
Sun, J., H. Gao, F. Scarpa, C. Lira, Y. Liu and J. Leng (2014). "Active inflatable auxetic honeycomb structural concept for morphing wingtips." Smart Materials and Structures **23**(12): 125023.
TECHNI-CABLE. (2019). "Stainless Steel Cable and Wire Rope." Retrieved 5/24, 2019, from http://www.tecni-cable.co.uk/Products/Stainless-Steel-Cable-and-Wire-Rope.
Tennekes, H. (2009). The Simple Science of Flight: From Insects to Jumbo Jets, MIT Press.
Thill, C., J. Etches, I. Bond, K. Potter and P. Weaver (2010). "Composite corrugated structures for morphing wing skin applications." Smart Materials and Structures **19**(12).
Tran, H. and J. Lee (2013). "Form-finding of tensegrity structures using double singular value decomposition." Engineering With Computers **29**(1): 71-86.
Transport, D. f. (2013). UK Aviation Forecasts. London, Department for Transport,**:** 1 online resource.
Tressler, J., T. Clement, H. Kazerooni and A. Lim (2002). Dynamic behavior of pneumatic systems for lower extremity extenders. Proceedings 2002 IEEE International Conference on Robotics and Automation (Cat. No. 02CH37292), IEEE.
U.S., A. (1966). The North American XB-70A V*alkyrie* (s/n 62-0207) just before the collision, 8 June 1966. N. A. X.-A. V. i. f. 061122-F-1234P-036.jpg, National Museum of the U.S. Air Force. **061122-F-1234P-036**.
Ursache, N., T. Melin, A. Isikveren and M. Friswell (2007). Morphing winglets for aircraft multi-phase improvement. 7th AIAA ATIO Conf, 2nd CEIAT Int'l Conf on Innov and Integr in Aero Sciences, 17th LTA Systems Tech Conf; followed by 2nd TEOS Forum.
Ursache, N. M., T. Melin, A. T. Isikveren and M. I. Friswell (2008). Technology integration for active poly-morphing winglets development. ASME 2008 Conference on Smart Materials, Adaptive Structures and Intelligent Systems, American Society of Mechanical Engineers.
Weisshaar, T. A. (2006). Morphing aircraft technology-new shapes for aircraft design, PURDUE UNIV LAFAYETTE IN.
Weisshaar, T. A. (2013). "Morphing aircraft systems: historical perspectives and future challenges." Journal of

Aircraft **50**(2): 337-353.
Woods, B. K., O. Bilgen and M. I. Friswell (2014). "Wind tunnel testing of the fish bone active camber morphing concept." Journal of Intelligent Material Systems and Structures **25**(7): 772-785.
Woods, B. K. S. and M. I. Friswell (2012). Preliminary investigation of a fishbone active camber concept. ASME 2012 Conference on Smart Materials, Adaptive Structures and Intelligent Systems, American Society of Mechanical Engineers.
Wright, O. and F. C. Kelly (1988). How we invented the airplane, Dover.
Zhang, J., S. Guest and M. Ohsaki (2009). "Symmetric prismatic tensegrity structures. Part II: Symmetry-adapted formulations." International Journal of Solids and Structures **46**(1): 15-30.
Zhang, L., B. Maurin and R. Motro (2006). "Form-finding of nonregular tensegrity systems." Journal of Structural Engineering-Asce **132**(9): 1435-1440.

Appendix

Wing twisting test result with 10m/s test speed

This set of data was recorded with ambient temperature 293.1K

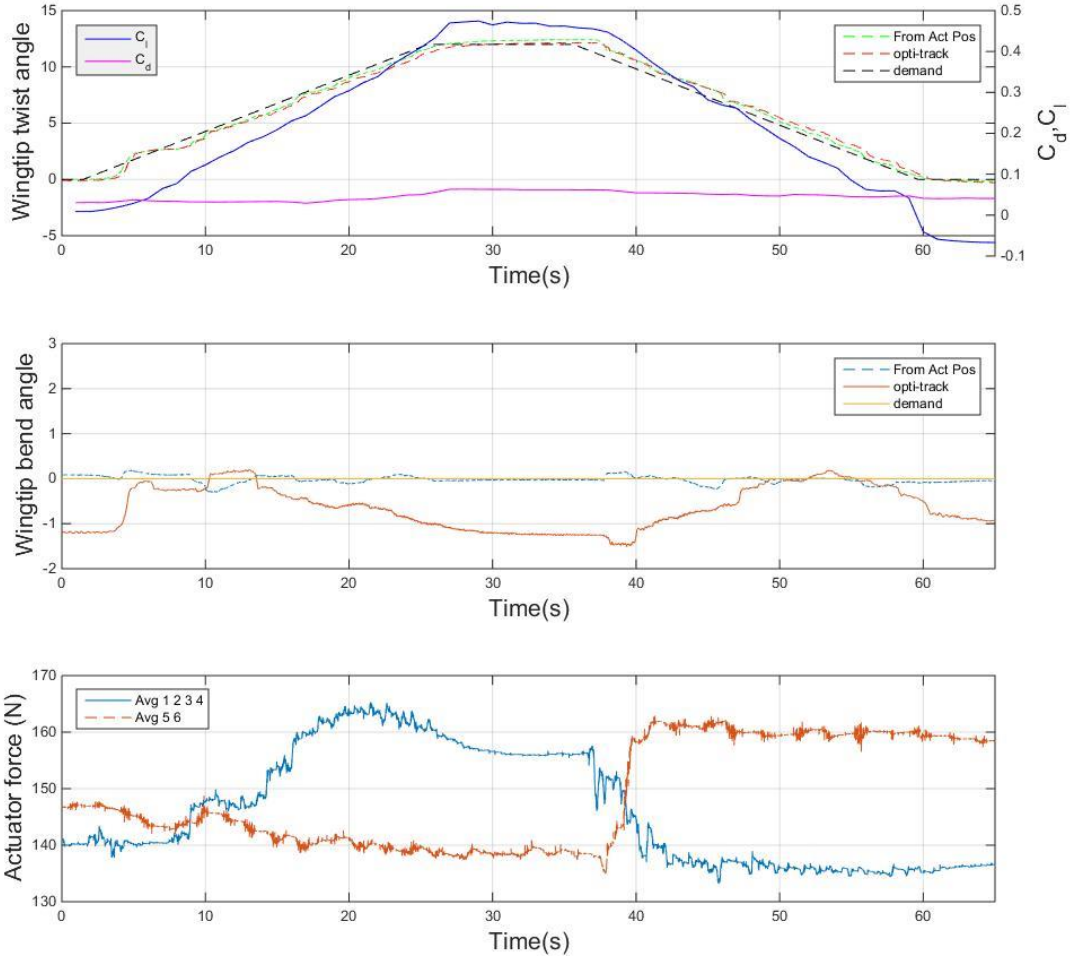

Figure A0.1Wingtip twist /bend optical track and sensor measure result with actuation force, at α_{root} =0°

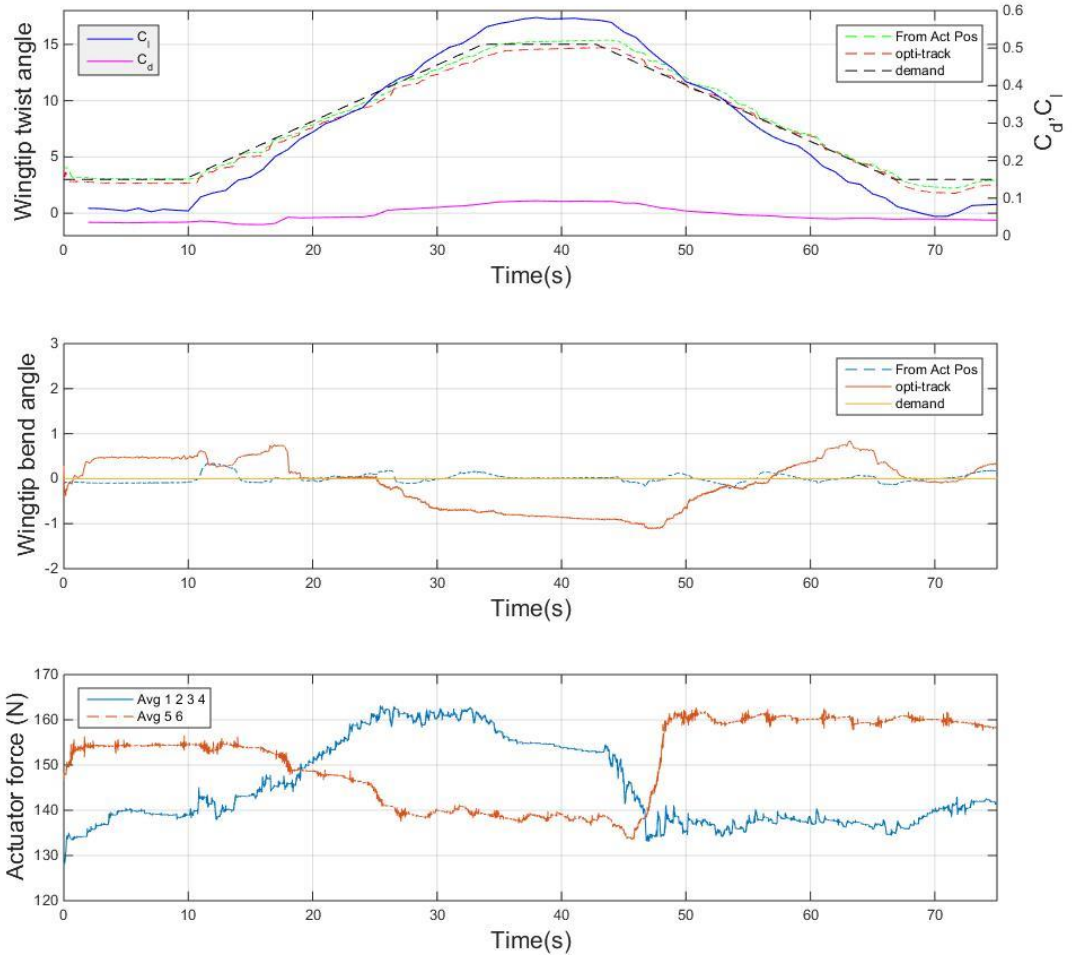

Figure A0.2 Wingtip twist /bend optical track and sensor measure result with actuation force, at α_{root} =3 °

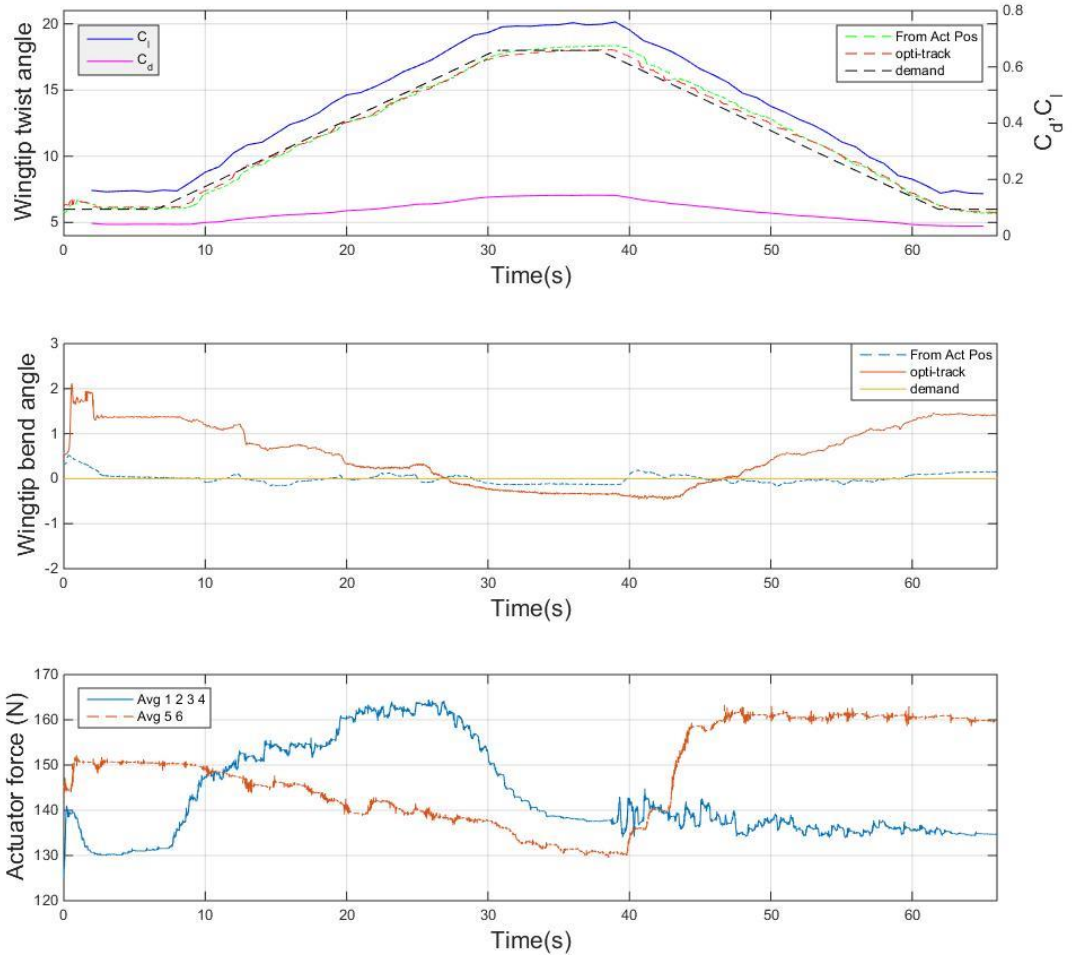

Figure A0.3 Wingtip twist /bend optical track and sensor measure result with actuation force, at α_{root} =6 °

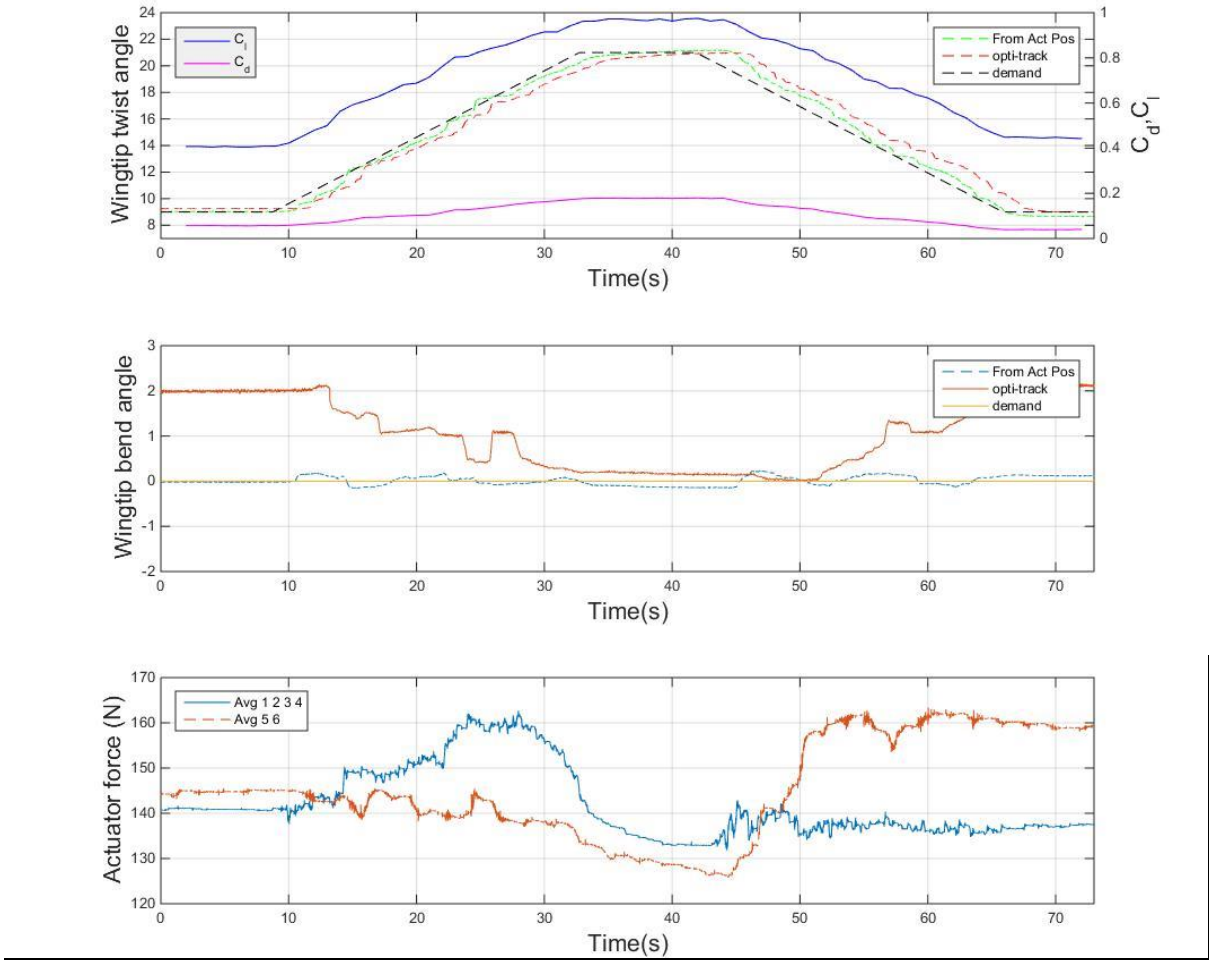

Figure A0.4 Wingtip twist /bend optical track and sensor measure result with actuation force, at α_{root} =9°